i)   Abstract

Due to widespread antibacterial resistance, the urgency to find novel methods of treating multidrug resistant bacteria is greater than ever before. Investigation into novel binding sites on pre-validated drug targets offers one possible new approach to successfully targeting resistant bacteria.

Herein, the exploration of two potential alternative binding sites (the NBTI binding site and the ATPase binding site) is discussed. Recent publications have highlighted possible toxicity issues of inhibitors of both sites, and addressing these problems forms the basis for the reported studies.

Novel bacterial type II topoisomerase inhibitors (NBTIs) of DNA gyrase subunit A, although well studied within the literature, are commonly found to be potent inhibitors of the human *Ether-à-go-go*-Related Gene (hERG) channel within the heart. Finding novel methods of alleviating this liability would prompt further investigation and allow the potential use of NBTIs within a clinical setting. An innovative tactic to prevent cardiotoxicity could be through using a soft drug approach. Reported herein are the discoveries of several chemical series with the potential to be optimised into antibacterial soft drugs. One such series has been successfully developed using computational and synthetic studies, prompting the synthesis and characterisation of (*S*)-REDX10371, an NBTI-type soft drug compound with the antibacterial potency, toxicity and stability profile required to allow *in vivo* PK properties to be assessed.

Inhibitors of DNA gyrase subunit B have also been well investigated. One series of inhibitors has been found to be particularly potent against *Mycobacterium tuberculosis*, but was observed to be cytotoxic to a hepG2 cell line. Due to the promising nature of the scaffold, further investigation was warranted. Studies surrounding the optimisation of the drug-like properties of a series of GyrB inhibitors were initiated, affording compounds with increased antibacterial activity against both gram-positive and gram-negative pathogens. These studies are presented herein through the enclosure of a short peer-reviewed publication.

ii) Declaration of authenticity

This thesis is the result of the author's original research. It has been composed by the author and has not been previously submitted for examination which has led to the award of a degree.

The copyright of this thesis belongs to the author under the terms of the United Kingdom Copyright Acts as qualified by University of Strathclyde Regulation 3.50. Due acknowledgement must always be made of the use of any material contained in, or derived from, this thesis.

Signed: Date:

iii)   Acknowledgments

I would like to sincerely thank both Professor William Kerr and Dr David Lindsay. I am most grateful for the opportunity to work with you both and appreciate the expert guidance you have provided.

Additionally, I would like to thank Mr Rolf Walker for his mentorship throughout the first year of my studies. I appreciate the time spent guiding me and reviewing reports, and for that, I am extremely grateful. It's easy to overlook your meticulous diligence until I note being made aware of an unreported proton signal for compound 96 on page 124 of an early draft of my thesis. Similarly, Dr Ian Cooper has provided expertise by being a fountain of knowledge on all things antibacterial, and for that, I can't thank you enough. For both of your continued support, even following what will hopefully be the most turbulent time in any of our careers, I am incredibly grateful. Also, thank you to Dr Thomas Pesnot and Dr Inder Bhamra for helping me guide the project, especially during the more unstable periods of my studies.

I gratefully acknowledge the support I have received from my colleagues in the lab, but in particular, Mr Paul Schofield and Dr Gary Noonan. The skilful guidance, expertise, reassurance and sweets I have received from you both has been indispensable to me, and has kept me sane and focussed throughout (most!) of my PhD. To both of you, and everyone I've worked with in the lab over the years, thank you.

Furthermore, I could not have written this thesis without results. The support from my colleagues in biology and DMPK has been overwhelming. In particular, Amy Cooke and Rebecca Taylor - thank you. Similarly, thank you to Mr John Maclean and Mr Andy Smith for their help and teaching in computational chemistry, Linux and all things geeky.

Robyn - for standing by me, having faith in me, listening to daily rants, putting up with the daily despair of the past couple of years, filling me with chocolate on the darkest days, and celebrating the lofty heights of finally obtaining relevant results - I cannot thank you enough. In many ways, we both wrote this.

Finally, and perhaps the biggest of all, a thank you to my mother, father, sister, friends and family. Understanding the crests and troughs of PhD life was always going to be an ambitious endeavour. Although it may seem abstract, your continuous support and belief in me has been overwhelming. In many ways, putting up with me has been more difficult than the entire process, and even throughout the worst moments of the project, your confidence in my success has been unwavering. Thank you.

iv)   Abbreviations

[α]	specific rotation
[M+H]+	positive mass ion
°C	degrees Celsius
μg	microgram(s)
μL	microlitre(s)
μM	micromolar
μm	micrometre(s)
μmol	micromole(s)
Å	Ångström(s)
A. baumannii	*Acinetobacter baumannii*
Ac	acetyl
ADHD	attention-deficit-hyperactivity disorder
ADME	absorption, distribution, metabolism and excretion
AIDS	acquired immunodeficiency syndrome
Ala	alanine
AM1	Austin Model 1
aq	aqueous
Ar	aryl
Arg	arginine
Asn	asparagine
Asp	aspartic acid
atm	atmosphere
ATP	adenosine triphosphate
ATPase	an enzyme that hydrolyses adenosine triphosphate
AUC	area under the curve of drug concentration vs. time graph
Boc	*tert*-butoxycarbonyl
bp	boiling point
Bu	butyl
CC_{50}	concentration of drug required for 50% reduction in cell viability
CD_3OD	deuterated methanol
$CDCl_3$	deuterated chloroform
CF	cystic fibrosis
$clogD_{7.4}$	calculated logD at pH 7.4
CLSI	Clinical and Laboratory Standards Institute
cm	centimetre(s)
COPD	chronic obstructive pulmonary disease
DCM	dichloromethane
DFT	density functional theory
DIPEA	*N,N*-di-*iso*-propylethylamine
DMF	dimethylformamide

DMPK	Drug metabolism and pharmacokinetics
DMSO	dimethylsulfoxide
DMSO-d_6	deuterated dimethyl sulfoxide
DNA	deoxyribonucleic acid
E. cloacae	*Enterobacter cloacae*
E. coli	*Escherichia coli*
E. faecalis	*Enterococcus faecalis*
EDG	electron donating group
EDTA	ethylenediaminetetraacetic acid
ee	enantiomeric excess
EPSRC	Engineering and Physical Sciences Research Council
eq	equivalent(s)
Et	ethyl
EWG	electron withdrawing group
FDA	Food and Drug Administration
FQ	fluoroquinolone
FTIR	Fourier transformed infra-red
g	gram(s)
Glu	glutamic acid
GSK	GlaxoSmithKline
GyrA	DNA gyrase subunit A
GyrB	DNA gyrase subunit B
h	hour(s)
H. influenzae	*Haemophilus influenza*
HEK	human embryonic kidney cells
hepG2	human liver cancer cell line
hERG	human *Ether-à-go-go*-Related Gene
His	histidine
HIV	human immunodeficiency virus
HMBC	heteronuclear multiple quantum coherence
HPLC	high-performance liquid chromatography
HRMS	high-resolution mass spectrometry
Hsp90	heat shock protein 90
Hz	hertz
IC_{50}	concentration of drug required for 50% inhibition
Ile	isoleucine
IPA	*iso*-propyl alcohol
IR	infra-red
IT	intratracheal
IV	intravenous
K	Kelvin
K. pnuemoniae	*Klebsiella pneumoniae*

LC	liquid chromatography
LCMS	liquid chromatography-mass spectrometry
$logD_{7.4}$	distribution coefficient at pH 7.4
Ltd	limited
M	mole(s) per litre
M. smegmatis	*Mycobacterium smegmatis*
M. tuberculosis	*Mycobacterium tuberculosis*
M.pt	melting point
m/z	mass/charge
MD	molecular dynamics
MDR-TB	multidrug-resistant tuberculosis
Me	methyl
Met	methionine
mg	milligram(s)
MHz	megahertz
MIC	minimum inhibitory concentration
MIC_{90}	minimum concentration required to inhibit 90% of the isolates
min	minute(s)
mL	millilitre(s)
mm	millimetre(s)
mM	millimolar
mmol	millimole(s)
MRSA	methicillin-resistant *Staphylococcus aureus*
MS	mass spectrometry
MW	microwave
NADPH	nicotinamide adenine dinucleotide phosphate
NBTI	novel bacterial type II topoisomerase inhibitor
ng	nanogram(s)
nM	nanomolar
nm	nanometre(s)
NMR	nuclear magnetic resonance
NMSF	National Mass Spectrometry Facility
NOE	nuclear Overhauser effect
NPT	constant-temperature, constant-pressure
ns	nanosecond(s)
P. aeruginosa	*Pseudomonas aeruginosa*
ParC	topoisomerase IV subunit C
ParE	topoisomerase IV subunit E
PBS	phosphate buffered saline
PDB	Protein Data Bank
Phe	phenylalanine
PK	pharmacokinetic

PON1	paraoxonase-1
PPB	plasma protein binding
ppm	parts per million
Pro	proline
ps	picosecond(s)
QNP	quadruple nucleus probe
rpm	revolution(s) per minute
RNA	ribonucleic acid
RT	room temperature
R_T	retention time
S. aureus	*Staphylococcus aureus*
S. pneumoniae	*Streptococcus pneumoniae*
SAR	structure-activity relationship
SCX	strong cation exchange sorbent
Ser	serine
SFC	supercritical fluid chromatography
SQD	single quadrupole detector
$t_{1/2}$	half-life
TB	tuberculosis
THF	tetrahydrofuran
TLC	thin layer chromatography
tol	tolyl
topo	topoisomerase
TPSA	topological polar surface area
Tris HCl	tris(hydroxymethyl)aminomethane hydrochloride
Tyr	tyrosine
wt%	percent by weight
XDR-TB	extensively drug-resistant tuberculosis

v)   **Contents**

Chapter 1: Introduction to antibacterial drug discovery

1   Introduction

1.1   The post-antibiotic age

The serendipitous discovery of penicillin **1** (**Figure 1**) in 1929 by Alexander Fleming marked a new age of medicine.[1] The human race was now able to treat certain gram-positive infections, allowing effective care for ailments which, previously, would have resulted in a significantly decreased life expectancy. This discovery paved the way for the golden age of antibacterial research, with most of these new pharmaceutical agents being derived from natural products. From a plethora of original discoveries came a new challenge; reducing the side effects and unwanted high doses associated with many naturally occurring antibiotics.[2] Medicinal chemists worldwide strove to adapt natural products in order to modify their biological properties, with great success. The development of semi-synthetic β-lactam ampicillin **2** (**Figure 1**) in 1961[3] signalled the ability to treat several gram-negative infections, resulting in common life-threatening infections being manageable for the first time in the history of the human race.
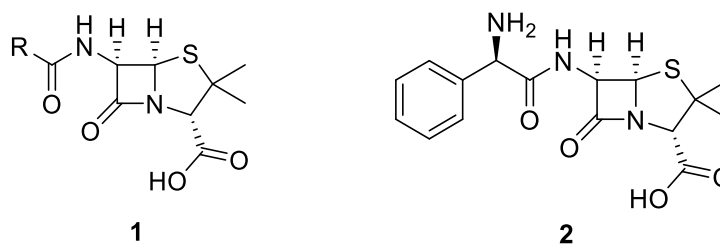
General structure of a penicillin **1** and ampicillin **2**.

Figure 1

As a result of these advances in antibiotics, routine surgery, chemotherapy, HIV patient care, organ transplants and premature infant care were all now possible without the high risk associated with deadly infections.[4] However, due to the rise of resistant bacteria, and low growth within the pharmaceutical sector for novel antibiotics, this era is coming to a rapid end. We are swiftly entering a dangerous post-antibiotic age, where deadly resistant infections could result in reduced life expectancy for the entire world population, regardless of wealth, gender and race.[2]

1.2   ESKAPE pathogens

Of particular danger are the so-called "ESKAPE" pathogens (*Enterococcus faecalis*, *Staphylococcus aureus, Klebsiella pneumoniae, Acinetobacter baumannii, Pseudomonas*

aeruginosa, and **_E_**nterobacter species).[5] A recent survey recorded that 7.5% of *P. aeruginosa* and 14.1% of *A. baumannii* pathogens in China were pandrug-resistant, meaning no clinically-used antibiotics were able to treat these infections.[6]

Enterococcus faecalis is a gram-positive bacterium that can cause serious urinary tract infections capable of developing into infections of the kidney. *Staphylococcus aureus*, a gram-positive pathogen, is perhaps one of the most notorious bacteria due to the publicity surrounding the "superbug" MRSA (methicillin-resistant *S. aureus*). Common symptoms of *S. aureus* infections include respiratory disease, skin infections, bloodstream infections and pneumonia. Currently, the mortality rate for *S. aureus* infections is higher than that for AIDS, tuberculosis and viral hepatitis combined, and this number will only increase with the emergence of more resistant strains.[7] Untreated *Klebsiella pneumoniae* (gram-negative) infections can result in bacterial pneumonia, which has a high mortality rate of up to 50%. Infection from the gram-negative bacterium *Acinetobacter baumannii* is commonly found within hospital settings, and can result in respiratory irritation, skin abnormalities, bacteraemia (bacteria in the blood) and urinary tract infections. *Pseudomonas aeruginosa* (gram-negative) infections are common in the intensive care setting due to the high-risk patients associated with this environment. Furthermore, chronic pulmonary infections from *P. aeruginosa* are frequently found in cystic fibrosis (CF) patients, with more than half of sufferers being infected with this bacterium.[8, 9] Finally, infections caused by *Enterobacter*, a gram-negative bacterium, commonly result in symptoms such as cough, purulent sputum (sputum containing pus and dead cells) and tachycardia. Due to the vast range of infections and symptoms caused by these bacteria, sepsis (blood poisoning) is common, resulting in a variable, though consistently high, mortality rate for the majority of victims. The effects of infections caused by the ESKAPE pathogens are summarised in **Table 1**.

Bacterium	Gram-positive or negative?	Results of bacterial infection
Enterococcus faecalis	Gram-positive	Urinary tract/kidney infections
Staphylococcus aureus	Gram-positive	Respiratory disease, pneumonia, septicaemia
Klebsiella pneumoniae	Gram-negative	Bacterial pneumonia
Acinetobacter baumannii	Gram-negative	Fever, skin irritation, respiratory complications
Pseudomonas aeruginosa	Gram-negative	Lung infections
Enterobacter	Gram-negative	Fever, tachycardia, cough

Summary of ESKAPE pathogens.

Table 1

1.3   Difficulties in antibacterial research

1.3.1   General complexities

Unfortunately, from a medicinal chemistry perspective, the area of antibacterial research is exceedingly complex. Very few other areas of medicine are presented with the challenge of having to affect live, multispecies targets, with varying active sites, cell permeabilities, efflux potentials and resistance determinations, while requiring the exceptionally low toxicities necessary for the high dosing strategies usually required to deliver efficacious blood concentrations.[4] As a direct result of these difficulties, a plethora of pharmaceutical companies have retreated from this area of research. Furthermore, the financial reward associated with obtaining a successful antibacterial therapy is low, due to the short course of treatment and the automatic recognition of any novel therapy as "last-line", preventing the drug from being used routinely in the clinic. Additionally, antibacterial drugs have a reduced lifetime compared to other pharmaceuticals due to antibacterial resistance, which will be discussed further below (**Section 1.3.3**).

Most effective antibacterial therapies rely on the drug's ability to cross the cellular membrane in order to bind to the biological target. This, in itself, is no easy feat. The cellular structures of gram-negative bacteria, gram-positive bacteria and mycobacteria differ greatly (**Figure 2**), presenting additional challenges in devising antibacterials that can target all pathogens - a so-called "magic bullet".

1.3.2   Differences in cellular structure

Gram-negative bacteria have a complex cellular structure (**Figure 2a**). Generally, the structure can be simplified into a thin layer of peptidoglycan (consisting of sugars and amino acids) sandwiched between two lipopolysaccharide-based membranes, termed the inner and the outer membranes. Due to the complexity of the gram-negative structure, a precarious balance of lipophilicity (in order to cross the inner and outer membranes) and polarity (in order to cross the peptidoglycan layer) is essential to ensuring permeability into the bacterial cell, thus increasing the challenge associated with antibacterial drug design. Porins are proteins that are present in the outer membrane of gram-negative bacteria that can form small channels across the cell membrane, through which a variety of molecules can pass.[10] Gram-negative bacteria have adapted these channels to allow the uptake of essential key nutrients; however, they can also allow the passage of a drug into the cell.

Gram-positive bacteria are slightly less complex targets from a medicinal chemistry perspective, as these pathogens are devoid of a lipophilic outer membrane (**Figure 2b**). Instead, a thick layer of peptidoglycan encases the lipophilic cell membrane. With one less hurdle to cross, gram-positive bacteria are, generally, more susceptible to a variety of antibiotics than their gram-negative counterparts.

Mycobacteria are structurally very different from both gram-positive and gram-negative bacteria (**Figure 2c**). As these pathogens have only a thin layer of peptidoglycan, the main difficulty in obtaining cell penetration is due to the thick layer of mycolic acid. Mycolic acid is a long-chain fatty acid, providing the mycobacterium with a waxy outer layer. This vast difference in cellular structure often results in antibacterial compounds that have been optimised for gram-positive and gram-negative bacteria having minimal activity against common mycobacteria, such as *Mycobacterium tuberculosis (M. tuberculosis)*, the pathogen responsible for tuberculosis infections.
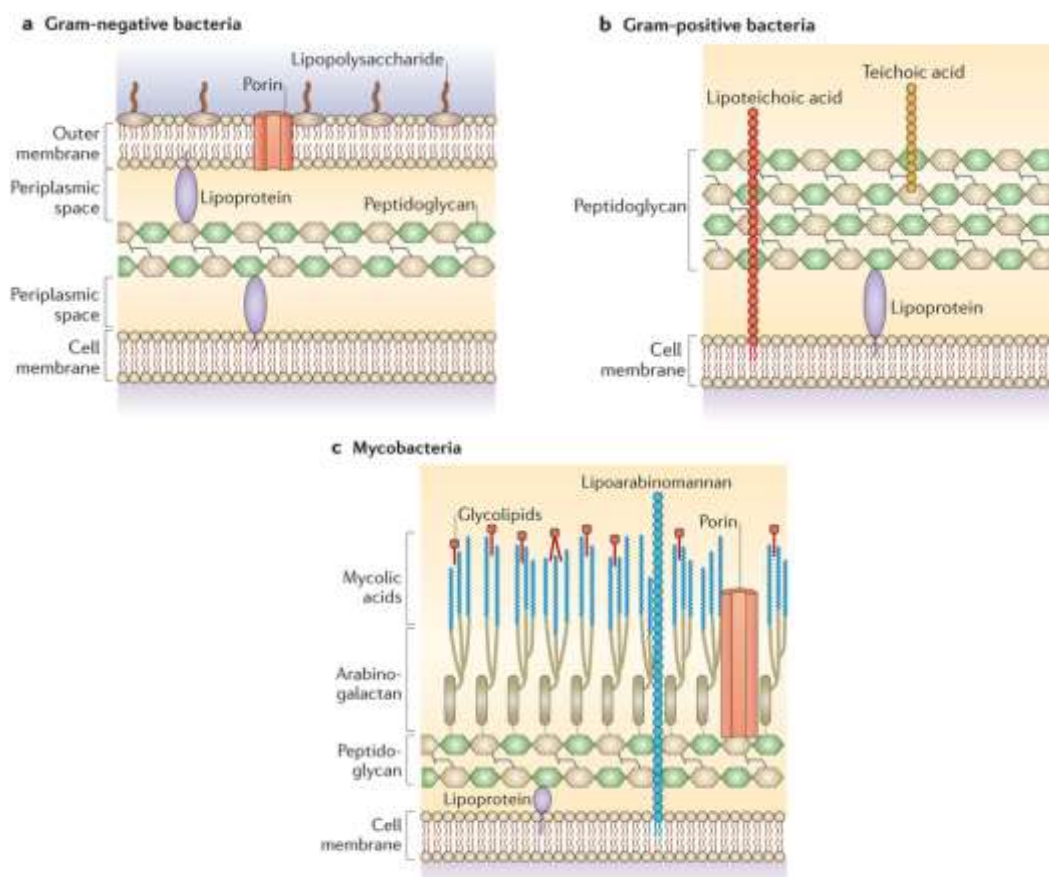
Diagrammatic representations of the cellular structures of a) gram-negative bacteria, b) gram-positive bacteria and c) mycobacteria. Used with permission from Brown *et al*.[11]

Figure 2

1.3.3   Antibacterial resistance

Research into antibacterial drugs would be more successful if the issues outlined above were the only hurdles to be overcome. Sadly, however, this is not the case. Bacteria have many possible methods of evading drug treatment, some of which are outlined below (**Figure 3**).
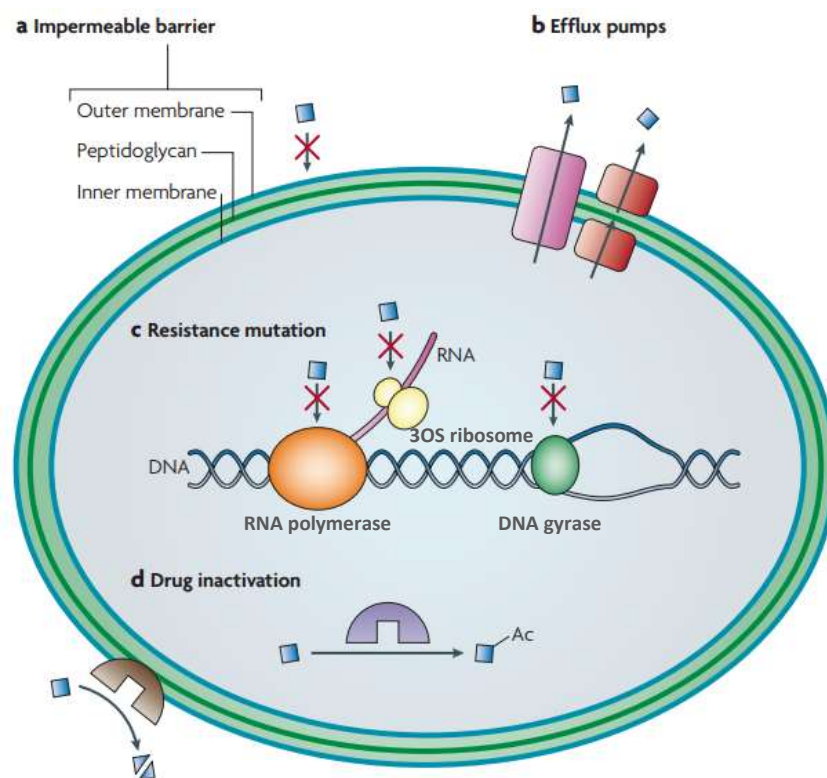
Common methods of antibacterial resistance; a) impermeable barrier, b) efflux pumps, c) resistance mutations and d) drug inactivation. Used with permission from Allen *et al*.[13]

Figure 3

Although the impermeable barrier has been previously discussed (**Section 1.3.2**), the bacteria in question may be able to further decrease susceptibility to a drug by removing or modifying porins, preventing drug entry to the cell (**Figure 3a**).[12] An extremely common method of resistance is removal of the drug from the cell through the use of efflux pumps (**Figure 3b**). These are naturally evolved proteins that are capable of efficiently removing toxic compounds from within the cell. Generally, lipophilic compounds are more likely to be effluxed from inside the cell. However, up-regulation of efflux pumps can result in broad substrate specificity and efflux is therefore a key driver of antibacterial resistance.[12] Specific mutation to the antibacterial target is another common cause for bacterial resistance to

antibiotics (**Figure 3c**). In this mechanism, a direct mutation of a key residue on the target protein may prevent efficient drug binding, eliminating potency against the target. This could be a mutation within the binding site of the protein, or, alternatively, on a distinct area of the protein that infers a structural change, preventing the compound from binding. Either method has a similar outcome: reduction of potency. Examples include direct mutations to DNA gyrase (**Figure 3c**, green), resulting in fluoroquinolone resistance, and mutations to RNA polymerase subunit B (**Figure 3c**, orange) or the 30S ribosomal subunit protein S12 (**Figure 3c**, yellow), which causes resistance to rifampicin and streptomycin A, respectively. A final method of antibacterial resistance is through secretion of drug inactivating enzymes (**Figure 3d**). A common example of this is the deactivation of β-lactams through the bacterial generation of β-lactamases. These enzymes are able to deactivate the drug through hydrolysis and opening of the lactam ring, neutralising its antibacterial properties.

Although the ability of bacteria to evade drug treatment is constantly growing, there has been historical success in treating bacterial infections. Furthermore, continued research into relevant biological pathways has resulted in increased opportunity for pharmaceutical intervention. For example, understanding of the underlying biological features of DNA and its manipulation has resulted in successful methods of selectively intervening in bacterial DNA processes, causing selective bacterial cell death.

1.4   DNA

The structure of DNA was established over fifty years ago. The double helical structure was famously hypothesised by Watson and Crick in 1953,[14] as a response to several alternative postulated structures.[15] The accepted proposal consisted of two phosphate sugar chains spiralled around a central axis, with base pairs forming hydrogen bonds between the helical strands (**Figure 4**).[14]
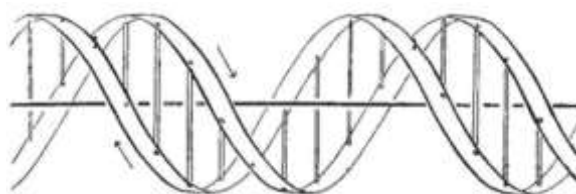
Hypothesised structure of DNA by Watson *et al*. Used with permission from Watson *et al*.[14]

Figure 4

This assembly was confirmed by X-ray crystallography in 1973, confirming the predictions made by Watson and Crick.[16] Many areas of research have since evolved from the elucidation of DNA's structure, including study into the cellular methods of DNA manipulation by proteins. DNA undergoes three main processes: replication, transcription and translation. Replication allows a DNA strand to be read and copied, forming two identical strands of DNA. Transcription allows messenger RNA, a copy of the primary DNA strand, to be made, following Watson-Crick base pairing rules. Proteins can then be made from translation of messenger RNA, allowing the encoding of an amino acid sequence. By understanding the role of DNA and the machinery available to manipulate it, drugs can be designed to intervene in those DNA processes. This hypothesis has paved the way for a variety of antibacterial drugs over the years, both naturally-occurring and fully synthetic. However, regardless of the progress of human-kind in devising effective antibacterial therapies, concerns surrounding bacterial resistance have been raised for almost as long, as confirmed by the reports of antibacterial resistance just one year after the introduction of the first antibacterial quinolone, nalidixic acid (**Figure 5**).
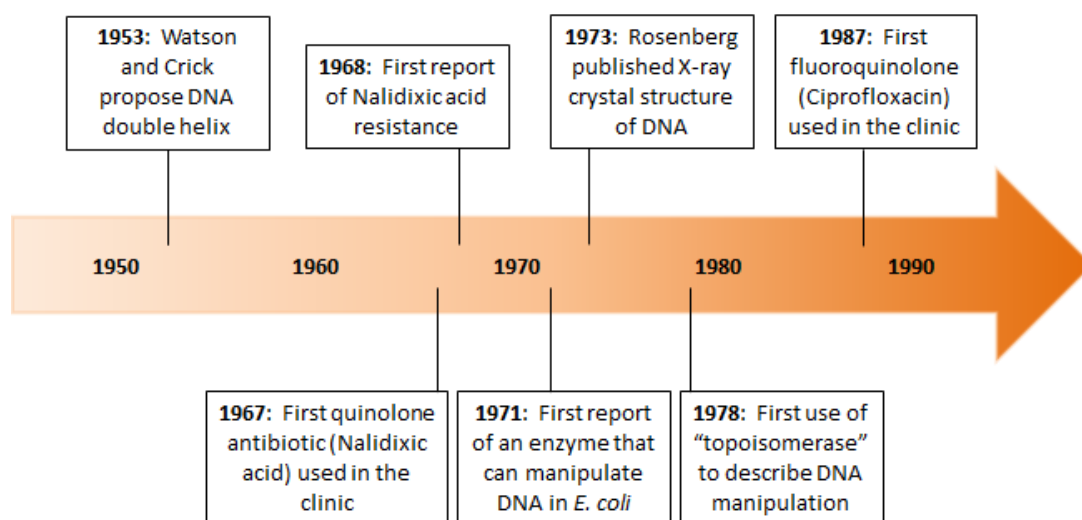
Timeline of DNA research and antibacterial discovery.[14, 16, 17, 18, 19, 20]

Figure 5

The absolute control of DNA structure and topology is essential for cellular life, and therefore both bacterial and human health relies on this fundamental principle. Simple DNA processes, such as transcription, translation and replication, rely on breaking of the DNA duplex in order to access the nucleotide sequence, resulting in alteration of the coiling of the DNA duplex.[21] An entangled chromosome can result in potentially cytotoxic or mutagenic material being released, therefore mechanisms for control and repair of DNA

topology are essential.[22] The structure of DNA itself can also pose a challenge, as it must be enzymatically manipulated to fit within the confines of the cell. These topological issues must all be overcome in order to maintain cell health. At the cellular level, DNA topology manipulation is achieved through the use of DNA topoisomerases.[23]

1.5 Topoisomerases

The first DNA topoisomerase was reported in 1978 by Wang,[20] and it has since been established that they are a family of enzymes present within all domains of life, having the unique ability to break, reorganise and religate DNA strands.[22] Broadly, topoisomerases can be subdivided into two families; type I and type II. Type I topoisomerases are responsible for introducing single strand fissions into a DNA sequence, whereas type II topoisomerases utilise the breaking of both DNA strands simultaneously in order to initiate their effect. Furthermore, each topoisomerase family is further split into subfamilies (A, B or C) depending on their mode of action, amino acid sequence, or global structure (**Table 2**).

Type	Mode of action	Substrate	Location
IA	Strand passage	Negative supercoiling	All domains of life
IB	Rotation	Positive/negative supercoiling	Mainly eukaryotes, some found in viruses/bacteria
IC	Rotation	Positive/negative supercoiling	*Methanopyrus*
IIA	Strand passage	Positive/negative supercoiling, intertwined chromosomes, DNA catenanes	All domains of life
IIB	Strand passage	Positive/negative supercoiling, intertwined chromosomes	Bacteria, archaea and plants

Topoisomerase families and functions.[22]

Table 2

Generally, many topoisomerases perform similar functions; the relaxing of positively and/or negatively supercoiled DNA, and, in the case of type II topoisomerases, the untangling of knotted DNA and the unlinking of DNA catenanes.[22] Bacterial DNA exists as circular, double helical loops and during DNA replication, over-winding occurs in front of the replication fork, causing tension that must be resolved (**Figure 6**). Topoisomerases are able to relieve the over/under-winding, allowing DNA replication to continue.
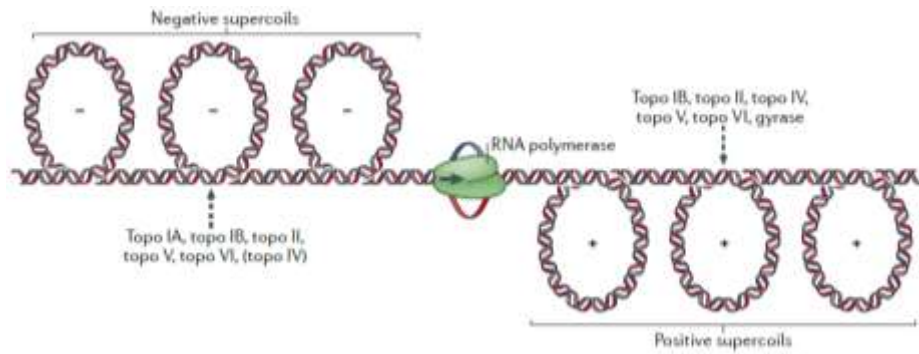
Positive and negative supercoiling, which are resolved by topoisomerases. Used with permission from Vos *et al*.[22]

Figure 6

Topoisomerases exert their effect through one of two mechanisms; strand passage or strand rotation (**Figure 7**). In the strand passage model (e.g. topo IA), one DNA strand is cut, followed by passage of the intact strand through the break. Religation of the DNA then occurs, resulting in the topologically altered duplex of DNA. Topo IA is able to use this mechanism to relax negatively supercoiled (i.e. under-wound) DNA, increasing the coil's stability by introducing additional turns in the helix. The strand passage method is also used by type II topoisomerases (e.g. topo IIA and IIB) to cause breaks in both strands of the duplex, followed by passage of another, intact, duplex through the break. This process allows complex intertwined chromosomes to be separated, and, similarly, allows DNA to be knotted in order to be compacted to fit within the confines of the cell wall.

Type IA (strand passage)   **Type IB (strand rotation)**
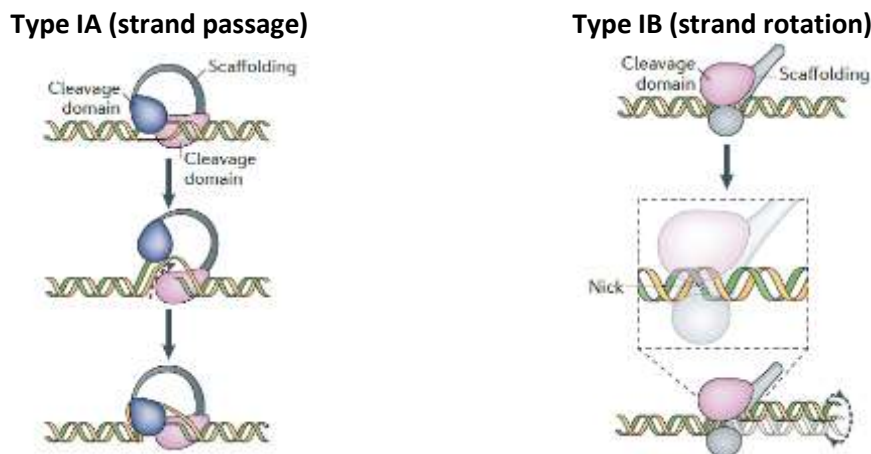
Schematic of strand passage and strand rotation mechanisms of DNA manipulation. Used with permission from Vos *et al*. [22]

Figure 7

The rotation method of manipulating DNA topology (e.g. topo IB) begins with the scission of a single DNA strand. The broken DNA strand can then rotate, with respect to the other strand, before being fused to reform the completed DNA duplex, with a resolved topological structure. Friction between the DNA strands controls the rotation and aids the alignment of base pairs in order for religation to occur.[22]

Type II topoisomerases are critical for maintaining the integrity of a DNA duplex, and therefore these enzymes' ability to manipulate DNA efficiently has a profound effect on the health of the host organism. DNA gyrase and topoisomerase IV are two examples of bacterial type IIA topoisomerases that are present in most bacterial strains. DNA gyrase and topoisomerase IV are highly homologous enzymes which consist of a tetramer (A_2B_2) structure, formed by two pairs of identical subunits. For DNA gyrase, these are named GyrA and GyrB, whereas for topoisomerase IV, they are designated ParC and ParE. Without these enzymes, bacteria are not able to appropriately manipulate the topology of their DNA, resulting in eventual cellular death. Some strains, such as *M. tuberculosis*, only have one type IIA topoisomerase: DNA gyrase. It has been hypothesised that topoisomerase IV evolved from DNA gyrase, resulting in two, almost homologous, type IIA topoisomerases. However, this evolutionary process did not occur in *M. tuberculosis*, leaving only one type IIA topoisomerase enzyme, DNA gyrase.[24] Regardless of the number of topoisomerases available to the bacterial strain, interfering with the ability to manipulate DNA has proved a successful mode of action for many clinically-used drugs.

1.5.1 Topoisomerase as a drug target

DNA gyrase and topoisomerase IV have been shown to be excellent antibacterial drug targets. A key reason for this is that both bacterial and mammalian cells have no alternative method of DNA topology manipulation.[22] Inhibition of DNA gyrase and topoisomerase IV therefore results in the bacteria being unable to maintain cellular health, resulting in eventual bacterial death. Furthermore, DNA gyrase and topoisomerase IV are highly homologous enzymes, meaning a dual targeting approach can be taken to designing antibacterial inhibitors.[25]

For a classical inhibitor, with a single binding site on a single enzyme, antibiotic resistance can become prevalent at an alarming rate. With bacterial replication rates for *S. aureus* of approximately one division every 30 min, the number of bacterial cells can exceed one million after just 10 h.[26] Due to a large turnover of bacterial iterations, the consequently

high probability of a mutation within the genetic sequence, resulting in a mutation in the active site of the enzyme, can result in rapid antibiotic resistance. Once a single bacterium has become resistant to the inhibitor, it is able to pass the genetic information to a different species of bacteria through horizontal gene transfer.[27] This is a process by which bacteria can transmit genetic material to other bacteria, allowing the passage of genetic resistance mechanisms to other bacteria.[27] Similarly, bacteria susceptible to antibiotic treatment are removed from the bacterial pool, enriching the amount of resistant bacteria in a Darwinian fashion. A novel approach to reducing the likelihood of resistance is to adopt a dual targeting strategy. For this method of drug targeting, two very similar binding sites on two highly homologous enzymes, such as DNA gyrase and topoisomerase IV, are targeted. By targeting both enzymes, the probability of mutations occurring in the active sites of both enzymes during a single replication cycle of the bacterium is extremely low, resulting in very low antibacterial resistance to a dual inhibitor.[28] A dual targeting approach is commonly used to ensure a low frequency of resistance when targeting gram-positive and gram-negative pathogens. However, the limitations of this method should be acknowledged when targeting mycobacteria such as *M. tuberculosis*. As *M. tuberculosis* contains only a single type IIA topoisomerase, DNA gyrase, a dual targeting strategy cannot be employed, and indeed, targeting a single enzyme may lead to faster accumulation of resistance. Existing reports in the literature confirm this, with frequency of resistance data for ciprofloxacin, a dual inhibitor, against *M. tuberculosis* in the range of 1 resistant colony in 10^6 to 10^8 colonies.[29] This is more frequent than observed for *E. coli* (1 in 10^9 to 10^{10}), implying the inability to dual target *M. tuberculosis* may pose an issue.[30] Although resistance may be acquired more quickly, this is an issue of lesser importance, due to the urgent need for an effective treatment for *M. tuberculosis* infections, as outlined by the World Health Organisation (WHO).[31]

A final reason to target topoisomerases is related to the success of fluoroquinolones in treating bacterial infections. Fluoroquinolones bind to well validated binding sites on DNA gyrase and topoisomerase IV, and exert the desired phenotypical response of bacterial cell death. This compound class has been well studied in the literature and has had success in the clinic. As the topoisomerase IIA target has previously been validated, alternative inhibitors that bind to different binding sites on DNA gyrase and topoisomerase IV could be effective antibacterial treatments, in light of increasing fluoroquinolone resistance.

1.6   Alternative binding sites

Due to increasing pressure from antibacterial resistance to fluoroquinolones, avoiding the well-established fluoroquinolone (FQ) binding site in topoisomerase IIA enzymes is becoming increasingly vital. Single residue mutations in the FQ active site have been shown to greatly affect the potency, and therefore utility, of an entire class of therapeutics, highlighting the need for inhibitors which bind to a novel site in the target enzyme.[32] Fortunately, alternatives to the FQ site, binding to which have been shown to exhibit the same phenotypical response, have been disclosed extensively in the literature.[33] In particular, two major binding sites have been thoroughly investigated as alternatives to the FQ site; the novel bacterial type II topoisomerase inhibitor (NBTI) binding site on GyrA/ParC and the adenosine triphosphate (ATP) site on GyrB/ParE (**Figure 8**).
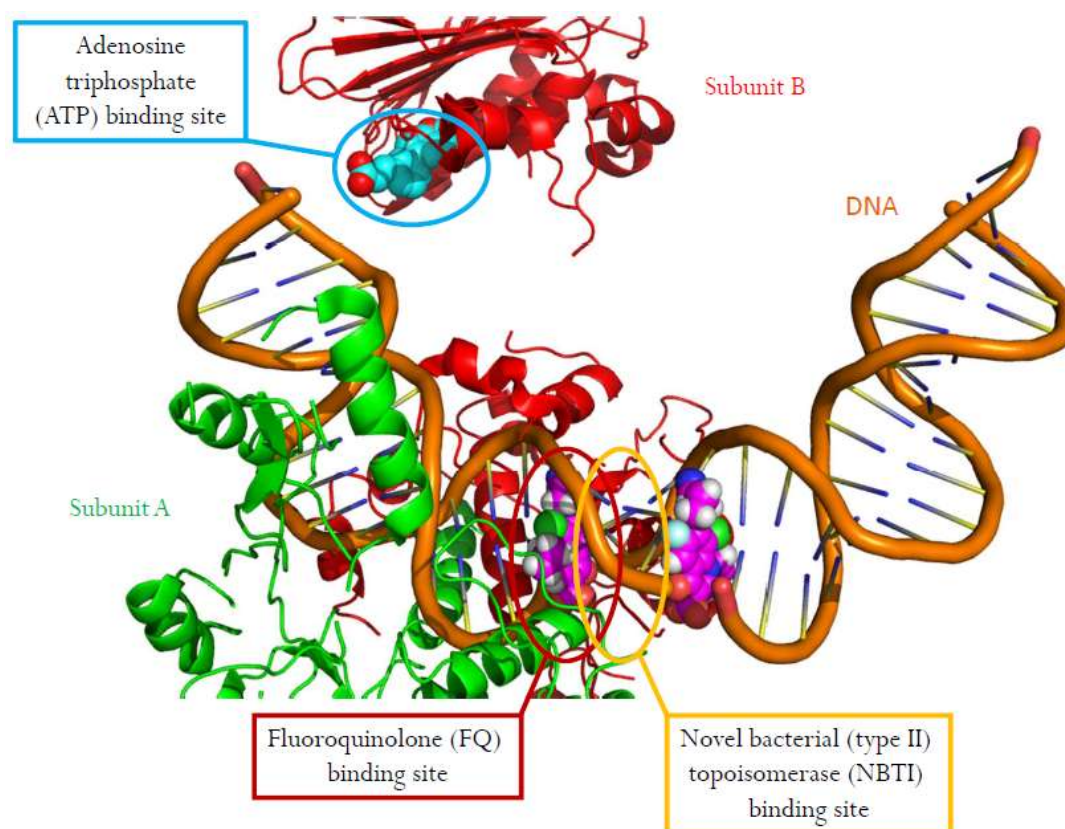
Diagram of DNA gyrase (PDB: 3FOE[34] and 4K4O[35]), visualised using Pymol (v1.1eval). GyrA (green), GyrB (red) and DNA (orange), with the relative positions of the active sites highlighted.

Figure 8

The NBTI binding site (**Section 2.1**) is located on the GyrA/ParC subunits of DNA gyrase/topoisomerase IV. Binding to this site has been shown to result in bacterial cell

death, albeit through a modified mechanism of action to fluoroquinolones.[36] NBTI inhibitors allow bridging between DNA and the topoisomerase enzyme, preventing the final release of the topologically altered DNA from the enzymatic cycle.[36] Without the release of the DNA from the enzyme, the enzyme is effectively poisoned, and bacterial cell death occurs.

Although much research has been performed on the NBTI series throughout recent years (**Section 2.1**), potent cardiotoxicity has resulted in minimal clinical success (**Section 2.2**). Consequently, a novel approach to alleviating series-wide cardiotoxicity was in high demand, and drove the development of soft drug inhibitors of the NBTI binding site (**Section 2.6**). A soft drug approach to NBTI research should result in minimal systemic exposure to the parent compound, reducing the cardiotoxicity risk associated with the chemical series. For this approach to be successful, a balanced strategy of optimising the antibacterial activity, cardiotoxicity, stability and physiochemical properties of the series, would be required (**Section 2.10**).

A second potential binding site (**Section 4.1**) has been reported by Lewis *et al*., suggesting that inhibition of the ATP site on the GyrB/ParE subunit of topoisomerase II enzymes resulted in the inability of the enzyme to process the hydrolysis of ATP.[37] As ATP is used as the primary source of energy for the topoisomerase function, deprivation of this energy source induces enzymatic failure, ultimately resulting in bacterial apoptosis. As a result, inhibitors of the ATPase site on DNA gyrase/topoisomerase IV were established as viable drug targets.[38]

Throughout the research programme, cytotoxicity was highlighted as a potential liability of a series of GyrB/ParE inhibitors (**Section 4.4**). As a result, further investigation into the relationship between the structure and the cytotoxicity of the series was pursued. Due to the impact of the research within the field, the findings have been published in a peer-reviewed paper, and will be included herein (**Section 4.7**).

Chapter 2:
A soft drug approach to bacterial pneumonia -
in vitro proof of concept

2   Inhibitors of GyrA/ParC

2.1   The NBTI binding site

An alternative to the fluoroquinolone binding site is the NBTI binding site. Although comparatively recent, research into this binding site has attracted considerable interest from the research community for almost 20 years,[39] due to the pressing demand for alternative bacterial topoisomerase inhibitors. As a result of studies reported by GlaxoSmithKline (GSK),[36] an X-ray crystal structure illustrating the key binding regions observed for a typical NBTI scaffold was disclosed (**Figure 9**).
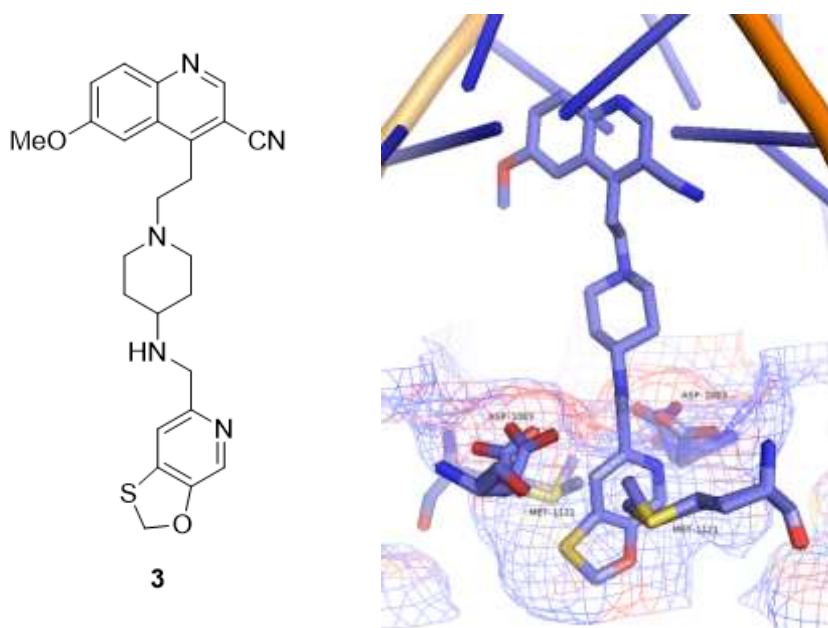
X-ray crystal structure (PDB: 2XCS) visualised using Maestro (v10.6) of GlaxoSmithKline NBTI **3** crystallised with *S. aureus* gyrase A active site.[36]

Figure 9

Two main areas of binding were observed for the GlaxoSmithKline NBTI **3** (**Figure 9**). Firstly, the southern bicyclic ring system accommodated a lipophilic pocket formed by Met1121 and other hydrophobic residues in the active site of the enzyme. A key binding interaction was observed in the form of a hydrogen bond between the aminopiperidine and Asp1083. Due to the symmetrical nature of the binding site, the mirror image of the above scenario was also possible, with binding to Asp1083 on the opposite face of the molecule. A second interaction (either direct or water-mediated) was hypothesised to occur between the pyridine nitrogen and Asp1083, strengthening binding with the active site. In addition to these interactions, the quinoline ring system was intercalated between the strands of DNA.

Due to the non-specific binding nature of the intercalation interaction, considerable effort has been directed towards optimising the physiochemical properties of the series through manipulation of the quinoline structure. The linear nature of the NBTI scaffold allowed the northern portion of the molecule to intercalate between the DNA base pairs, while the southern tail interacted with residues in the lipophilic pocket of the enzyme. By bridging between the DNA and the enzyme, the final release of the topologically altered DNA from the enzymatic cycle was prevented.[36] Without the release of the DNA from the enzyme, the enzyme was effectively poisoned, and bacterial cell death occurred.

2.2 Toxicity issues in NBTI research

Although the area of NBTI research is still developing, with recent publications suggesting a continued high interest in the field, the issue of cardiotoxicity can be observed throughout the literature in this area (**Figure 10**).[40-43]

NXL101 – Novexel   **Cyclohexanes – GSK**   **Cyclobutanes – Pfizer**

4   **5**   **6**

MIC *S. aureus* ≤ 0.25 µg/mL[44]   MIC *S. aureus* = 0.12 µg/mL[40]   MIC *S. aureus* = 0.09 µg/mL[42]

Withdrawn from Phase I due
to hERG liability[45]   hERG IC_{50} = 2 µM[40]   hERG IC_{50} = 47.6 µM[42]

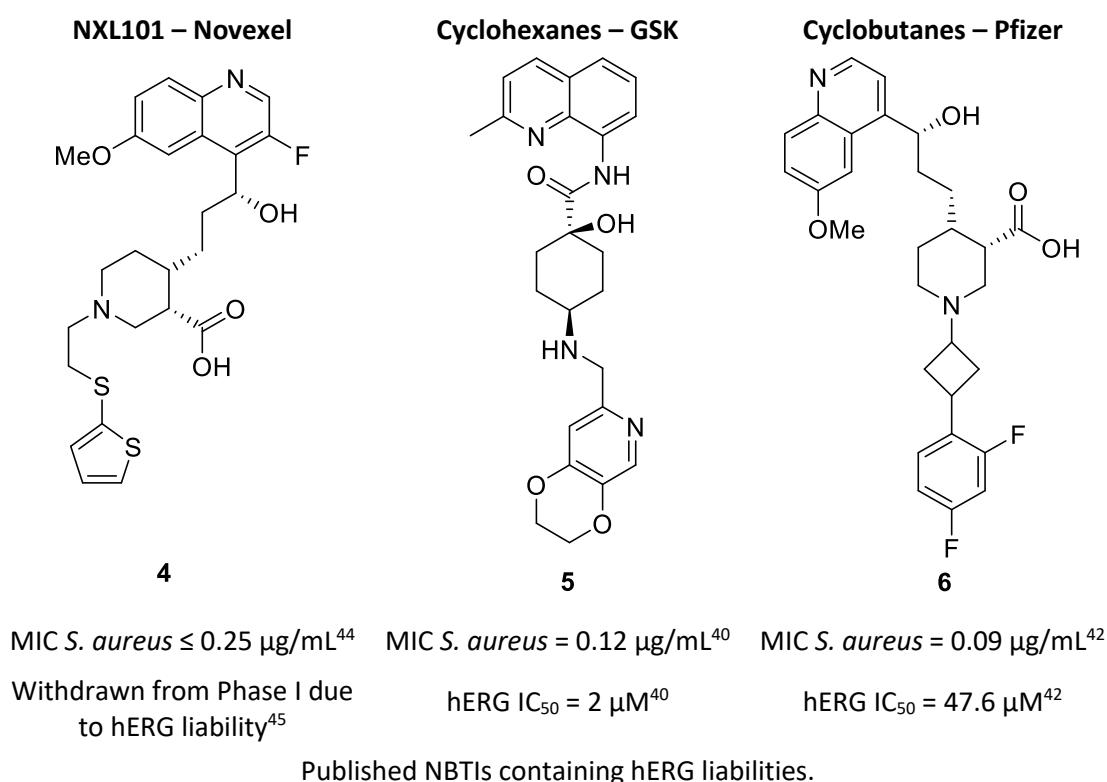Published NBTIs containing hERG liabilities.

Figure 10

Many pharmaceutical companies have published data on their NBTI series, highlighting a high level of bioisosterism within NBTI research, and many northern, southern and linker groups are well tolerated (**Figure 10**).[33] However, the success of the NBTI class of therapeutics has thus far been severely limited due to recurring issues of toxicity,

particularly through the inhibition of the human *Ether-à-go-go*-Related Gene (hERG) channel within the heart. The hERG channel is a potassium ion (K^+) channel that is involved in the repolarisation phase of the standard cardiac action potential. Inhibition of the hERG ion channel has been linked with prolongation of the QT phase on an electrocardiogram, which can result in episodes of *torsades de pointes*, an irregular heartbeat that can lead to arrhythmias, fainting, and in severe cases, ventricular fibrillation and sudden cardiac death.[46] Attempts to lower cardiotoxicity using the methods outlined below have yielded a plethora of NBTI compounds, however, most suffer still from hERG liabilities.

2.3 Strategies for minimising hERG inhibition

2.3.1 Cardiotoxicity

During the early stages of the drug discovery process, assessing a compound's toxicity becomes of utmost importance. Highly cytotoxic (e.g. against the hepG2 cell line) or cardiotoxic (e.g. hERG inhibiting) scaffolds can be difficult to optimise while maintaining high potencies. The complexities and relevance of this type of optimisation within the pharmaceutical industry can be seen extensively in the literature.[41, 47, 48]

2.3.2 Manipulation of polarity

Although the hERG channel is known to possess a promiscuous binding site, with many potent, structurally varied inhibitors, several well-studied strategies have been adopted to disfavour binding to this target.[48] Increasing the polarity of the molecule (i.e. lowering of $logD_{7.4}$ and increasing topological polar surface area (TPSA)) are common methods used to prevent hERG inhibition due to the hERG channel's affinity for lipophilic, rod-like molecules. Increasing the hydrophilicity of the compound can discourage strong binding interactions with the hERG channel (**Figure 11**). However, when adopting this strategy in antibacterial research, an appreciation of how minor changes in $logD_{7.4}$ may affect potency is vital. Each bacterium is permeable to a narrow window of compounds that are of acceptable polarity to diffuse across the cell membrane.[49] Making minor alterations in $logD_{7.4}$, although improving hERG inhibition, can have a negative effect on a compound's ability to permeate the bacteria, possibly to the detriment of antibacterial activity. Thus, although manipulating $logD_{7.4}$ has been a successful strategy in preventing hERG inhibition in other therapeutic areas,[50] this approach can be problematic in antibacterial research. Indeed, the literature in this area documents numerous failed attempts to optimise antibacterial activity and hERG inhibition simultaneously.[40-43] Recent efforts in NBTI research have sought to lower $logD_{7.4}$,

mainly through increasing the hydrophilicity of the northern head group, in order to reduce affinity for the hERG channel while maintaining the key binding interactions required for antibacterial activity.[41]
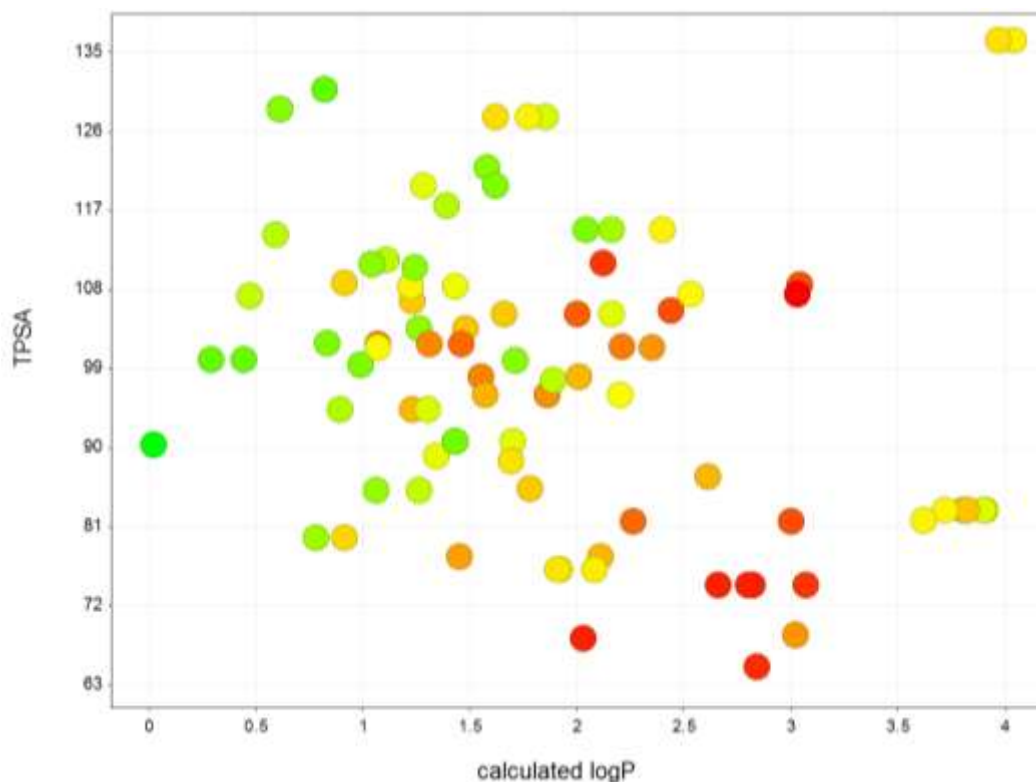
A graph depicting the trend between calculated logP (clogP), TPSA and hERG channel affinity (coloured green for low inhibition to red for higher inhibition) for published NBTI compounds. In general, a decrease in clogP and an increase in TPSA resulted in lower inhibition of the hERG channel.

Figure 11

Statistical analysis of published NBTI-type compounds allowed a trend to be observed between the clogP, TPSA and hERG channel inhibition. In general, compounds with higher TPSA (> 90) and lower clogP (< 1.5) had lower hERG affinity than those compounds with higher clogP (> 2) and lower TPSA (< 90), highlighting the important relationship between polarity and hERG inhibition (**Figure 11**).

A similar method to disfavour binding to the hERG channel is through the introduction of zwitterions. This has a similar effect to lowering the $logD_{7.4}$ of the compound, and as a result, zwitterionic compounds tend not to bind as strongly to the hERG channel. Although this is a common strategy, introduction of a zwitterion can have the same unfortunate effect as lowering $logD_{7.4}$, reducing permeability and lowering bacterial exposure to the

drug. A carefully considered charge-distribution approach must therefore be used to ensure diffusion into the cell is successful.

2.3.3 Manipulation of basicity

Although harder to predict, making minor changes to the pK_a of amines in the molecule can have remarkable effects on hERG inhibition, as observed by Zhang *et. al.*[51]

7	**8**
pK_a = 9.41	pK_a = 7.45
hERG activity = 0.025 µM	hERG activity = 0.85 µM

Optimisation of hERG inhibition by manipulation of pK_a.
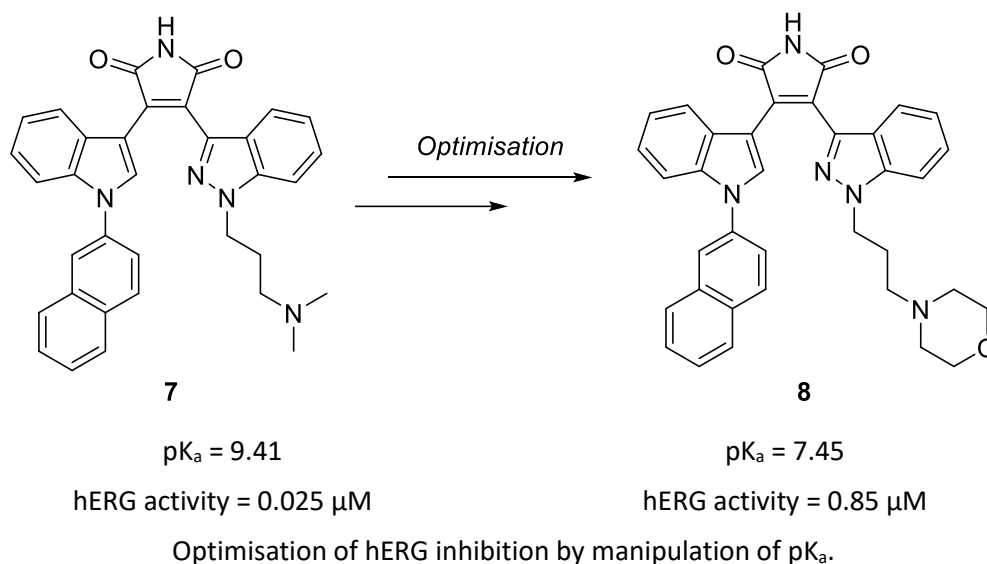
Figure 12

Altering the pK_a of the tertiary amine in lead compound **7** (**Figure 12**) was hypothesised to disrupt the π-cation interactions between the charged amine in the target molecule with aromatic regions of the hERG channel.[48] Reducing the pK_a of the amine from 9.41 to 7.45 resulted in an approximate 5-fold reduction in hERG activity from 0.025 µM to 0.85 µM.

Nearby substitution with electron-withdrawing groups may reduce the proportion of cationic amine at physiological pH, preventing π-cation interactions with the hERG channel. Similarly, removing the amine, or shielding through introduction of a hydroxy- or alkoxy-substituent nearby to the amine, may also disrupt the π-cation interactions and reduce hERG inhibition. Utilising this method of reducing hERG inhibition could prove useful in NBTI research. However, as the amines in the NBTI structure provide key binding interactions with the active site (**Section 2.1**), modifying these positions often results in significant loss of activity.

2.3.4   A successful NBTI?

Although several NBTIs have entered clinical trials, only one has progressed as far as Phase II. After extensive research and fine tuning of physiochemical properties, researchers at GlaxoSmithKline developed an NBTI featuring a tricyclic northern group **9** (**Figure 13**).[52]

9
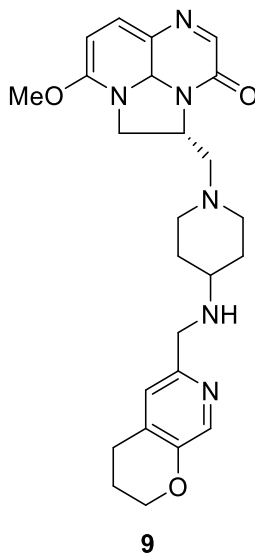
S. aureus MIC_{90} = 0.5 µg/mL[53]

hERG IC_{50} = 1400 µM[33]

Phase II GSK compound (GSK2140944 **9**).

Figure 13

GSK2140944 **9**, also known as gepotidacin, was found to display broad-spectrum activity against a variety of gram-positive and gram-negative pathogens, including high potencies for *S. aureus* and MRSA pathogens, while maintaining a low hERG IC_{50} of 1400 µM. The combination of high potency and low cardiotoxicity has provided a large enough safety window to progress the compound into clinical trials, which are currently ongoing.[33, 52]

From the extensive research in the area, and due to the unpredictable nature of hERG inhibition, particularly with respect to antibacterial drug design, alternative methods of circumventing cardiotoxicity risks are in high demand. An unfortunate result of the amine-rich, linear nature of NBTI structures, is their affinity for the hERG channel through hypothesised π-cation interactions. As the amines in the NBTI structure are integral to binding (**Section 2.1**), altering these positions in the molecule may eliminate antibacterial activity. However, a novel and innovative method that could deliver a successful, non-cardiotoxic NBTI therapy is through using a soft drug approach.

2.4   Soft drug design

A soft drug has been defined by Bodor and Buchwald as the following:[54]

"[Soft drugs] are isosteric-isoelectronic analogues of a lead compound, and they are deactivated in a predictable and controllable way after achieving their therapeutic role."

Simplistically, soft drugs can be thought of as the opposite of prodrugs. The drug should be applied directly to the site of action, where it can have the desired effect immediately. However, it differs from a normal therapy in a critical way. Whereas a regular drug would pass into the blood and result in systemic exposure, an ideal soft drug is destroyed immediately in the blood to give an inactive compound. This has considerable consequences in minimising side effects caused by systemic exposure, and instead only the inactive compound is circulated in the blood. In relation to hERG inhibition for an NBTI-type compound, even though a potential soft drug may be hERG active, it would undergo controlled degradation to result in a hERG inactive compound reaching the heart, lowering the risk associated with cardiotoxicity. Although the use of a soft drug approach to minimising systemic side effects has been published,[55] using this approach to derisk a series with potent hERG channel inhibition has yet to be reported within the literature.

2.4.1   Soft drug successes

Utilising a soft drug approach to drug design can minimise the systemic exposure of a compound to the patient by using well-defined deactivation mechanisms to render the substance inactive and non-toxic. Proof of concept in this area has been achieved in the clinic through the success of loteprednol etabonate **10** (**Figure 14**) which uses esterases to initiate hydrolysis, forming the inactive metabolite **11** (**Figure 14**) from the active parent soft drug.[55]
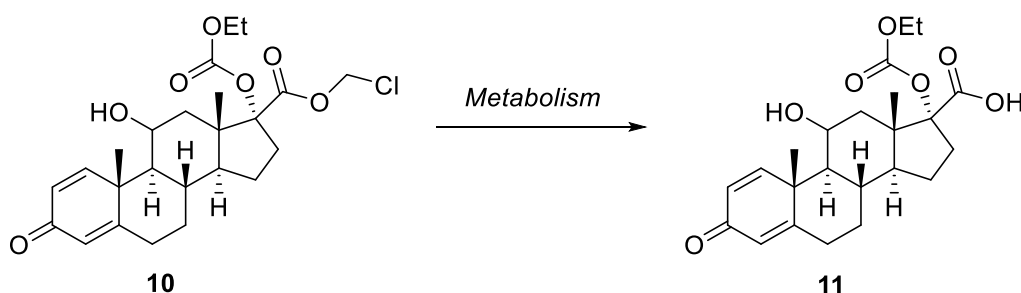

Metabolic hydrolysis of loteprednol etabonate **10** to inactive metabolite **11**.

Figure 14

Loteprednol etabonate **10** was shown to be a potent topical corticosteroid used to reduce inflammation and allergic responses of the eyes, while not affecting intraocular pressure through minimising systemic exposure. The success of loteprednol etabonate in the clinic provided proof that soft drugs can be viable therapies.

The potential use of soft drugs has since been reinforced. Based on the success of the soft drug concept with loteprednol etabonate **10**, a serendipitously discovered soft drug could potentially make it to the clinic, without full knowledge of its metabolic pathways.[56] For example, methylphenidate **12** (**Figure 15**), a psychostimulant commonly used for the treatment of attention-deficit-hyperactivity disorder (ADHD), can be considered a soft drug, even though it was never designed as such.[56]
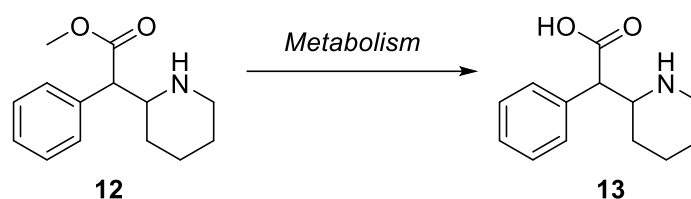
Metabolic hydrolysis of methylphenidate **12** to inactive metabolite **13**.

Figure 15

The methyl ester in methylphenidate was rapidly hydrolysed to its inactive metabolite, ritalinic acid **13** (**Figure 15**). The rapid metabolism of methylphenidate resulted in a larger therapeutic window, allowing safer use for paediatric patients. However, this also resulted in the unfortunate drawback of the requirement for regular administration to maintain a therapeutic dose.

Many successful soft drugs have utilised the ester-hydrolysing capabilities of esterases. These enzymes are found in most bodily tissues, usually resulting in the rapid metabolism of the compound, as observed for methylphenidate.[57] An issue arising from the use of esterases is that, due to the variable concentrations of these enzymes within the body, the rate of metabolism can be inconsistent within the human population.[58] However, theoretically, any enzyme capable of hydrolysing a metabolically liable compound can be exploited. This conclusion helped lead researchers at GlaxoSmithKline to discover a metabolic liability within their corticosteroid series (**Figure 16**).[59]
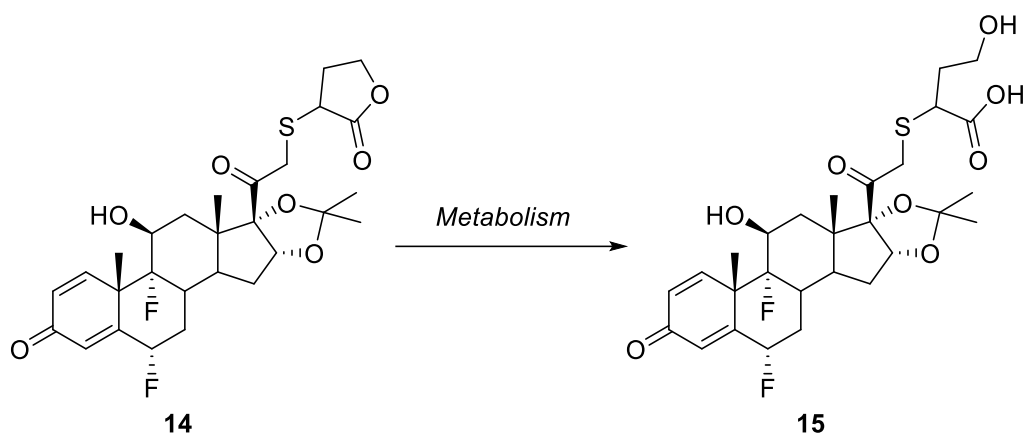
Potential "soft" corticosteroid **14** and hydrolysed metabolite **15**.

Figure 16

It was established that corticosteroid **14** (**Figure 16**) was stable within S9 lung fraction ($t_{1/2}$ > 480 min), suggesting its suitability as an inhaled asthma treatment. However, it was observed that the compound was hydrolytically metabolised within human plasma to metabolite **15** ($t_{1/2}$ < 1 min). Upon further investigation, it was concluded that the enzyme paraoxonase was responsible for the selective metabolism, serendipitously resulting in a potential soft drug therapy. Paraoxonase is an esterase found in high concentrations in the blood plasma, however, its concentration in the lungs is relatively low.[57] The possibility for soft drug use was reinforced by the receptor affinities of both compounds. The parent compound **14** was measured to have an IC_{50} of 6.6 nM, whereas the hydrolysed compound **15** (**Figure 16**) had a much higher IC_{50} of 827 nM, suggesting the act of hydrolysing the γ-lactone resulted in deactivation of the substrate, and that this process could thus prevent systemic exposure to the parent compound.[59]

2.4.2 Terfenadine

As illustrated by the previous examples, the viability of the soft drug therapy strategy is well-established. However, to date, a selectively metabolised antibacterial agent has not been disclosed in the literature. Fortunately, attempts to repurpose the antihistamine terfenadine **16** (**Figure 17**) for antibacterial use has yielded an interesting and highly relevant crossover with the current research programme.

Terfenadine **16** was initially marketed as an antihistamine, however, it also had modest antibacterial properties against small-colony forms of *S. aureus* (MIC = 16 µg/mL).[60] Twelve years after coming to market in 1985, the FDA chose to withdraw the drug due to evidence of ventricular arrhythmias associated with inhibition of the hERG K^+ channel.[61]
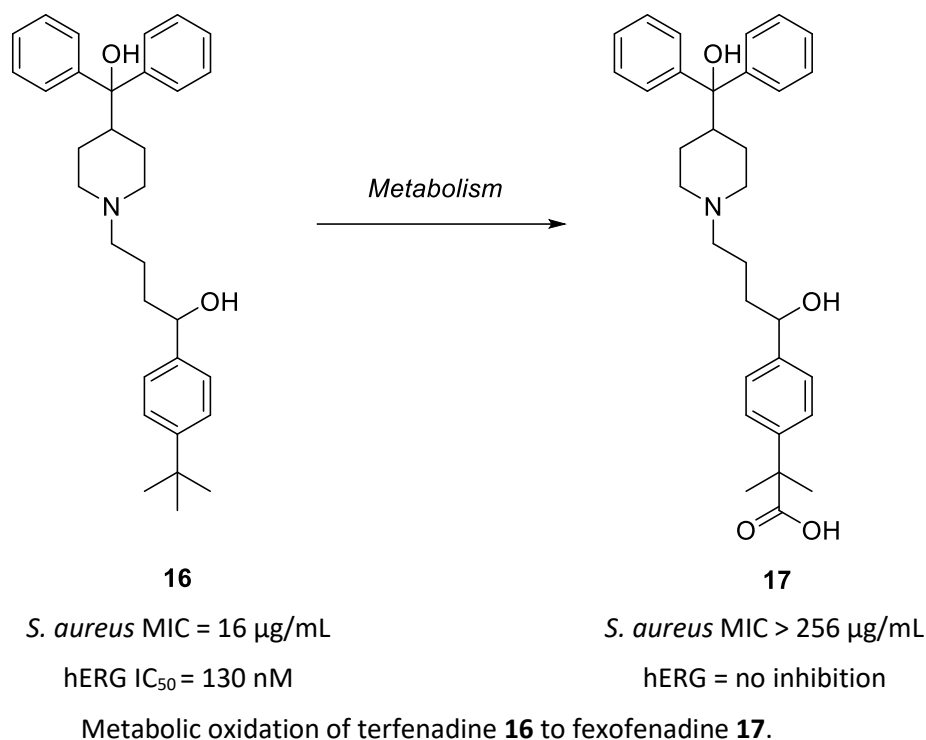
16

S. aureus MIC = 16 µg/mL

hERG IC_{50} = 130 nM

17

S. aureus MIC > 256 µg/mL

hERG = no inhibition

Metabolic oxidation of terfenadine **16** to fexofenadine **17**.

Figure 17

Fexofenadine **17** (**Figure 17**), the active metabolite of terfenadine **16** was marketed as Allegra, which still retained the required antihistamine properties of terfenadine, but did not inhibit the hERG channel. Recently, due to increasing antibiotic resistance to fluoroquinolones, the repurposing of terfenadine **16** as an antibiotic has been investigated.[60] From the structure of terfenadine, it was hypothesised that the molecule would occupy the NBTI binding site of DNA gyrase in order to cause the observed antibacterial activity against *S. aureus*. However, metabolic oxidation of terfenadine **16**, yielding fexofenadine **17**, was found to eliminate the antibacterial properties of the molecule (MIC = 16 µg/mL to > 256 µg/mL). Furthermore, metabolism was determined to occur on the southern *tert*-butyl group, which was hypothesised to bind to the lipophilic pocket of the NBTI binding site. This was proposed to result in a polar carboxylic acid moiety being directed into this region instead, causing repulsion with the lipophilic pocket and eliminating antibacterial activity. Although fexofenadine **17** had no antibacterial properties, it also had no affinity for the hERG ion channel. This was assumed to be due to the decrease in $logD_{7.4}$ and increase in TPSA, and introduction of a zwitterion that was expected to occur upon oxidation of the *tert*-butyl group, in accordance with the commonly used strategies of lowering hERG inhibition (**Section 2.3**).

2.5   Infections suitable for an inhaled therapy

Building upon the work reported by GlaxoSmithKline for their corticosteroid series, it was proposed that an inhaled antibacterial soft drug could be developed, potentially yielding a potent antibacterial compound which showed minimal systemic exposure.

A variety of bacterial strains could be targeted with an inhaled therapy. For example, the gram-positive pathogen *S. pneumoniae* can be particularly prevalent within the lungs, especially in patients suffering from chronic obstructive pulmonary disease (COPD) and asthma exacerbations.[62] *S. pneumoniae* is also considered the pathogen responsible for the majority of bacterial pneumonia cases within the USA, with over 500,000 cases recorded each year, and is also a frequent cause of infections in post lung-transplant patients.[63, 64] However, *S. aureus* (gram-positive) is also a common cause of infection in this patient set, and is a leading cause of bacterial pneumonia, particularly in mechanically ventilated patients.[63, 64] Furthermore, the majority of colonies that have been isolated from post lung-transplant patients are resistant to treatment from methicillin (MRSA). This is of particular interest as the current research programme could yield compounds equally as potent against both *S. aureus* and MRSA, by exploiting a completely distinct binding site, different from the currently used fluoroquinolone binding site on DNA gyrase subunit A. A final important pathogen is *H. influenzae*, a gram-negative bacteria associated with lower respiratory tract infections, COPD and asthma exacerbations.[62] Although patients suffering from pneumonia could benefit greatly from an inhaled antibacterial therapy, chronic infections from the gram-negative pathogen *P. aeruginosa* in cystic fibrosis patients was considered a second, highly lucrative, patient population to target. It has been reported that almost 55% of cystic fibrosis patients are infected with *P. aeruginosa*, a subset that increases to 80% of patients by the age of 18 years.[65] Without treatment, *P. aeruginosa* infections cannot be cleared by the body's natural defence mechanisms and most patients die at a young age due to pulmonary complications. However, with suitable treatment regimens, the average life expectancy has been raised to over 50 years in some cases.[66]

2.5.1   Currently utilised inhaled antibiotics

Current treatments of chronic *P. aeruginosa* lung infections in cystic fibrosis patients include the use of intravenous and oral antibiotics (aminoglycosides and fluoroquinolones), and, more recently, inhaled antibiotics (tobramycin **18** and colistin **19**, **Figure 18**).[8]

18

19
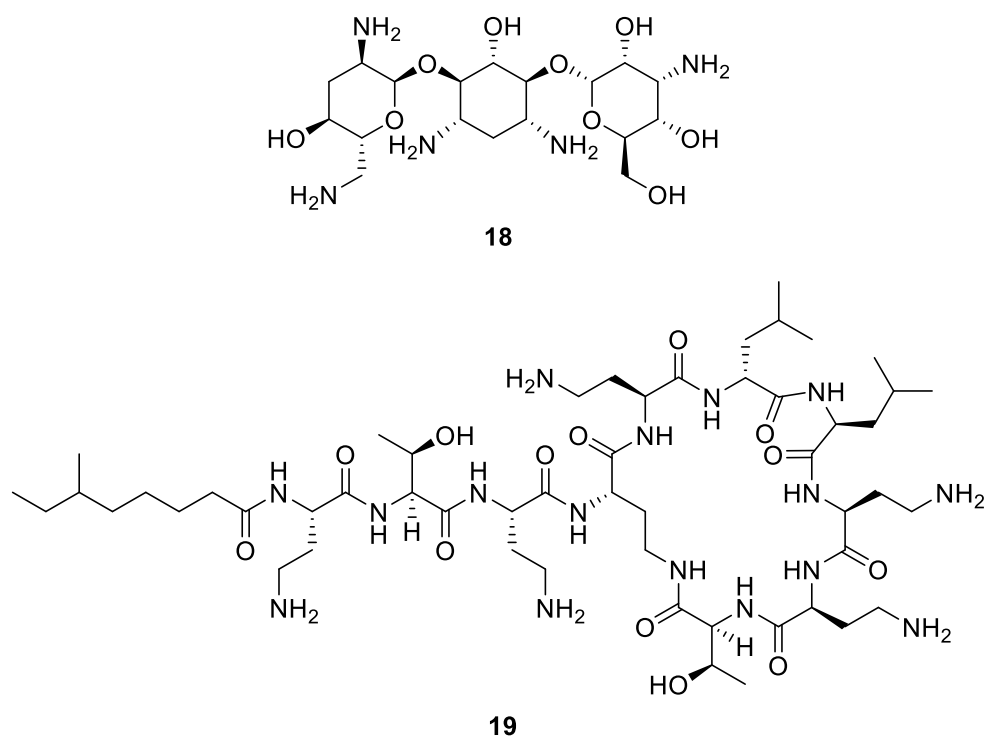
Structures of inhaled antibiotics tobramycin **18** and colistin **19**.

Figure 18

Nebulised tobramycin **18** was approved in 1998 and has since been accepted as a standard treatment for pulmonary infections in cystic fibrosis patients.[67] It was determined that toxicity caused by an inhaled antibiotic was minimised due to reducing systemic exposure to the drug, and mortality among CF patients has been considerably reduced as a result of nebulised tobramycin **18** treatment.[68]

Although colistin **19** was first released in the 1950s, high toxicity resulted in poor patient compliance and low marketability, which was only recently modified after re-evaluation of dosing regimens. Until very recently, colistin **19** was considered one of the only antibiotics clinically available that had no recorded resistant bacterial strains. However, recent worldwide colistin resistant bacteria have been observed, causing fear within the scientific community.[69] Due to newly observed colistin resistance and increasing levels of antibacterial resistance as a whole, there is an urgent requirement for novel antibiotics that are potent against resistant bacterial strains.

2.5.2   Summary of bacterial strains suited for an inhaled antibiotic

As a result, an antibacterial with activity against the strains outlined in **Table 3** could be of high commercial interest, and increased the scope of a potential inhaled antibiotic to several key bacterial strains.

Bacteria	Gram-positive/negative	Prevalence[62-64]
S. pneumoniae	Gram-positive	Pneumonia, COPD, asthma, post lung-transplant
S. aureus	Gram-positive	Pneumonia (mechanically ventilated), post lung-transplant
H. influenzae	Gram-negative	Lower respiratory tract infections, COPD, asthma exacerbations
AND/OR		
P. aeruginosa	Gram-negative	Cystic fibrosis patients

Bacterial strains to be targeted by an inhaled antibacterial soft drug.

Table 3

One potential compound class with potency reported against the above bacterial strains is the novel bacterial type II topoisomerase inhibitors (NBTIs). These compounds, although comparatively modern compared to the commonly utilised fluoroquinolones, have been subject to a high level of research in recent years, and could yield a successful antibacterial therapy.

2.6   Proposed work

To date, neither an antibacterial soft drug, nor the utilisation of a soft drug approach to explicitly minimise the inhibition of the hERG channel, have ever been published within the literature. However, based on work already published in the area of NBTI research, such an antibacterial soft drug could hypothetically be designed. Such a compound could be used to treat bacterial infections topically within the lungs, using an inhaler to direct the compound to the site of action. In order to make the hypothesised therapy clinically relevant, *S. pneumoniae*, *S. aureus*, *H. influenza* and *P. aeruginosa* were considered worthy targets due to the high prevalence of these infections within the lungs (**Section 2.5**).[62, 63, 70] The hypothetical drug molecule should be stable within the lungs, but should undergo controlled enzymatic degradation to non-toxic metabolites. The extremely subtle nature of the required instability of the scaffold will be key to its success. If the compound is too metabolically labile, premature hydrolysis may occur before it reaches its target. Conversely, if the compound is not prone to rapid metabolism, it may result in systemic

exposure. Importantly, the metabolising enzyme should not be present in bacteria, preventing premature degradation. Paraoxonase is one such enzyme that has not been isolated in bacteria, and should result in selective degradation in the human body.[71] Analysis of the physiochemical properties of published NBTIs was used to provide evidence for a working hypothesis (**Figure 19**). A correlation between clogP, topological polar surface area (TPSA) and *S. aureus* activity was observed, highlighting a set of properties that may result in high activity (circled, blue). Overlaying the properties desired for *S. aureus* activity with a similar analysis of hERG inhibition provided evidence that the soft drug hypothesis may be successful.
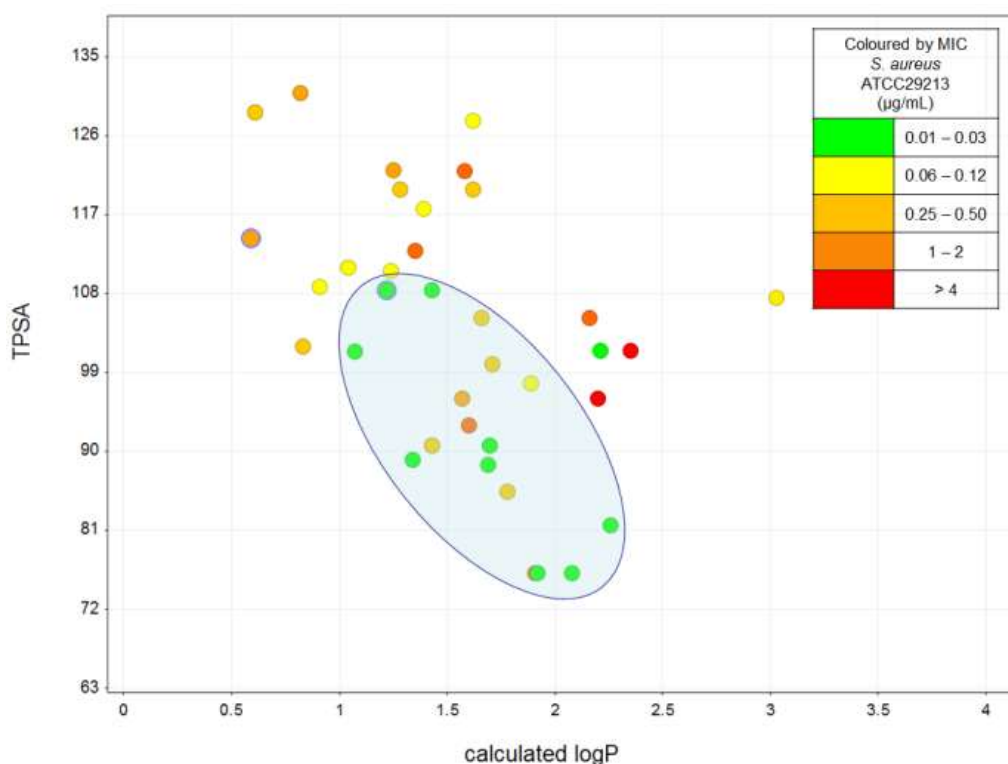
Graph depicting the trend between clogP, TPSA and *S. aureus* activity (coloured according to legend) for published NBTI compounds. Optimal physiochemical properties are circled (blue).
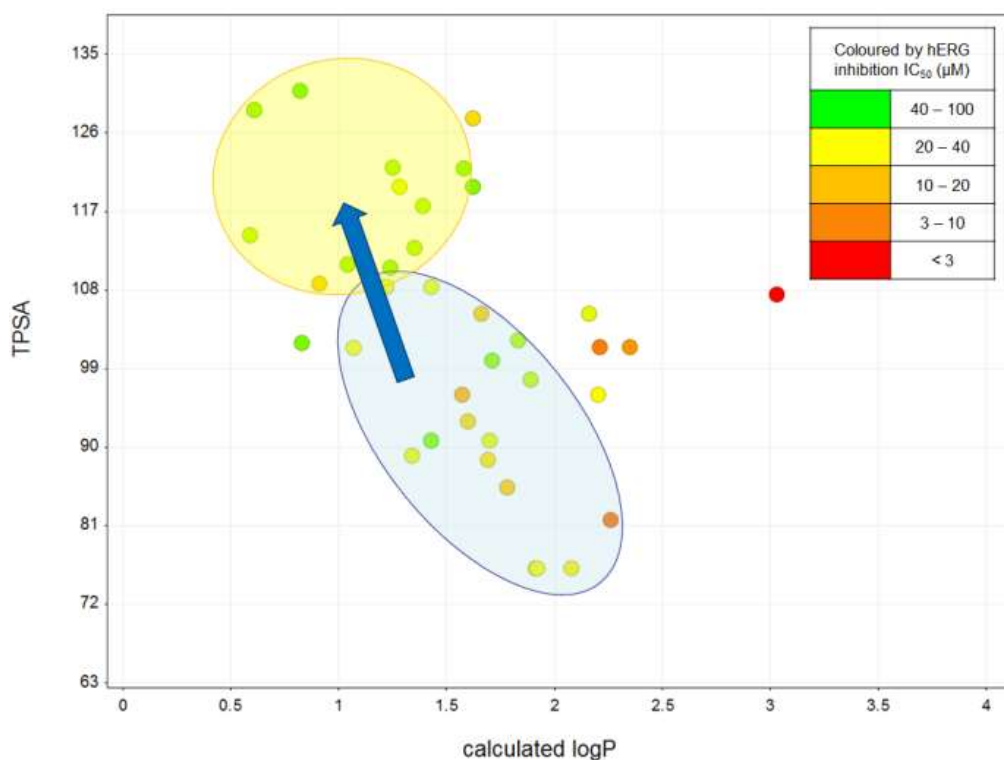
Graph depicting the differing physiochemical properties required for *S. aureus* activity
(blue) and low hERG inhibition (yellow) (coloured according to legend).

Figure 19

The hypothesised soft drug should have similar physiochemical properties to the
compounds highlighted in the blue area of **Figure 19**, providing the permeability required
for *S. aureus* activity. Upon metabolic hydrolysis, a polar moiety will be unmasked.
This should decrease the lipophilicity and increase the TPSA of the compound, ideally
removing both hERG affinity and *S. aureus* activity simultaneously, by shifting the
physiochemical properties into the area highlighted in yellow in **Figure 19**. Although useful,
the above data should only be taken as a guide to the ideal physiochemical properties
required for activity. Without synthesising and assessing individual compounds in a series, it
is extremely difficult to determine the ideal $logD_{7.4}$ and TPSA needed to provide adequate
potency. Instead, the above analysis highlights the possible physiochemical differences
between a parent soft drug compound and its metabolite, reflecting that a lowering of
polarity and an increase in TPSA as a result of metabolism could alleviate undesired hERG
inhibition.

2.7   Objectives

During the course of the research programme, the following objectives were set in order to determine if a soft drug approach to antibacterial research could be successful:

1. Review the literature to assess the most promising soft drug probe compounds.
2. Computationally and synthetically assess the selected targets in order to triage compounds deemed less attractive.
3. Conduct the synthesis of probe compound(s) and the proposed hydrolysed metabolite(s).
4. Assess synthesised compounds in terms of:
   a. The antibacterial potency of the parent compound and its suspected metabolite.
   b. The plasma and lung stability of the parent compound and its suspected metabolite.
   c. The cytotoxicity and cardiotoxicity of the parent compound and its suspected metabolite.
5. Obtain metabolite identification to conclude if the metabolic hotspot was successfully being targeted in the degradation mechanism.

2.8   Results and discussion

2.8.1   Target compound selection

Target compound selection was initiated through assessment of possible sites of metabolism on the NBTI scaffold, and using published studies to guide potential structural modifications.[59, 60, 72] Hybridising a standard NBTI scaffold with a metabolically unstable moiety was expected to provide initial proof of concept for a potential antibacterial soft drug.

There were several areas of the NBTI scaffold that were considered to yield plausible soft drug candidates. Broadly, an NBTI structure can be split into three units; the northern ring system, the linker, and the southern scaffold (**Figure 20**).

3
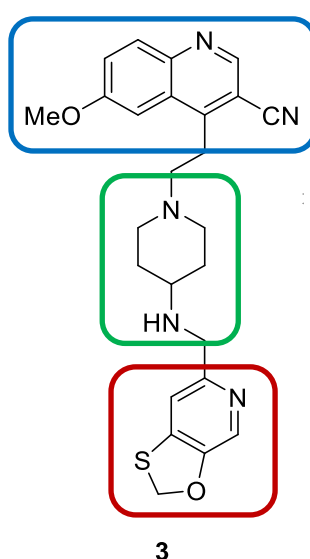
Modular design of NBTI **3**, with northern ring system (blue), linker (green) and southern scaffold (red).

Figure 20

Theoretically, a "metabolic hotspot" could be introduced into any of these three sections, yielding equally suitable probe compounds to assess the soft drug hypothesis. In order to prioritise the synthesis of compounds with appropriate positions of the metabolic liability, the crystal structure of paraoxonase (PDB: 3SRG[73]), containing 2-hydroxyquinolone as a ligand, was examined to determine the steric limitations of the active site (**Figure 21**).
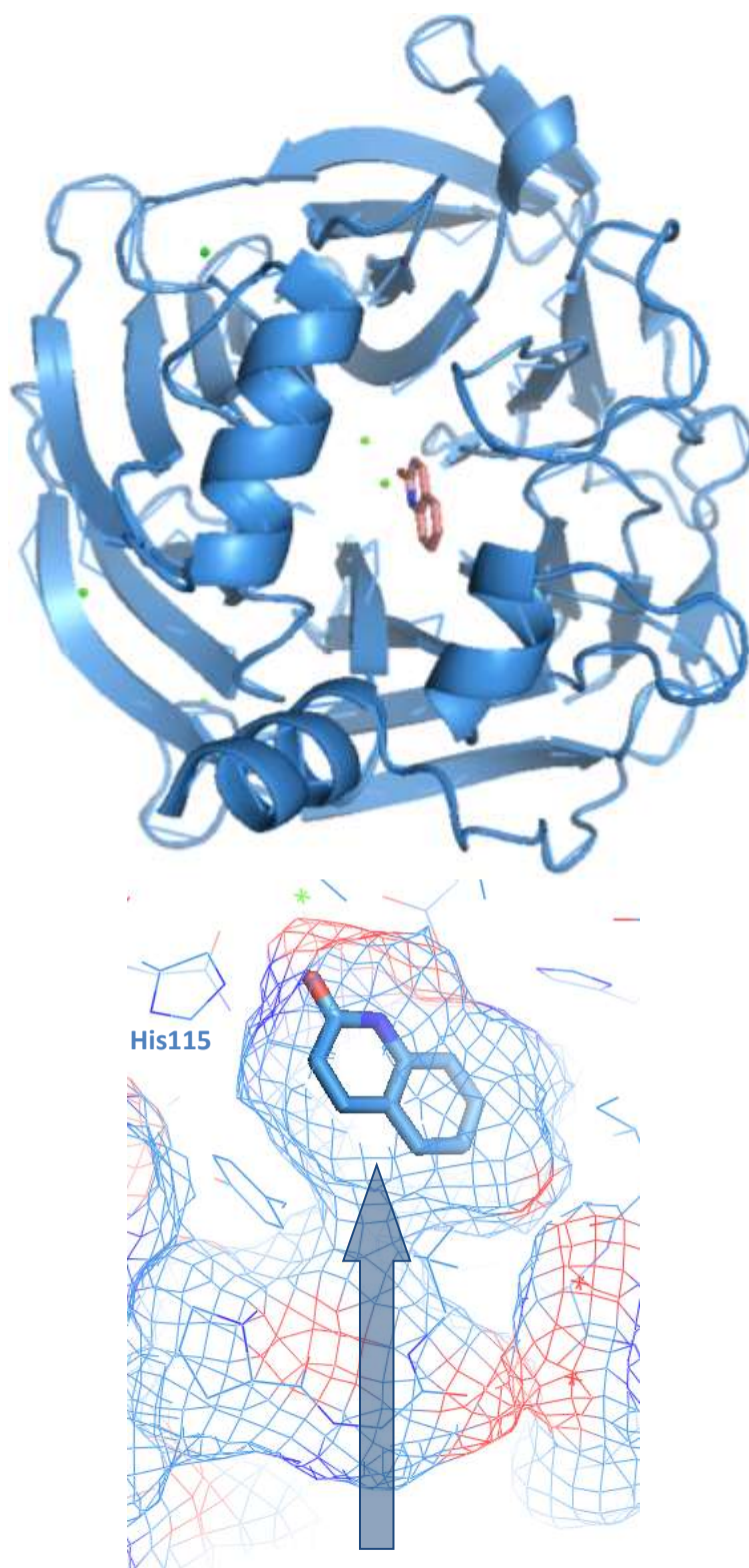
X-ray crystal structure (PDB: 3SRG[73]), as displayed using Pymol (v1.1eval). Paraoxonase was observed to have a catalytic site situated at the bottom of a deep trench (top: top-down view, bottom: side-on view).

Figure 21

Analysis of the paraoxonase crystal structure provided evidence for a tight channel leading to the active site. A catalytic Ca^{2+} ion, which has been reported to be integral to the catalytic activity of the enzyme, resides at the bottom of this trench.[73] Furthermore, studies have shown a possible mechanism by which paraoxonase is able to metabolise hydrolytically labile substrates.
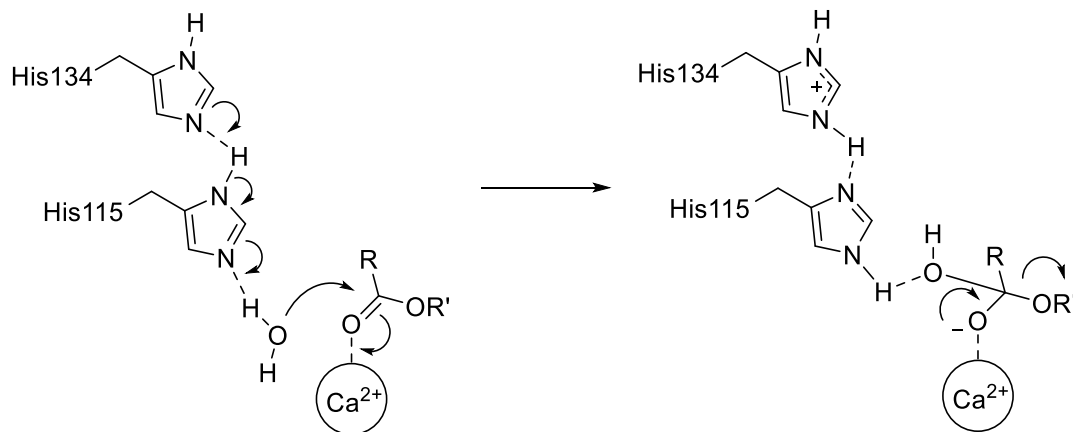
Potential mechanism resulting in substrate hydrolysis within the paraoxonase active site.

Figure 22

Coordination to the catalytic Ca^{2+} ion allows the substrate to be positioned correctly within the active site. Following binding, it has been reported in the literature that His115, stabilised by nearby His134, is able to direct the nucleophilic attack of a nearby water molecule to the reactive carbonyl centre. Hydrolysis proceeds, resulting, in the case above, in ester hydrolysis.[73] As a result of the hypothesised mechanism, careful consideration to the steric bulk surrounding the carbonyl unit of the hydrolytically labile unit must be given.

Hydrolysis of the linker unit was considered to provide the most dramatic structural change to the soft drug scaffold, and therefore the most likely method to eliminate the cardiotoxicity of the series. However, after examination of the crystal structure of paraoxonase, these analogues were deprioritised due to the steric limitations of the active site, hypothetically preventing the metabolic liability from binding near the catalytic Ca^{2+} ion. Instead, it was hypothesised that positioning of the metabolically labile unit in the NBTI series would be optimal at the ends of the molecule. Due to the research published regarding the repurposing of terfenadine and its metabolite fexofenadine for antibacterial use (**Section 2.4.2**), it was hypothesised that introducing a metabolically unstable southern unit could provide the greatest chance of success for delivering initial proof of concept for an antibacterial soft drug (**Figure 23**).

Importantly, it was expected that unmasking a polar moiety in the southern lipophilic region of the binding pocket would aid elimination of antibacterial activity and hERG related cardiotoxicity, by disfavouring binding interactions, lowering logD$_{7.4}$ and increasing TPSA. Furthermore, introducing a zwitterionic structure may further enhance the reduction of antibacterial activity and cardiotoxicity. NBTIs with metabolically unstable southern ring units were therefore considered as initially lucrative targets.
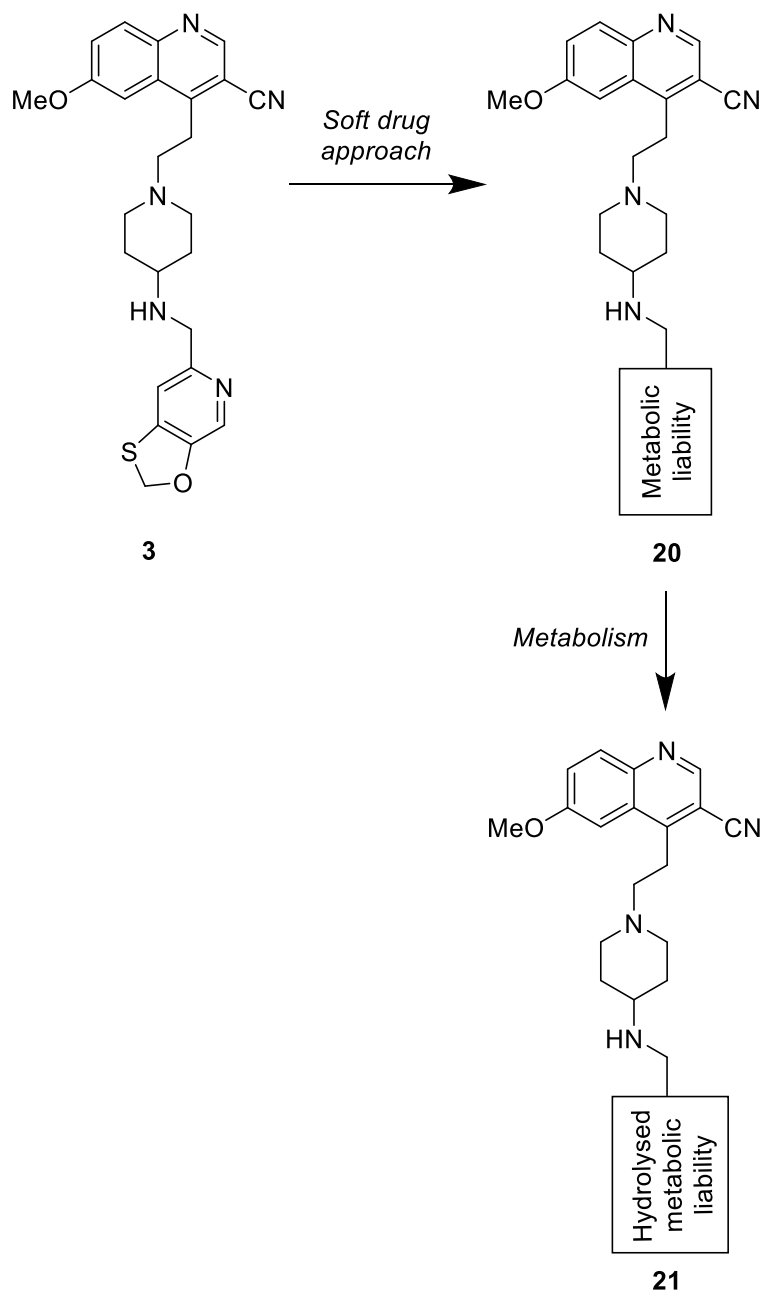
GSK299423[36] **3**, possible soft drug NBTI hybrid **20**, and hypothetical metabolic deactivation route to metabolite **21**.

Figure 23

In order to provide the greatest chance of success in delivering proof of concept for the soft drug hypothesis, a variety of hydrolysable southern ring systems were considered. Fortunately, hydrolytically unstable cyclic units have been briefly reported in the literature to be potential substrates for the paraoxonase enzyme, providing an initial basis for compound design (**Figure 24**).[74]
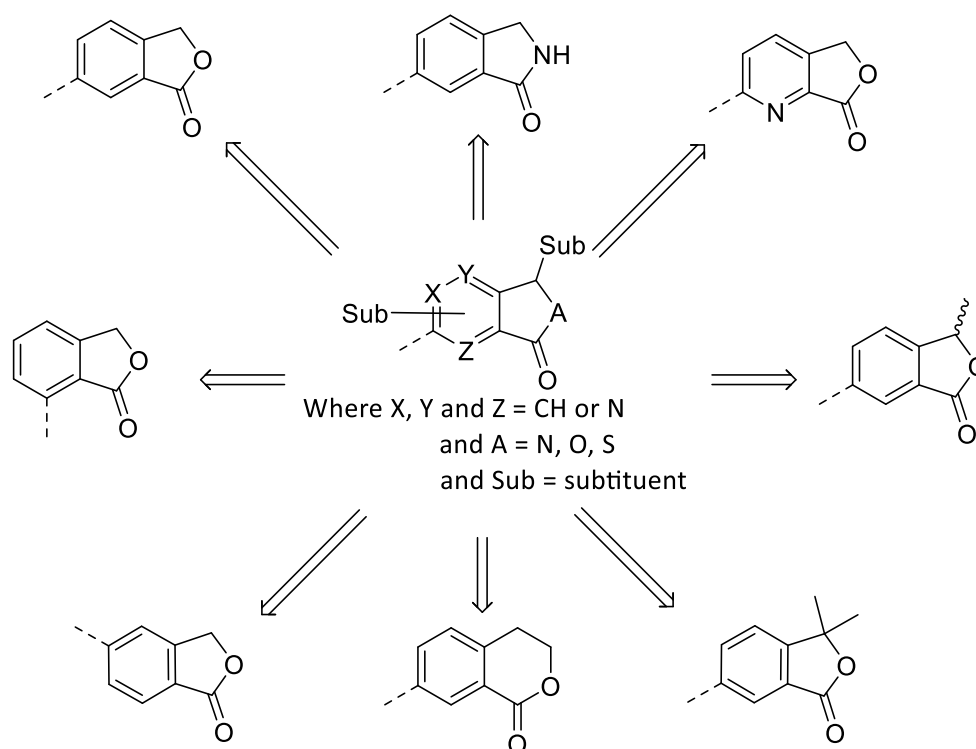
Possible metabolically liable southern groups.

Figure 24

As recent literature focused primarily on metabolically unstable lactones,[74, 75] compounds containing this metabolic liability were selected as the first soft drug targets to be synthesised. Furthermore, a strong similarity was observed between the southern group in GSK299423, and a hypothetical fused pyridyl lactone (**Figure 25**).

Southern group of GSK299423 **3** (left, green), proposed lactone derivative (right, blue) and overlay (centre).

Figure 25

Due to the large number of possible isomers of the desired pyridyl lactone system, potential target compounds were assessed computationally, by overlaying a previously published NBTI crystal structure[36] with the hypothetical compounds using Forge (v10.4.1). The resulting compound with the highest degree of similarity to literature compound **3** is shown (**Figure 26**).
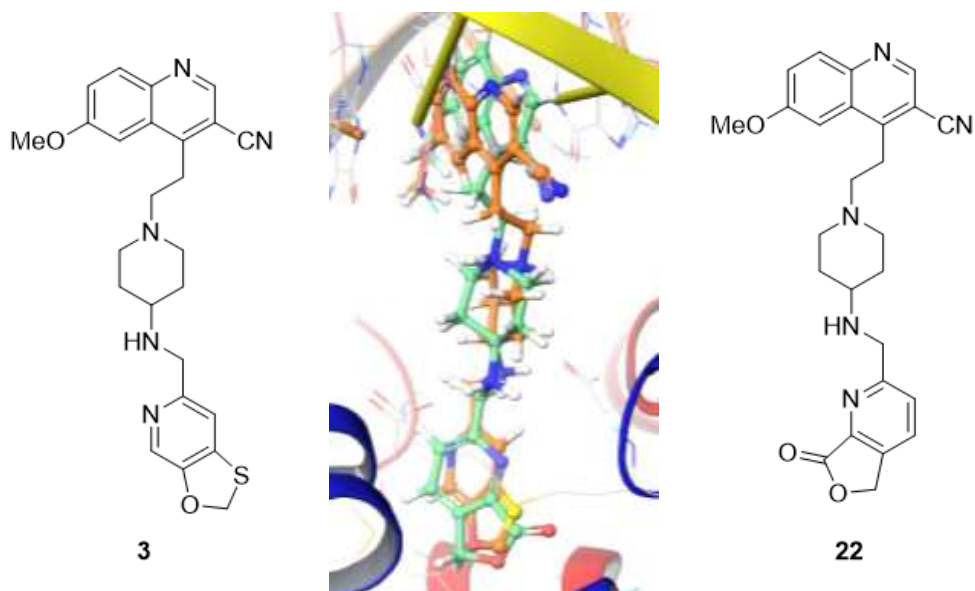
GSK299423 **3** (left, and yellow in overlay)[36] with hypothetical soft drug hybrid **22** (right, and blue in overlay). Figure generated using Maestro (v10.6).

Figure 26

A high level of overlap was observed with the two above compounds, reinforcing the potential of this scaffold. The quinoline units were suspected to not overlap directly due to limitations with the software, as opposed to a direct difference in binding modes, whereas the poor overlap of the piperidine linker indicated the inherent flexibility in this region. Although the fused lactone system in compound **22** was predicted to partially direct polarity into the lipophilic pocket, the probe compound was selected in order to provide an initial proof of concept for a potential antibacterial soft drug therapy.

Fortunately, an overlap between an existing in-house project and the current research programme resulted in the availability of many relevant northern ring systems. Thus, using a combination of the computational overlays, calculated physiochemical data and the available intermediates, the initial target to be selected for synthesis was compound **23** (**Figure 27**).

23
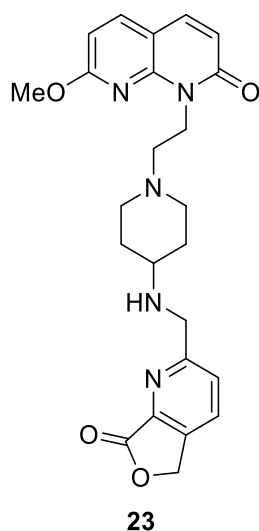
Target probe soft drug compound **23**.

Figure 27

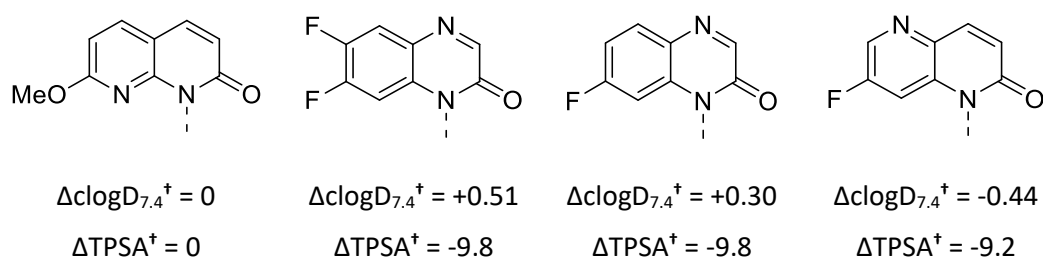Due to the modular nature of the NBTI structure and the selection of the southern ring system as the metabolic liability, modifications to physiochemical properties were hypothesised to be easily performed through alterations to the northern bicyclic scaffold. Fine-tuning of $\log D_{7.4}$ could be achieved by using more lipophilic/polar head groups, while keeping the metabolically labile group consistent between analogues (**Figure 28**).

| ΔclogD$_{7.4}$† = 0 | ΔclogD$_{7.4}$† = +0.51 | ΔclogD$_{7.4}$† = +0.30 | ΔclogD$_{7.4}$† = -0.44 |
| ΔTPSA† = 0 | ΔTPSA† = -9.8 | ΔTPSA† = -9.8 | ΔTPSA† = -9.2 |

†Calculated using ACD/Percepta 14.0.0, probe compound **23** as a baseline.

Possible northern ring systems of varying polarity, allowing the fine tuning of physiochemical properties.

Figure 28

Thus, depending on the initial antibacterial activity of the suggested probe compound, similar analogues could be readily prepared to efficiently determine trends in how the lipophilicity ($\log D_{7.4}$) of the series affected antibacterial potency. Prior to the commencement of the synthesis of target compound **23**, a thorough investigation into the potential interactions with both DNA gyrase and paraoxonase was initiated in order to aid rationalisation of the observed antibacterial and stability results.

2.8.2   Computational assessment of target compound in DNA gyrase

In order to increase the efficiency of the synthetic effort, computational analysis of the suggested soft drug target **23** within the active site of DNA gyrase was performed, prior to initiating the synthesis. The crystallised ligand, GSK299423 **3**, was computationally edited and minimised within the active site of the published crystal structure (PDB: 2XCS[36]), resulting in an initial simulation used to assess the likelihood of maintaining favourable binding interactions. Of particular interest was whether modification of the southern group altered binding, therefore, a truncated ligand is shown in **Figure 29**, highlighting the key area of interest.
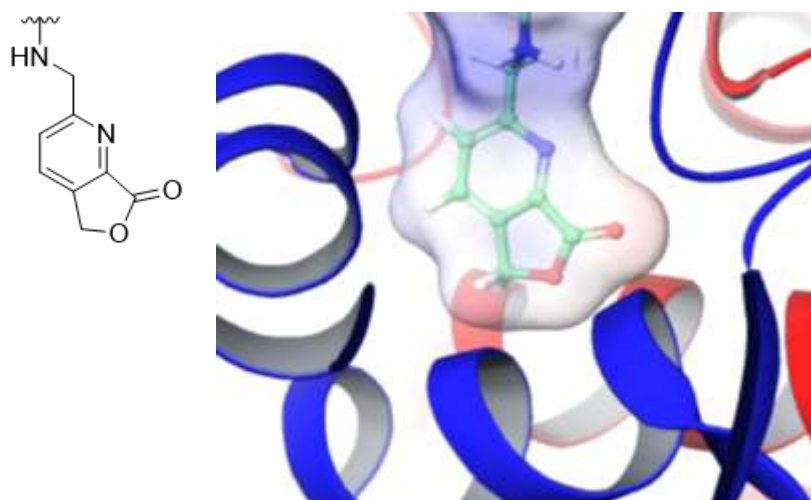
Hypothesised target probe soft drug compound **23** (left) in DNA gyrase (PDB: 2XCS[36], right). Figure generated using Maestro (v10.6).

Figure 29

A high level of space-fit was observed between ligand **23** and the active site of DNA gyrase. Although a small amount of electronic repulsion could be hypothesised between the lactone-containing region of the ligand and the lipophilic pocket of the active site, this was considered to be tolerable. As a result, the ligand was deemed to be an appropriate target to challenge the antibacterial soft drug hypothesis, and prompted further investigation. As high paraoxonase-based metabolism was desired, literature-guided studies of metabolic rates of published compounds could be utilised. However, publications surrounding the metabolism of larger drug-like compounds by paraoxonase were sparse. As a result, a computational effort was initiated in order to assess metabolically liable structures within paraoxonase.

2.8.3   Computational assessment of target compound in paraoxonase

A knowledge-based alignment of target compound **23** in the active site of paraoxonase (PDB: 3SRG[73]) was performed, using the binding mode observed for the crystallised ligand, quinolin-2(1*H*)-one, as a guide for lactone positioning. The central linker and northern portion of the molecule were directed through a tunnel created between the catalytic region and the extremities of the enzyme, resulting in an alignment based on existing knowledge of the binding site (**Figure 30**).
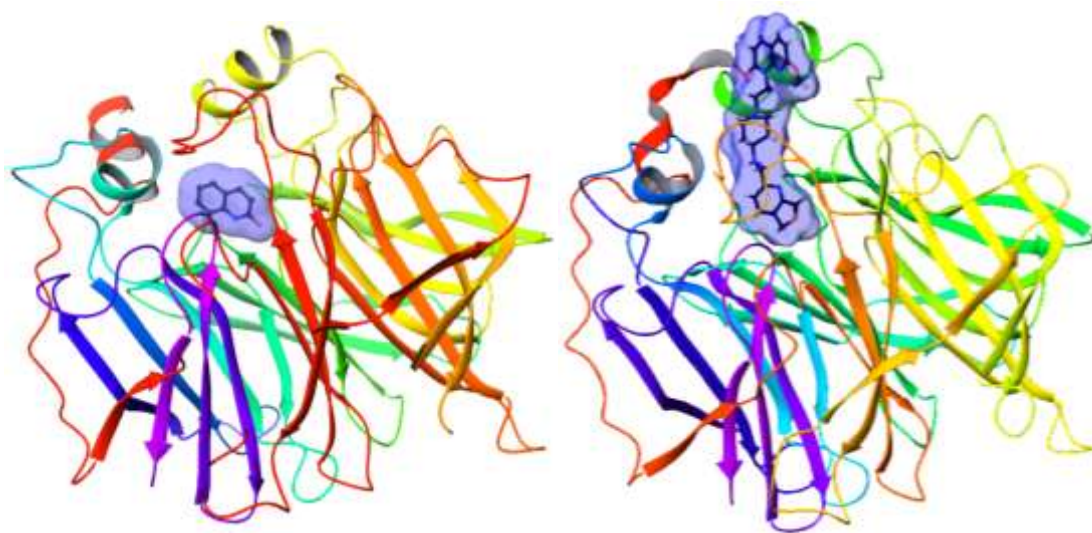
Visualisations of quinolin-2(1*H*)-one (left) and hypothetical target soft drug **23** (right) within paraoxonase (PDB: 3SRG[73]). Figures generated using Maestro (v10.6).

Figure 30

It was hypothesised that performing molecular dynamics (MD) simulations of the target soft drug **23** within paraoxonase could aid visualisation and generation of theories surrounding binding mode and rates of hydrolysis for larger drug-like substrates. Therefore, a molecular dynamics simulation was performed, as outlined in **Section 3.11.3.1**, providing a visual tool in order to assess binding affinity for the target metabolising enzyme. The resulting interactions map is shown in **Figure 31**.
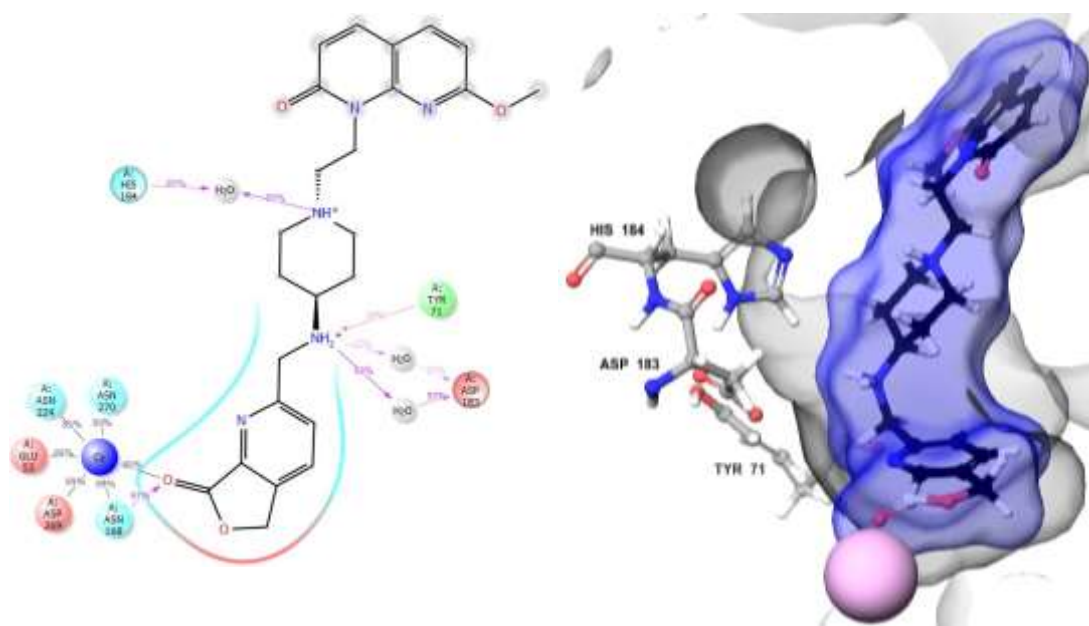
Interaction map (left) and an individual frame (right) from the molecular dynamics simulation of compound **23**, with interacting residues shown.

Figure 31

As can be seen from **Figure 31**, the lactone ring was observed to bind efficiently to the catalytic calcium ion in the active site (pink sphere). Furthermore, no prohibitive steric clashes were recorded throughout the simulation. Additionally, a π-cation interaction was observed between the aminopiperidine secondary amine and the aromatic system of Tyr71. Finally, a water-mediated interaction to Asp183 was observed to occur during 93% of the simulation, consistent with a highly efficient binding interaction being made (**Figure 31**).

Within the published literature, Tyr71 has been shown to reside on a flexible loop near the catalytic active site. The loop is believed to move during the catalytic action of the enzyme, preventing water from entering the active site. As Tyr71 was observed to interact with the ligand, this may suggest the ligand-protein interaction, combined with the exclusion of water molecules from the active site, may result in the tethering of the flexible loop to the soft drug structure (**Figure 32**).
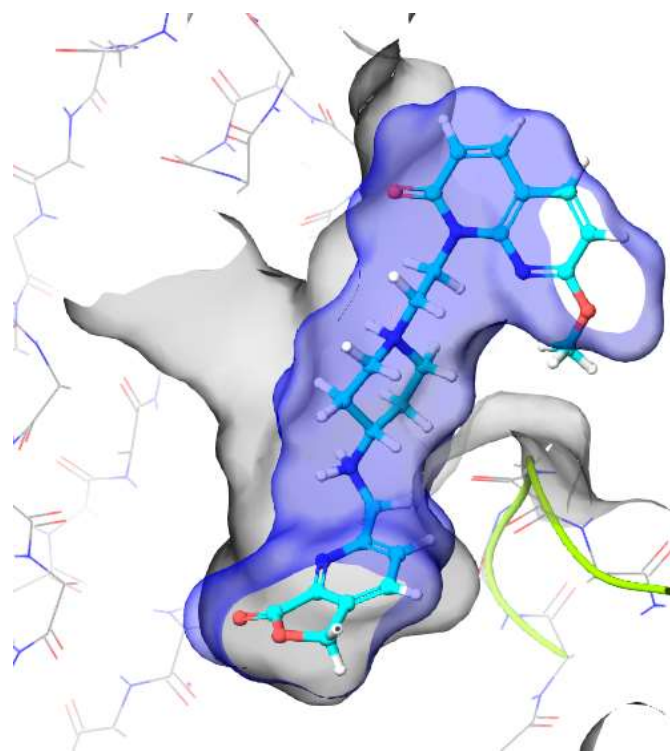
A flexible loop of residues (green ribbon) is held against the ligand (blue), covering the active site (grey). The northern group is observed to reside in solvent, however transient lipophilic interactions with nearby aromatic systems were observed, which may contribute to binding.

Figure 32

It was recognised that computational studies of relatively large, drug-like molecules with paraoxonase have not been performed in the literature prior to this investigation. Therefore, the suitability of the initial binding mode and the adaptation of the protein to the ligand were not supported by previously published data. As a result, this pilot study could guide the project and the research area towards understanding the tolerability of larger structures within the active site of paraoxonase, aiding compound design and furthering the knowledge of the capabilities of paraoxonase in a wider field. It was determined from the molecular dynamics studies that the soft drug molecule was likely to fit in the active site, at a trajectory that may encourage metabolism by paraoxonase. Encouraged by the computational evidence that was generated, the synthesis of target compound **23** was initiated, followed by a range of similar analogues. Compounds were successfully prepared following retrosynthetic analysis (**Section 2.9**), yielding a variety of analogues which could be assessed for their antibacterial and stability properties.

2.9 Synthetic route

2.9.1 Retrosynthetic analysis of target compound (23)

Retrosynthetic analysis was performed on target compound **23**, allowing a forward synthesis to be proposed from three building blocks, **24**, **25** and **26** (**Scheme 1**).
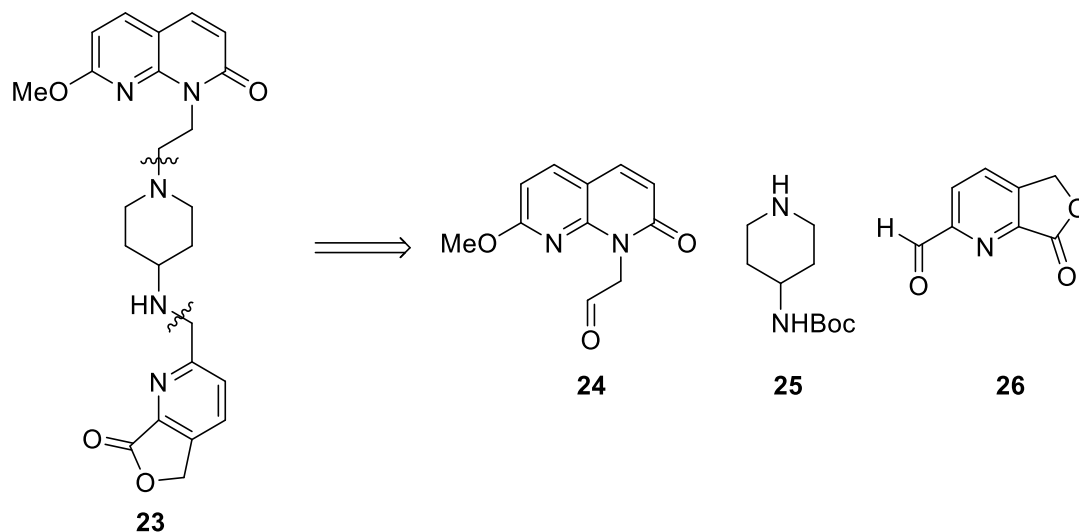
Retrosynthetic analysis of target compound **23**.

Scheme 1

Due to an overlap with an existing Redx Pharma project, the northern bicyclic aldehyde unit **24** was available from the Redx Pharma compound collection, preventing the need for a bespoke synthesis at this stage, and the central aminopiperidine linker **25** was purchased with the appropriate protecting groups in place. Since bicyclic lactone **26** was not commercially available, a second retrosynthetic analysis was performed, resulting in the proposed synthesis from commercially available starting materials (**Scheme 2**).
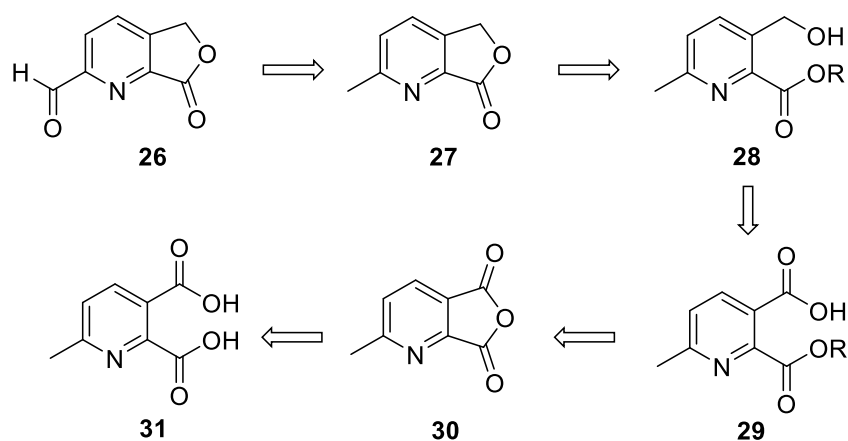
Retrosynthetic analysis of aldehyde **26** (R = alkyl group).

Scheme 2

2.9.2   Preparation of aldehyde (26)

The route below was followed in an attempt to obtain aldehyde **26** as a building block.

Initial forward synthesis of aldehyde **26**.

Scheme 3

The synthesis began with the formation of cyclic anhydride **30** from 6-methylpyridine-2,3-dicarboxylic acid **31** and acetic anhydride in quantitative yield. Anhydride **30** was then ring opened with methanol in the presence of indium(III) triflate, following the procedure published by Metobo.[76] Coordination of the In^{3+} ion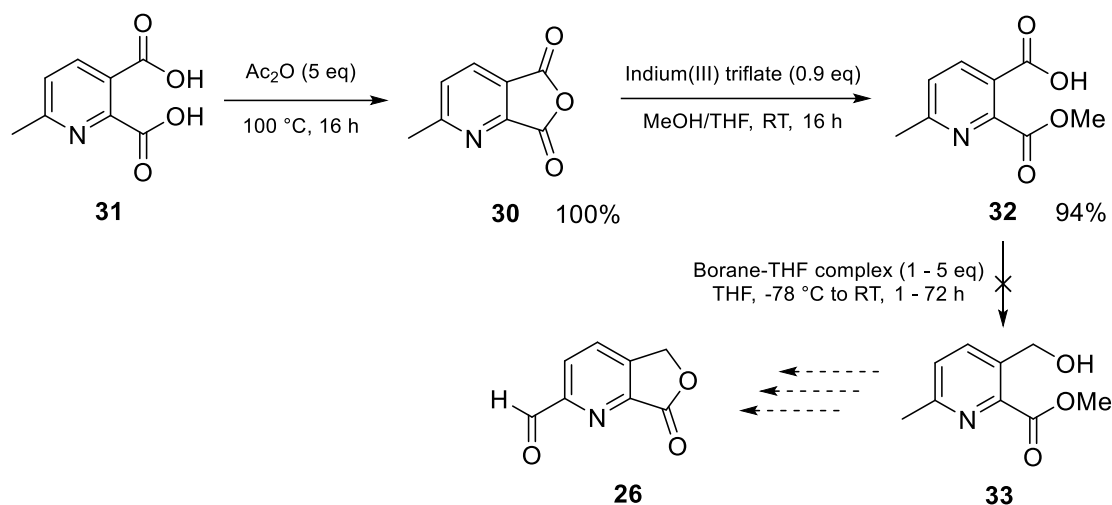 to the pyridine nitrogen and lactone carbonyl oxygen were suspected to increase the electrophilicity of the carbonyl carbon, selectively forming picoline ester **32**. However, several attempts at performing the selective reduction of the carboxylic acid using varying conditions proved unsuccessful (**Table 4**).

As borane is commonly used for selective reduction of a carboxylic acid while leaving an ester intact, it was selected as the reagent of choice. Initial attempts to reduce the acid using stoichiometric levels, or a slight excess, of borane were unsuccessful (entries 1, 2 and 3, **Table 4**), giving no evidence of product formation. Since borane was proving unsuccessful in reducing either functional group, an alternative synthetic route became desirable. Acid chloride formation followed by rapid reduction with sodium borohydride yielded only over reduction (entry 4, **Table 4**). After proving reduction was possible, if not selective, borane reductions were considered a favourable option. Extending the reaction time was considered a potential method of increasing the likelihood of reaction, but was found to result in starting material degradation (entry 5, **Table 4**). In order to assess the reduction potential of the reagent, 5 equivalents were used with an increased reaction time, successfully forcing over reduction (entry 6, **Table 4**). After proving borane could reduce

both functional groups, a range of reaction temperatures (entries 7, 8 and 9, **Table 4**) were used to investigate if by-product formation could be prevented at lower temperatures. Unfortunately, over reduction and product formation were observed to occur simultaneously.

32 → **33**
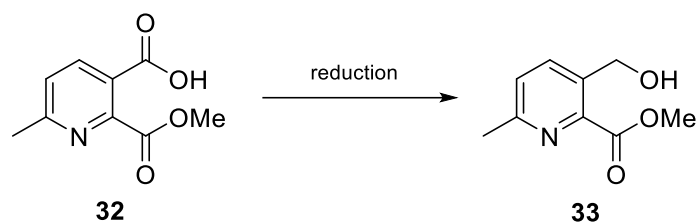
Entry No.	Reagent	Solvent	Equivalents	Temp (℃)	Time (h)	Outcome
1	BH₃.THF	THF (wet)	1	25	24	No reaction
2	BH₃.THF	THF (dry)	1	25	3	No reaction
3	BH₃.THF	THF (dry)	2	25	2	No reaction
4	SOCl₂/ NaBH₄	THF (dry)	18.5 (SOCl₂), 1 (NaBH₄)	80, then 0	2, then 1	Over reduction
5	BH₃.THF	THF (dry)	1	25	48	Degradation
6	BH₃.THF	THF (dry)	5	25	72	Over reduction
7	BH₃.THF	THF (dry)	4	-78	3	Trace product
8	BH₃.THF	THF (dry)	4	-40	1	Trace product
9	BH₃.THF	THF (dry)	4	-10	0.5	Over reduction

Conditions used to reduce carboxylic acid in the presence of methyl ester.

Table 4

Due to the failure to selectively reduce carboxylic acid **32**, a more sterically hindered ester was required to increase the selectivity of the reduction. *Iso*-propyl ester **34** was successfully synthesised using *iso*-propyl alcohol and indium(III) triflate to direct the anhydride opening.
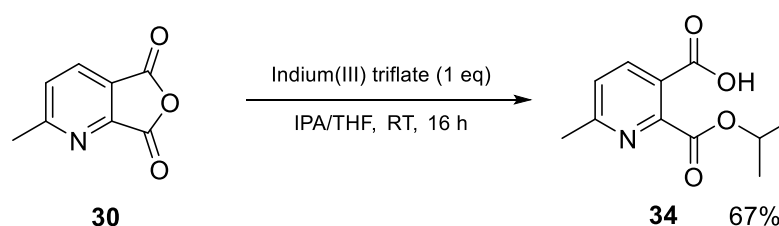
Synthesis of *iso*-propyl ester **34**.

Scheme 4

Full structural determination was performed on *iso*-propyl ester **34** to ensure the correct relative configuration. A HMBC cross-peak was observed between the carboxylic acid carbonyl (165.9 ppm) and the aromatic proton nearest the carboxylic acid group, whereas

no cross-peak was observed for the ester carbonyl in the structure (166.0 ppm), proving the anhydride had selectively opened to give the desired structural isomer. This was in agreement with the results obtained by Metobo *et al.*[76] With a more sterically hindered starting material synthesised, the reduction conditions were optimised. **Table 5** shows a summary of borane-THF conditions used, in anhydrous THF.
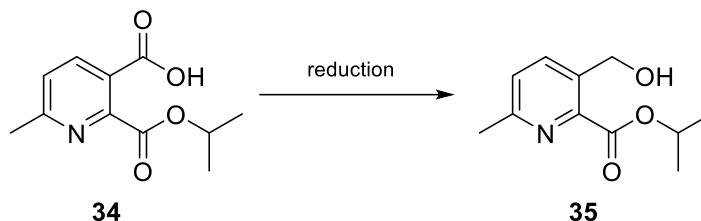

Entry No.	Eq. of BH$_3$.THF	Temp (°C)	Time (h)	Outcome
1	5	25	72	Trace product
2	10	25	4	Reaction (not isolated)
3	**10**	**25**	**5**	**Reaction (isolated in 40% yield)**

Conditions used to reduce carboxylic acid in the presence of *iso*-propyl ester.

Table 5

Borane reduction of the *iso*-propyl ester intermediate was at first unsuccessful, with only trace amounts of product being formed (entry 1, **Table 5**). However, over reduction was not observed with long reaction times, highlighting the additional stability provided by the bulkier ester. Therefore, additional equivalents of borane were used (entry 2, **Table 5**) in order to drive the reaction to completion, yielding final reaction conditions (entry 3, **Table 5**) of excess borane (10 eq.) at 25 °C for 5 h, giving alcohol **35** in 40% isolated yield. Product formation was confirmed by LCMS (R$_T$ = 1.64 min, [M+H]+ 210.0) and ^{1}H NMR spectroscopy, where a peak at 4.64 ppm was interpreted to represent the newly formed methylene CH$_2$.

Synthesis of aldehyde **26** was continued by cyclising **35** to form lactone **27** (**Scheme 5**), using substoichiometric hydrochloric acid, in high yield (90%). The final step consisted of a Riley oxidation, using SeO$_2$ to form aldehyde **26**, which was used as a key building block in the synthesis of the initial soft drug target.
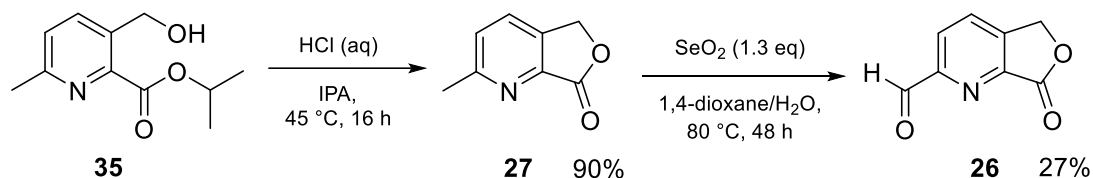
Successful synthesis of aldehyde **26**.

Scheme 5

2.9.3 Preparation of target compound (23)

The northern quinoline aldehyde **24** (**Scheme 6**) was selected from the Redx Pharma compound library. Although this intermediate did not have optimised $logD_{7.4}$ and potency for a soft drug analogue, it was chosen in order to efficiently establish a proof of concept. Reductive amination with amine **25** followed by Boc deprotection yielded amine **37**, which could be reacted in a second reductive amination with aldehyde **26** to give soft drug probe compound **23** (**Scheme 6**). The route was designed to permit late stage diversity, allowing a variety of potentially hydrolysable southern groups to be attached at the end of the synthesis. An unfortunate consequence of the final reductive amination was the presence of starting material **37** in the sample of product. Quadrapure® AK solid supported resin was used to remove the primary amine impurity, in the presence of the secondary amine product,[77] giving the soft drug probe in 7% yield over two steps.
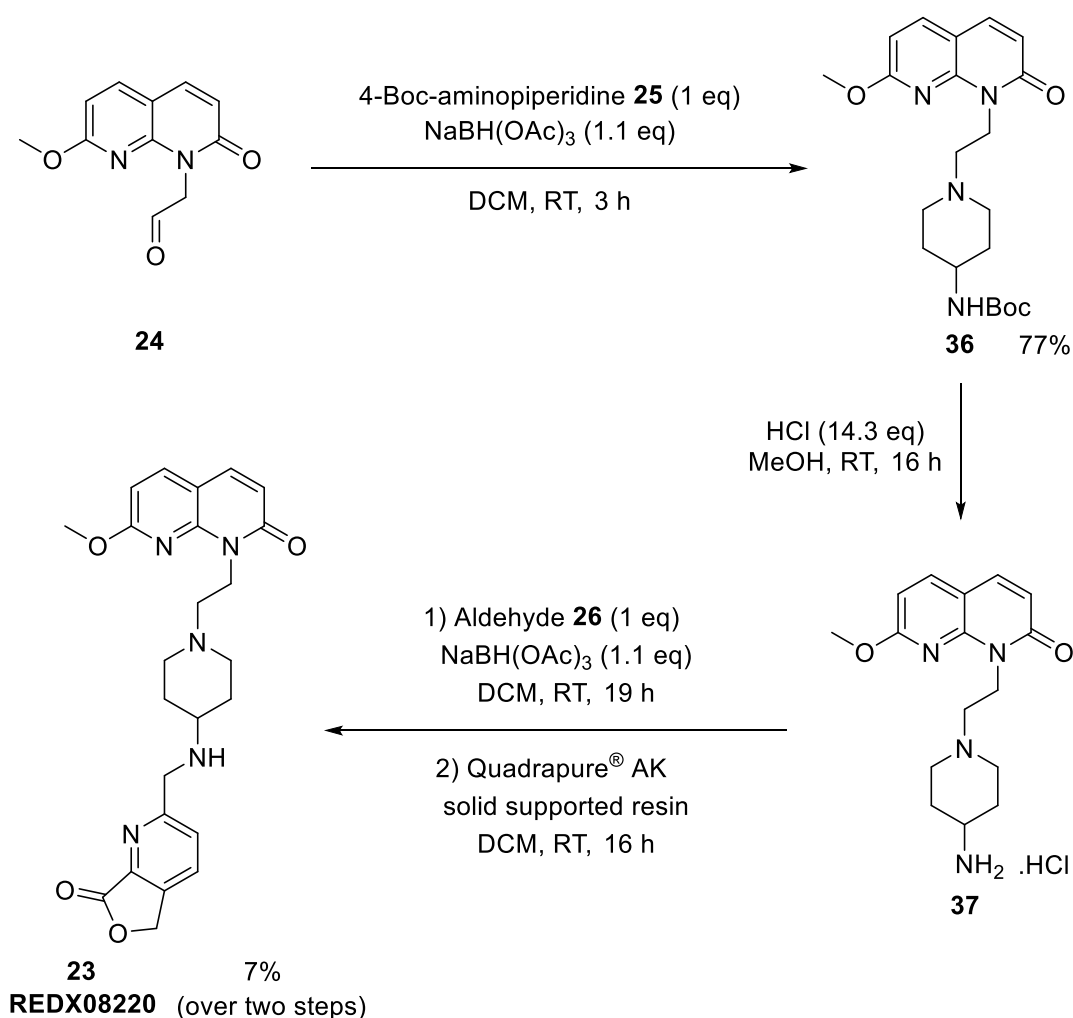
Forward synthesis of REDX08220 **23**.

Scheme 6

2.9.4 Preparation of analogues of REDX08220 (23)

A similar analogue to REDX08220 **23** was prepared following the route shown in **Scheme 7**, replacing aldehyde **24** with a northern group expected to alter the lipophilicity of the soft drug probe, yielding REDX08881 **41** (**Scheme 7**).
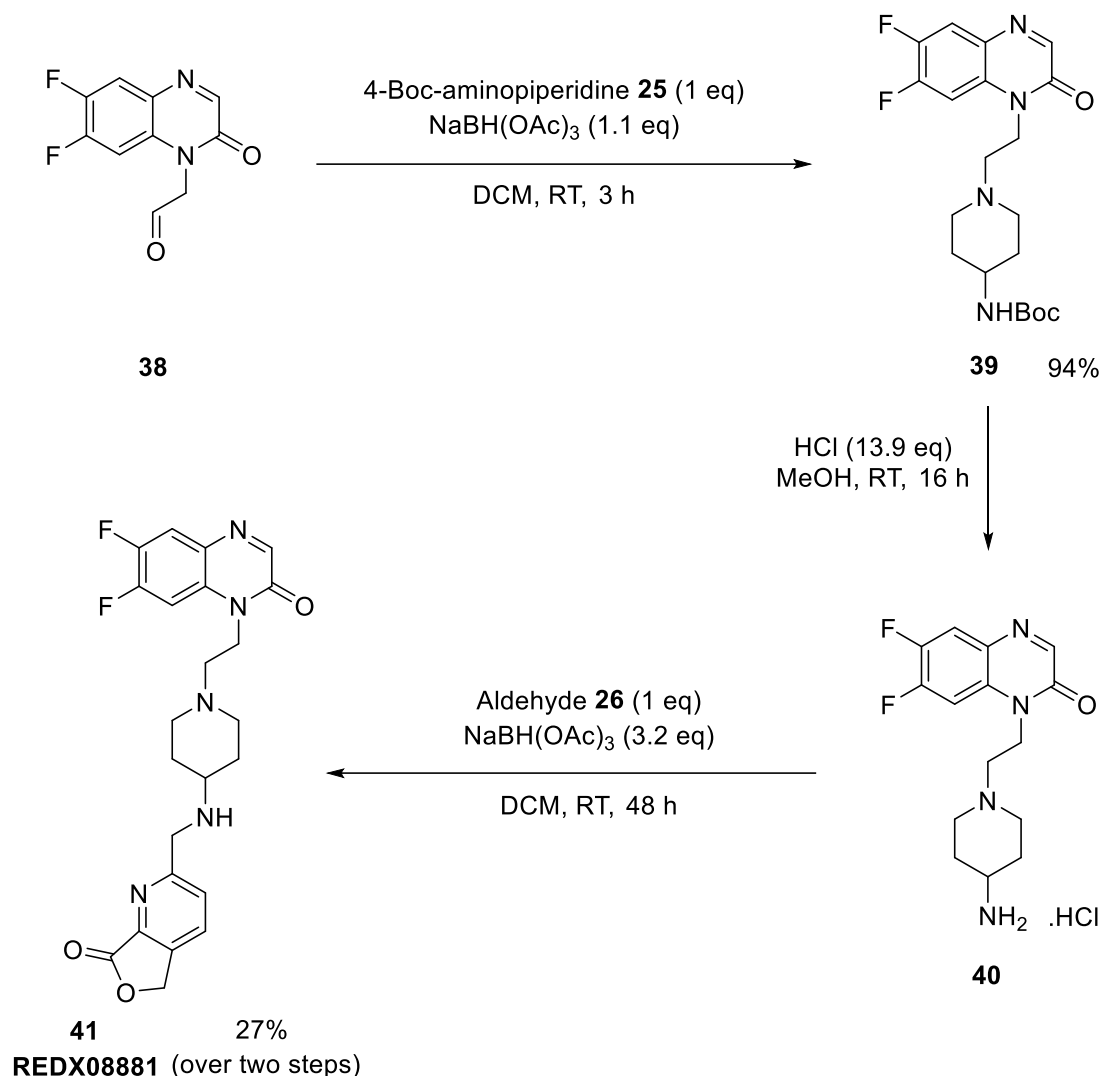
Synthetic route to of REDX08881 **41**.

Scheme 7

To determine the antibacterial properties of the suspected metabolites of REDX08220 **23** and REDX08881 **41**, lactone hydrolyses were performed. REDX08220 **23** was treated with 7 equivalents of lithium hydroxide monohydrate in aqueous medium, and purified by preparative HPLC to give the hydrolysed product, REDX08495 **42**, in 67% yield, as shown in **Scheme 8**.
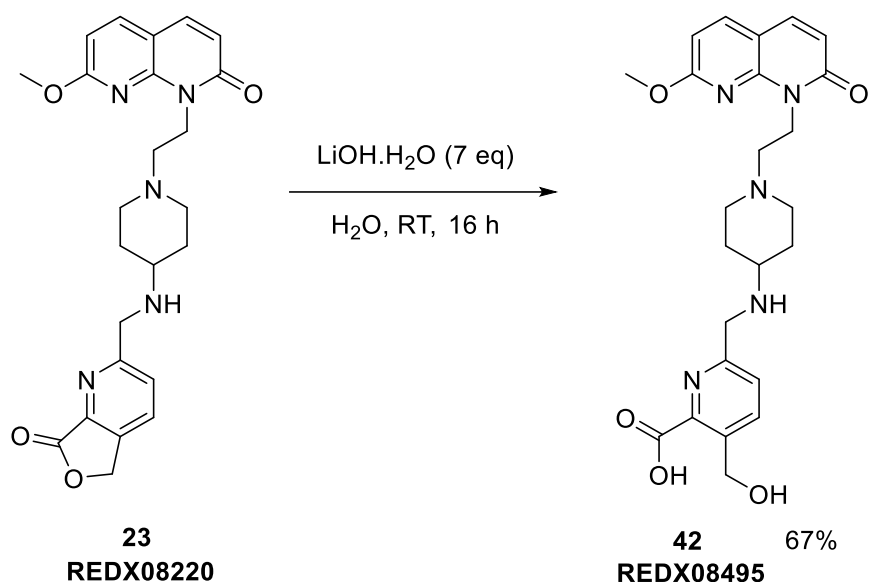
Lactone hydrolysis of REDX08220 **23** to yield expected soft drug metabolite REDX08495 **42**.

Scheme 8

Similarly, the hydrolysis of REDX08881 **41** in 6 equivalents of lithium hydroxide monohydrate afforded REDX08911 **43** in 77% yield, as shown in **Scheme 9**.
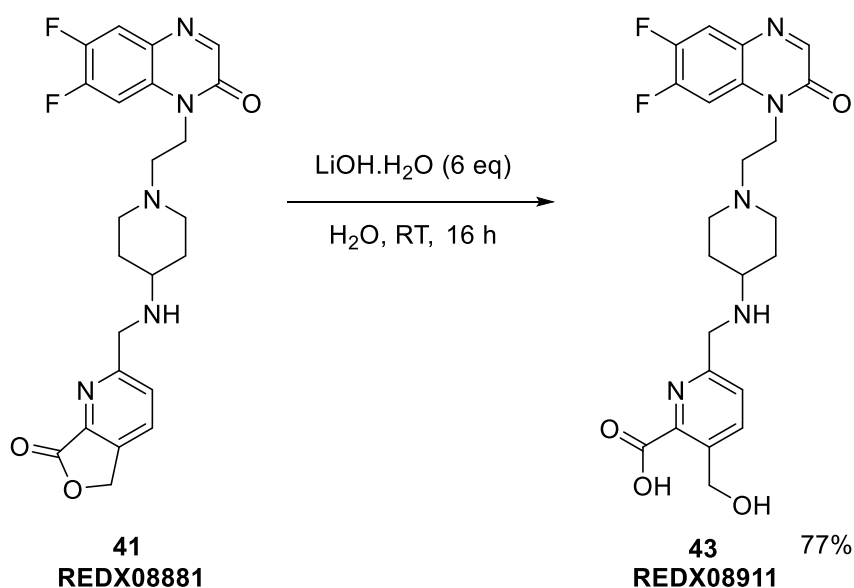
Lactone hydrolysis of REDX08881 **41** to yield expected soft drug metabolite REDX08911 **43**.

Scheme 9

In order to assess how the lactone positioning of the southern group influenced the antibacterial activity and the stability of the compound, an isomer of aldehyde **26** was prepared using a route previously published by Boral et al.[78] as outlined in **Scheme 10**.
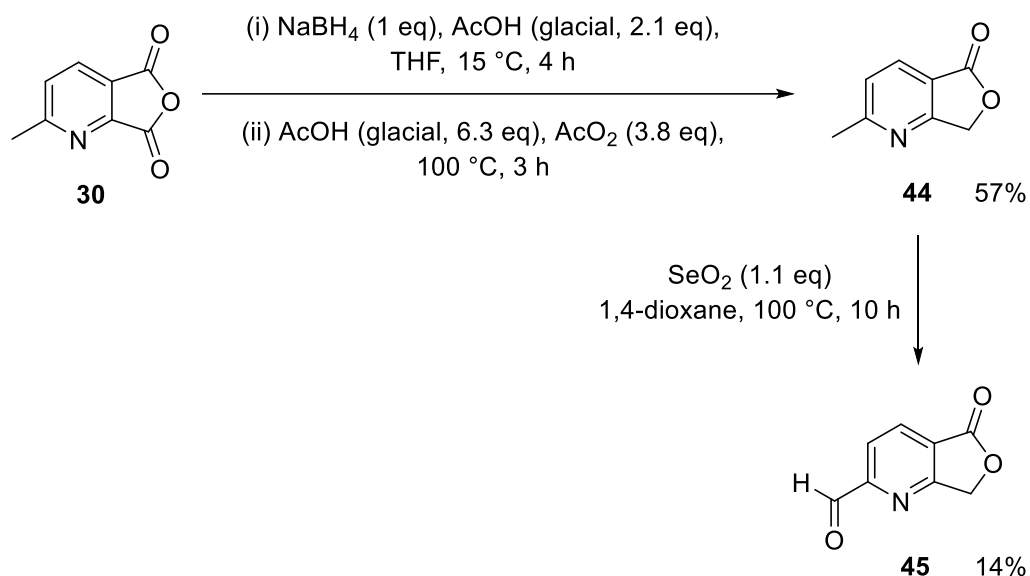
Synthetic route to alternative fused γ-lactone aldehyde **45**.

Scheme 10

The regioselective reduction using NaBH₄ was successfully completed. Comparison of
^{1}H and ^{13}C NMR spectroscopic data from the previously synthesised isomer of the aldehyde
confirmed that the alternative isomer to **26** was prepared. Aldehyde **45** was then used in a
manner analogous to that used to prepare REDX08220 **23** (**Scheme 6**), giving compounds
REDX08730 **46** and REDX08942 **47** (**Scheme 11** and **Scheme 12**).
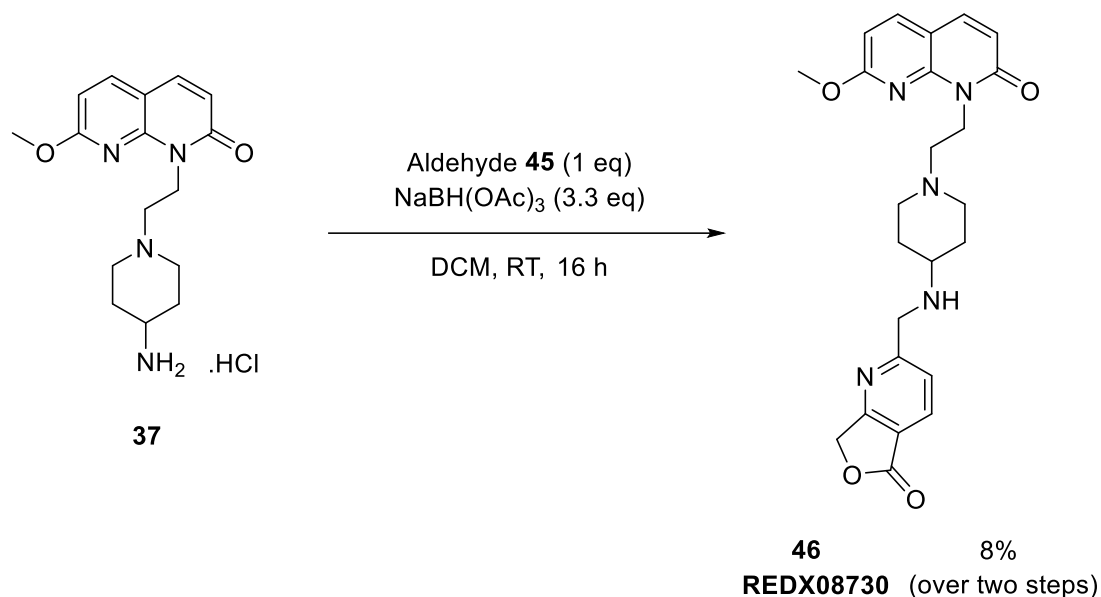
Synthesis of REDX08730 **46**.

Scheme 11
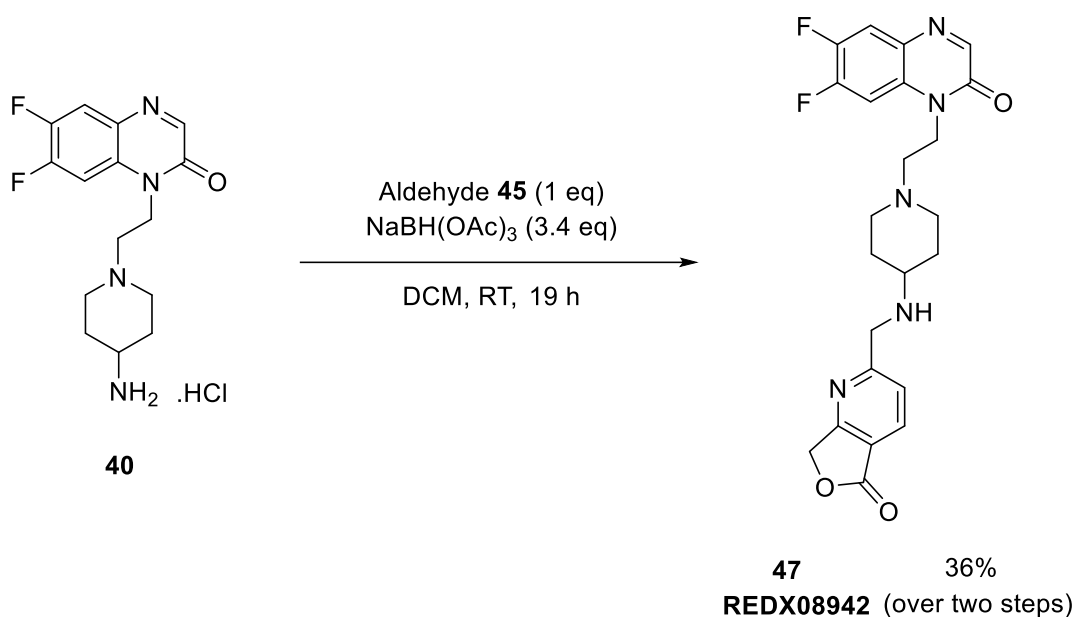
Synthesis of REDX08942 **47**.

Scheme 12

2.10 Desirable properties of successful lead antibacterial soft drug

In order to assess the progress of the soft drug antibacterial programme, clear guidelines on the desirable antibacterial and physiochemical properties of a potential lead compound were established.

2.10.1 Antibacterial properties

A successful lead compound should have a minimum inhibitory concentration (MIC) of ≤ 1 μg/mL against the relevant gram-positive and gram-negative pathogens (*P. aeruginosa, S. pneumoniae, S. aureus, H. influenzae*). This will be assessed by obtaining minimum inhibitory concentrations for each compound, relating to the lowest concentration of the compound required to prevent visible growth of the bacteria. An MIC ≤ 1 μg/mL would infer a suitably potent lead compound that could continue to be optimised. Additional antibacterial activity against a wider panel of gram-positive and gram-negative strains would be preferable, but not required. These will be monitored to assess for the possibility of optimising the activity into a pharmaceutical with wider-spectrum antibacterial properties.

The lead compound should have a low frequency of resistance (≤ 10^{-8} at 4 × MIC), suggesting bacterial resistance will not become immediately prevalent. Furthermore, no

cross-resistance to clinically relevant antibiotics should be observed. Cross-resistance will be assessed by testing the lead compound against a panel of resistant clinical isolates.

A known method of action will be determined through testing of the lead compound against the enzymatic target, DNA gyrase.

2.10.2 ADME properties

The ADME (Absorption, Distribution, Metabolism and Excretion) properties of a lead compound must also be considered. As the therapeutic window relies on the stability of the compound in human plasma compared to human lung tissue, priorities will be placed upon these ADME properties. S9 lung fraction contains cytosol and microsomes, and therefore contains a variety of proteins and other macromolecules. However, it has been well documented that S9 lung fraction contains only low concentrations of paraoxonase, the enzyme targeted to metabolise the parent soft drug compound.[59] Low stability in human plasma is an essential property for a successful inhaled antibacterial soft drug, and therefore instantaneous degradation is ideal. However, for a lead compound, a window for optimisation is expected, resulting in a lead having a target half-life of < 2 h in human plasma. Stability of the lead in human S9 lung fraction is also crucial, however, due to the novelty of the project, exact values of target half-lives are unknown with respect to how this value will effect dosing regimens. The lead, should, however, be highly stable in S9 lung fraction, and dose related studies would need to be performed in order to obtain more appropriate guidelines.

2.10.3 Physiochemical properties

The lead compound should have appropriate physiochemical properties to ensure suitable dosing can occur. Furthermore, the physiochemical properties should be sufficient to allow assessment of other properties to occur without issues being encountered during the assay conditions. The compound should be stable under the buffered conditions (pH = 7.4) encountered in most biological assays (< 20% degradation after 24 h). The compound must have a high enough solubility (> 15 µM) so precipitation during assay conditions is not problematic.

2.10.4 Toxicity

A lead compound should be non-cytotoxic against at least one human cell line (i.e. hepG2 or HEK), with a CC_{50} value of > 32 µg/mL. A CC_{50} value relates to the concentration of

compound required to initiate a 50% reduction in cell viability. Furthermore, assessment of cardiotoxicity *via* hERG IonWorks model should result in an $IC_{50} > 33$ μM for the hydrolysed metabolite of the parent. This should reduce the risk associated with *torsades de pointes*, giving a window for further optimisation. Due to the nature of the soft drug project, the hERG IC_{50} for the parent compound should not be relevant; however it will be measured in order to reinforce the benefits of a soft drug approach to antibacterial research.

2.10.5 Summary of desirable properties of lead antibacterial soft drug

It should be noted that although these guidelines (**Table 6**) were put in place to help assess the progress of the project towards obtaining a lead compound, there is room for flexibility on a case-by-case basis.

Antibacterial properties		
MICs	*S. pneumoniae*	≤ 1 μg/mL
	S. aureus	≤ 1 μg/mL
	H. influenzae	≤ 1 μg/mL
	AND/OR	
	P. aeruginosa	≤ 1 μg/mL
	Gram-positive and gram-negative strains	Monitor for additional antibacterial activity
Frequency of resistance		≤ 10^{-8} at 4 × MIC
Cross-resistance		No cross-resistance to current antibiotics
Method of action		Proven method of action against the isolated enzyme
ADME properties		
Plasma stability		Low stability in human plasma ($t_{1/2} < 2$ h)
S9 lung fraction stability		High stability in human S9 lung fraction
Physiochemical properties		
Chemical stability		Stable under buffered conditions (pH = 7.4)
Solubility		> 15 μM
Toxicity		
Cytotoxicity		hepG2 $CC_{50} > 32$ μg/mL
Cardiotoxicity		hERG IC_{50} (metabolite) > 33 μM (IonWorks)

Table 6

2.10.6 Discussion of chosen assays

Minimum inhibitory concentrations (MICs) were used to determine how active the compound was against each bacterium, with lower MICs inferring a lower concentration of the selected compound was required to induce an inhibitory response. Therefore a lower MIC corresponds to a more potent pharmaceutical.

Physiochemical and ADME properties were deemed important to measure from an early stage in order to assess potential trends in the data. Of particular interest to the soft drug approach to antibacterial research was the relative human plasma and human lung stabilities of the compounds. These values were determined through incubation of the compound with either human plasma or human S9 lung fraction, and monitoring of the parent compound concentration by LC at a series of time points throughout the 24 h incubation. The use of an internal standard allowed quantitative measurement of the amount of parent remaining, and appropriate positive and negative controls allowed the success of the assay to be monitored. In the initial wave of stability assays, phosphate buffer was used to maintain a constant pH (pH = 7.4), to eliminate the possibility of pH dependant instability. It was therefore assumed that the inclusion of phosphate buffer had no effect on the stability of the compound in question. Throughout the research programme, analysis of the effect of aqueous phosphate buffer on stability was pursued, resulting in modified assay conditions containing neat human plasma/S9 lung fraction and a reduced incubation time of 2 h as a result.

The kinetic solubility was measured to determine if the ligand was likely to be soluble in aqueous media, a property which has a large impact on the success of further studies such as hERG inhibition and hepG2 cell viability.

Cytotoxicity was assessed through incubation of the chosen compound at 37 °C for 24 h with hepG2 cells. The viability of the cells was then measured using CellTiter-Glow®, giving an indication to the general cellular toxicity of the compound. The greater the CC_{50} value (in μg/mL), the greater the concentration of the compound that was required to result in a toxic response, i.e. the less toxic the compound was to hepG2 cells.

Cardiotoxicity was determined either through measuring the inhibition of the hERG channel at a standard concentration (11 μM or 100 μM), or through obtaining an IC_{50} for the selected compound. A percentage inhibition of the hERG channel was observed through analysis of the current difference before and after addition of the compound. A lower percentage inhibition should correspond to a decreased likelihood of cardiotoxicity associated with inhibition of the hERG ion channel.

2.11 Antibacterial and ADME results

2.11.1 Key for relevant biological and physiochemical results

To aid understanding of results, a portion the following data is colour coded, according to the key below. Desired properties are designated green, whereas undesired are coloured red. Intermediary results are coloured orange due to their ability to lead to desired criteria through optimisation.

MICs		≤ 1 µg/mL	2 − 16 µg/mL	≥ 32 µg/mL
Kinetic solubility		> 15 µM	10 − 15 µM	< 10 µM
hERG inhibition (% at 11 µM)		< 10%	10 − 30%	> 30%
hERG inhibition (% at 100 µM)		< 20%	20 − 50%	> 50%
hERG inhibition (IC$_{50}$)		> 33 µM		≤ 33 µM
hepG2 (CC$_{50}$)		> 32 µg/mL		≤ 32 µg/mL
Human plasma stability	% parent remaining at end of assay	< 50%	50 − 70%	> 70%
	% metabolite remaining at end of assay	> 70%	50 − 70%	< 50%
Human plasma stability (with 5 mM EDTA)	% parent remaining at end of assay	> 70%	50 − 70%	< 50%
	% metabolite remaining at end of assay	> 70%	50 − 70%	< 50%
Human S9 lung stability	% compound remaining at end of assay	> 70%	50 − 70%	< 50%
Buffer stability	% compound remaining at end of assay	> 70%	50 − 70%	< 50%

Table 7

2.11.2 Antibacterial results: soft drug probe molecules

Based on the previously established guidelines, the antibacterial results for compounds **23**, **41** − **43**, **46** and **47** are shown in **Table 8**, coloured according to the key defined in **Section 2.11.1**.
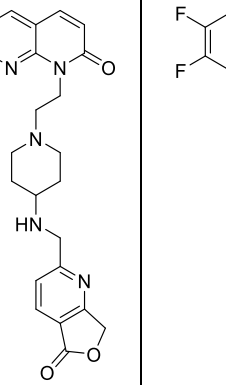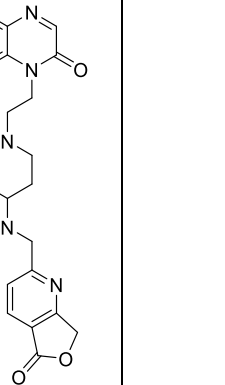
Redx No.		REDX08220 **23**	REDX08495 **42**	REDX08881 **41**	REDX08911 **43**	REDX08730 **46**	REDX08942 **47**
Structure							
MICs (µg/mL)	*A. baumannii* NCTC13420	32	> 64	> 64	> 64	> 64	> 64
	E. cloacae NCTC13406	64	> 64	> 64	> 64	> 64	> 64
	E. coli ATCC25922	8	> 64	32	> 64	> 64	> 64
	H. influenzae ATCC49247	16	> 64	64	> 64	> 64	> 64
	K. pneumoniae ATCC700603	> 64	> 64	> 64	> 64	> 64	> 64
	P. aeruginosa ATCC27853	> 64	> 64	> 64	> 64	> 64	> 64
	S. aureus ATCC29213	0.5	> 64	16	> 64	16	> 64
	S. pneumoniae ATCC49619	2	> 64	8	> 64	> 64	> 64
	E. coli W4573	16	> 64	> 64	> 64	> 64	> 64
	E. coli N43	1	> 64	4	> 64	64	32

Table 8

2.11.3 Physiochemical and toxicity results: soft drug probe molecules

Each compound was profiled for its physiochemical properties and toxicity, in order to assess its suitability for an inhaled antibacterial soft drug.

The results of these assays for compounds **23**, **41** – **43**, **46** and **47** are shown in **Table 9**, coloured according to the key defined in **Section 2.11.1**.
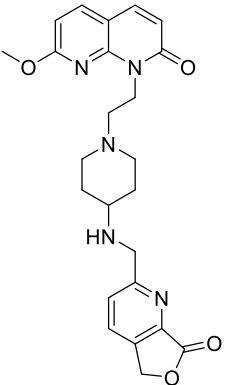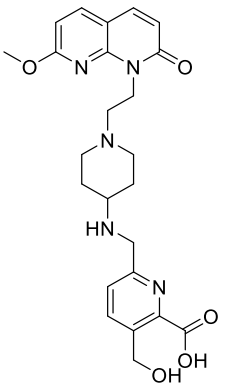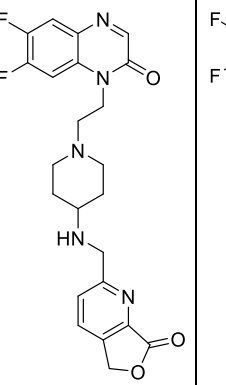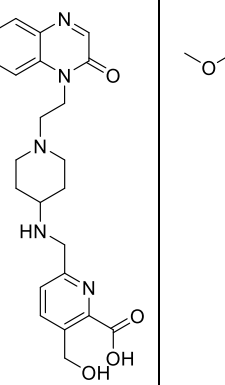
Redx No.	REDX08220 **23**	REDX08495 **42**	REDX08881 **41**	REDX08911 **43**	REDX08730 **46**	REDX08942 **47**
TPSA†	96.9	128.1	87.1	118.4	96.9	87.1
clogP†	1.23	0.66	1.32	0.65	1.32	1.48
clogD$_{7.4}$	0.19	-1.89	0.69	-1.90	0.26	0.80
Measured logD$_{7.4}$	< 0.2	< 0.2	< 0.2	-	-	0.58
Kinetic solubility	70.9 µM	> 100 µM	-	-	-	> 100 µM
hERG inhibition (IC$_{50}$)	> 33 µM	> 33 µM	-	-	-	-
hERG inhibition (% at standard concentration)	31% at 100 µM	7% at 100 µM	25% at 11 µM	10% at 11 µM	4% at 11 µM	93% at 11 µM
hepG2 (CC$_{50}$, µg/mL)	> 128	> 128	> 128	> 128	> 128	> 128

† Calculated using ACD/Percepta 14.0.0.

Table 9

2.11.4 ADME results: soft drug probe molecules

The synthesised compounds were assessed for their stability properties, in order to assess their suitability for an inhaled antibacterial soft drug.

The results of these assays for compounds **23**, **41** – **43**, **46** and **47** are shown in **Table 10**, coloured according to the key defined in **Section 2.11.1**.

Assay type	Conc.	Temp.	Time	REDX08220 23	REDX08495 42	REDX08881 41	REDX08911 43	REDX08730 46	REDX08942 47
Human plasma stability (% remaining)									
Plasma/phosphate buffer	1:1	37 °C	5 h	41%	100%	1%	88%	4%	20%
Plasma/phosphate buffer + EDTA (5 mM)	1:1	37 °C	5 h	71%	100%	74%	95%	89%	95%
Plasma/Tris HCl buffer	1:1	37 °C	5 h	62%	95%	44%	80%	-	93%
Plasma/Tris HCl buffer + EDTA (5 mM)	1:1	37 °C	5 h	78%	89%	67%	78%	-	96%
Plasma	100%	37 °C	2 h	55%	100%	16%	70%	22%	53%
Human S9 lung fraction stability (% remaining)									
S9/phosphate buffer	0.5 mg/mL	37 °C	5 h	68%	100%	72%	98%	45%	52%
S9	5 mg/mL	37 °C	2 h	100%	-	100%	-	52%	100%
Buffer stability (% remaining)									
Phosphate buffer	0.1 M	37 °C	5 h	50%	100%	58%	100%	89%	79%
Phosphate buffer	0.1 M	RT	5 h	68%	-	58%	-	100%	87%
Tris HCl buffer	0.1 M	37 °C	5 h	83%	-	79%	-	100%	89%
Tris HCl buffer	0.1 M	RT	5 h	95%	-	88%	-	100%	100%

Table 10

2.12 Discussion of antibacterial and ADME results

2.12.1 Antibacterial properties of REDX08220 (23)

REDX08220 **23**, as prepared in **Section 2.9.3**, was found to show marginal activity against several gram-positive and gram-negative pathogens. Importantly, activity was not completely eliminated by introduction of a hydrolysable bicyclic system.

Redx No.	REDX08220 **23**	GSK Comparison Compound[41] **48**
Structure		
E. coli	8	5
H. influenzae	16	-
K. pneumoniae	> 64	-
P. aeruginosa	> 64	> 8
S. aureus	0.5	0.02
S. pneumoniae	2	0.05
E. coli W4573	16	-
E. coli N43	1	-

(The *E. coli* through *E. coli N43* rows are labelled collectively: MICs (µg/mL))

Comparison of antibacterial properties of REDX08220 **23** against GSK NBTI compound **48**.

Table 11

Unfortunately, data was limited regarding the potency of comparator compound **48** (**Table 11**).[41] In general, REDX08220 **23** was less potent against the tested bacteria. However, as the bacterial strains reported in the literature were not identical to those in-house, only general comparisons could be made. Broadly, REDX08220 **23** retained potency against the gram-positive strains (*S. aureus* and *S. pneumoniae*), consistent with the less complex nature of the bacterial cell wall. Similarly, potency was observed against *E. coli* N43, a lab-mutated efflux-knockout gram-negative strain used for allowing efflux liabilities to be characterised in a bacterial setting. Without the ability to efflux the compound out of the cell, this strain was more susceptible to pharmaceutical intervention.

However, encouraging activity against gram-negative strains, *E. coli* ATCC25922 (8 µg/mL) and *H. influenzae* ATCC49247 (16 µg/mL), were considered as indicative of initial positive gram-negative antibacterial activity for the soft drug series. It could be postulated that the reduction in antibacterial activity was consistent with the increase in polarity in the southern portion of the molecule. As this area of the structure binds to the lipophilic pocket in DNA gyrase subunit A, increasing polarity along this vector could be detrimental to binding affinity. Furthermore, the connectivity of the lactone-containing region may be suboptimal, suggesting the assessment of alternative connection points could result in a more potent compound (**Figure 33**).
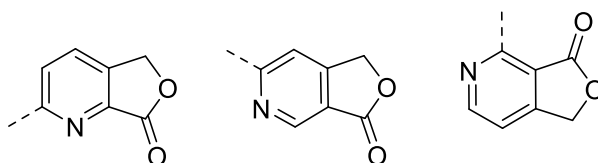
Potential analogues of REDX08220 **23** with varying attachment point to the southern group.

Figure 33

2.12.2 Analysis of antibacterial trends for REDX08220 analogues

Several analogues of REDX08220 **23** were synthesised in order to assess potential trends in potency. Although six compounds were reported (**Section 2.11.1**), particular attention should be directed towards REDX08220 **23** and its suspected metabolite REDX08495 **42** (**Table 12**).

The probe compound, REDX08220 **23**, was found to have moderate antibacterial activity against a variety of bacterial strains, as previously discussed. However, in order to assess compliance with the soft drug hypothesis, the expected metabolite, REDX08495 **42**, was also tested against the antibacterial panel. The compound was found to be consistently inactive against the entire spectrum of tested bacteria, suggesting hydrolysis of the lactone moiety was sufficient to remove the antibacterial activity of the series. This provided further encouraging results for proof of the antibacterial soft drug hypothesis.
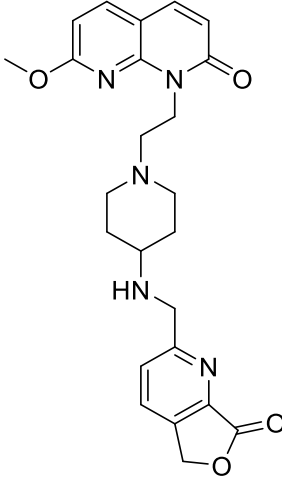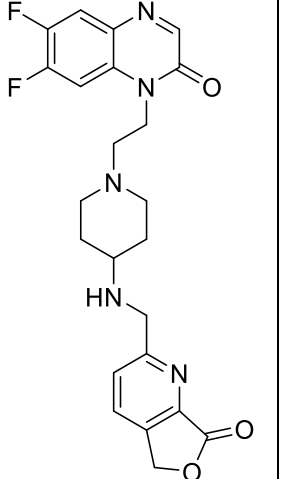
Redx No.		REDX08220 **23**	REDX08495 **42**
		"Parent"	*"Metabolite"*
Structure			
MICs (µg/mL)	*A. baumannii* NCTC13420	32	> 64
	E. cloacae NCTC13406	64	> 64
	E. coli ATCC25922	8	> 64
	H. influenzae ATCC49247	16	> 64
	K. pneumoniae ATCC700603	> 64	> 64
	P. aeruginosa ATCC27853	> 64	> 64
	S. aureus ATCC29213	0.5	> 64
	S. pneumoniae ATCC49619	2	> 64
	E. coli W4573	16	> 64
	E. coli N43 (efflux-knockout)	1	> 64
Measured $logD_{7.4}$		< 0.2	< 0.2
$\Delta clogD_{7.4}$[†]		0	-2.08
ΔTPSA[†]		0	+31.2

[†]Calculated using ACD/Percepta 14.0.0, using REDX08220 **23** as a baseline.

Comparison of antibacterial properties for REDX08220 **23** against the suspected metabolite, REDX08495 **42**.

Table 12

It was postulated that the $logD_{7.4}$ of REDX08220 **23** was suboptimal, resulting in poor permeability and therefore lowering the observed antibacterial activity. Thus, the use of a different northern group was adopted in order to alter the $logD_{7.4}$, while maintaining a similar metabolic liability in the southern region of the molecule. Unfortunately, the resulting compound, REDX08881 **41**, showed a reduction in antibacterial activity (**Table 13**).

Redx No.	REDX08220 **23**	REDX08881 **41**
Structure		

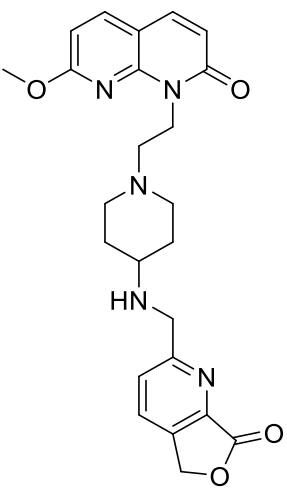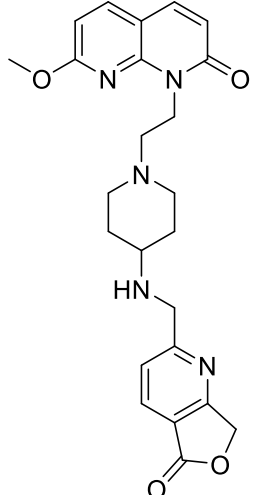|		REDX08220 **23**	REDX08881 **41**
MICs (µg/mL)	*A. baumannii* NCTC13420	32	> 64
	E. cloacae NCTC13406	64	> 64
	E. coli ATCC25922	8	32
	H. influenzae ATCC49247	16	64
	K. pneumoniae ATCC700603	> 64	> 64
	P. aeruginosa ATCC27853	> 64	> 64
	S. aureus ATCC29213	0.5	16
	S. pneumoniae ATCC49619	2	8
	E. coli W4573	16	> 64
	E. coli N43 (efflux-knockout)	1	4
Measured logD$_{7.4}$		< 0.2	< 0.2
ΔclogD$_{7.4}$[†]		0	+0.50
ΔTPSA[†]		0	-9.8

[†]Calculated using ACD/Percepta 14.0.0, using REDX08220 **23** as a baseline.

Comparison of antibacterial properties for REDX08220 **23** against a similar analogue, REDX08881 **41**.

Table 13

REDX08881 **41** was prepared (**Section 2.9.4**) and was found to be weakly active against both the gram-positive strains and efflux deficient *E. coli*. The resulting drop in potency was rationalised to be due to a decrease in the permeability of the bacteria to the compound. Although the calculated values suggested REDX08881 **41** was more lipophilic than REDX08220 **23**, it could be postulated that this is not the case. It has recently been reported that the methoxypyridine substituents follow an inverse logD$_{7.4}$ trend to that conventionally expected.[79] Due to the nature of antibacterial research, and each bacterial strain's permeability window for a drug series, it is near impossible to predict the exact balance of polarity and lipophilicity required to result in optimal permeability. The simplest method of determining the ideal logD$_{7.4}$ window is through the synthesis of analogues of varying

polarity, and monitoring for trends in antibacterial activity. Therefore, further analogue synthesis and experimentally monitoring for $logD_{7.4}$ should allow comparison of calculated $logD_{7.4}$ ($clogD_{7.4}$) values with measured $logD_{7.4}$ values, aiding interpretation of the results. Gratifyingly, the antibacterial differences between REDX08220 **23** and REDX08730 **46** could be easily rationalised.

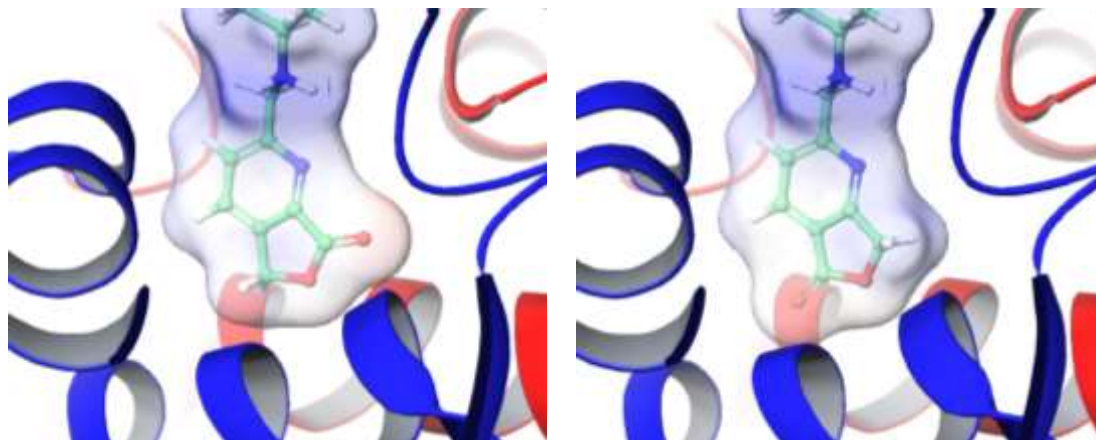| Redx No.		REDX08220 **23**	REDX08730 **46**
Structure			
MICs (µg/mL)	*A. baumannii* NCTC13420	32	> 64
	E. cloacae NCTC13406	64	> 64
	E. coli ATCC25922	8	> 64
	H. influenzae ATCC49247	16	> 64
	K. pneumoniae ATCC700603	> 64	> 64
	P. aeruginosa ATCC27853	> 64	> 64
	S. aureus ATCC29213	0.5	16
	S. pneumoniae ATCC49619	2	> 64
	E. coli W4573	16	> 64
	E. coli N43 (efflux-knockout)	1	64
Measured $logD_{7.4}$		< 0.2	-
$\Delta clogD_{7.4}$†		0	+0.07
ΔTPSA†		0	0

†Calculated using ACD/Percepta 14.0.0, using REDX08220 **23** as a baseline.

Comparison of antibacterial properties for REDX08220 **23** against an isomeric compound, REDX08730 **46**.

Table 14

Moving the position of the lactone carbonyl resulted in a dramatic decrease in antibacterial activity for REDX08730 **46** when compared to its isomer REDX08220 **23** (**Table 14**). It was therefore rationalised that modifications in the southern region of the molecule either resulted in a subtle steric clash with the binding site, or directed a region of polarity into

the lipophilic area of the protein active site. Literature-guided and computational investigation of this result suggested polarity was not tolerated within the confines of the southern binding pocket, validating the experimentally determined hypothesis.[80]

REDX08220 **23** and REDX08730 **46** in DNA gyrase (PDB: 2XCS[36]), highlighting the detrimental effect of directing polarity into the lipophilic pocket.

Figure 34

2.12.3 Analysis of toxicity trends for REDX08220 analogues

In order to preliminarily assess the suitability of the synthesised compounds as a potential therapy, cytotoxicty and cardiotoxicty data (**Table 15**) was collected on a selection of the prepared compounds as outlined in **Section 2.10.4**.

Redx No.	REDX08220 **23**	REDX08495 **42**
Structure		
hepG2 (CC$_{50}$, µg/mL)	> 128	> 128
hERG inhibition	31% at 100 µM	7% at 100 µM

Toxicity data for REDX08820 **23** and REDX08495 **42**.

Table 15

No cytotoxicity liabilities were observed for the soft drug probe compounds, with hepG2 CC_{50} values consistently > 128 μg/mL. It was unknown how the bicyclic lactone would effect the cytotoxicity of the series, and therefore the non-cytotoxic properties of REDX08220 **23** represented a highly encouraging result.

Obtaining hERG inhibition data for REDX08220 **23** and REDX08495 **42** provided initial results to suggest how hERG inhibition was positively effected by metabolic hydrolysis (REDX08220 **23**: 31% at 100 μM, REDX08495 **42**: 7% at 100 μM). As hERG inhibition was successfully reduced for REDX08495 **42**, the soft drug hypothesis was validated with regards to how adjustments to $logD_{7.4}$ and TPSA could be used to positively effect cardiotoxicity.

The low values for hERG inhibition of the parent compounds suggested cardiotoxicity for the series was not an immediate issue. However, it was envisioned that optimisation of antibacterial activity would result in potent hERG inhibition for the parent compounds, reinforcing the merits of a soft drug approach to antibacterial research.

2.12.4 Analysis of stability trends for REDX08220 analogues

An initial indication of the low stability of the scaffold in human plasma was extrapolated from the poor recovery of the compound from a plasma protein binding assay, suggesting the compound was degrading during the course of the assay (**Table 16**).

Redx No.	REDX08220 **23**		REDX08495 **42**		REDX08881 **41**	
Structure						
Kinetic solubility	70.92 μM		> 100 μM		-	
	% Free	% Recovery	% Free	% Recovery	% Free	% Recovery
Human PPB	NV	< 30%	25%	97%	NV	< 30%

Initial physiochemical data for REDX08220 **23**, REDX08495 **42** and REDX08881 **41**.

Table 16

2.12.5 Initial human plasma and human S9 lung stability assays

The stability of the soft drug compounds in human plasma and human S9 lung fraction was of particular interest throughout the research programme. It was envisioned that low plasma stability may be indicative of paraoxonase induced metabolism, due to high levels of paraoxonase within the blood plasma. Furthermore, as lung tissue and S9 lung fraction are presumed to contain low levels of paraoxonase, the increased stability in this medium may suggest targeting of paraoxonase.

In order to assess this, each compound was incubated with the desired medium and the percentage of parent compound remaining by LC was reported at a series of time points (**Table 17**). It was hypothesised that using in-house protocols established for a microsomal stability assay, an S9 lung fraction stability assay could be performed through replacing the microsomes with S9 lung fraction. In both the plasma and the S9 lung stability assays, the biological medium was diluted with phosphate buffer (pH = 7.4) to prevent pH fluctuations during the assay, allowing incubation times of up to 24 h. It is generally accepted that the inclusion of phosphate buffer during an assay has minimal effect on the stability of the compound being investigated, resulting in its widespread use throughout most biological and ADME assays.

Redx No.	REDX08220 **23**	REDX08495 **42**	REDX08881 **41**	REDX08911 **43**	REDX08730 **46**
	"Parent"	*"Metabolite"*	*"Parent"*	*"Metabolite"*	*"Parent"*
Plasma/ phosphate buffer (1:1)	41%	100%	1%	88%	4%
Plasma/ phosphate buffer (1:1) + EDTA (5 mM)	71%	100%	74%	95%	89%
S9/phosphate buffer (0.5 mg/mL)	68%	100%	72%	98%	45%

Stability data (% remaining after 5 h) for compounds **23**, **41** – **43** and **46**.

Table 17

It was found that REDX08881 **41** was metabolised much more readily in plasma than in S9 lung fraction, however a narrower window of stability was observed for REDX08220 **23** (**Table 17**). Although REDX08220 **23** and REDX08881 **41** shared an identical southern group, REDX08881 **41** was found to be hydrolysed more rapidly in human plasma. This suggested

the lipophilicity of the compound also had implications for the rate of hydrolysis, with a change in $logD_{7.4}$ yielding a more rapidly metabolised compound. Unfortunately, literature precedent for hydrolysis of large molecules by paraoxonase is severely limited. Therefore any trends observed between the lipophilicity and the enzymatic instability of the compounds must rely upon in-house data. Synthesis of further analogues was determined to be necessary before trends could be postulated. Additionally, it was observed that altering the configuration of the lactone (REDX08730 **46**) resulted in decreased stability in both the plasma and S9 lung stability assays. Although this proved interesting, further investigation of this trend was deprioritised due to the poor antibacterial properties of these compounds.

Pleasingly, the suspected hydrolysed metabolites, REDX08495 **42** and REDX08911 **43**, were found to be stable in both human plasma and in human S9 lung fraction. This was consistent with the hydrolysed compounds no longer being a substrate for paraoxonase, suggesting the location of instability was situated in the southern portion of the scaffold. Although preliminary data was positive, it was observed that none of the parent compounds showed complete stability in the S9 lung fraction stability assay. Although this was noted, it was not immediately clear why the compounds were unstable, and instead this was attributed to the limitations of the current assay set-up.

Furthermore, to indirectly determine if paraoxonase concentrations effected the rate of metabolism of the parent compounds, EDTA was used as an additive, following similar protocols to those described by Boland *et al*.[81] It was hypothesised that spiking the plasma stability assay with EDTA (5 mM) would inhibit the paraoxonase in the plasma, reducing the amount of metabolism observed throughout the course of the incubation. This modification was successful, with levels of metabolism falling between 30% to 85%, depending on the parent compound in question. As a decrease in metabolism was recorded, this could be indicative of paraoxonase-based metabolism of the parent compounds, however, without profiling the compounds against the isolated enzyme, this could not be confirmed. Although encouraged by the increase in compound stability associated with EDTA addition, partial instability was still observed in the EDTA spiked assay, suggesting a second metabolic route was of growing importance.

2.12.6 Optimised human plasma and human S9 lung stability assays

To determine the cause of the instability, a series of control experiments were performed (**Table 18**). The stability of each compound was assessed in 100% plasma, and in the highest concentration of S9 lung fraction available (5 mg/mL). By removing phosphate buffer from the assay conditions, one possible cause of instability could be eliminated, and the resulting data could highlight the window of stability between human plasma and S9 lung fraction.

	REDX08220 **23**	REDX08495 **42**	REDX08881 **41**	REDX08911 **43**	REDX08730 **46**
	"Parent"	*"Metabolite"*	*"Parent"*	*"Metabolite"*	*"Parent"*
Plasma (100%)	55%	100%	16%	70%	22%
S9 (5 mg/mL)	100%	-	100%	-	52%

Optimised human plasma and human S9 lung stability results (% remaining after 2 h) for compounds **23, 41 – 43** and **46**.
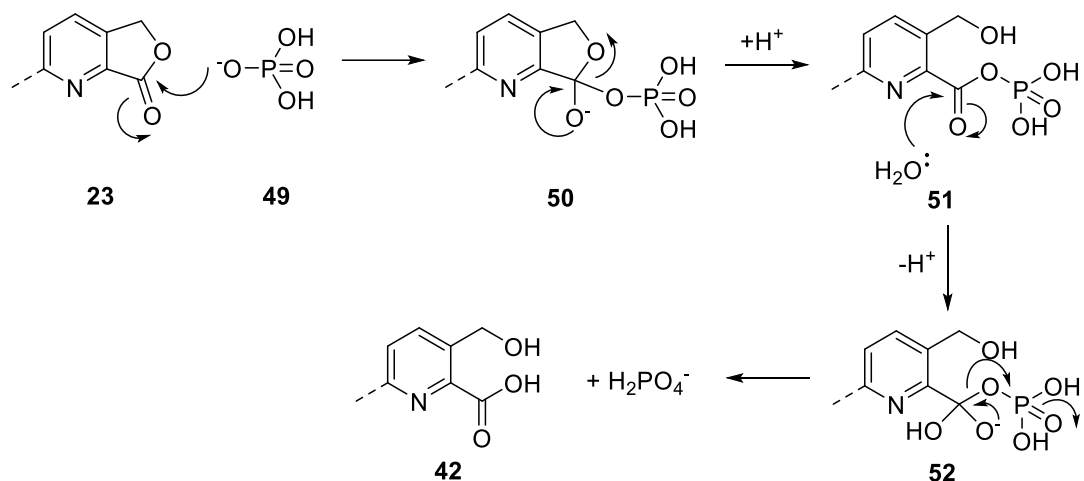
Table 18

Pleasingly, each parent compound showed an increased window of stability, when compared to the buffered assay conditions, with most compounds showing quantitative concentrations at the end of the S9 lung fraction stability experiment. This suggested the instability observed in the first wave of stability assays was explained through instability to the buffered conditions.

The variable stability observed between the different biological media could be attributed to paraoxonase concentrations. Human plasma was considered to have high levels of paraoxonase, whereas lung tissue has been reported to contain very low levels.[57] Therefore, the data reinforced the possibility of optimising a soft drug compound that would be selectively metabolised by paraoxonase within the blood. However, it should be noted that due to the absence of buffer during the assay, the incubation of each compound was limited to 2 h before a change in pH prevented the continuation of the experiment.

Although the results obtained were positive proof of concept for a viable soft drug antibacterial therapy, it was recognised that the parent compound was currently too stable in human plasma, and further efforts were required to promote the rate of metabolism in order to increase the therapeutic window. It was hypothesised that this could be achieved through the synthesis of structural isomers, evaluation of substituted derivatives of the fused lactone systems, and by assessment of alternative derivatives of the metabolically liable group.

2.12.7 Buffer stability assays

The relationship observed between the experiments containing, and in the absence of phosphate buffer, heavily suggested an incompatibility with aqueous phosphate ions. Furthermore, phosphate-activated ester hydrolysis has been reported in the literature and could be playing an important role in the degradation of the parent soft drugs (**Scheme 13**).[82]

Possible mechanistic route to lactone degradation of REDX08220 **23**.

Scheme 13

In order to conclude if the parent compounds were prone to aqueous phosphate-based degradation, a series of control experiments (**Table 19**) were performed, incubating each compound in question with phosphate buffer, and with tris(hydroxymethyl)aminomethane hydrochloride (Tris HCl) **53** buffer (**Figure 35**).
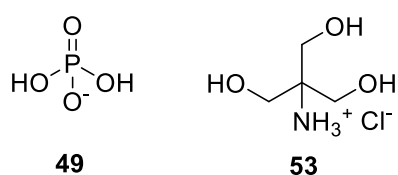
Structures of $H_2PO_4^-$ **49** (an ion involved in phosphate buffer equilibria) and Tris HCl **53**.

Figure 35

Tris HCl was specifically selected for the study due to its ability to buffer at pH 7.4 without the need for phosphate ions. All other variables were kept consistent, including concentration (0.1 M) and pH (7.4).

Redx No.	REDX08220 **23**	REDX08495 **42**	REDX08881 **41**	REDX08911 **43**	REDX08730 **46**
Phosphate buffer (37 °C)	50%	100%	58%	100%	89%
Phosphate buffer (RT)	68%	-	58%	-	100%
Tris HCl buffer (37 °C)	83%	-	79%	-	100%
Tris HCl buffer (RT)	95%	-	88%	-	100%

Buffer stability data (% remaining after 5 h) for compounds **23, 41 − 43** and **46**.

Table 19

The results of the control experiments confirmed the hypothesis; the observed instability appeared to be caused by the presence of phosphate ions in the incubation. Furthermore, temperature dependence was determined through performing parallel experiments at 37 °C and at room temperature (RT), indicating that a rise in the temperature increased the rate of degradation of the compounds. It was therefore assumed that the lactones in question were highly activated substrates that could be attacked by an excess of phosphate ions during the course of the assay. Further plasma stability assays were performed to test the hypothesis, replacing the phosphate buffer with Tris HCl (**Table 20**).

Redx No.	REDX08220 **23**	REDX08495 **42**	REDX08881 **41**	REDX08911 **43**
Plasma/Tris HCl buffer	62%	95%	44%	80%
Plasma/Tris HCl buffer + EDTA (5 mM)	78%	89%	67%	78%

Plasma stability results (% remaining after 5 h) for compounds **23** and **41 − 43**, replacing the previously used phosphate buffer with Tris HCl.

Table 20

The results of the human plasma/Tris HCl stability assays suggested increased stability in the absence of phosphate buffer. Furthermore, the addition of EDTA (5 mM) reduced the amount of compound that was metabolised during the course of the assay, reinforcing paraoxonase concentrations could be influential in the stability of the compounds. These results provided additional data to support the soft drug hypothesis, and that the observed instability in phosphate buffer could be optimised to create a selectively metabolised pharmaceutical.

Although it was critical to rationalise the instability of the parent compounds to phosphate buffer, further investigation into this property was deprioritised. Performing a more extensive screen of alternative buffers could provide interesting results around the stability of the lactone scaffold, allowing future stability studies to be carried out in a buffer that does not cause any breakdown of the parent compound. However, as opposed to further profiling the instability of the series, prioritises were placed on a combined approach of understanding the stability of the scaffold to plasma, and the avoidance of metabolism by phosphate ions.

In order to gain evidence to support that metabolism was occurring in the southern region of the scaffold, metabolite identification studies were undertaken, focussing on the metabolites that were generated upon incubation with human plasma.

2.13   Identification of metabolites of REDX08220 (23)

In order to assess whether the γ-lactone moiety was metabolically unstable in human plasma, identification of the metabolites of REDX08220 **23** was required. This was achieved through incubation of the parent compound with human plasma, and subsequent analysis of aliquots at standard time points by high-resolution mass spectrometry (HRMS).[†] Both the consumption of the parent compound and the formation of two new metabolic species were monitored throughout the course of the experiment. The results suggested the formation of two metabolites, one relating to methylation of the parent compound ([M+H]+14), and one corresponding to a hydration product ([M+H]+18).
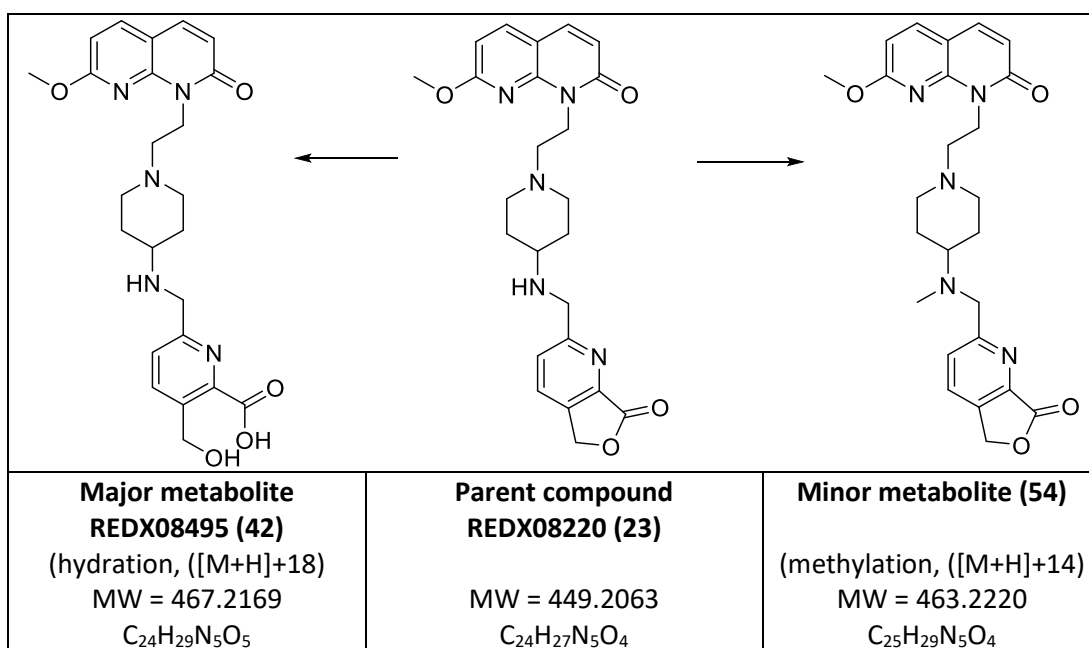

[†] High-resolution mass spectrometry was performed by Ciprotex, with human plasma samples prepared in-house by Redx Pharma.

Metabolite Identification of REDX08220 (23)
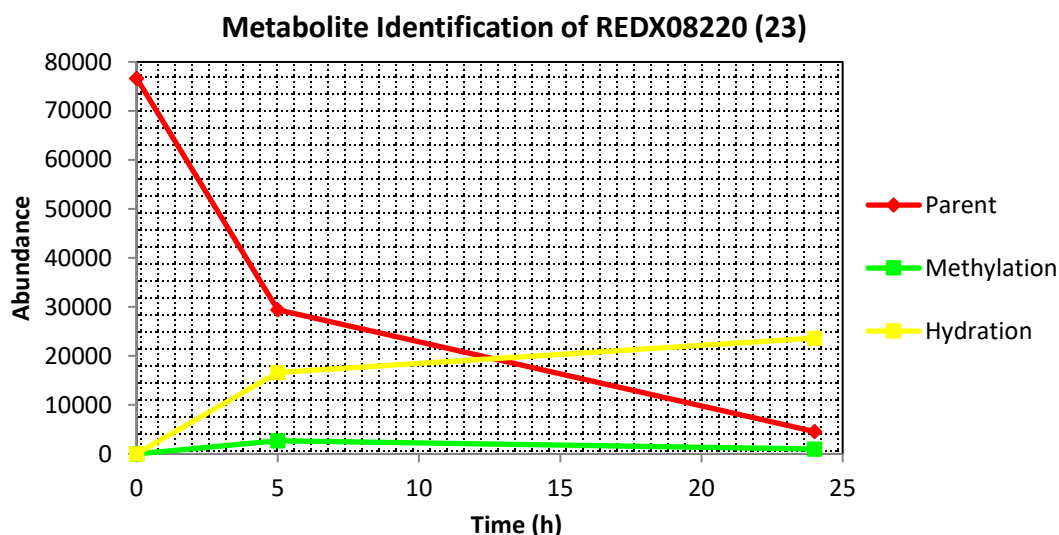
Graph of metabolic decay of REDX08220 **23** (parent) and formation of metabolites.
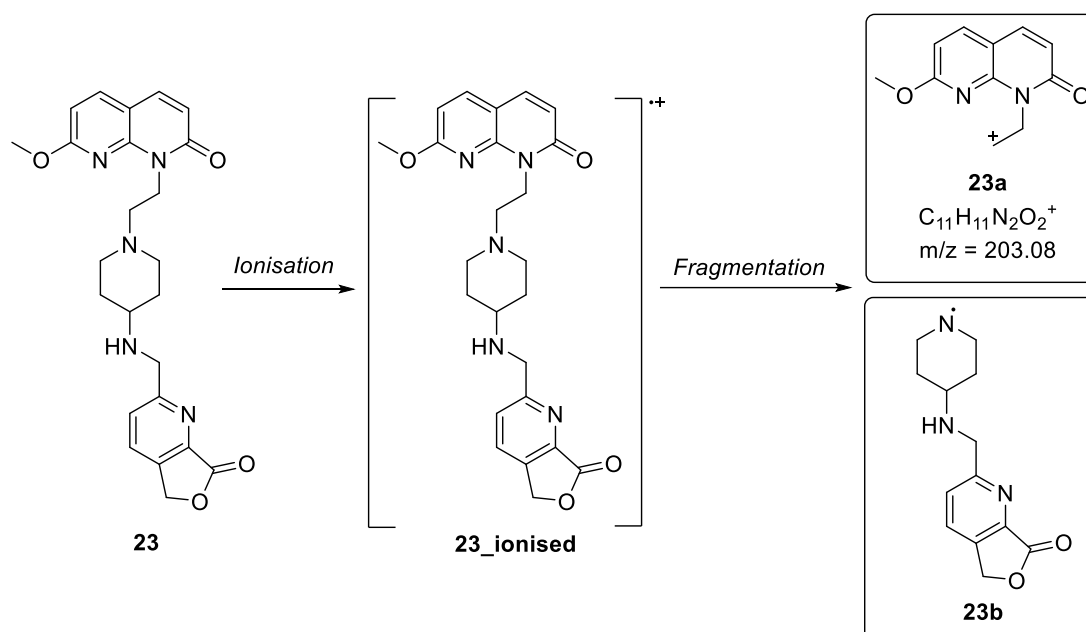
Figure 36

As shown in **Figure 36**, consumption of the parent (shown in red) was recorded over the course of the experiment. The data was consistent with metabolism and subsequent formation of two metabolites (shown in green (methylation) and yellow (hydration)). The mass of the major metabolite (yellow) was an agreement with the expected metabolic pathway; γ-lactone hydrolysis (**Figure 37**).

Major metabolite REDX08495 (42)	Parent compound REDX08220 (23)	Minor metabolite (54)
(hydration, ([M+H]+18)		(methylation, ([M+H]+14)
MW = 467.2169	MW = 449.2063	MW = 463.2220
$C_{24}H_{29}N_5O_5$	$C_{24}H_{27}N_5O_4$	$C_{25}H_{29}N_5O_4$

Diagrammatic depiction of metabolic pathways.

Figure 37

In order to assess the position where hydrolysis had occurred, analysis of the metabolite fragments was performed by HRMS. A fragment relating to the intact northern portion **23a** of the molecule was observed on the mass spectrum (m/z = 203.08), indicating hydration must have occurred in the lower section of the parent molecule (**Figure 38**).

Fragmentation of REDX08220 **23** to give northern group **23a** and southern group **23b**.

Figure 38

The formation of the metabolite was accompanied by an increase in polarity, consistent with unmasking the carboxylic acid, providing further evidence for γ-lactone hydrolysis.

Computational analysis of the fragmentation pattern and retention times from the second (methylated) metabolite peak corresponded to the *N*-methylated analogue of the parent. Although this was an interesting observation, methylation of the parent compound was a minor metabolic pathway, with very low levels of this metabolite being formed during the course of the experiment.

2.14   Summary

Investigation into the literature surrounding NBTI inhibitors of DNA gyrase highlighted potential cardiotoxic liabilities for the series. A novel method for overcoming the potent toxicity was hypothesised to be *via* adopting a soft drug approach. As a result, regions of the NBTI scaffold were assessed for their relative abilities to accommodate a metabolically liable feature.

Guided by computational modelling, structures with the highest likelihood of challenging the hypothesis were selected. The synthesis of several potential soft drug analogues followed, allowing subsequent profiling of their antibacterial and physiochemical properties.

A moderately potent compound, REDX08220 **23**, was successfully prepared and showed promising antibacterial properties against a selection of gram-positive and gram-negative pathogens. Furthermore, a preliminary investigation into the structure-activity relationship of soft drug NBTI inhibitors suggested areas in which the lactone carbonyl group was more tolerated, directing the development of the research programme. Additionally, varying the polarity ($logD_{7.4}$) of the inhibitors highlighted the importance of bacterial cell permeability in obtaining high antibacterial activity.

The suitability of the scaffold as a soft drug therapy has been emphasised by the removal of antibacterial activity upon lactone hydrolysis. Importantly, hERG inhibition was also observed to decrease upon hydrolysis of the lactone, supporting the benefits of a soft drug approach.

Furthermore, important data surrounding the metabolic instability of the fused pyridyl lactone has been generated. Initial insight into the stability profile of the soft drug was obtained through observing degradation of the parent compound upon incubation with human plasma. Structural identification of the compounds formed upon metabolism with human plasma yielded evidence to support lactone hydrolysis. Gratifyingly, minimal metabolism was observed when REDX08220 **23** was incubated with neat S9 lung fraction (5 mg/mL), suggesting varying paraoxonase concentrations in the incubation media may be responsible for the differences in stability.

Promising antibacterial activity and cardiotoxicity results, combined with an initial indication of differential stability properties in human plasma and human lung, provided proof of concept for a completely novel approach to antibacterial drug design.

Although the individual Objectives for the research project were met, further work was required to fully determine if an antibacterial soft drug could be a viable therapy. In particular, several biological and chemical parameters required optimisation, prior to selection of a lead compound.

Importantly, although the antibacterial properties of REDX08220 **23** were promising, the potency of the compound required improvement if it was to be a successful antibacterial therapy. Furthermore, the stability of REDX08220 **23** was of equal concern. Although the stability contrast between human plasma and human S9 lung fraction was encouraging, improving the stability of the series to phosphate buffer was hypothesised to simplify the elucidation of results obtained *in vitro*. Therefore, optimisation of the southern ring system was of equal priority to improving the antibacterial activity of the series.

Building on the success of REDX08220 **23**, investigation into the structure-activity and structure-stability relationships of the series was continued through the development of new, more focussed, Objectives.

Chapter 3:
A soft drug approach to bacterial pneumonia - optimisation and *in vivo* assessment

3 Optimisation of antibacterial soft drug series

3.1 Proposed work

Building on the successes of REDX08220 **23** (**Figure 39**) in providing proof of concept for a potential soft drug antibacterial therapy, research now focussed on optimising the drug-like properties of the series. Antibacterial activity and phosphate stability were determined to be the most important parameters to improve.

REDX08220 **23**		
MIC	*S. aureus*	0.5 µg/mL
	S. pneumoniae	2 µg/mL
	H. influenzae	16 µg/mL
Phosphate stability	Unstable	
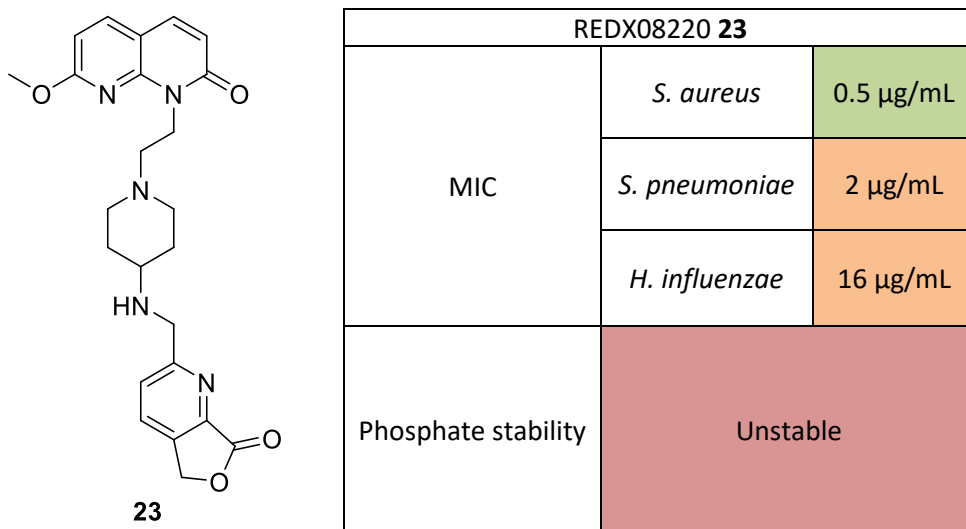
Areas of optimisation for REDX08220 **23**.

Figure 39

It was hypothesised that the pyridyl nitrogen of the fused lactone moiety may have been contributing to the incompatibility with phosphate buffer. Furthermore, to date, no FDA approved pharmaceuticals contain a fused pyridyl lactone. Encouraged by this finding, Objective 1 was set to prompt the discovery of a suitable replacement to the pyridyl lactone southern group (**Figure 40**).
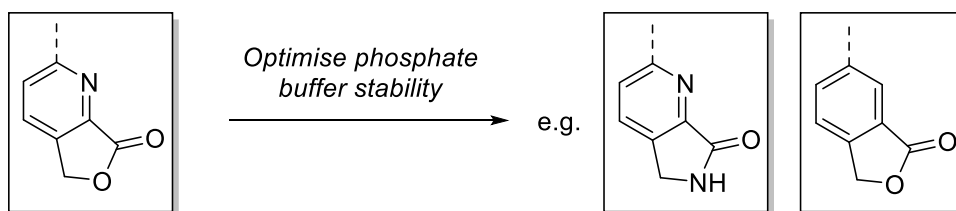
Optimisation of stability through modifications to the southern lactone containing region.

Figure 40

Upon selection of a suitable replacement for the pyridyl lactone moiety, optimisation of the synthetic route was essential. Thus, Objective 2 involved establishing a scalable,

reproducible and facile synthesis, allowing a range of analogues to be prepared. Importantly, utilising readily available starting materials and avoiding the low-yielding and unreliable Riley oxidation used in the preparation of REDX08220 **23**, was desired.

Upon development of a more streamlined synthetic route, Objective 3 focused on assessing the newly synthesised compounds for their antibacterial activity, to determine if an appropriately potent replacement for the unstable pyridyl lactone had been discovered.

With a more appropriate southern group installed, Objective 4 would focus towards optimising the antibacterial properties of the series through the synthesis of similar analogues with varying lipophilicities (**Figure 41**). By manipulating the $logD_{7.4}$ of the soft drug probe compounds, an optimal $logD_{7.4}$ window may be found, resulting in increased bacterial permeability and an overall boost in antibacterial activity.

55
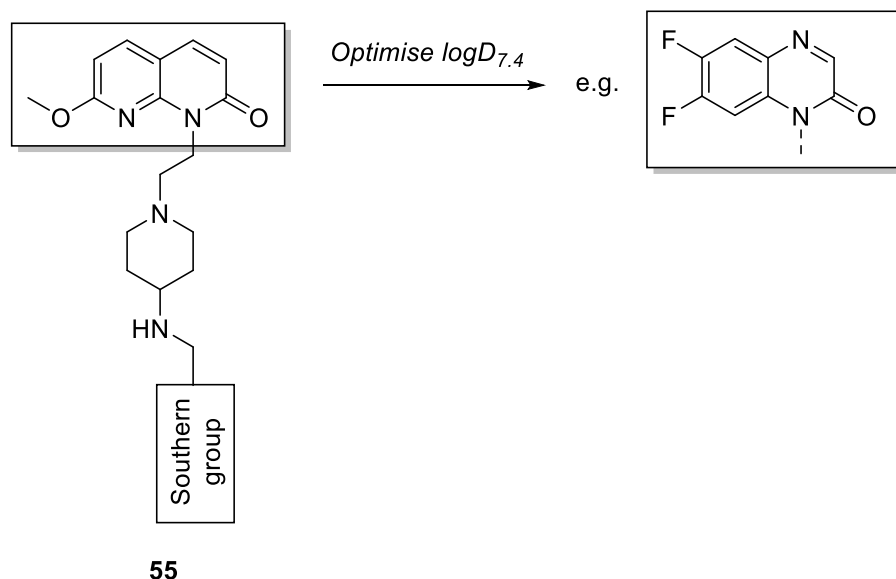
Altering $logD_{7.4}$ may aid bacterial permeability, improving antibacterial activity.

Figure 41

It was hypothesised that in order to challenge the structure-activity relationship of the southern lactone containing region fully, an appropriately potent northern group should be initially selected. Thus, following the selection of acceptably potent and drug-like northern groups, exploration of the southern group could proceed further. This investigation would be guided by the literature precedence for hydrolysable substrates, combined with computational assessment of potential modifications. Several alterations to this region were deemed worthy of investigation. Thus, Objectives 5a-c focussed on improving the antibacterial potency, and manipulation of stability to human plasma and S9 lung fraction.
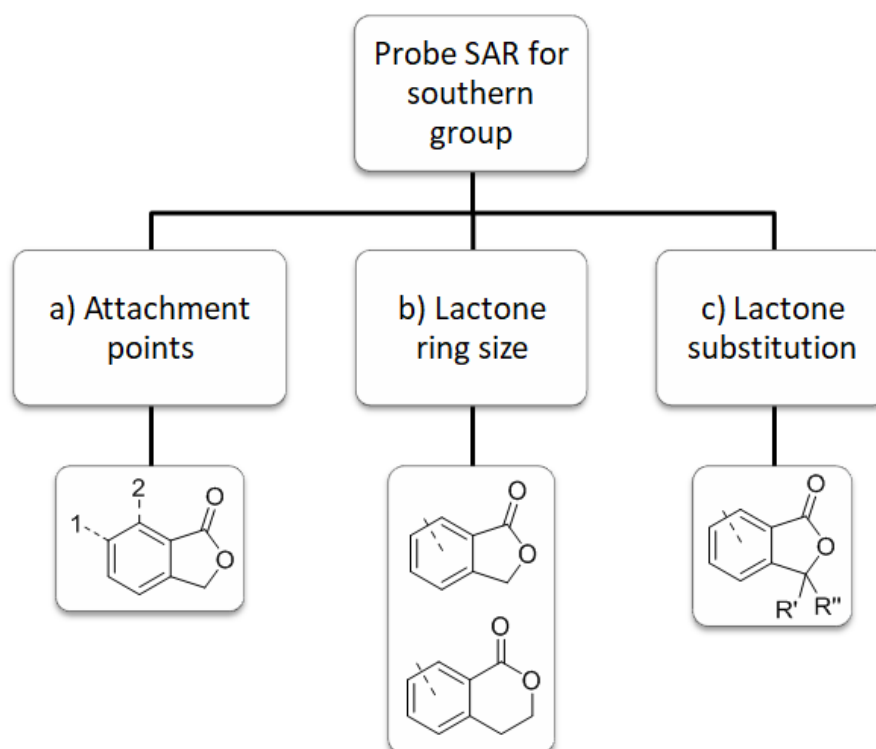
Challenging the structure-activity relationship of lactone containing region to allow better understanding of its contribution to binding and stability.

Figure 42

Three potential modifications were prioritised (**Figure 42**). Initially, work would progress around determining the optimal attachment point for the fused lactone moiety (**Figure 42a**). This was to be directed by computational assessment in both DNA gyrase and in paraoxonase enzymatic systems (dual targeting of both enzymes), with synthesis following where appropriate. Understanding the optimal vector to attach the southern group would be vital in challenging the computational model, and would provide further evidence of the binding mode in comparison to literature compounds. The preferential attachment point would be determined by the influence on the antibacterial properties of the series, however, stability profiling would also aid compound selection.

Upon determining the favoured attachment point, the size of the lactone ring could then be challenged (**Figure 42b**). This could yield important results regarding the steric confinements of the active site of DNA gyrase subunit A. Furthermore, the stability of 6-membered lactone rings to paraoxonase may be more suitable to a soft drug therapy, compared to their 5-membered counterparts.

A final method of probing the structure-activity relationship in this region was to assess substituted lactone derivatives (**Figure 42c**). Guided by published literature on potential paraoxonase substrates, lactone substitution could yield a useful method of fine-tuning the human plasma stability. Additionally, raising the lipophilicity of the southern group through increasing ring size, or from lactone substitution, could afford higher bacterial permeability and affinity for the lipophilic pocket in the binding site, boosting the antibacterial activity of the series.

Finally, the viability of an antibacterial soft drug therapy, and therefore the success of the research project, was envisioned to rely heavily on the generation of results. Therefore, setting an objective which focused on obtaining sufficient antibacterial, physiochemical and toxicological data to assess the advancement of the research programme, was particularly pertinent. Furthermore, in order to progress the research efficiently, it was envisioned that the author would be actively involved in establishing these results. Consequently, Objective 6 focussed on the generation of key data and included the responsibility of the author to perform the relevant ADME and computational chemistry work required to fully profile the synthesised compounds.
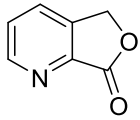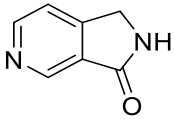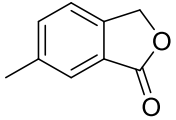
3.2　　　　Revised objectives

In light of the successes achieved in obtaining proof of concept for an antibacterial soft drug therapy with REDX08220 **23**, revised objectives were set. These objectives were used to guide the project to obtaining a more potent pharmaceutical, with properties more attune to a soft drug therapy. Therefore, the following objectives were set:

1. With the aid of computational assessment, determine if a replacement for the southern pyridyl lactone could infer increased stability to phosphate buffer, while maintaining a window of stability between human plasma and human S9 lung fraction.

2. After selection of a suitable alternative southern group, streamline the synthesis of soft drug compounds to afford a more facile synthesis, which could yield analogues more readily.

3. Assess if proposed replacements for the pyridyl lactone were appropriate, through analysis of their antibacterial activities.

4. Understand if minor changes in the lipophilicity of the parent compound could yield a more potent antibacterial by effecting bacterial permeability.

5. Challenge the structure-activity relationship of the lactone-containing region using computational and synthetic chemistry, to determine if:

   a. The most appropriate attachment point was being utilised.

   b. Alternative lactone ring sizes optimised the human plasma and human S9 lung fraction stability.

   c. Lactone-substitution could alter the human plasma and human S9 lung fraction stability.

6. Continue to obtain key antibacterial, physiochemical and toxicological data for parent compounds and their suspected metabolites. Where appropriate, ADME and computational chemistry data would be used to support the progress of the research programme, and would be generated by the author, in addition to developing the synthetic chemistry relating to the project.

3.3   Results and discussion

3.3.1   Alternative southern groups for REDX08220 (23)

In order to optimise the stability of the soft drug analogues to phosphate buffer, human plasma and human S9 lung fraction, the use of alternative southern groups was explored. Although literature surrounding hydrolysable substrates for paraoxonase was relatively sparse, lactam ring systems were reported to be metabolised by paraoxonase. Thus, a stability check on commercially available lactam **57** compared to lactone **58** was performed, prior to initiating a synthetic effort.

Stability assay	Pyridyl lactone **56**	Pyridyl lactam **57**	Phenyl lactone **58**
Human plasma (100%) (% remaining after 2 h)	0%	93%	69%
Human S9 lung fraction/ phosphate buffer (0.5 mg/mL) (% remaining after 5 h)	59%	92%	-
Human S9 lung fraction (5 mg/mL) (% remaining after 2 h)	100%	-	97%

Stability of pyridyl lactone **56**, pyridyl lactam **57** and phenyl lactone **58** to human plasma and human S9 lung fraction.

Table 24

Although it was noted that a lactam matched pair could not be efficiently sourced, similar analogue **57** proved to be stable to human plasma (**Table 24**). It was also observed that lactam replacement resulted in additional phosphate buffer stability, as observed by the increased amount of parent compound remaining in the human S9/phosphate buffer assay, when compared to lactone analogue **56**. The additional stability of lactam **57** compared to lactone **56** was considered concordant with the increased bond strength of the amide, due to the resonance-induced double-bond character, compared to the ester. As a result of the increased stability to human plasma, further research into lactam analogues was deprioritised. Fortunately, degradation was observed for phenyl lactone fragment **58** when incubated with human plasma. Furthermore, no instability was recorded upon exposure to human S9 lung fraction. Upon review of the literature, it was recognised that although no FDA approved pharmaceuticals contained a pyridyl lactone moiety, a phenyl lactone scaffold was found in several approved drugs (e.g. mycophenolic acid, fluorescein and

talniflumate). Encouraged by the possibility of replacing the pyridyl lactone with a phenyl analogue, a computational investigation was launched to determine the suitability of the phenyl replacement with respect to antibacterial activity.

Initially, the proposed structures were overlaid in the binding site of DNA gyrase subunit A, as a means to visually assess the hypothetical alteration (**Figure 43**).
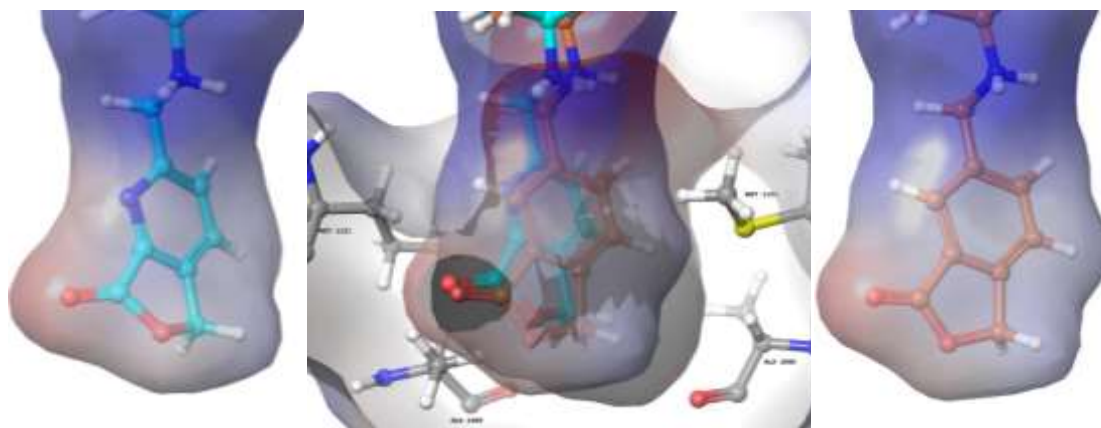
Overlays of REDX08220 **23** (left) and phenyl_REDX08220 **59** (right) in DNA gyrase active site (PDB: 2XCS[36]), visualised using Maestro (v10.6).

Figure 43

As the overlays suggested a high level of similarity, and no immediately obvious energy penalties for binding, it was deemed appropriate to consider the potency driving interactions of the series, to allow modifiable portions of the scaffold to be highlighted. Using the previously reported knowledge of the binding site, computational analysis of the binding interactions of a crystallised ligand was undertaken. Using these results as a reference, REDX08220 **23** and phenyl_REDX08220 **59** were then compared for their ability to maintain potency-driving interactions. Of particular importance was the contribution of the southern group to binding, especially the ability of the pyridyl nitrogen in the southern group to make a H-bonding interaction with Asp1083 (**Figure 44**).
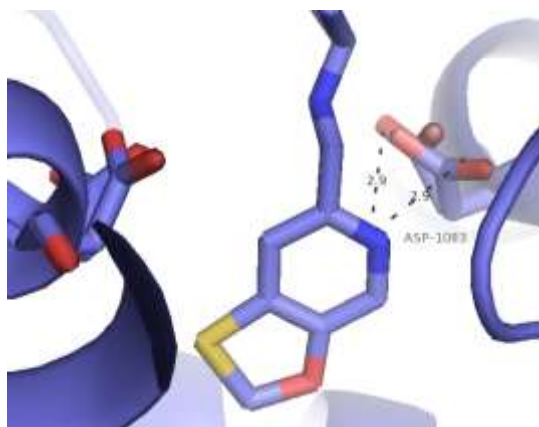
Potential H-bond interaction between Asp1083 of DNA gyrase subunit A and pyridyl moiety in GSK NBTI **3** visualised using Pymol (v1.1eval).

Figure 44

It was considered appropriate to use molecular dynamics simulations to monitor for potential interactions between the ligand and the binding site of DNA gyrase subunit A. Therefore each ligand was docked using a knowledge-based alignment, and was subjected to molecular dynamics simulations (following the methods outlined in **Section 3.11.3.1**), with the results shown in **Figure 45**. As modifications focussed on replacements to the southern group, the northern group and linker region were maintained constant throughout the simulations.
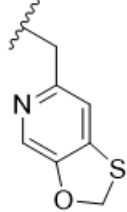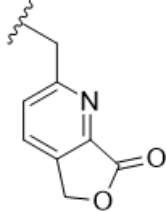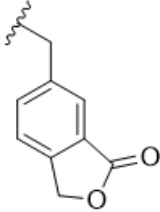
It was observed that the proposed pyridyl H-bond to Asp1083, as suggested from the X-ray crystal structure published by GlaxoSmithKline,[36] may not be as important as first hypothesised. The simulation of the literature compound suggested only 35% likelihood of the water-mediated interaction being observed (**Figure 45a**). Instead, for REDX08220 **23**, a water-mediated interaction to the carbonyl unit of the lactone was observed (**Figure 45b**). However, this was not observed in phenyl_REDX08220 **59**, suggesting this interaction may be relatively weak (**Figure 45c**).

Overall, phenyl_REDX08220 **59** was observed to maintain the majority of interactions observed in the simulation of REDX08220 **23**. The results of the molecular dynamics simulations suggested the key binding interactions were in fact due to the aminopiperidine template (consistent with the findings from Bax *et al*.[36]), and not the pyridine moiety. Therefore, the loss of the binding interactions from the lactone carbonyl moiety were considered to be trivial.
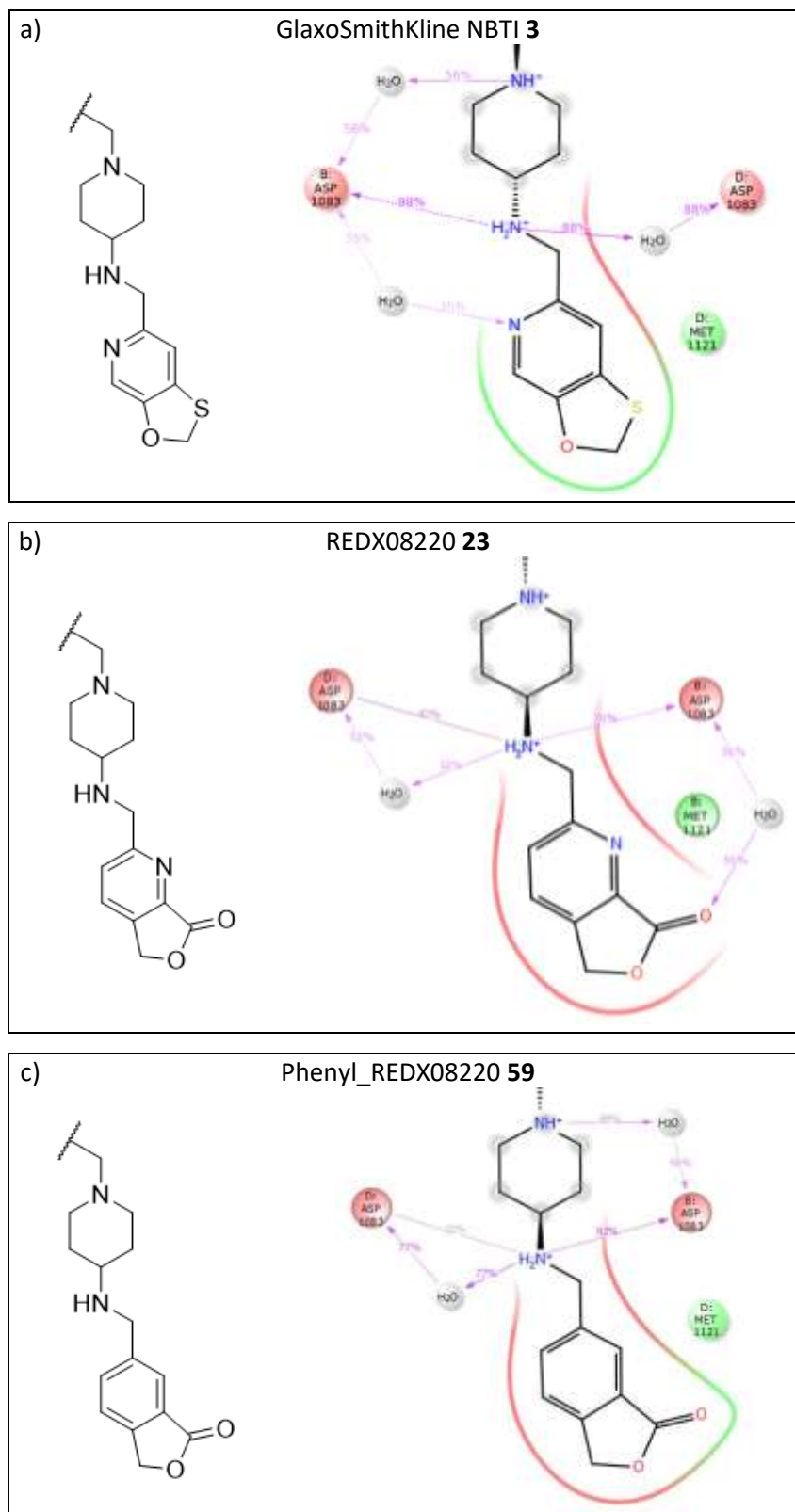
Molecular dynamics simulations for a) GlaxoSmithKline NBTI **3**, b) REDX08220 **23** and
c) phenyl_REDX08220 **59**.

Figure 45

	GSK NBTI **3**	REDX08220 **23**	Phenyl_REDX08220 **59**
Direct interaction to Asp1083(a)	98%	43%	22%
Water-mediated interaction to Asp1083(a)	35%	52%	77%
Direct interaction to Asp1083(b)	-	70%	92%
Water-mediated interaction to Asp1083(b)	88%	-	-
Additional water-mediated interaction to Asp1083	a) piperidine (56%) b) pyridine (35%)	a) lactone (56%)	a) piperidine (48%)

Summary of interactions for GSK NBTI **3**, REDX08220 **23** and phenyl_REDX08220 **59**.

Table 25

In addition to the ability to maintain key interactions, increasing hydrophobicity in the southern area of the molecule may encourage binding to the lipophilic pocket of GyrA, increasing the observed antibacterial activity.

| REDX08220-type fused lactone | Phenyl_REDX08220-type fused lactone |
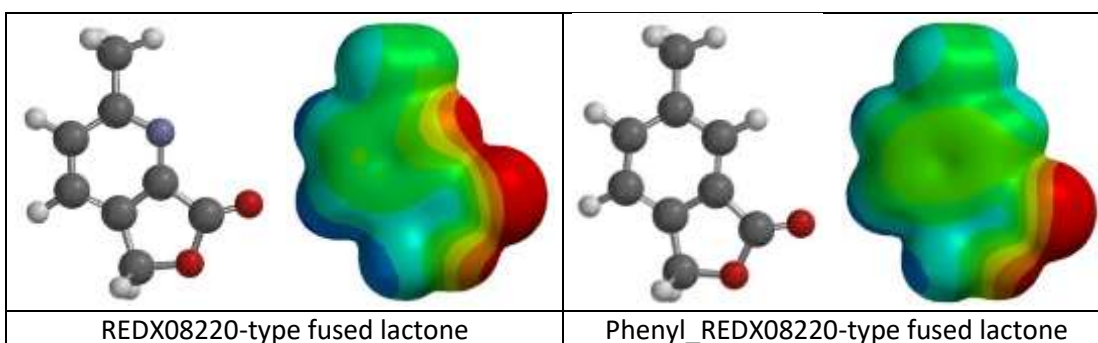
Electrostatic potential surfaces of pyridyl lactone and phenyl lactone, as simulated using Spartan'14 (v1.1.10).

Figure 46

The polarity of the southern group would be subtly effected by the removal of the nitrogen atom in the pyridyl ring (**Figure 46**). Minimisation of polarity in this region could be accompanied with an increase in target based potency due to the highly lipophilic region of the active site in which it resides. As a result of computational assessment and a potentially simplified synthetic route, several iterations of structure-activity relationship guided synthesis were performed (**Section 3.4**), and the subsequent results will be discussed (**Section 3.7**).

3.4   Synthetic route

### 3.4.1   Synthesis of phenyl_REDX08220 (59)

Utilising the previously reported synthesis of REDX08220 **23**, aldehyde **60** was considered a key intermediate for synthesising phenyl derivatives of soft drug compounds (**Scheme 14**).
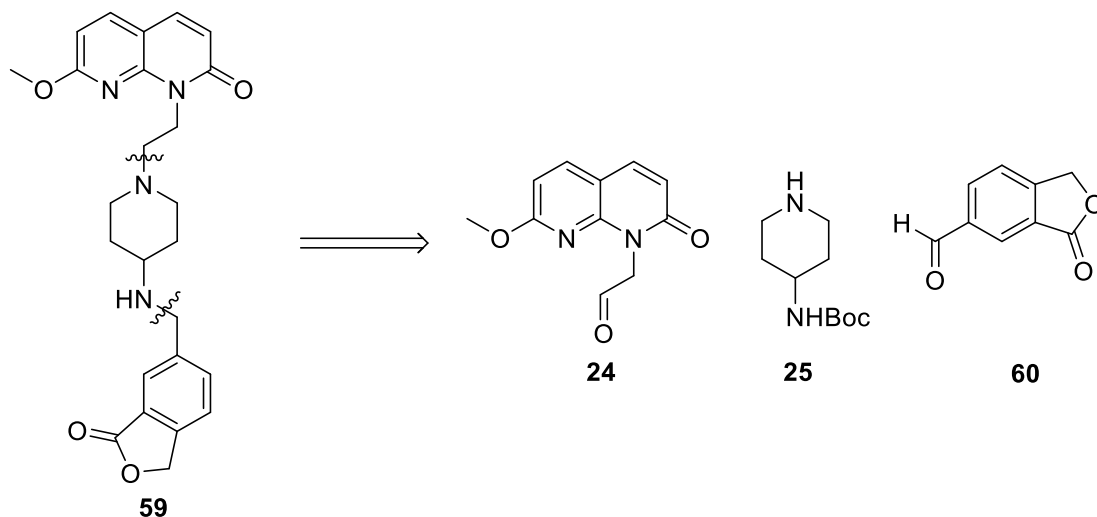
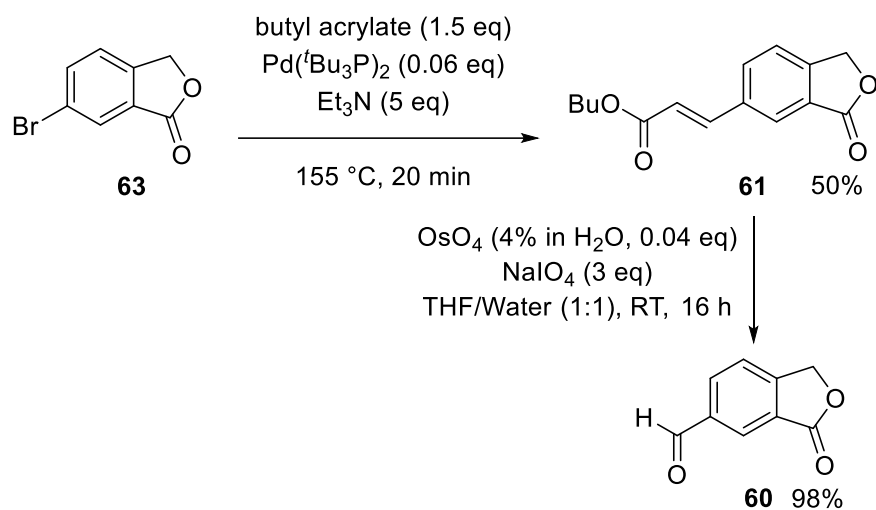Retrosynthetic analysis of phenyl_REDX08220 **59**.

Scheme 14

The synthesis of the pyridyl derivative of aldehyde **60** proved to be complex, particularly due to a low-yielding Riley oxidation as a final step. Thus, an alternative synthetic route was sought. Fortunately, unlike their pyridyl analogues, halogenated examples of fused phenyl lactones were commercially available, and lent themselves to a much more efficient route. Aryl halide **62** was considered an ideal starting material to generate the aldehyde building block in two steps (**Scheme 15**). Furthermore, experience with oxidative cleavage reactions suggested potentially higher yields than the previously used Riley oxidation.

Retrosynthesis of aldehyde **60**, starting from commercially available fused lactone **62**.
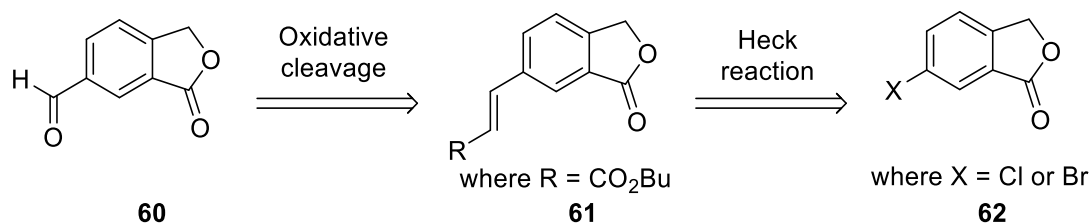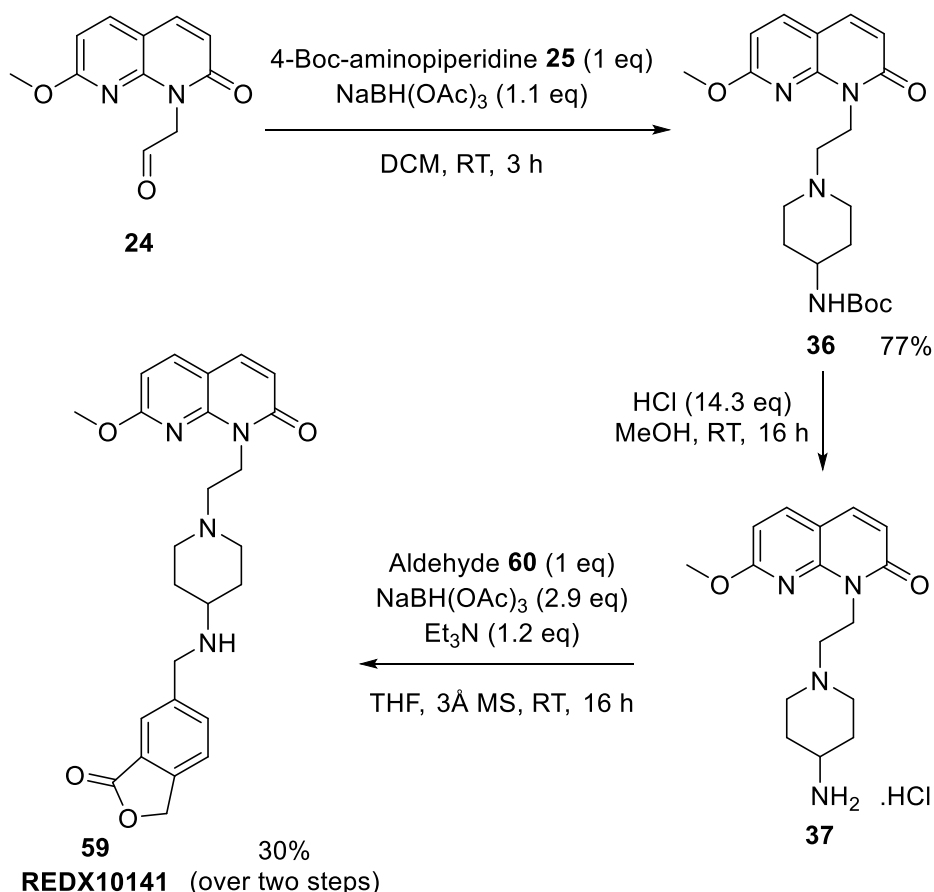
Scheme 15

The synthesis of aldehyde **60** was initiated with a Heck reaction of **63** (**Scheme 16**), and was completed by oxidative cleavage of **61**, using substoichiometric osmium(VIII) tetroxide and sodium periodate, giving aldehyde **60** in almost quantitative yield.

butyl acrylate (1.5 eq)
Pd(^{t}Bu$_3$P)$_2$ (0.06 eq)
Et$_3$N (5 eq)

155 °C, 20 min

63

BuO

61 50%

OsO$_4$ (4% in H$_2$O, 0.04 eq)
NaIO$_4$ (3 eq)
THF/Water (1:1), RT, 16 h

60 98%

Route to aldehyde building block **60**.

Scheme 16

With fused aldehyde **60** successfully synthesised, a range of analogues, including target compound **59**, were prepared through reductive amination, in a similar manner to the method used to synthesise REDX08220 **23** and other soft drug analogues (**Scheme 17**).

4-Boc-aminopiperidine **25** (1 eq)
NaBH(OAc)$_3$ (1.1 eq)

DCM, RT, 3 h

24

NHBoc

36 77%

HCl (14.3 eq)
MeOH, RT, 16 h

Aldehyde **60** (1 eq)
NaBH(OAc)$_3$ (2.9 eq)
Et$_3$N (1.2 eq)

THF, 3Å MS, RT, 16 h

NH$_2$ .HCl

37

59 30%
REDX10141 (over two steps)

Synthetic route to REDX10141 **59**.

Scheme 17

### 3.4.2   Synthesis of regioisomer analogues to REDX10141 (59)

A regioisomer of the fused phenyl lactone moiety was prepared (**Scheme 18**) to reinforce the hypothesised structure-activity relationship from analogues of REDX08220 **23**.
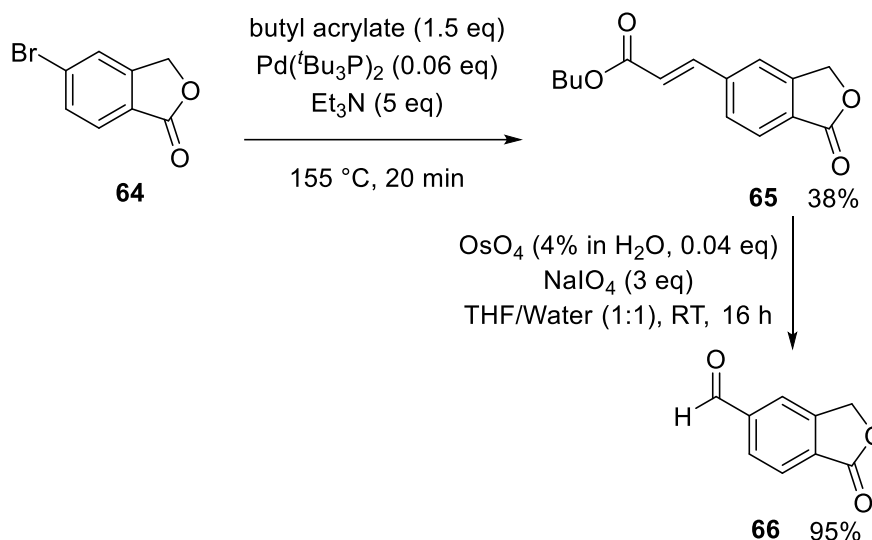
Synthetic route to reverse lactone aldehyde **66**.

Scheme 18

The synthesis proceeded efficiently, giving aldehyde **66**, which was used in an analogous manner to **60**, affording REDX10012 **67** (**Scheme 19**). Comparison of the antibacterial potency of REDX10012 **67** with REDX10141 **59** was then used to suggest a preferred vector for the carbonyl group of the lactone ring to occupy. It was hypothesised that low antibacterial activity in this case may result in compounds with similar lactone configurations being triaged.
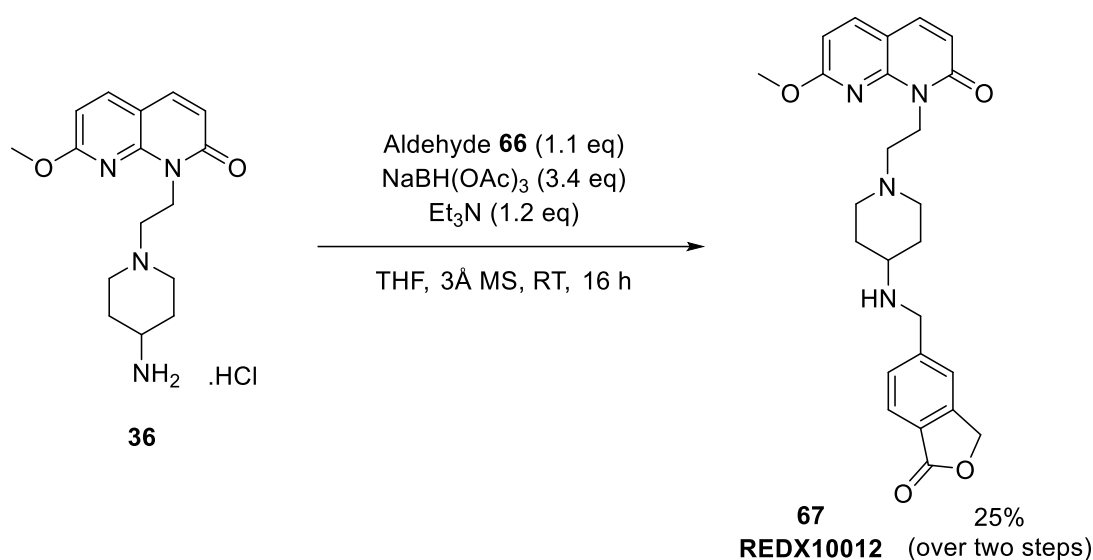

Synthesis of REDX10012 **67**.

Scheme 19

3.4.3 Synthesis of northern group analogues of REDX10141 (59)

Due to advancements in the synthetic route towards REDX10141 **59** compared to REDX08220 **23**, analogues that varied with respect to the northern group could be easily prepared. A small selection of bicyclic northern groups were thus selected from the Redx Pharma compound collection, providing a range of clogD$_{7.4}$ values to initially determine a target lipophilicity that would result in optimal bacterial permeability (**Figure 47**).

REDX10141 **59**

ΔclogD$_{7.4}$† = 0 ΔclogD$_{7.4}$† = +0.32 ΔclogD$_{7.4}$† = +0.12 ΔclogD$_{7.4}$† = -0.31
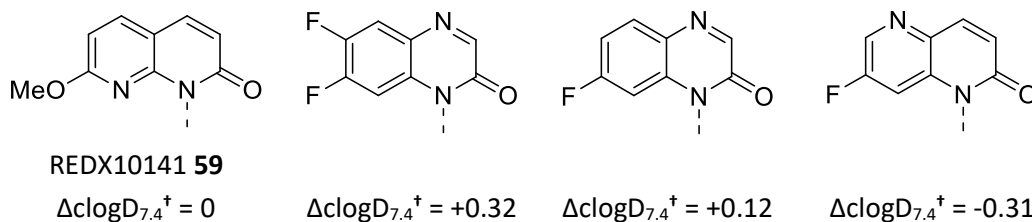
†Calculated using ACD/Percepta 14.0.0, using REDX10141 **59** as a baseline.
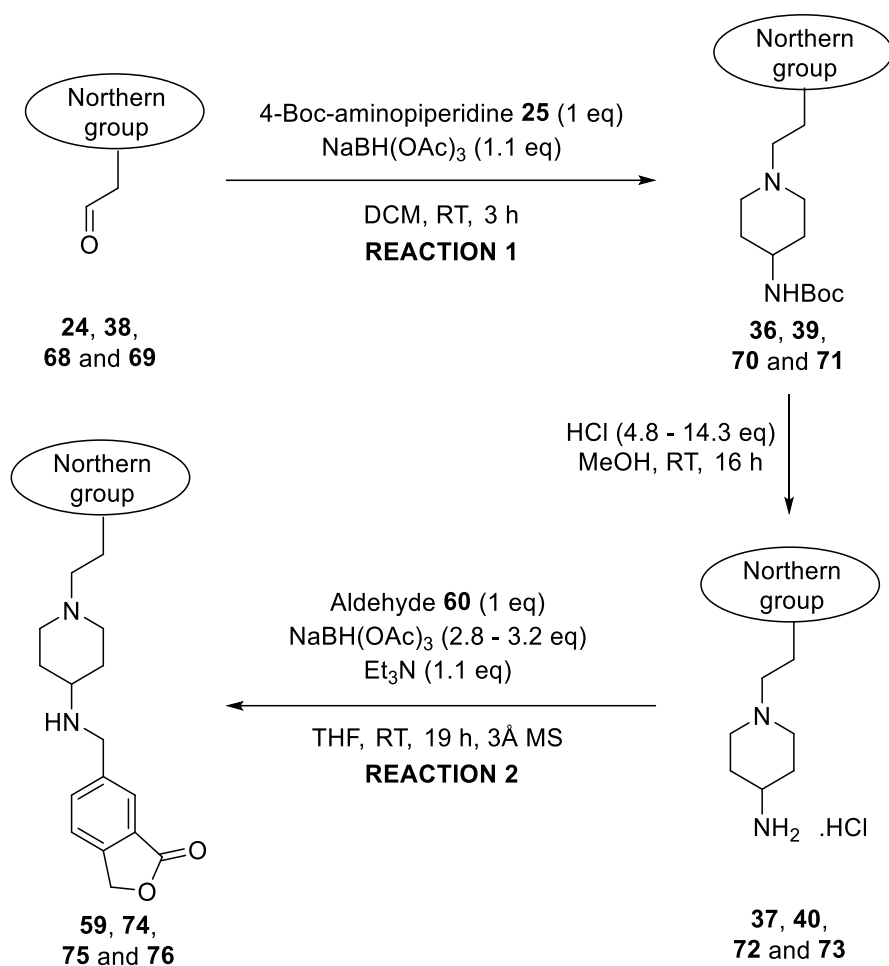
Northern groups selected to probe trends in lipophilicity and potency.

Figure 47

The synthesis of analogous compounds to REDX10141 **59** proceeded *via* the previously described route, replacing the methoxypyridine northern group aldehyde with a suitable alternative. Each northern group was taken from the Redx Pharma compound collection and reacted in a reductive amination with 4-Boc-aminopiperidine **25** (**Scheme 20**). Boc deprotection using hydrochloric acid in dioxane (4 M) furnished primary amines of the structure **37**, **40**, **72** and **73**, which could then be used in a second reductive amination with aldehyde **60** to yield a series of analogues of REDX10141 **59** that varied with respect to the lipophilicity of the northern group.

Unfortunately, reductive aminations to form the target compounds were consistently associated with poor yields. Although the reactions were observed to go to completion by LCMS and TLC, the chromophore of the final compounds was often much more intense than the starting material primary amines, resulting in potentially premature reaction quenching. Furthermore, both the primary and secondary amines were found to have similar retention times, causing material loss during purification.

Each compound (**59** and **74 – 76**) would be assessed for its antibacterial properties, and trends between activity and lipophilicity could be analysed. An optimal northern group could then be selected on the basis of the antibacterial activity, allowing a preferential northern group to be used when challenging the structure-activity relationship of the lactone-containing group.

The scheme shows:

Northern group attached to an aldehyde (CHO)

24, **38**, **68** and **69**

4-Boc-aminopiperidine **25** (1 eq)
NaBH(OAc)$_3$ (1.1 eq)

DCM, RT, 3 h
REACTION 1

Northern group with piperidine-NHBoc

36, **39**, **70** and **71**

HCl (4.8 - 14.3 eq)
MeOH, RT, 16 h

Northern group with piperidine-NH$_2$ .HCl

37, **40**, **72** and **73**

Aldehyde **60** (1 eq)
NaBH(OAc)$_3$ (2.8 - 3.2 eq)
Et$_3$N (1.1 eq)

THF, RT, 19 h, 3Å MS
REACTION 2

Northern group product

59, **74**, **75** and **76**

Redx No.	Northern group	Product/Yield	
		Reaction 1	Reaction 2
REDX10141 **59**	MeO-(naphthyridinone with N, N=O)	**36**, 77%	**59**, 30%
REDX10307 **74**	F, F-(quinoxalinone with N, N=O)	**39**, 94%	**74**, 14%
REDX10159 **75**	F-(quinoxalinone with N, N=O)	**70**, 68%	**75**, 28%
REDX10306 **76**	F-(naphthyridinone with N, N=O)	**71**, 77%	**76**, 9%

Synthetic route to analogues of REDX10141 **59**.

Scheme 20

3.4.4 Synthesis of suspected hydrolysed metabolites (77 and 78)

In order to assess the merits of a soft drug approach to antibacterial research, the hypothesised metabolites of compounds **59** and **75** were also synthesised (**Scheme 21**). It was envisioned that the synthesis of the hypothesised metabolites of the parent compounds would allow the benefits of a soft drug approach to antibacterial research to be demonstrated. In particular, the cardiotoxicity trend between a parent and its expected metabolite could drive the direction of the research project. Accordingly, REDX10141 **59** and REDX10159 **75** were subjected to basic hydrolysis conditions to afford the hypothesised metabolites REDX10142 **77** and REDX10204 **78**, respectively.
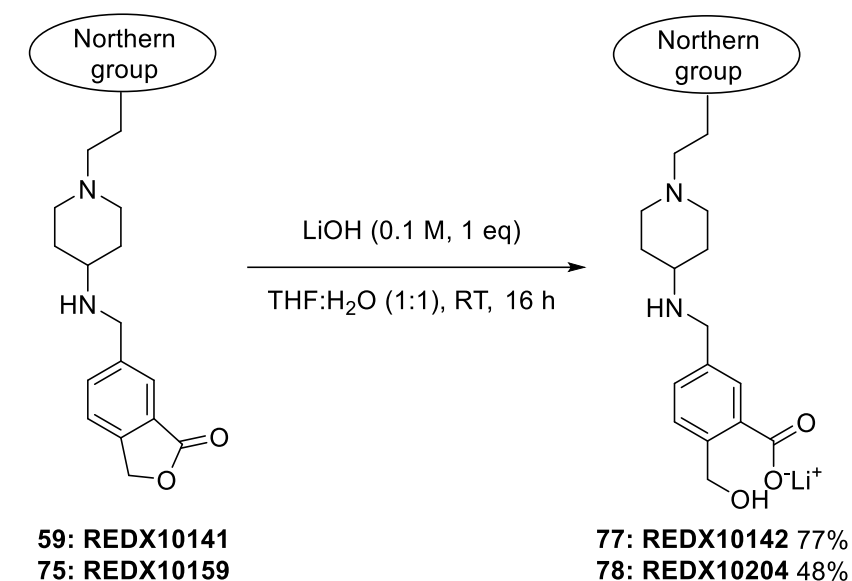
59: REDX10141
75: REDX10159

77: REDX10142 77%
78: REDX10204 48%

Northern group	Product/Yield
REDX10141 **59** → REDX10142 **77**	**77**, 77%
REDX10159 **75** → REDX10204 **78**	**78**, 48%

Lactone hydrolysis of REDX10141 **59** and REDX10159 **75** to yield expected soft drug metabolite REDX10142 **77** and REDX10204 **78**, respectively.

Scheme 21

3.4.5   Synthesis of 7-substituted analogues of REDX10141 (59)

Upon selection of a northern group that provided high bacterial permeability, the structure-activity relationship of the southern group could then be challenged. Alternative attachment points for the lactone containing system could be utilised to determine the optimal lactone-directing vector to bind with the active site in DNA gyrase.
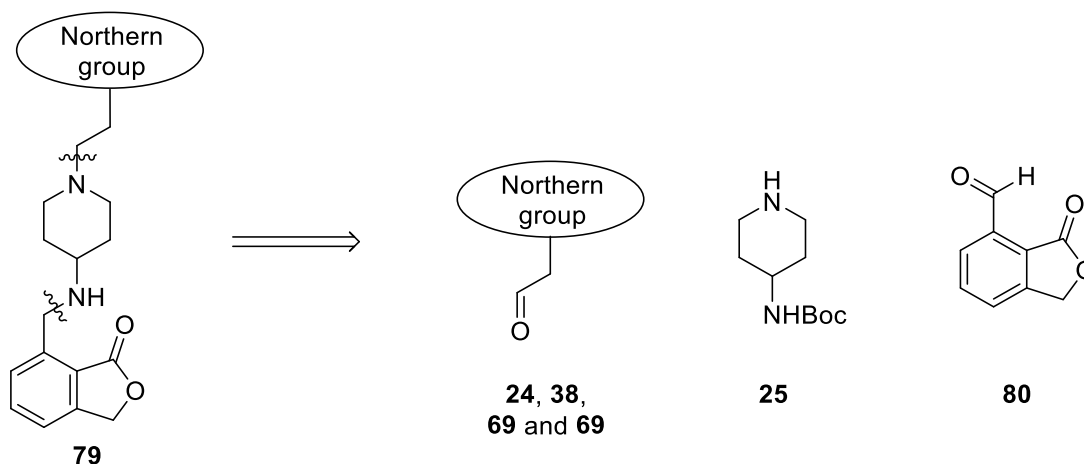
Retrosynthetic analysis of 7-substituted phenyl lactone analogues of REDX10141 **59**.

Scheme 22

As with REDX10141 **59**, the corresponding aromatic aldehyde **80** was deemed an important intermediate (**Scheme 22**). The synthesis of aldehyde **80** progressed analogously to the previously disclosed 6-substituted phenyl lactone (**Scheme 23**).
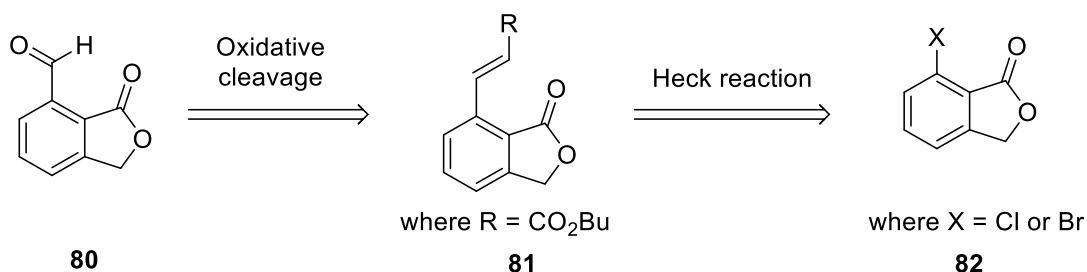
Proposed synthetic route to 7-substituted phenyl lactone **80**.

Scheme 23

The corresponding aryl chloride was considered an ideal commercially available starting material to generate the aldehyde building block in two steps. The synthesis of aldehyde **80** was initiated with a Heck reaction of chloride starting material **83** (**Scheme 24**), which progressed in 55% yield. The synthesis was completed by an oxidative cleavage of **81** using substoichiometric osmium(VIII) tetroxide and sodium periodate, yielding aldehyde **80** in 77% yield.
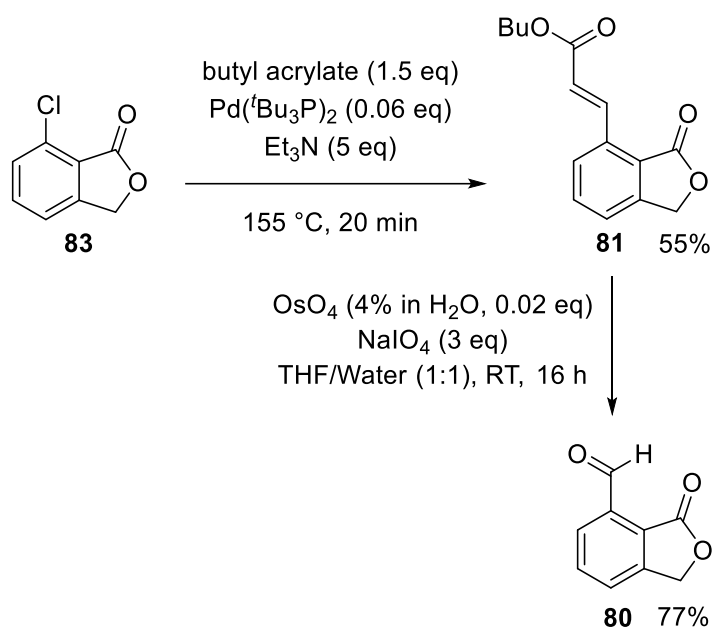
Route to 7-subtituted aldehyde building block **80**.

Scheme 24

With aldehyde **80** successfully synthesised, a range of analogues could be prepared through a reductive amination, in an identical manner to the method used to synthesise REDX10141 **59** and other previous soft drug analogues (**Scheme 25**).


Redx No.	Northern group	Yield
REDX10248 **84**		28%
REDX10281 **85**		30%

Synthetic route to 7-subtituted phenyl lactone soft drug compounds **84** and **85**.

Scheme 25

Assessment of each 7-substituted compound for its antibacterial properties, compared to its 6-substituted matched pair, would allow a comparison of affinity for the binding site. Comparing this data should allow an optimal attachment point to be determined, and subsequently drive further optimisation.

3.4.6 Synthesis of hydrolysed metabolite of REDX10248 (84)

To aid in understanding of how metabolism affected their biological properties, the antibacterial activity and toxicity of suspected metabolites were to be monitored. Thus, lactone hydrolysis provided REDX10284 **86** in 97% yield (**Scheme 26**).
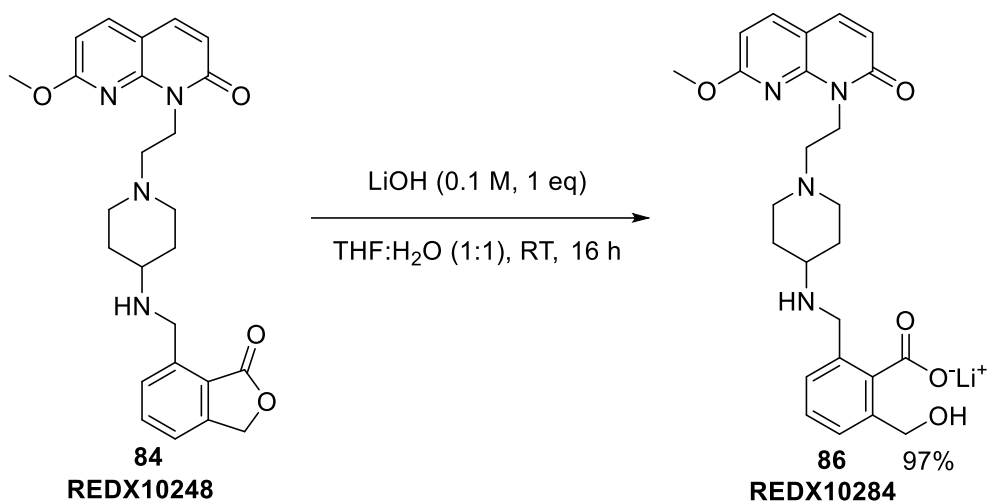

Lactone hydrolysis of REDX10248 **84** to give expected metabolite REDX10284 **86**.

Scheme 26

3.4.7 Synthesis of 6-membered analogues of REDX10141 (59)

The steric limits of the active site were challenged through manipulation of the lactone ring. Accordingly, fused δ-lactones were selected for synthesis due to their larger size and capacity for metabolism by paraoxonase. Corresponding halogenated aryl lactones were commercially available, allowing the successful preparation of aldehyde **89** (**Scheme 27**).
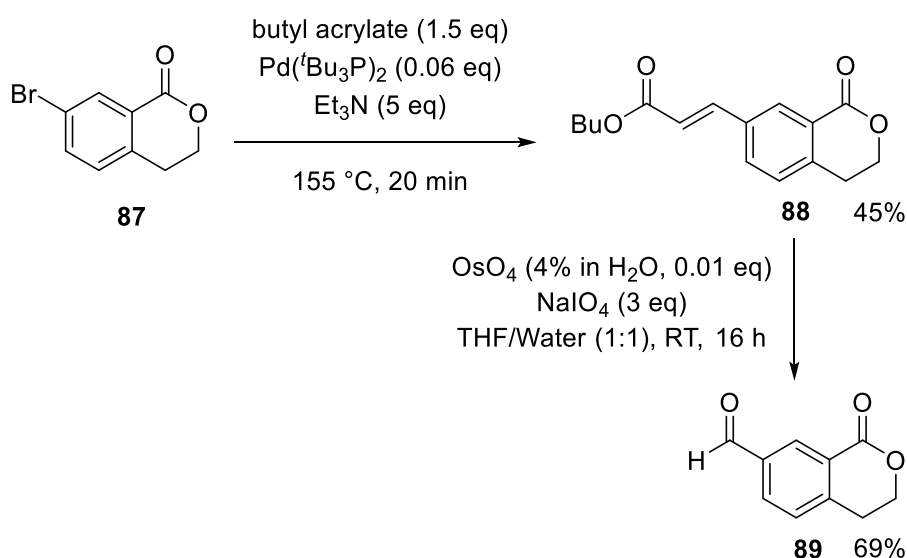
Route to 6-membered lactone aldehyde building block **89**.

Scheme 27

Aldehyde **89** could then be combined with the northern scaffold, allowing efficient exploration of a range of 6-membered lactone analogues (**Scheme 28**). Assessment of antibacterial and stability properties could then proceed, comparing against 5-membered matched pairs to determine the most promising template to progress for optimisation.


Redx No.	Northern group	Yield
REDX10359 **90**	MeO [structure]	18%
REDX10386 **91**	F [structure]	48%
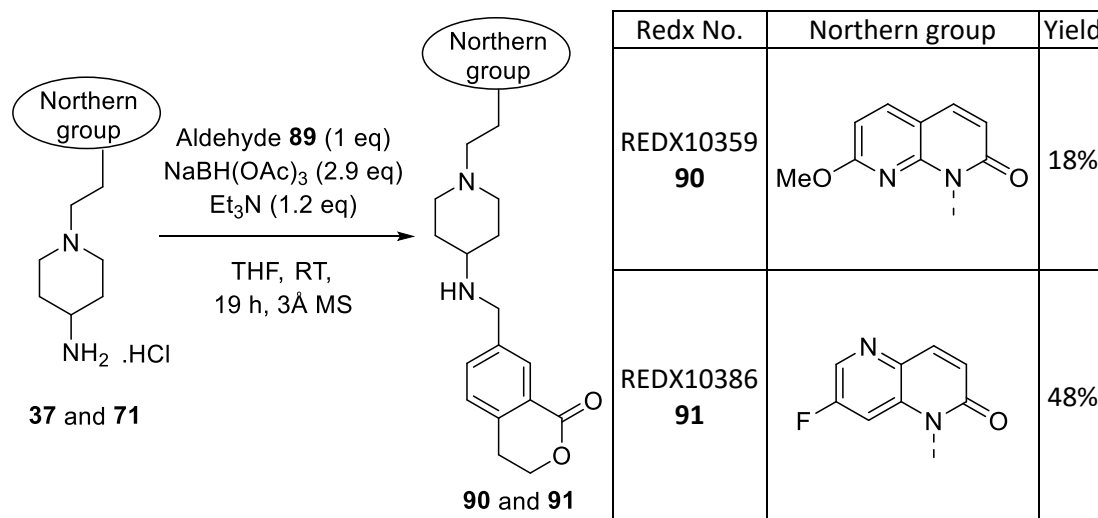
Synthetic route to REDX10359 **90** and REDX10386 **91**.

Scheme 28

3.4.8 Synthesis of hydrolysed metabolite of REDX10386 (91)

REDX10403 **92**, the hydrolysed derivative of REDX10386 **91**, was prepared (**Scheme 29**), allowing its antibacterial activity and toxicity to be assessed. A reduction in hERG inhibition may highlight the benefits of a soft drug approach.
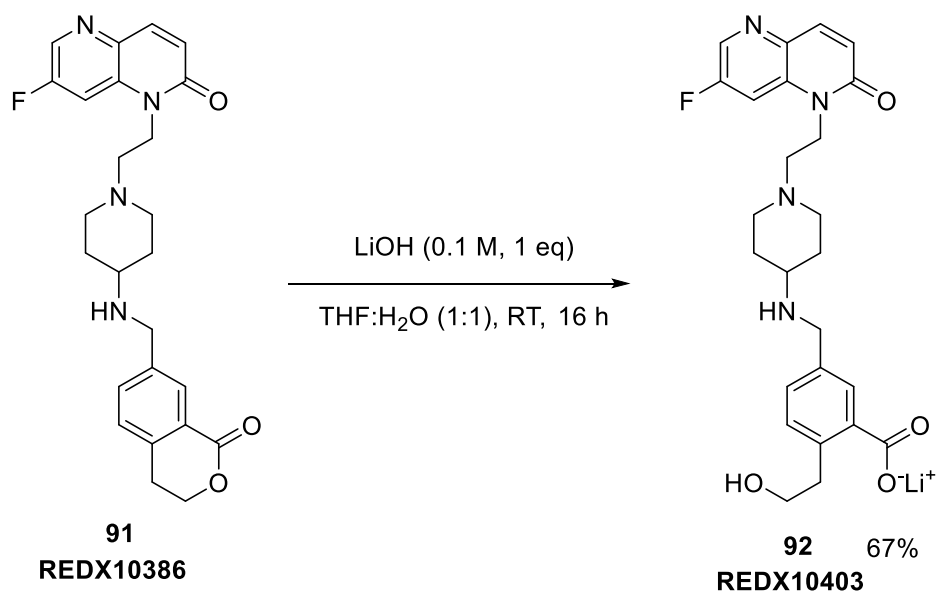
Lactone hydrolysis of REDX10386 **91** to give expected metabolite REDX10403 **92**.

Scheme 29

3.4.9 Synthesis of 3-methyl analogues of REDX10141 (59)

Guided by the literature surrounding paraoxonase-labile substrates, 3-methylated and 3,3-dimethylated lactone derivatives of REDX10141 **59** were targeted. It was envisioned that the stability of the parent molecule to human plasma could be manipulated through subsequent methylations to the 3-position on the lactone ring. Unsurprisingly, the increased complexity of the alkylated scaffold resulted in no appropriate commercially available starting material. Thus, a bespoke retrosynthesis was performed (**Scheme 30**).
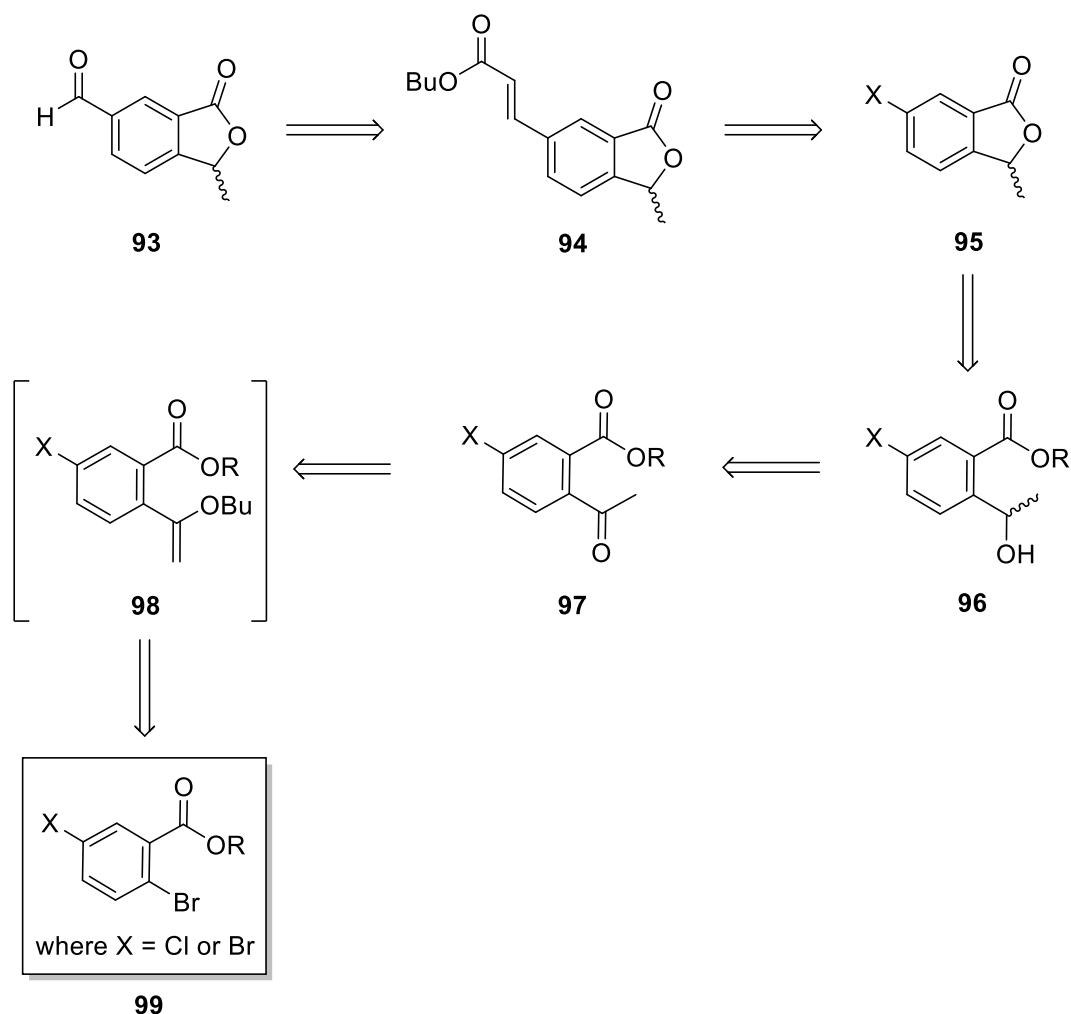
Retrosynthetic analysis of 3-methylated lactone aldehyde **93**.

Scheme 30

It was hypothesised that aldehyde **93** could be generated from halogenated fused lactone **95**, repeating the previously validated Heck coupling-oxidative cleavage route. Unlike similar scaffolds, compound **95** was commercially unavailable, and instead, an intramolecular cyclisation was proposed from alcohol **96**, which, in turn, could be synthesised by reduction of ketone **97**. Installation of the methyl ketone at the 2-position of

the aromatic ring was deemed a pivotal reaction, and could be performed *via* a Heck-type olefination from corresponding aryl bromide **99**, followed by acidic hydrolysis of the olefin to give ketone **97**. The resulting forward synthesis allowed the production of aldehyde **93** in moderate yield from commercially available methyl 2-bromo-5-chlorobenzoate **100** (**Scheme 31**).
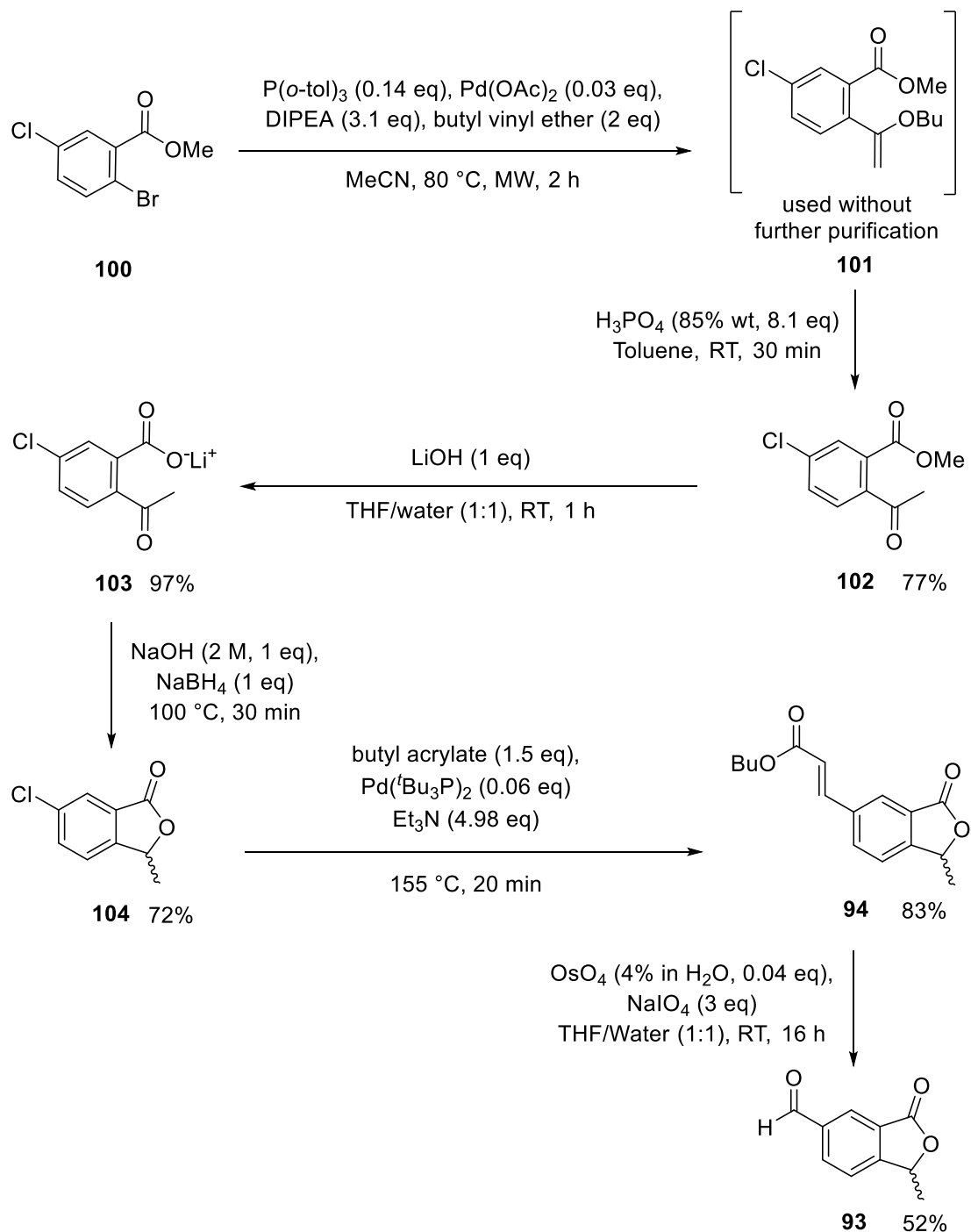
Synthesis of 3-methylated lactone aldehyde **93**.

Scheme 31

The synthesis of methylated lactone aldehyde **93** was initiated with a Heck-type olefination of methyl 2-bromo-5-chlorobenzoate **100** (**Scheme 31**). The resulting alkylated product underwent acidic hydrolysis with phosphoric acid to give the methyl ketone substituted compound **102** in a combined yield of 77% over 2 steps. Subsequent hydrolysis of methyl ester **102** gave corresponding lithium salt **103** in practically quantitative yields. Reduction of the ketone carbonyl group with sodium borohydride resulted in the appropriate functionality required for cyclisation to occur, forming halogenated fused lactone **104**. The synthesis was completed by a Heck reaction, followed by oxidative cleavage, yielding aldehyde **93**. Soft drug probe compounds **105** and **106** were subsequently synthesised *via* reductive amination of the 3-methylated lactone aldehyde **93** with the desired amine counterpart (**Scheme 32**).

Redx No.	Northern group	Yield
REDX10370 **105**		10%
REDX10371 **106**		17%
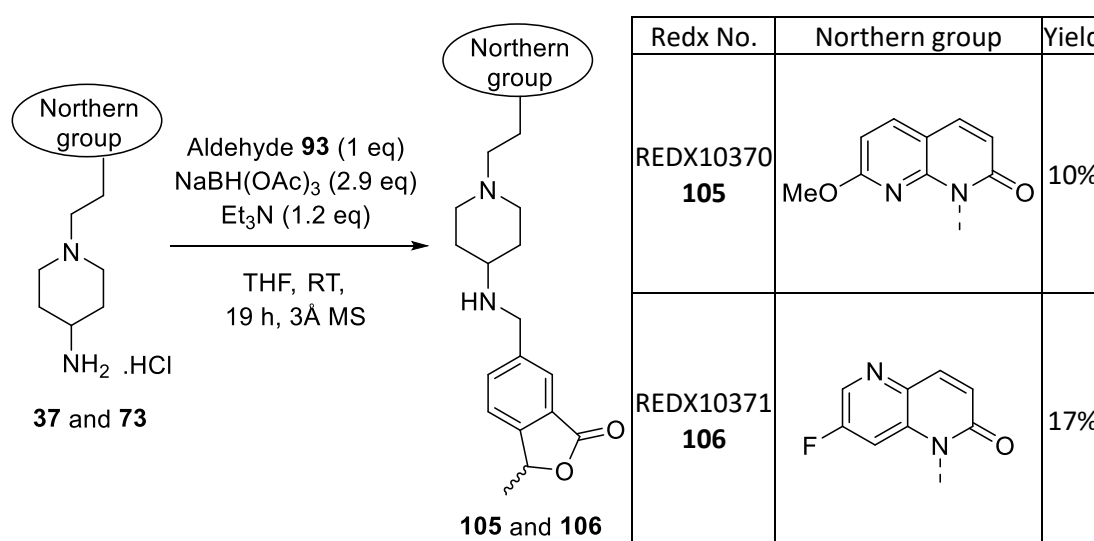
Synthetic route to REDX10370 **105** and REDX10371 **106**.

Scheme 32

3.4.10 Separation of 3-methyl substituted enantiomers

Building on the encouraging antibacterial and stability properties of the 3-methylated series (**Section 3.6.8**), and to provide data to optimise the computational model, enantiomeric separation was desired. Initially, synthetic routes to each enantiomer were evaluated, however, pre-existing literature in this area was sparse. Instead, the most rational method of obtaining enantiomerically pure material was by chiral chromatography. As a result, the racemic mixture was separated by chiral supercritical fluid chromatography (SFC)[†]

[†]Chiral SFC was performed by WuXi AppTec

(**Scheme 33**) and each resulting enantiomer was evaluated for its enantiomeric excess (both > 99% ee), before being assessed for antibacterial and stability properties.
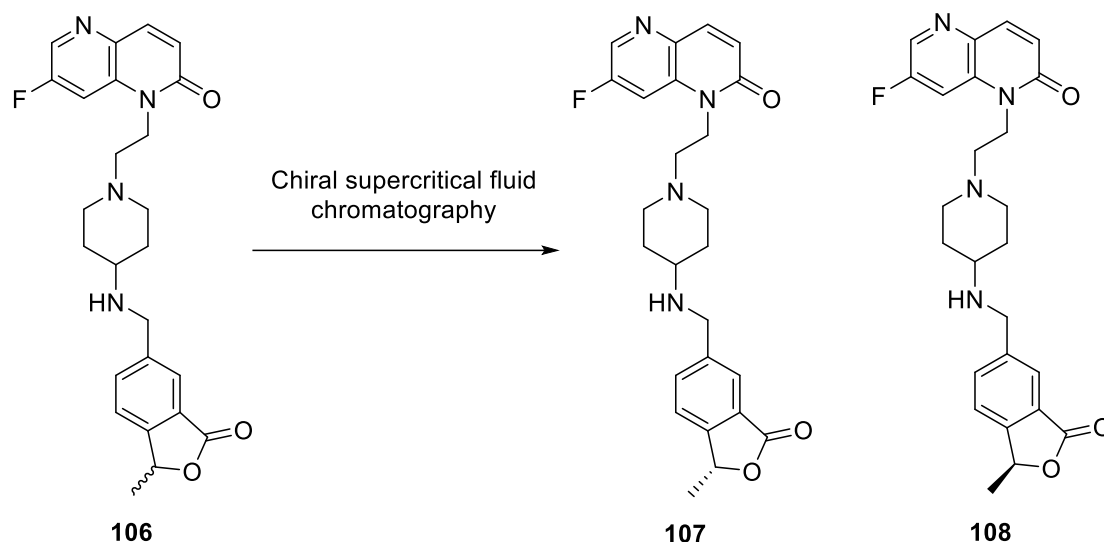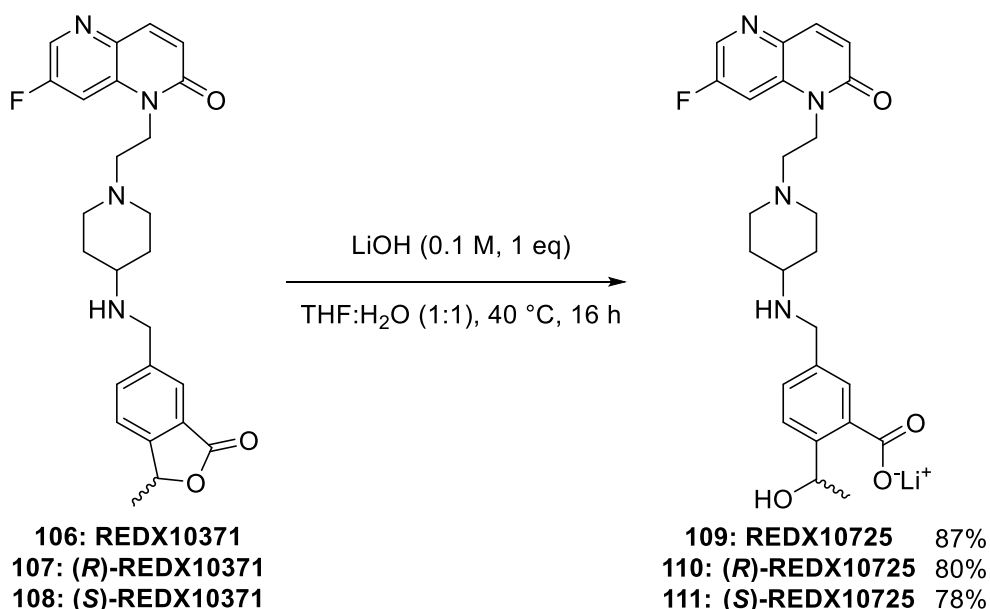

Separation of racemic REDX10371 **106** was performed by chiral SFC, yielding enantiomers (*R*)-REDX10371 **107** and (*S*)-REDX10371 **108**.

Scheme 33

3.4.11 Synthesis of hydrolysed metabolites of REDX10371 (106)

The preparation of hydrolysed metabolites of the 3-methylated soft drug parent compounds proceeded using lithium hydroxide (**Scheme 34**), allowing the antibacterial activity and the hERG inhibition of the suspected metabolites **109** - **111** to be assessed.


LiOH (0.1 M, 1 eq)

THF:H_2O (1:1), 40 °C, 16 h

106: REDX10371
107: (*R*)-REDX10371
108: (*S*)-REDX10371

109: REDX10725   87%
110: (*R*)-REDX10725 80%
111: (*S*)-REDX10725 78%

Lactone hydrolysis of REDX10371 **106** to give expected metabolite REDX10725 **109**.

Scheme 34

3.4.12 Synthesis of 3,3-dimethyl analogues of REDX10141 (59)

As previously reported, monomethylation of the 3-position was expected to provide a means to decrease the human plasma and human paraoxonase stability of the lactone scaffold. It was speculated that, if the trend continued, 3,3-dimethylated targets may be of even more interest. Therefore, intermediate **103** in the synthesis of the 3-methylated aldehyde lactone was identified as a potential starting material for the synthesis of the 3,3-dimethylated analogue (**Scheme 35**).
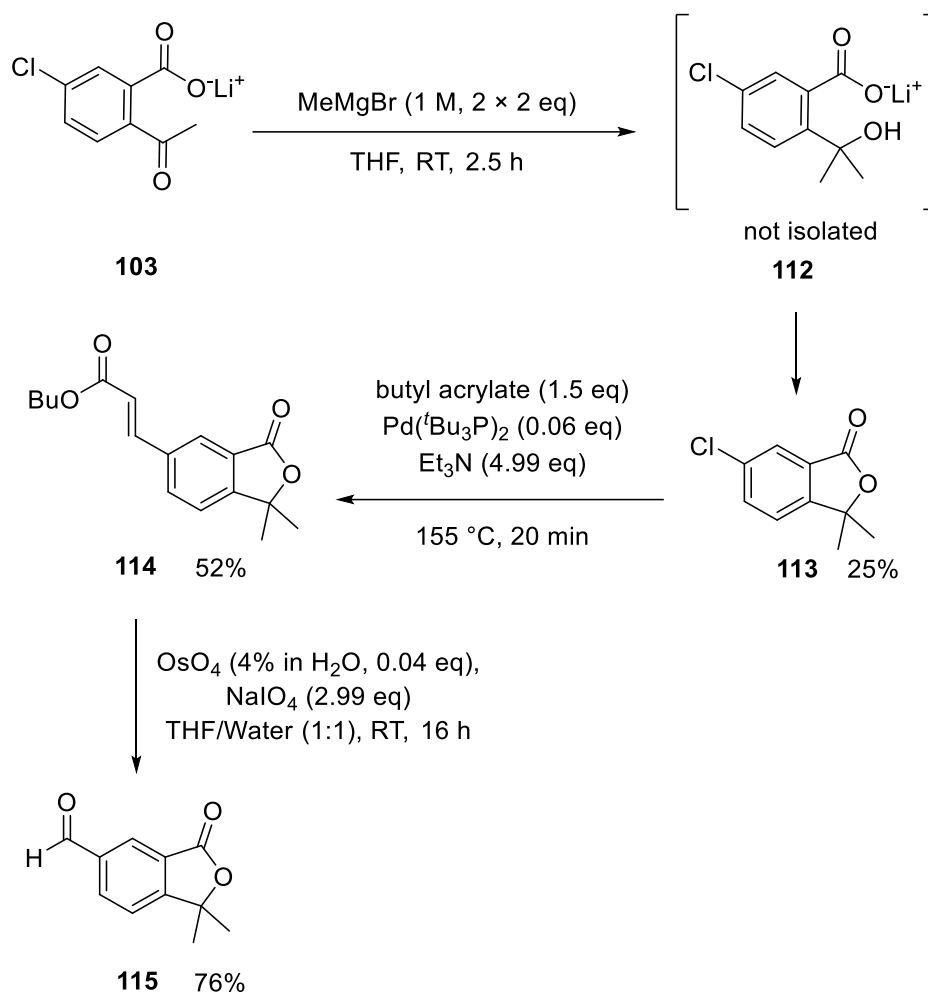
Synthesis of 3,3-dimethylated lactone aldehyde **115**.

Scheme 35

Utilising lithium salt **103** allowed a divergent synthesis to be performed, which was continued through methylation using methylmagnesium bromide. Tertiary alcohol **112** cyclised to form lactone **113**, which could be used in a similar manner to previous halogenated lactones, through a Heck coupling followed by oxidative cleavage with

substoichiometric osmium(VIII) tetroxide. Aldehyde **115** was then used to synthesise target compounds **116** and **117**, following the route observed for similar analogues (**Scheme 36**). Final compounds could be assessed for their antibacterial activity and stability profiles in human plasma and human S9 lung fraction. Where appropriate, additional studies could be performed on the synthesised compounds in order to further the understanding surrounding the series.

Redx No.	Northern group	Yield
REDX10387 **116**	MeO, methoxy-naphthyridinone structure	6%
REDX10388 **117**	F, fluoro-naphthyridinone structure	9%
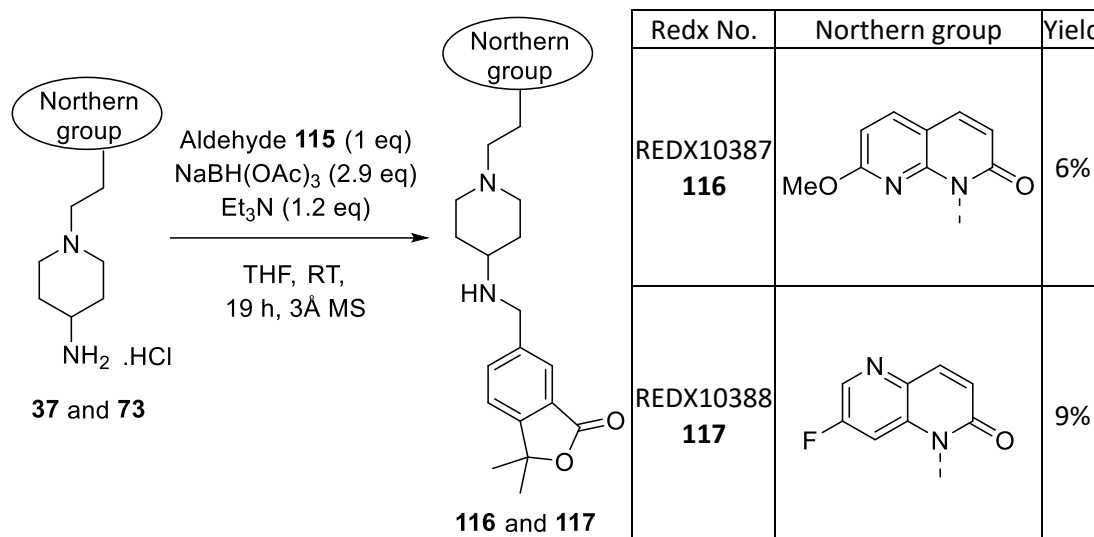
Synthetic route to REDX10387 **116** and REDX10388 **117**.

Scheme 36

3.5 Summary of desirable properties for a lead antibacterial soft drug

The antibacterial activity of the test compounds was assessed through obtaining minimum inhibitory concentrations (MICs) against selected pathogens. Certain bacterial strains with high prevalence in lung infections were prioritised, and activity against these pathogens was deemed essential. Furthermore, in order to fully understand the whole cell MIC data, supercoiling inhibition data against DNA gyrase subunit A was utilised where required. Frequency of resistance was monitored for key compounds, and cross-resistance was assessed against selected resistant and susceptible bacterial strains.

Human plasma and human S9 lung fraction stability was determined where appropriate, with target stability profiles highlighted in **Table 26**. In line with a soft drug therapy, a window of stability should be observed between human plasma and human S9 lung fraction, in order to allow further optimisation to proceed.

The compounds should be stable under buffered conditions and soluble in the assay conditions, ensuring accurate data can be generated.

Finally, determining the toxicity of the compounds was hypothesised to be critical to the success of the research programme. Firstly, the parent and expected metabolite should be non-cytotoxic. The success of the research project could be broadly be evaluated from the reduction of hERG K^+ channel inhibition between the parent compound and its expected metabolite. Therefore, monitoring of cardiotoxicity for key compounds would be fundamental in assessing the suitability of a soft drug therapy for antibacterial research.

Although these guidelines were adopted to help assess the progress of the programme towards obtaining a lead compound, there was room for flexibility on a case-by-case basis. A full discussion of the target properties required for an antibacterial soft drug has been previously reported (**Section 2.10**), however, for convenience, a summary of the relevant properties is shown in **Table 26**.

Antibacterial properties		
MICs	P. aeruginosa	≤ 1 µg/mL
	AND/OR	
	S. pneumoniae	≤ 1 µg/mL
	S. aureus	≤ 1 µg/mL
	H. influenzae	≤ 1 µg/mL
	Gram-positive and gram-negative strains	Monitor for additional activity
Frequency of resistance		≤ 10^{-8} at 4 × MIC
Cross-resistance		No cross-resistance to current antibiotics
Method of action		Proven against the isolated enzyme
ADME properties		
Human plasma stability		Low stability in human plasma ($t_{1/2}$ < 2 h)
Human S9 lung fraction stability		High stability in human S9 lung fraction
Physiochemical properties		
Chemical stability		Stable in buffered conditions (pH = 7.4)
Solubility		> 15 µM
Toxicity		
Cytotoxicity		hepG2 CC_{50} > 32 µg/mL
Cardiotoxicity		hERG IC_{50} (metabolite) > 33 µM

Table 26

3.6 Antibacterial and ADME results

3.6.1 Key for relevant biological and physiochemical results

To aid understanding of results, a portion of the following data is colour coded, according to the key below (**Table 27**). Desired properties are designated green, whereas undesired are coloured red. Intermediary results are coloured orange due to their ability to lead to desired criteria through optimisation. Where appropriate, calculated physiochemical properties are indicated by a dagger (†), and were calculated using ACD/Percepta 14.0.0. Key stability assays (human plasma stability, human S9 lung fraction stability and paraoxonase stability) were performed by the author, following tuition from ADME scientists.

MICs (µg/mL)		≤ 1	$2 - 16$	≥ 32
E. coli gyrase supercoiling (IC$_{50}$, µg/mL)		< 0.25	$0.25 - 5$	> 5
Kinetic solubility (µM)		> 15	$10 - 15$	< 10
Thermodynamic solubility (µM)		> 100	$50 - 100$	< 50
hERG inhibition (IC$_{50}$, µM)		> 33		≤ 33
hepG2 (CC$_{50}$, µg/mL)		> 32		≤ 32
Human plasma stability	% parent remaining after 2 h	$< 50\%$	$50 - 70\%$	$> 70\%$
	% metabolite remaining after 2 h	$> 70\%$	$50 - 70\%$	$< 50\%$
Human S9 lung fraction stability	% compound remaining after 2 h	$> 70\%$	$50 - 70\%$	$< 50\%$
Paraoxonase stability	% parent remaining after 6 h	$< 50\%$	$50 - 70\%$	$> 70\%$

Table 27

3.6.2 Antibacterial results: benzyl soft drug analogues

The antibacterial results for compounds **23**, **59**, **67** and **77** are shown below in **Table 28**, coloured according to the key defined in **Section 3.6.1**.

Redx No.	REDX08220 **23**	REDX10141 **59**	REDX10142 **77**	REDX10012 **67**
Structure				
S. aureus ATCC29213	0.5	0.06	8	2
S. pneumoniae ATCC49619	2	0.25	32	16
H. influenzae ATCC49247	16	4	> 64	> 32
E. cloacae NCTC13406	64	8	> 64	> 32
A. baumannii NCTC13420	32	1	> 64	> 32
P. aeruginosa ATCC27853	> 64	32	> 64	> 32
E. coli ATCC25922	8	2	> 64	> 32
E. coli N43 (efflux-knockout)	1	0.06	8	8
K. pneumoniae ATCC700603	> 64	> 32	> 64	> 32
E. coli gyrase supercoiling (IC$_{50}$, µg/mL)	0.49	0.06	23 – 47	-

(MICs (µg/mL) is the label for the rows from *S. aureus* to *K. pneumoniae*.)

Table 28

3.6.3 Physiochemical/ADME results: benzyl soft drug analogues

Based on the previously established guidelines, the ADME results for compounds **23**, **59**, **67** and **77** are shown below in **Table 29**, coloured according to the key defined in **Section 3.6.1**.

Redx No.	REDX08220 **23**	REDX10141 **59**	REDX10142 **77**	REDX10012 **67**
Structure				
TPSA[†]	96.9	84.0	115.2	84.0
clogP[†]	1.23	2.21	1.72	2.21
clogD$_{7.4}$[†]	0.19	0.24	-0.95	0.44
Measured logD$_{7.4}$	< 0.2	0.95	< 0.2	1.21
Kinetic solubility	71 µM	-	-	94 µM
Thermodynamic solubility	-	849 µM	-	56 µM
hERG inhibition (IC$_{50}$, µM)	> 33	2	> 33	-
hepG2 (CC$_{50}$, µg/mL)	> 128	120.8	> 128	-
Human plasma (100%, % parent remaining after 2 h)	55%	96%	100%	-
Human S9 lung fraction (5 mg/mL, % parent remaining after 2 h)	100%	100%	-	-

Table 29

3.6.4 Antibacterial results: alternative northern group analogues

Based on the previously established guidelines, the antibacterial results for compounds **59**, **74 – 76** and **78** are shown below in **Table 30**, coloured according to the key defined in **Section 3.6.1**.
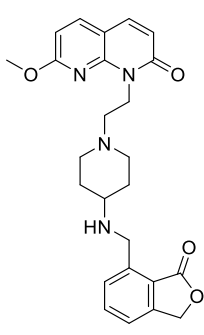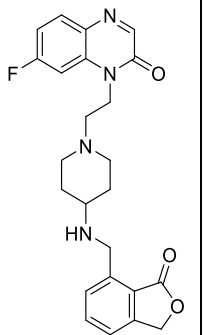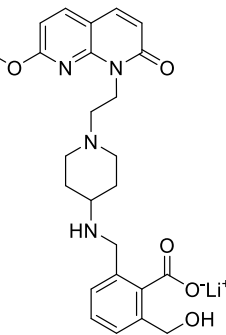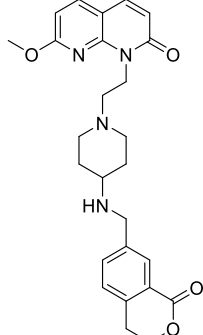
Redx No.	REDX10141 **59**	REDX10307 **74**	REDX10159 **75**	REDX10306 **76**	REDX10204 **78**
Structure					

		REDX10141 **59**	REDX10307 **74**	REDX10159 **75**	REDX10306 **76**	REDX10204 **78**
MICs (µg/mL)	*S. aureus* ATCC29213	0.06	0.25	0.25	0.25	> 128
	S. pneumoniae ATCC49619	0.25	0.5	0.5	0.5	> 128
	H. influenzae ATCC49247	4	4	2	1	> 128
	E. cloacae NCTC13406	8	32	64	16	> 128
	A. baumannii NCTC13420	1	8	4	4	> 128
	P. aeruginosa ATCC27853	32	> 64	> 64	64	> 128
	E. coli ATCC25922	2	8	8	4	> 128
	E. coli N43 (efflux-knockout)	0.06	0.12	0.12	< 0.06	16
	K. pneumoniae ATCC700603	> 32	> 64	> 64	64	> 128

Table 30

3.6.5 Physiochemical/ADME results: alternative northern group analogues

Based on the previously established guidelines, the ADME results for compounds **59**, **74 – 76** and **78** are shown below in **Table 31**, coloured according to the key defined in **Section 3.6.1**.
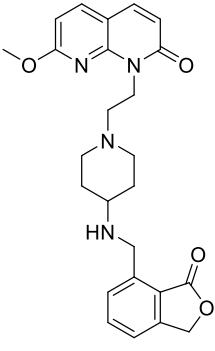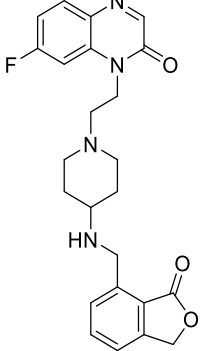
Redx No.	REDX10141 **59**	REDX10307 **74**	REDX10159 **75**	REDX10306 **76**	REDX10204 **78**
Structure					
TPSA[†]	84.0	74.2	74.2	74.8	105.5
clogP[†]	2.21	2.36	2.18	1.83	1.95
clogD$_{7.4}$[†]	0.24	0.56	0.36	-0.07	-0.63
Measured logD$_{7.4}$	0.95	-	0.52	-	-
Thermodynamic solubility	849 µM	-	764 µM	-	851 µM
hERG inhibition (IC$_{50}$, µM)	2	-	-	-	-
hepG2 (CC$_{50}$, µg/mL)	120.8	-	-	-	-
Human plasma (100%, % parent remaining after 2 h)	96%	82%	70%	75%	-
Human S9 lung fraction (5 mg/mL, % parent remaining after 2 h)	100%	-	95%	-	-

Table 31

3.6.6 Antibacterial results: 7-substituted/6-membered analogues

Based on the previously established guidelines, the antibacterial results for compounds **84 − 86** and **90 − 92** are shown below in **Table 32**, coloured according to the key defined in **Section 3.6.1**.
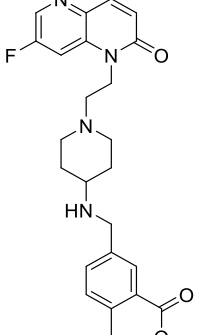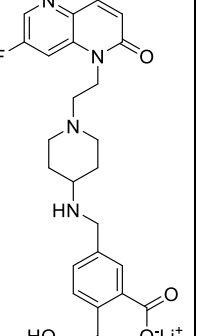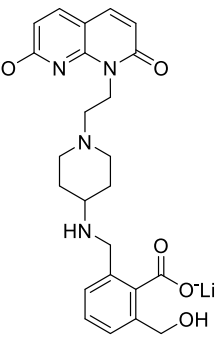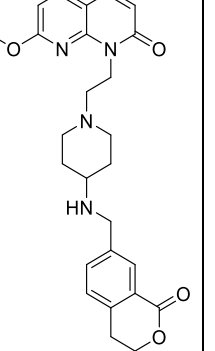
	Redx No.	REDX10248 **84**	REDX10281 **85**	REDX10284 **86**	REDX10359 **90**	REDX10386 **91**	REDX10403 **92**
	Structure						
MICs (µg/mL)	*S. aureus* ATCC29213	2	4	8	0.06	0.12	8
	S. aureus VRS8	-	-	-	0.06	0.25	8
	S. aureus NRS482	-	-	-	0.06	0.12	16
	S. pneumoniae ATCC49619	1	4	4	0.06	0.12	8
	H. influenzae ATCC49247	> 64	> 64	> 64	1	1	64
	E. cloacae NCTC13406	> 64	> 64	> 64	4	4	64
	A. baumannii NCTC13420	> 64	> 64	> 64	0.25	0.5	64
	P. aeruginosa ATCC27853	> 64	> 64	> 64	16	16	> 64
	E. coli ATCC25922	> 64	> 64	> 64	0.5	0.5	> 64
	E. coli N43 (efflux-knockout)	4	8	32	0.015	0.03	4
	K. pneumoniae ATCC700603	> 64	> 64	> 64	32	32	> 64
	E. coli gyrase supercoiling (IC$_{50}$, µg/mL)	1.96	-	-	0.03	-	-

Table 32

3.6.7 Physiochemical/ADME results: 7-substituted/6-membered analogues

Based on the previously established guidelines, the ADME results for compounds **84** − **86** and **90** − **92** are shown below in **Table 33**, coloured according to the key defined in **Section 3.6.1**.
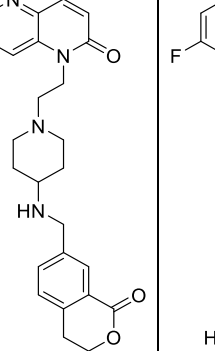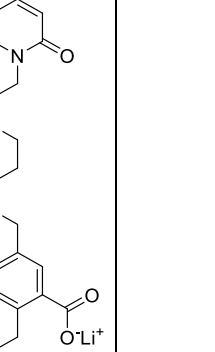
Redx No.	REDX10248 **84**	REDX10281 **85**	REDX10284 **86**	REDX10359 **90**	REDX10386 **91**	REDX10403 **92**
Structure						
TPSA†	84.0	74.2	115.2	84.0	74.8	106.0
clogP†	1.98	2.21	1.72	2.85	2.23	1.59
clogD$_{7.4}$†	0.12	0.51	-0.95	0.88	0.33	-1.00
Measured logD$_{7.4}$	1.03	0.75	< 0.2	0.78	< 0.2	< 0.2
Thermodynamic solubility	912 µM	228 µM	851 µM	1784 µM	2037 µM	-
hERG inhibition (IC$_{50}$, µM)	-	-	-	-	20.6	> 33
hepG2 (CC$_{50}$, µg/mL)	-	-	-	-	> 128	> 128
Human plasma (100%, % parent remaining after 2 h)	99%	93%	100%	100%	94%	-

Table 33

3.6.8 Antibacterial results: methyl/dimethyl lactone analogues

The antibacterial results for **105**, **106, 109**, **116** and **117** are shown below in **Table 34**, coloured according to the key defined in **Section 3.6.1**.
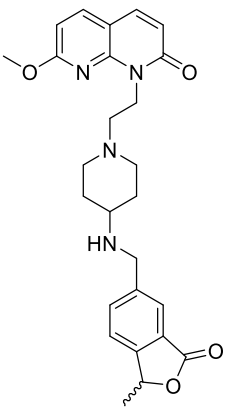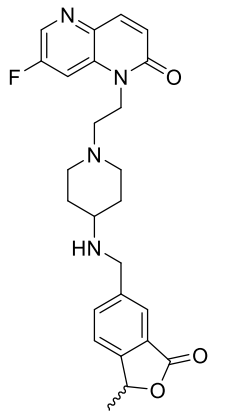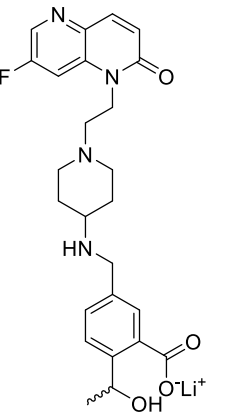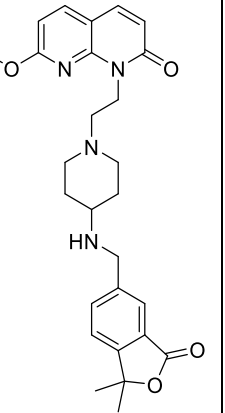
Redx No.	REDX10370 **105**	REDX10371 **106**	REDX10725 **109**	REDX10387 **116**	REDX10388 **117**
Structure					
MICs (µg/mL) *S. aureus* ATCC29213	0.5	0.12	8	0.015	0.12
S. aureus VRS8	0.03	-	8	0.06	0.25
S. aureus NRS482	0.12	0.12	16	0.06	0.12
S. pneumoniae ATCC49619	0.06	0.12	4	0.06	0.12
H. influenzae ATCC49247	0.5	0.5	32	1	1
E. cloacae NCTC13406	2	4	> 64	8	16
A. baumannii NCTC13420	0.25	0.25	32	0.5	1
P. aeruginosa ATCC27853	8	16	> 64	16	32
E. coli ATCC25922	0.5	0.5	64	1	2
E. coli N43 (efflux-knockout)	0.008	0.015	2	0.03	0.06
K. pneumoniae ATCC700603	32	16	> 64	64	64

Table 34

3.6.9 Physiochemical/ADME results: methyl/dimethyl lactone analogues

Based on the previously established guidelines, the ADME results for compounds **105**, **106, 109**, **116** and **117** are shown below in **Table 35**, coloured according to the key defined in **Section 3.6.1**.
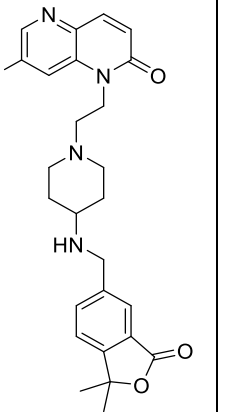
Redx No.	REDX10370 **105**	REDX10371 **106**	REDX10725 **109**	REDX10387 **116**	REDX10388 **117**
Structure					
TPSA[†]	84.0	74.8	106.0	84.0	74.8
clogP[†]	2.60	2.11	1.73	2.88	2.43
clogD$_{7.4}$[†]	0.63	0.21	-0.90	0.93	0.55
Measured logD$_{7.4}$	1.44	0.50	< 0.2	1.76	0.84
Thermodynamic solubility	1396 μM	2193 μM	-	831 μM	1075 μM
hERG inhibition (IC$_{50}$, μM)	1.3	6.1	> 33	3.6	-
hepG2 (CC$_{50}$, μg/mL)	87.2	> 256	> 128	-	-
Human plasma (100%, % parent remaining after 2 h)	100%	49%	85%	96%	100%
Human S9 lung fraction (5 mg/mL, % parent remaining after 2 h)	-	100%	100%	-	-

Table 35

3.6.10 Antibacterial results: REDX10371/REDX10725 enantiomers

The antibacterial results for compounds **106 – 111** are shown below in **Table 36**, coloured according to the key defined in **Section 3.6.1**.

Redx No.		REDX10371 **106**	REDX10725 **109**	(*S*)-REDX10371 **108**	(*S*)-REDX10725 **111**	(*R*)-REDX10371 **107**	(*R*)-REDX10725 **110**
Structure							
MICs (µg/mL)	*S. aureus* ATCC29213	0.12	8	0.12	32	0.06	4
	S. aureus VRS8	2	8	0.06	16	0.06	4
	S. aureus NRS482	0.12	16	0.25	32	0.12	8
	S. pneumoniae ATCC49619	0.12	4	0.06	4	0.06	2
	H. influenzae ATCC49247	0.5	32	0.25	16	0.5	32
	E. cloacae NCTC13406	4	> 64	2	> 64	2	> 64
	A. baumannii NCTC13420	0.25	32	0.25	32	0.5	32
	P. aeruginosa ATCC27853	16	> 64	8	> 64	8	> 64
	E. coli ATCC25922	0.5	64	0.5	32	0.5	32
	E. coli N43 (efflux-knockout)	0.015	2	0.03	4	0.06	4
	K. pneumoniae ATCC700603	16	> 64	8	> 64	16	> 64

Table 36

3.6.11 Physiochemical/ADME results: REDX10371/REDX10725 enantiomers

The ADME results for compounds **106** – **111** are shown below in **Table 37**, coloured according to the key defined in **Section 3.6.1**.

Redx No.	REDX10371 **106**	REDX10725 **109**	(*S*)-REDX10371 **108**	(*S*)-REDX10725 **111**	(*R*)-REDX10371 **107**	(*R*)-REDX10725 **110**
Structure						
TPSA[†]	74.8	106.0	74.8	106.0	74.8	106.0
clogP[†]	2.11	1.73	2.11	1.73	2.11	1.73
clogD$_{7.4}$[†]	0.21	-0.90	0.21	-0.90	0.21	-0.90
Measured logD$_{7.4}$	0.50	< 0.2	0.52	< 0.2	-	< 0.2
Thermodynamic solubility	2193 µM	-	-	-	-	-
hERG inhibition (IC$_{50}$, µM)	6.1	> 33	8.5	> 33	6.0	> 33
hepG2 (CC$_{50}$, µg/mL)	> 256	> 128	> 128	> 128	> 128	> 128
Human plasma (100%, % parent remaining after 2 h)	49%	85%	72%	100%	57%	100%
Human S9 lung fraction (5 mg/mL, % parent remaining after 2 h)	100%	100%	100%	-	100%	-
Paraoxonase stability (1:5 with PBS, % parent remaining after 6 h)	-	-	58%	-	64%	-

Table 37

3.7 Discussion of antibacterial and ADME results

3.7.1 6-substituted phenyl lactone series

3.7.1.1 Antibacterial properties of REDX10141 (59)
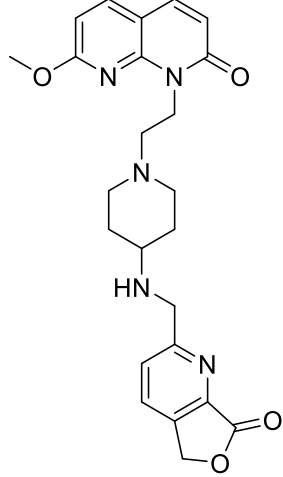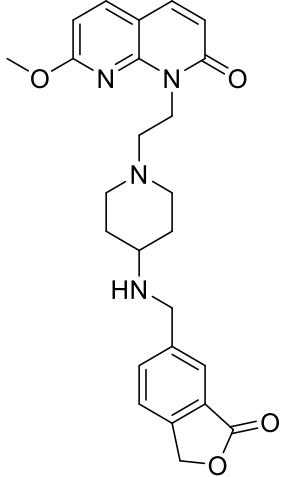
Following the preparation of REDX10141 **59** and REDX10012 **67** (**Section 3.4.1** and **Section 3.4.2** respectively), assessment of antibacterial activity was required to determine if the phenyl alternative to the pyridyl group was a successful modification. For both compounds, an increase in antibacterial activity compared to their pyridyl counterparts was recorded. Although replacement of the pyridyl ring in REDX08730 **46** with a phenyl ring modestly improved potency (MIC (*S. aureus*): REDX08730 **46** = 16 µg/mL, REDX10012 **67** = 2 µg/mL), this was not deemed successful enough to warrant the synthesis of similar analogues. As a result, no further analogues with the carbonyl group of the lactone on the opposing face to the attachment point were considered (**Figure 48**).
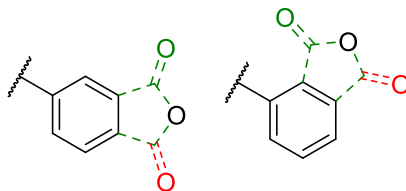
Lactones with carbonyl units on the opposite face from the linkage (red) were deprioritised in favour of those with carbonyl units closer to the linkage point (green).

Figure 48

Of particular importance was the antibacterial activity of REDX10141 **59** (**Table 38**). Improved MICs (< 1 µg/mL) against key pneumonia-causing pathogens (*S. aureus* and *S. pneumoniae*) satisfied the antibacterial potency guidelines set at the outset of the project, indicating significant progress was made by manipulating the fused pyridyl lactone moiety. Furthermore, as the potency of REDX10141 **59** increased approximately 3-fold on average compared to REDX08220 **23**, potency against *A. baumannii* was now observed. This was of particular interest as *A. baumannii* is a notoriously difficult gram-negative pathogen to maintain activity against, and can be prevalent in lung infections.[83]

Redx No.	REDX08220 **23**	REDX10141 **59**
Structure		

		REDX08220 **23**	REDX10141 **59**
MIC (µg/mL)	*A. baumannii* NCTC134203	32	1
	E. coli ATCC25922	8	2
	H. influenzae ATCC49247	16	4
	P. aeruginosa ATCC27853	> 64	32
	S. aureus ATCC29213	0.5	0.06
	S. pneumoniae ATCC49619	2	0.25
	E. coli N43	1	0.06
E. coli gyrase supercoiling IC$_{50}$ (µg/mL)		0.49	0.06
Measured logD$_{7.4}$		< 0.2	0.95
Phosphate stability (pH 7.4)		68% remaining (5 h)	No degradation observed

Comparison of antibacterial properties for REDX08220 **23** and REDX10141 **59**.

Table 38

The positive antibacterial and phosphate stability results were considered proof of concept for the replacement of the pyridyl lactone with a phenyl lactone. The increase in potency could be attributed either to an increase in permeability, ensuring a higher concentration of compound reached the target, or due to an increase in target based potency. In order to elucidate the findings, inhibition of DNA gyrase supercoiling was measured using REDX08220 **23** and REDX10141 **59**. As the supercoiling assay utilises the isolated enzyme, the necessity for bacterial permeability is removed. It was determined that REDX10141 **59** was over eight times more potent at inhibiting DNA gyrase supercoiling in a model system (*E. coli*) than its pyridyl counterpart, REDX08220 **23**. Thus, the improved ability to inhibit supercoiling confirmed an increase in target based potency, reinforcing the computationally observed benefit in minimising the polarity of the southern group. Furthermore, it suggested the hypothesised H-bonding interaction between the pyridyl nitrogen and Asp1083 of DNA gyrase was of minimal importance in contributing to binding affinity, supporting the computationally obtained results (**Section 3.3.1**).

It was hypothesised that an increase of $logD_{7.4}$ may also have contributed to the increase in potency due to higher bacterial permeability. Regardless, the reinforced boost in target potency was used as rationale to direct the research project away from unstable fused pyridyl lactones, and towards more active phenyl derivatives.

3.7.1.2   Optimisation of $logD_{7.4}$ in increasing bacterial permeability

Encouraged by the increase in potency observed between REDX08220 **23** and REDX10141 **59**, the synthesis of compounds that varied with respect to their northern groups was used to search for an optimal $logD_{7.4}$ window that inferred maximal permeability (**Section 3.4.3**). It was envisioned that small manipulations in the lipophilicity of the compound could produce large improvements in antibacterial potency (**Table 39**).

Strain and optimal permeable $logD_{7.4}$ range[84]				REDX10141 **59**	REDX10307 **74**	REDX10159 **75**	REDX10306 **76**
MIC (µg/mL)	*H. influenzae* ATCC49247	0.0 → 0.3	← Increased permeability to more lipophilic molecules	4	4	2	1
				→ *increase* in potency, with increasing polarity			
	S. pneumoniae ATCC49619	1.2 → 1.6		0.25	0.5	0.5	0.5
				→ *decrease* in potency, with increasing polarity			
	S. aureus ATCC29213	1.4 → 2.0		0.06	0.25	0.25	0.25
				→ *decrease* in potency, with increasing polarity			
Key:				≤ 0.25	0.5 – 1		≥ 2
clogD$_{7.4}$[†]				0.24*	0.56	0.36	-0.07
Measured $logD_{7.4}$				0.95	Estimate = 0.6	0.52	Estimate = 0.1

*Calculated $logD_{7.4}$ values for methoxypyridines have been shown in the literature to be inaccurate.[79] †Calculated using ACD/Percepta 14.0.0.

Antibacterial activity for REDX10141 **59**, REDX10307 **74**, REDX10159 **75** and REDX10306 **76**.

Table 39

Although it is broadly accepted that a two-fold difference in MIC values is within the expected error values for the assay, it could be postulated that lowering the $logD_{7.4}$ of the analogues was accompanied by a small drop in activity against the gram-positive strains *S. aureus* and *S. pneumoniae*. However, increasing polarity was associated with a marginal increase in antibacterial activity for *H. influenza* (gram-negative). Gram-positive bacteria tend to be more permeable to compounds with higher lipophilicities than their gram-negative counterparts. It was therefore concluded that the observed trends in bacterial

activity were small but consistent with the published literature surrounding bacterial membrane permeabilities.[84]

Where resources allowed, measured $logD_{7.4}$ values were used to assess the accuracy of the computationally calculated values (**Table 39**). Additionally, matched pair analysis allowed for estimates for missing values, allowing trends to be postulated. Overall, calculated $logD_{7.4}$ values were seen to be fairly accurate for the series. However, important exceptions were compounds which contained the methoxypyridine moiety in the northern group, which were consistently calculated to be more hydrophilic than their experimentally determined values (**Figure 49**).
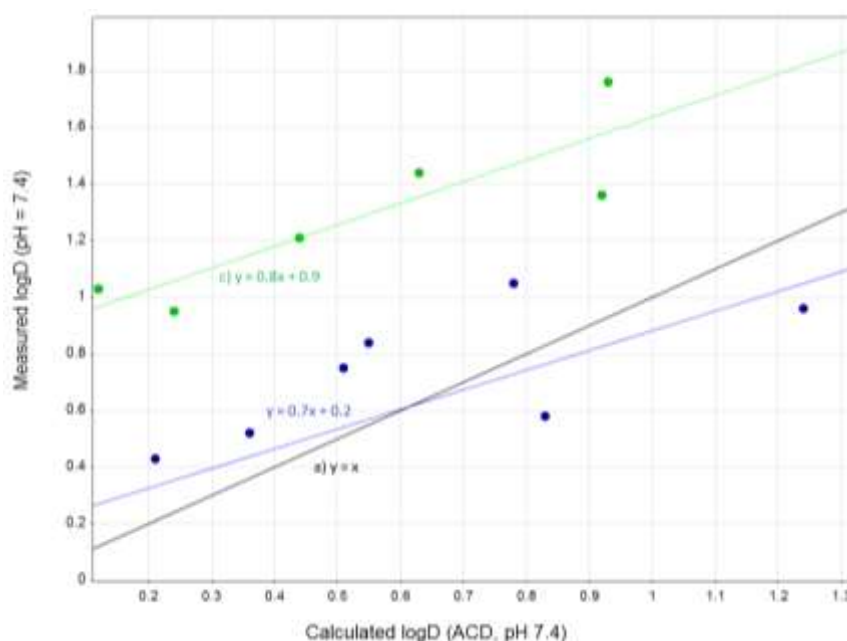
Graph showing correlation between measured $logD_{7.4}$ and calculated $logD_{7.4}$ (using ACD/Percepta 14.0.0) for a) ideal scenario where calculated $logD_{7.4}$ equals measured $logD_{7.4}$ (black, equation of the line: y = x), b) non-methoxypyridine northern groups (blue, equation of the line: y = 0.7x + 0.2) and c) methoxypyridine northern groups (green, equation of the line: y = 0.8x + 0.9). It was observed that the methoxypyridine northern group results in the measured $logD_{7.4}$ being consistently higher than the calculated $logD_{7.4}$ (as in agreement with Barlaam *et al*.[79]).

Figure 49

This finding was consistent with the literature, which suggested the methoxy oxygen lone pair may be partially conjugated with the heterocycle, increasing the lipophilicity of the compound.[79] As the antibacterial activity of REDX10141 **59** was not highly affected by

simple modification of the northern group, resources were focussed upon optimising the southern group. In order to efficiently cover as much chemical space as possible, the 7-methoxy-1,8-naphthyridin-2(1*H*)-one and 7-fluoro-1,5-naphthyridin-2(1*H*)-one northern groups (**Figure 50**) were selected for further analogue synthesis. These groups spanned the largest $logD_{7.4}$ range, and both inferred acceptable antibacterial potency, highlighting their worthiness for additional investigation.
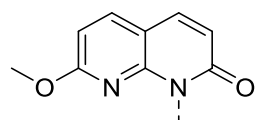
7-methoxy-1,8-naphthyridin-2(1*H*)-one   7-fluoro-1,5-naphthyridin-2(1*H*)-one
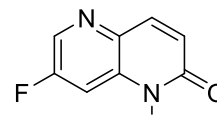
Northern groups selected to provide the largest span of $logD_{7.4}$ values, without negatively affecting antibacterial activity.

Figure 50

3.7.1.3   Comparison of soft drug parents and their metabolites

In order to reinforce the potential merits of a soft drug approach to antibacterial research, the hypothesised lactone-hydrolysed metabolites of REDX10141 **59** and REDX10159 **75** were prepared (**Section 3.4.4**), yielding REDX10142 **77** and REDX10204 **78** respectively.

		REDX10141 **59**	REDX10142 **77**	REDX10159 **75**	REDX10204 **78**
		"Parent"	*"Metabolite"*	*"Parent"*	*"Metabolite"*
MIC (µg/mL)	*A. baumannii* NCTC13420	1	> 64	4	> 128
	E. coli ATCC25922	2	> 64	8	> 128
	H. influenzae ATCC49247	4	> 64	2	> 128
	S. aureus ATCC29213	0.06	8	0.25	> 128
	S. pneumoniae ATCC49619	0.25	32	0.5	> 128
E. coli gyrase supercoiling IC_{50} (µg/mL)		0.06	23 – 47	-	-

Antibacterial potency of REDX10141 **59**, REDX10142 **77**, REDX10159 **75** and REDX10204 **78**.

Table 40

The parent compounds, REDX10141 **59** and REDX10159 **75**, were seen to be potent against several key strains, including *S. aureus* and *S. pneumoniae* (**Table 40**). Lactone hydrolysis, to yield REDX10142 **77** and REDX10204 **78** respectively, was accompanied by a dramatic loss

of potency. It should be noted, however, that a moderate MIC of 8 μg/mL against *S. aureus* was observed for REDX10142 **77**. This was considered either to be due to the exceptionally high potency of the parent compound against *S. aureus*, or the potential of the scaffold to ring close back to the active lactone, resulting in a small amount of perceived activity for the metabolite against this strain. The reduction in antibacterial activity of REDX10142 **77** was reinforced by the trend observed between REDX10159 **75** and REDX10204 **78**, which lost all antibacterial activity upon lactone hydrolysis. Additionally, measuring the ability of the compounds to inhibit supercoiling in DNA gyrase indicated that inactivity of the metabolite was not solely caused by poor permeability. As predicted computationally, hydrolysis of the southern group revealed a highly polar moiety in a lipophilic region of the active site, disfavouring binding. Thus, the antibacterial results for both the parent, and the metabolite, are in agreement with the soft drug strategy. However, more importantly, a difference between the cardiotoxicity of the parent and suspected metabolite was also observed.

	REDX10141 **59**	REDX10142 **77**
	"Parent"	*"Metabolite"*
hepG2 (CC$_{50}$)	> 120.8 μg/mL	> 128 μg/mL
hERG (IC$_{50}$)	2 μM	> 33 μM
hERG inhibition profiles		

Toxicity of REDX10141 **59** and REDX10142 **77**.

Table 41

Gratifyingly, the suspected metabolite was observed to be non-cytotoxic, as shown from the high viability of the cells in the hepG2 assay (**Table 41**). Although a nontoxic result was not obtained for REDX10141 **59**, the high value suggested further work in the area could proceed. Additionally, it was observed that 50% inhibition (IC_{50}) of the hERG ion channel for REDX10141 **59** was observed to occur at a low concentration of 2 μM, however this increased to > 33 μM upon lactone hydrolysis. The cardiotoxicity trends provided useful evidence to suggest a soft drug approach could be utilised to alleviate systemic exposure to a compound with potent hERG inhibition. Encouraged by the generated *in vitro* toxicity and antibacterial results, the potential for a soft drug therapy relied on the relative stability of the parent and metabolite compounds to human plasma and human S9 lung fraction.

3.7.1.4 Stability studies of phenyl soft drug analogues

In order to assess the suitability of a compound to become a viable antibacterial soft drug therapy, the stability of the compound in human plasma and human S9 lung fraction was determined. Utilising previously validated assay conditions, the following results were generated for phenyl lactone compounds **59** and **74** – **76** (**Table 42**).

	REDX10141 **59**	REDX10307 **74**	REDX10159 **75**	REDX10306 **76**
Measured $logD_{7.4}$	0.95	0.6*	0.52	0.1*
Human plasma stability (100% plasma, % remaining after 2 h)	96%	82%	70%	75%
Human S9 lung fraction stability (5 mg/mL, % remaining after 2 h)	100%	-	95%	-

*Value predicted using previously observed trends. Human plasma and human S9 lung fraction stability for soft drug probe compounds **59** and **74** - **76**.

Table 42

Although the compounds were observed to be highly to moderately stable in human plasma, a window of stability was observed between human plasma and human S9 lung fraction. Of particular interest was REDX10159 **75** which was identified to be partially metabolised in human plasma, but stable within the lung media, suggesting potential metabolism by paraoxonase.

In addition, a possible trend between instability and $logD_{7.4}$ was identified from the series. Namely, a decrease in lipophilicity was associated with an increase in metabolic lability. Unfortunately, investigations connecting $logD_{7.4}$ and paraoxonase metabolism have not

been reported within the literature to date. As a result of the computational investigation into the plausible binding mode of NBTI substrates within paraoxonase (**Section 2.8.3**), a potential involvement of the northern group to binding was observed. Although the bicyclic system was predicted to protrude from the enzyme, a nearby collection of lipophilic residues may be involved in binding within this area. As a result, small changes in the lipophilicity of the northern group may have an effect on the affinity for the active site, providing potential rationale for the differing metabolic rates of similar substrates. Further analogue synthesis spanning a larger $logD_{7.4}$ range could help identify an ideal $logD_{7.4}$ window for paraoxonase metabolism. However, it was considered that a further decrease in $logD_{7.4}$ would be counterproductive with regards to antibacterial activity, particularly against the target gram-positive pathogens. Therefore, an alternative method to improve the stability profile, while maintaining antibacterial potency, was required.

3.7.2 7-substituted phenyl lactone series

3.7.2.1 Assessment of alternative connection point in DNA gyrase

With preferential northern groups selected, focus was placed on the optimisation of the southern lactone group. Hypothesised replacements were modelled computationally, by overlaying the published ligand and crystal structure with potential replacements.

Initially, the structure-activity relationship surrounding the attachment point to the southern group was challenged through assessing 7-substituted bicyclic lactones and comparing them to their 6-subsituted counterparts.

| REDX10141 **59** | | REDX10248 **84** |
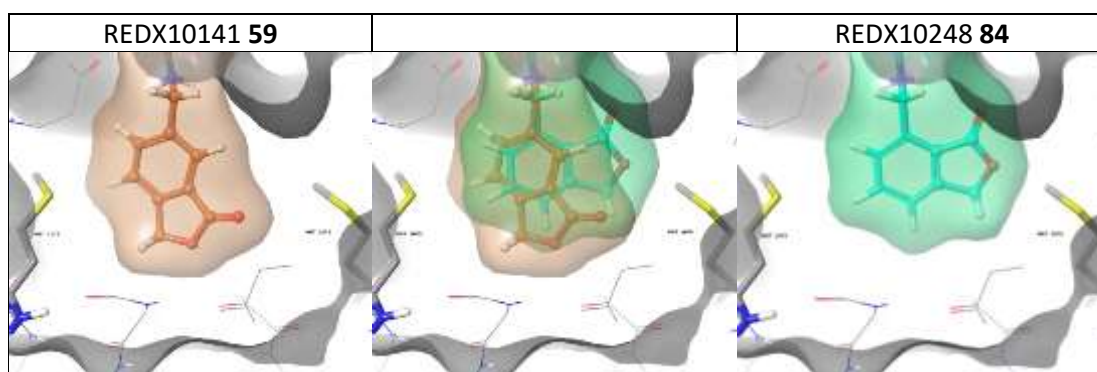
Computationally derived binding poses for 6-substituted (REDX10141 **59**, orange, left) and 7-substituted (REDX10248 **84**, green, right) attachment points for the southern group in PDB:2XCS.[36] Overlay of both compounds shown for comparison (centre).

Figure 51

It was postulated that the connectivity of the 7-substituted bicyclic ring system (green surface) may prevent efficient space-fit with the non-polar residues in the lipophilic pocket (**Figure 51**). Additionally, a minor clash between the lactone ring and Met1075 could be hypothesised, which may result in a decrease in binding affinity. Although the 7-substituted derivative may not bind as efficiently as the previously synthesised 6-substituted phenyl lactones, the alternative attachment point was thought to allow an internal H-bond to be maintained between the aminopiperidine linker region and the carbonyl in the lactone ring (**Figure 52**).

6-substituted benzyl
lactone e.g. REDX10141 **59**

*Alternative attachment
point*

7-substituted benzyl
lactone e.g. REDX10248 **84**
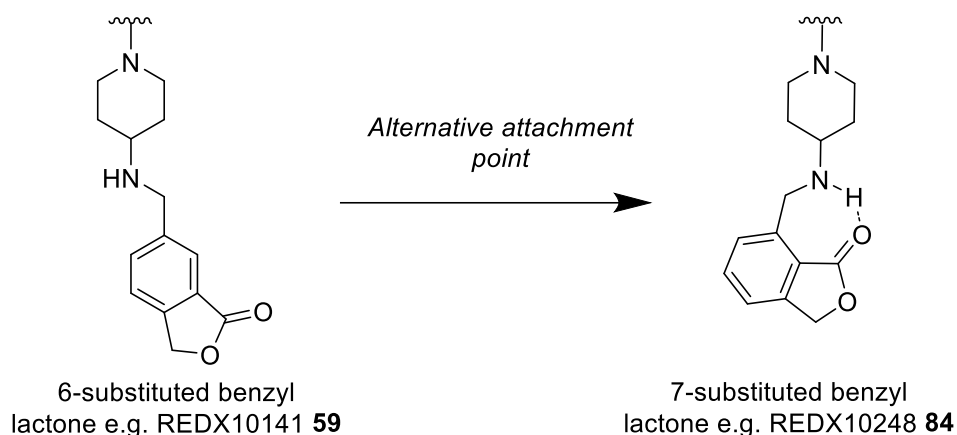
Possible internal H-bond made in 7-substituted phenyl lactone analogues.

Figure 52

The introduction of internal H-bonds is a well published strategy to increase the permeability of pharmaceuticals through masking of polar moieties.[85] Additionally, regardless of the effect of the alternative attachment point on antibacterial activity, the synthesis of 7-substituted phenyl lactone compounds could provide evidence to support the computational chemistry campaign, reinforcing the merits of the current model in providing an appropriate means for simulating the compounds.

3.7.2.2 Assessment of alternative connection point in paraoxonase

In order for the soft drug therapy to be viable, metabolism by paraoxonase was integral. Thus, a dual targeting strategy was adopted in order to computationally screen potential modifications to the southern group against both DNA gyrase and paraoxonase. Consequently, a 7-substituted alternative to the previously explored 6-substituted analogue was assessed for its ability to bind to paraoxonase in a molecular dynamics model (**Figure 53**).
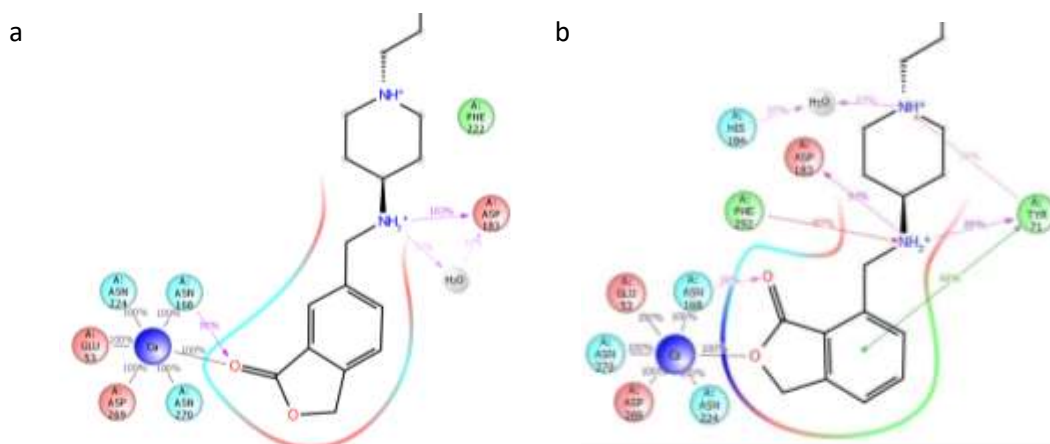
Molecular dynamics interactions diagrams for a) 6-substituted phenyl analogue and b) 7-substituted phenyl analogue in PON1 (PDB: 3SRG[73]).

Figure 53
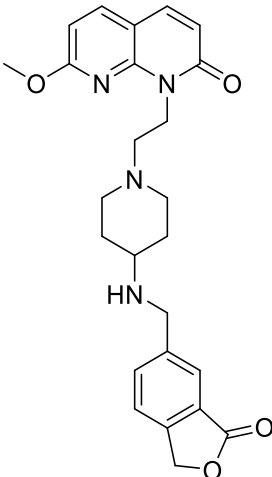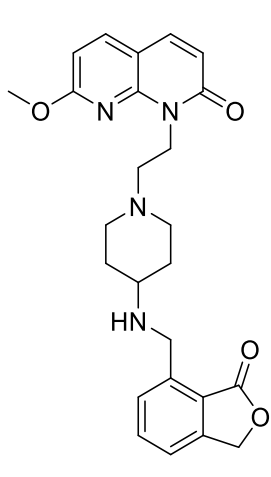
It was observed that several interactions were maintained between the 6-substituted analogue and the 7-substituted derivative. Importantly, key interactions were observed to be preserved between the catalytic calcium ion and the lactone region of the southern group, consistent with the interaction that was expected to be integral to metabolism. Furthermore, interaction with Asp183 was also maintained. Although the linear, trench-like nature of the paraoxonase binding site is well documented,[73] no major steric clashes with the active site were observed throughout the simulation. This was attributed to the inherent flexibility of the molecular dynamics model, and thus the output was tentatively accepted, pending further experimentally derived results. Subsequently, the synthesis of 7-substituted analogues was successfully performed (**Section 3.4.5**).

3.7.2.3 Antibacterial activity of 7-substituted phenyl lactones

In order to determine a preferential position to attach the fused phenyl lactone, and help strengthen the computational model, the 7-substituted phenyl lactone compounds were assessed for their antibacterial activity against a panel of key bacterial pathogens. Comparison against matched pairs from the 6-substituted series allowed a more favourable vector to be selected for further investigation. For comparative purposes, REDX10141 **59** was used as a hit compound, from which differences in antibacterial potency could be rationalised.

The 7-substituted analogue, REDX10248 **84**, was found to have reduced potency against all the bacterial strains in question (**Table 43**). Furthermore, with minimal change in $logD_{7.4}$ being observed, this was presumed to be caused by a property independent of

permeability. Although the data suggested lower target-based potency, this was confirmed through obtaining supercoiling inhibition data for DNA gyrase. REDX10248 **84** was seen to be over 30 times less potent that REDX10141 **59** at inhibiting DNA gyrase supercoiling, reinforcing the preferential attachment point of the series to be at the 6-position.

Redx No.		REDX10141 **59**	REDX10248 **84**
Structure			
MIC (µg/mL)	*A. baumannii* NCTC134203	1	> 64
	E. cloacae NCTC13406	8	> 64
	E. coli ATCC25922	2	> 64
	H. influenzae ATCC49247	4	> 64
	K. pneumoniae ATCC70060	> 32	> 64
	P. aeruginosa ATCC27853	32	> 64
	S. aureus ATCC29213	0.06	2
	S. pneumoniae ATCC49619	0.25	1
	E. coli W4573	2	> 64
	E. coli N43	0.06	4
E. coli gyrase supercoiling IC_{50} (µg/mL)		0.06	1.96
Measured $logD_{7.4}$		0.95	1.03

Comparison of antibacterial properties for REDX10141 **59** and REDX10248 **84**.

Table 43

Gratifyingly, the poor antibacterial potency complimented the computational modelling, which suggested a poorer fit for the active site, combined with a potential steric clash with Met1075. Although a clear result with regards to a preferential attachment point that inferred high antibacterial activity was determined, investigations into the influence the connection point had on the stability of the scaffold were also undertaken. This was to allow a structure-stability relationship to be developed alongside a structure-activity relationship, with the intention that the data may aid future compound selection.

3.7.2.4 Stability studies of 7-substituted phenyl lactones

The stabilities of REDX10141 **59** and REDX10248 **84** were measured through incubation with human plasma, with the percentage of the parent remaining shown in **Table 44**.

Redx No.	REDX10141 **59**	REDX10248 **84**
Human plasma stability (100% plasma, % remaining after 2 h)	96%	99%

Comparison of stability profiles for REDX10141 **59** and REDX10248 **84**.
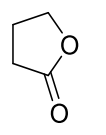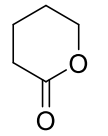
Table 44

Due to both REDX10141 **59** and REDX10248 **84** being highly stable, no clear difference in the stability profiles was observed. Although the high stability of REDX10248 **84** may suggest a poor fit for the active site of paraoxonase, this could not be confirmed. Due to the poor antibacterial and stability properties of the 7-substituted analogue, no further work was performed on compounds utilising this attachment point to the southern group.

With a preferred configuration of southern group identified, further investigations into the structure-activity and structure-stability relationships of the southern group could be undertaken. As previously outlined, a potential method of challenging the structure-activity relationship of the series was through expanding the steric confines of the soft drug, resulting in either increased space-fit, or clash, with the active site.

3.7.3 6-membered phenyl lactone series
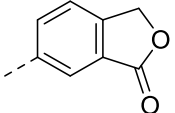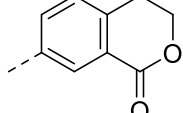
Building on the results surrounding the optimal attachment point for the southern group, challenging the SAR was continued through further alterations to the phenyl lactone system. Guided by the increased stability of the phenyl lactone system to human plasma, alternative methods of increasing the susceptibility of the scaffold to metabolism were considered. Although published literature surrounding hydrolysable paraoxonase substrates was sparse, unsubstituted, saturated 6-membered lactone rings were shown to be metabolised more efficiently than their 5-membered analogues (**Table 45**).

Substrate		
Paraoxonase activity (µmol of substrate metabolised/min)	32	671

Paraoxonase metabolic activity of γ-butyrolactone **118** and δ-valerolactone **119**.[86]

Table 45

Although these results were not directly comparable due to the fragments not being fused to an aromatic ring, a similar trend was desired for the soft drug analogues (**Table 46**).

Substrate	REDX10141 **59**	REDX10359 **90**
Plasma stability (100% plasma, % parent remaining after 2 h)	96%	*Unknown but hypothesised to be <100%*

Percentage of substrate remaining for REDX10141 **59** and REDX10359 **90**.

Table 46

As a result, computational overlays of potential 6-membered phenyl lactone compounds were used as an initial screen of target compound suitability, with respect to binding to DNA gyrase and paraoxonase, prior to synthesis.

3.7.3.1 Assessment of 6-membered phenyl lactones in DNA gyrase

Of particular interest was the effect a larger ring system may have on binding to the active site of DNA gyrase. In particular, the influence of the increased steric bulk of the southern group, and how the larger ring size may alter the positioning of the lactone carbonyl unit, were monitored during potential replacements. Computationally simulated overlays were used to assess possible modifications, and the resulting effects on binding to DNA gyrase that may occur.
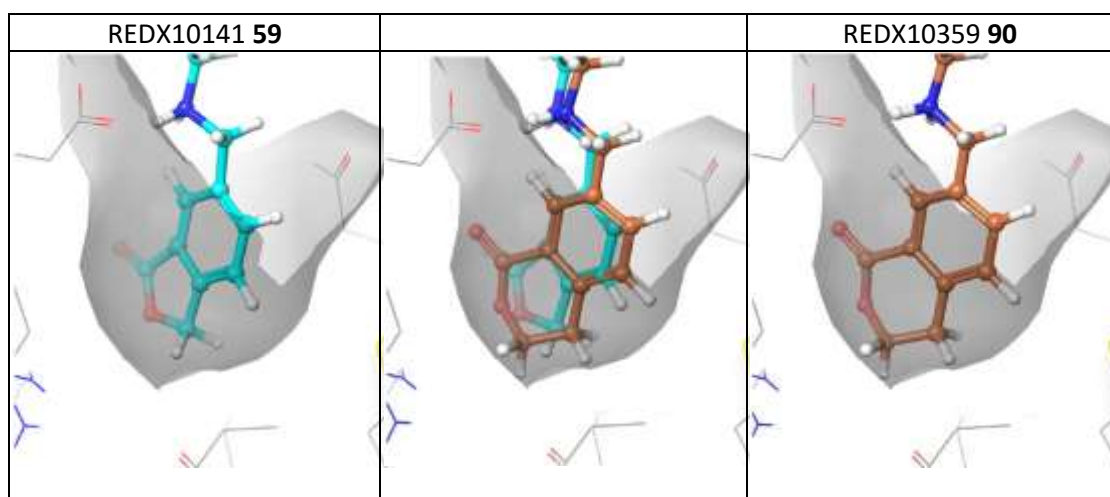
Computationally derived binding poses for 6,5-phenyl lactone (REDX10141 **59**, blue, left) and 6,6-phenyl lactone (REDX10359 **90**, orange, right) in PDB:2XCS.[36] Overlay of both compounds shown for comparison (centre).

Figure 54

As a result of the computational work performed on the scaffold, 6,6-phenyl lactone systems were hypothesised to be tolerated within the active site of DNA gyrase (**Figure 54**). It was observed that a minor increase in steric bulk in the lipophilic pocket resulted in minimal clash with the active site, and may result in a higher degree of lipophilicity along this vector. Furthermore, it could be hypothesised that the additional methylene unit in the 6,6-phenyl lactone may push the polarity of the lactone carbonyl away from the lipophilic pocket in DNA gyrase, favouring binding. Encouraged by the initially positive results, computational evaluation of the 6,6-phenyl lactone in paraoxonase was performed.

3.7.3.2 Assessment of 6-membered phenyl lactones in paraoxonase

In order to predict the susceptibility of the scaffold to metabolism by human plasma, computational evaluation was used. As a result, the 6,6-phenyl lactone alternative to the previously explored 6,5-phenyl lactone was assessed for its ability to bind to paraoxonase in a molecular dynamics model.
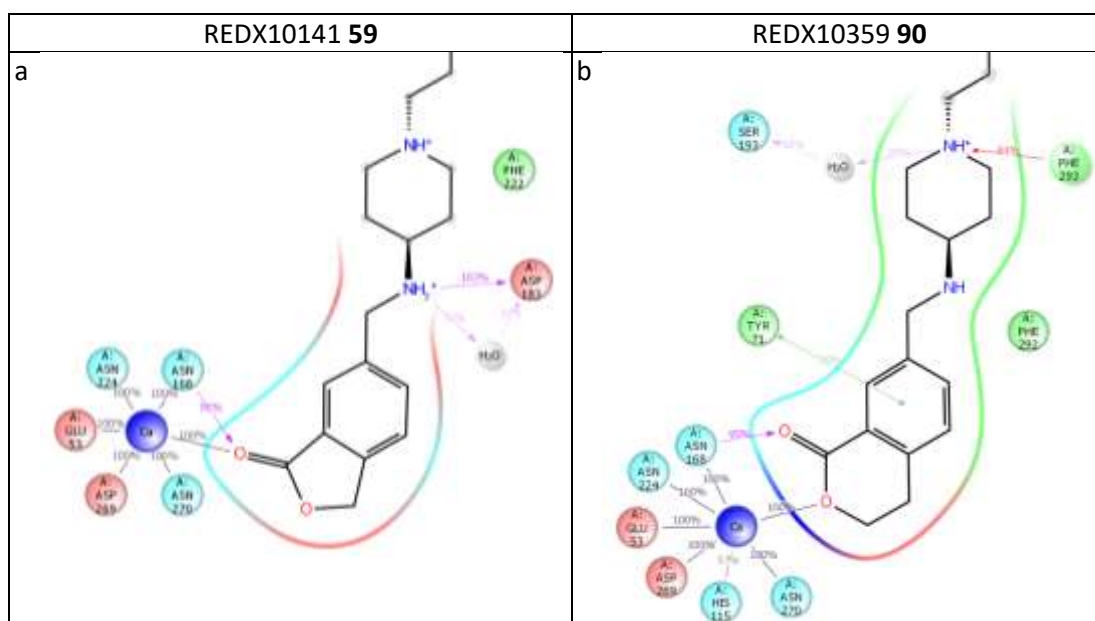
Molecular dynamics interactions diagrams for a) 6,5-phenyl lactone analogue **59** and b) 6,6-phenyl lactone analogue **90** in PON1 (PDB: 3SRG[73]).
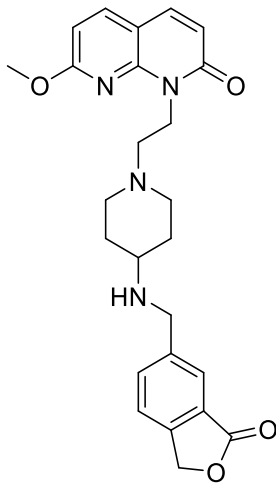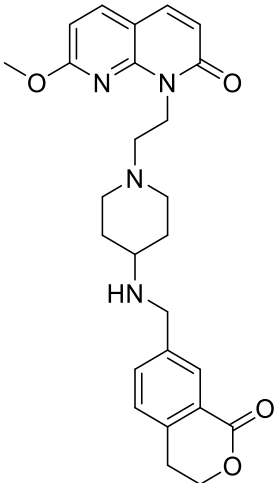
Figure 55

It was observed that several interactions were maintained with the 6,6-phenyl lactone system. Crucially, interactions between the carbonyl group of the lactone and the catalytic calcium ion within the active site were observed to be maintained, suggesting the increase in ring size did not have a detrimental effect on binding to the active site of paraoxonase.

Although the remainder of observed interactions made between the substrate and the enzyme active site were inconsistent between ligands, this was considered to be due to the inherent flexibility of the molecular model. As no major steric repulsions were observed for the 6,6-phenyl lactone scaffold, the synthesis of these analogues was successfully completed (**Section 3.4.7**), affording material that could be biologically assessed.

3.7.3.3　　　Antibacterial activity of 6-membered phenyl lactone series

In order to determine if a 6,6-phenyl lactone southern group was tolerated within the active site of DNA gyrase, REDX10359 **90** was assessed for its antibacterial activity against a panel of key bacterial pathogens, and compared to REDX10141 **59**.

Redx No.		REDX10141 **59**	REDX10359 **90**
Structure			
MIC (µg/mL)	*A. baumannii* NCTC134203	1	0.25
	E. cloacae NCTC13406	8	4
	E. coli ATCC25922	2	0.5
	H. influenzae ATCC49247	4	1
	K. pneumoniae ATCC70060	> 32	32
	P. aeruginosa ATCC27853	32	16
	S. aureus ATCC29213	0.06	0.06
	S. pneumoniae ATCC49619	0.25	0.06
	E. coli W4573	2	1
	E. coli N43	0.06	0.015
E. coli gyrase supercoiling IC$_{50}$ (µg/mL)		0.06	0.03
Measured logD$_{7.4}$		0.95	0.78

Comparison of antibacterial properties for REDX10141 **59** and REDX10359 **90**.

Table 47

The 6,6-phenyl lactone was not only observed to be tolerated within the active site of DNA gyrase, but preferred. A boost in antibacterial activity was seen across nearly all the tested

bacterial strains, reinforcing a higher degree of binding affinity for the target (**Table 47**). This hypothesis was confirmed through the observation of improved DNA gyrase supercoiling inhibition activity of REDX10359 **90**. Gratifyingly, the results reinforced the merits of a computational approach to compound selection, which indicated greater space-fit for the active site could be tolerated with a larger ring size, and that lipophilicity in this area of the ligand may result in increased binding affinity.

3.7.3.4   Stability studies of 6-membered phenyl lactones

Encouraged by the improved antibacterial activity of the 6,6-phenyl lactone scaffold, human plasma stability was of key importance for understanding the structure-stability relationship of the series.

Redx No.	REDX10141 **59**	REDX10359 **90**
Human plasma stability (100% plasma, % remaining after 2 h)	96%	100%

Comparison of stability profiles for REDX10141 **59** and REDX10359 **90**.

Table 48

It was observed that both REDX10141 **59** and REDX10359 **90** were stable within human plasma (**Table 48**). The lack of metabolism found upon incubation with human plasma suggested an increased lactone ring size was not an appropriate modification to improve the plasma instability, challenging the existing literature surrounding hydrolysable paraoxonase substrates. As a result of computational assessment of the 6,6-phenyl lactone system, no striking steric clashes were observed between the ligand and the active site of paraoxonase. However, it could hypothesised that the increased steric bulk of the larger fused system may subtly prevent efficient binding to the active site of paraoxonase, preventing metabolism from occurring. The slight change in steric bulk could be minimal, precluding its observation in the molecular dynamics simulations. Furthermore, no metabolic rates of fused systems identical to the lactones in question have been described in the literature, further complicating the understanding of the experimental results.

As no steric clashes with the active site of paraoxonase were observed throughout the current computational effort, a possible modification of the electronics of the lactone ring system could be an unfortunate detrimental result of the increase in ring size. In order to assess the potential differences in electronic nature of the 6,5- and 6,6-lactone rings, computational analysis using Spartan'14 allowed possible changes in electronic density to

be estimated. A ground state equilibrium geometry optimisation was performed on REDX10141 **59** and REDX10359 **90**, initially using semi-empirical AM1 to find a starting geometry, then density functional theory (DFT) at the B3LYP/6-31G* level to obtain a more accurate equilibration geometry. Both calculations were performed with the ligand in a vacuum, assuming a neutral charge.

REDX10141 **59**	REDX10359 **90**
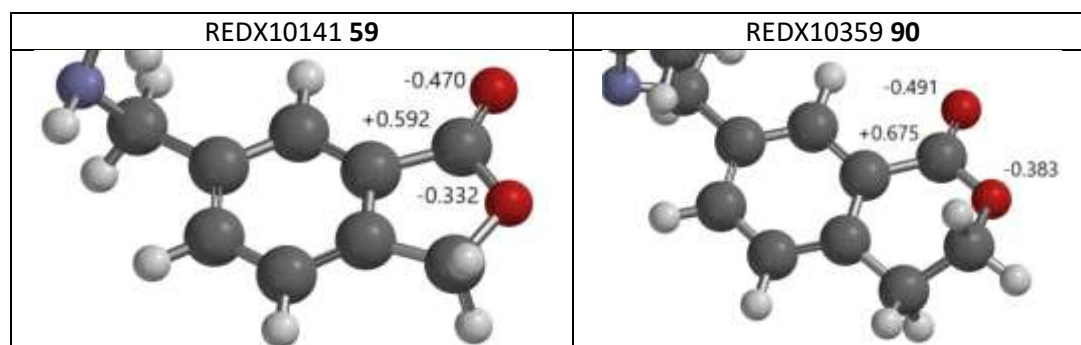
Lowest energy geometry (using Spartan'14, (v1.1.10)) of REDX10141 **59** and REDX10359 **90**, highlighting the differing charge on the carbonyl carbon with varying lactone ring size.

Figure 56
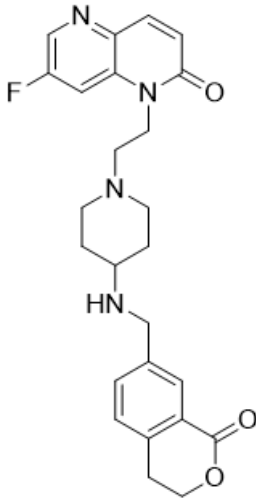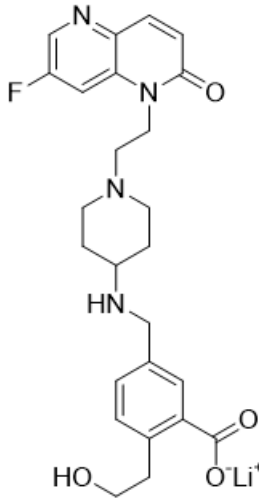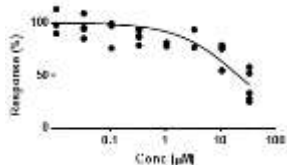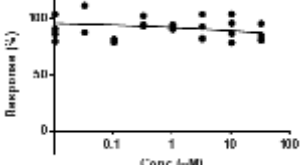
It was predicted from the computationally derived geometry that REDX10141 **59** had less polarised lactone oxygen atoms, resulting in a lower partial positive charge residing on the lactone carbonyl-carbon atom (**Figure 56**). Consequently, this should infer a higher affinity for the lactone carbonyl in REDX10359 **90** to be attacked by a nucleophile. However, this was not observed experimentally, with no appreciable difference in the percentage of parent remaining after 2 hours being recorded.

Alternatively, as a result of the in-house generated experimental data, differences in metabolic rate could tentatively be attributed to trends in lipophilicity. It could be postulated that a change in $logD_{7.4}$ for the 6-membered lactones may result in a change in metabolic rate, as observed for similar analogues of REDX10141 **59** (**Section 3.7.1.4**).

Further work in this area would be required to rationalise the observed trends. In particular, the stability of additional 6,6-phenyl lactone analogues, and a crystal structure of the ligand within paraoxonase could aid rationalisation of the observed experimental results. However, as high human plasma stability was undesirable for the research project, no further investigation into the stability of the 6,6-phenyl lactone series was initiated. Conversely, understanding toxicity trends for the series was deemed worthwhile and may aid future compound selection.

3.7.3.5 Toxicity studies of 6-membered phenyl lactone series

To increase the understanding of cytotoxicity and cardiotoxicity trends for the soft drug series', REDX10403 **92** was successfully prepared (**Section 3.4.8**) and profiled in comparison to the parent compound REDX10386 **91** for hepG2 cell viability and hERG inhibition.

Redx No.	REDX10386 **91**	REDX10403 **92**
	"Parent"	*"Metabolite"*
Structure		
hepG2 (CC_{50})	> 128 µg/mL	> 128 µg/mL
hERG (IC_{50})	20.6 µM	> 33 µM
hERG inhibition profile		

Cytotoxicity and cardiotoxicity results for REDX10386 **91** and REDX10403 **92**.
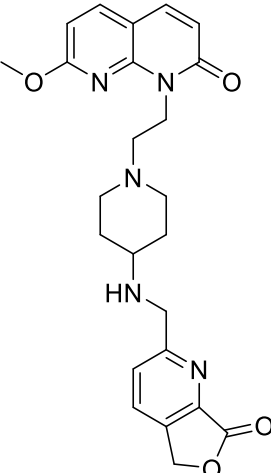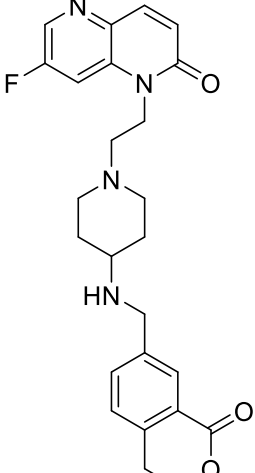
Table 49

Gratifyingly, both REDX10386 **91** and its suspected metabolite **92** were found to show no cytotoxicity when incubated with hepG2 cells (**Table 49**). Furthermore, the reduction in hERG channel inhibition observed between the parent and suspected metabolite provided additional evidence for the merits of a soft drug approach to reducing the cardiotoxicity of a series.

3.7.3.6 Summary of research progress

In order to highlight the progress made throughout the research project, a first generation compound (REDX08220 **23**) and a second generation compound (REDX10386 **91**) were compared for their suitability as a soft drug against the predefined target criteria (**Table 50**).

The potency of the soft drug compounds were successfully improved to satisfy the target criteria for antibacterial activity, yielding compounds with activity against the target pathogens of ≤ 1 μg/mL. More importantly, the stability of the scaffold was improved, preventing premature degradation in buffered conditions, simplifying the collection of physiochemical and stability data. As a result of the increased chemical stability, the unfortunate consequence of higher plasma stability has also been observed. Overall, this was determined to be the key parameter required to progress the soft drug series further.

Redx No.		REDX08220 **23**	REDX10386 **91**
Structure	Target criteria		
MIC (μg/mL) S. aureus ATCC29213	≤ 1	0.5	0.12
MIC (μg/mL) S. pneumoniae ATCC49619	≤ 1	2	0.12
MIC (μg/mL) H. influenzae ATCC49247	≤ 1	16	1
MIC (μg/mL) P. aeruginosa ATCC27853	(or ≤ 1)	> 64	16
Stability to buffered conditions	Stable	69% parent remaining after 5 h	Stable
Plasma stability (% parent remaining after 2 h)	< 50%	55%	94%
S9 lung fraction stability	Stable	Stable	Stable
hepG2 (CC$_{50}$, μg/mL) Parent	> 128	> 128	> 128
hepG2 (CC$_{50}$, μg/mL) Metabolite	> 128	> 128	> 128
hERG (IC$_{50}$, μM) Parent	-	> 33	20.6
hERG (IC$_{50}$, μM) Metabolite	> 33	> 33	> 33

Project progress from initial hit compound REDX08220 **23** to REDX10386 **91**.
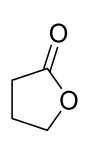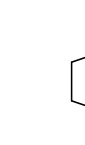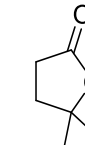
Table 50

Due to the high plasma stability of the 6,6-phenyl lactone series, no further optimisation was performed on this scaffold. Instead, alternative southern groups which could be used to improve the metabolic profile were prioritised. Computational- and literature-guided

methods were utilised to optimise the synthetic effort, challenging the structure-activity and structure-stability relationships of the series.

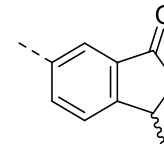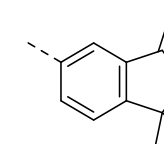### 3.7.4 3-methyl and 3,3-dimethyl phenyl lactone series'
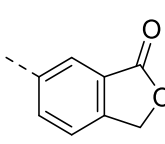
Building on the previously investigated southern group modifications, a method of optimising the metabolic instability of the phenyl lactone portion was still required. The promising antibacterial activity of REDX10306 **76** provided a suitable starting point, from which alterations could be made to encourage plasma instability. Examination of the literature surrounding paraoxonase-metabolised substrates, and monitoring for trends that were reported, allowed potential modifications to be highlighted. As a result, a possible method of increasing the hydrolytic nature of the southern lactone was proposed, emanating from work published by Draganov *et al.*[86]

Substrate			
PON1 activity (μmol of substrate metabolised/min)	32	45	N/A

PON1 activity of γ-butyrolactone **118**, γ-valerolactone **120** and γ-isocaprolactone **121**.[86]

Table 51

It was found that methylation of the 5-position of γ-butyrolactone **118** resulted in increased metabolic activity of the substrate (**Table 51**). However, the result of dimethylation at the 5-position, yielding lactone **121**, was unreported. As with the 6,6-phenyl lactone series, no direct comparison in the literature was available, however, a similar trend was proposed (**Table 52**), warranting further assessment of the targets.

	REDX10306 **76**	REDX10371 **106**	REDX10388 **117**
Substrate			
Human plasma stability (% parent remaining after 2 h)	75%	*Unknown, but hypothesised to be <100%*	*Unknown*

Percentage of substrate remaining for REDX10306 **76**, REDX10371 **106** and REDX10388 **117**, when incubated with human plasma.

Table 52

Importantly, although the introduction of a methyl group at the 3-position may increase metabolic instability, the introduction of a stereogenic centre could also increase the complexity of the evaluation of the targets. Careful consideration to each enantiomer would have to be given, to allow a balanced assessment of the target compounds. Furthermore, it was acknowledged that methylation and dimethylation would increase the steric bulk of the lactone. Therefore, evaluation of the proposed modifications to the target were first computationally undertaken, allowing initial understanding of the binding to DNA gyrase subunit A and paraoxonase independently, prior to initiation of the synthesis.

3.7.4.1 Assessment of 3-methyl phenyl lactone series in DNA gyrase

Upon selection of potential modifications to the soft drug scaffold, assessment was continued with computationally simulated overlays being generated for the new targets in the crystal structure of DNA gyrase subunit A (PDB: 2XCS[36]). Particular attention would be paid to the steric effect of adding subsequent methyl groups to the lactone ring, and whether this induced a steric clash with the lipophilic residues in the active site.
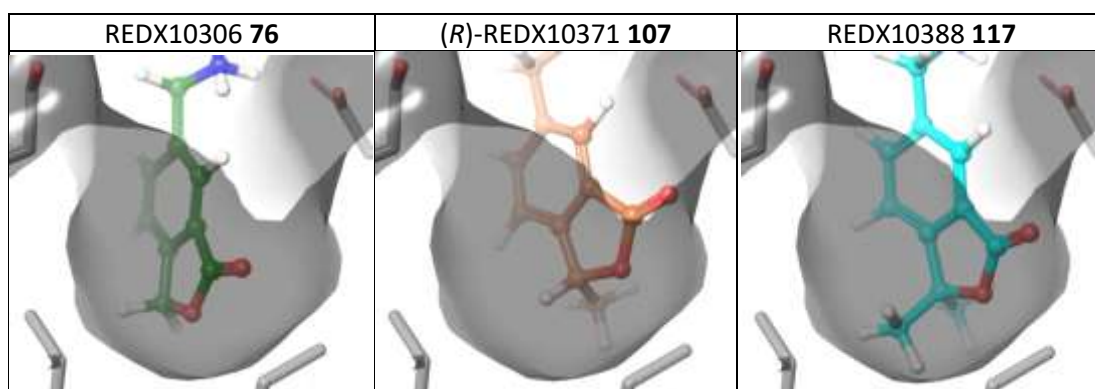
| REDX10306 **76**	(*R*)-REDX10371 **107**	REDX10388 **117**

Computationally derived binding poses for 6,5-phenyl lactone (REDX10306 **76**, green, left) 3-methylated ((*R*)-REDX10371 **107**, orange, centre) and 3,3-dimethylated analogues (REDX10388 **117**, blue, right) in DNA gyrase (PDB: 2XCS[36]), visualised using Maestro (v10.6).

Figure 57

It was observed from the computational overlays that methylation and dimethylation increased the steric bulk of the ligand, as expected (**Figure 57**). However, the result of 3-methylation was hypothesised to be tolerated within the active site of DNA gyrase, and no major steric clashes were observed. Although (*S*)-REDX10371 **108** was not explicitly modelled, it was proposed that it would be equally tolerated due to the symmetrical nature of the DNA gyrase binding pocket (**Section 2.1**). Additionally, the introduction of non-polar substituents in the lipophilic pocket may increase the affinity of the compound for the

active site, causing a potential increase in antibacterial activity. It could be postulated that REDX10388 **117**, the result of 3,3-dimethylation of REDX10306 **76**, may cause a subtle clash with the active site, however, this was not conclusive. As no major prohibitive interactions were observed between the hypothesised compounds and the active site of DNA gyrase, further computational assessment of the soft drug targets was continued within a paraoxonase model system.

3.7.4.2   Assessment of 3-methyl phenyl lactone series in paraoxonase

The resulting overlays of REDX10306 **76**, (*S*)-REDX10371 **108** and REDX10388 **117** within the active site of paraoxonase (PDB: 3SRG[73]) are shown in **Figure 58**.
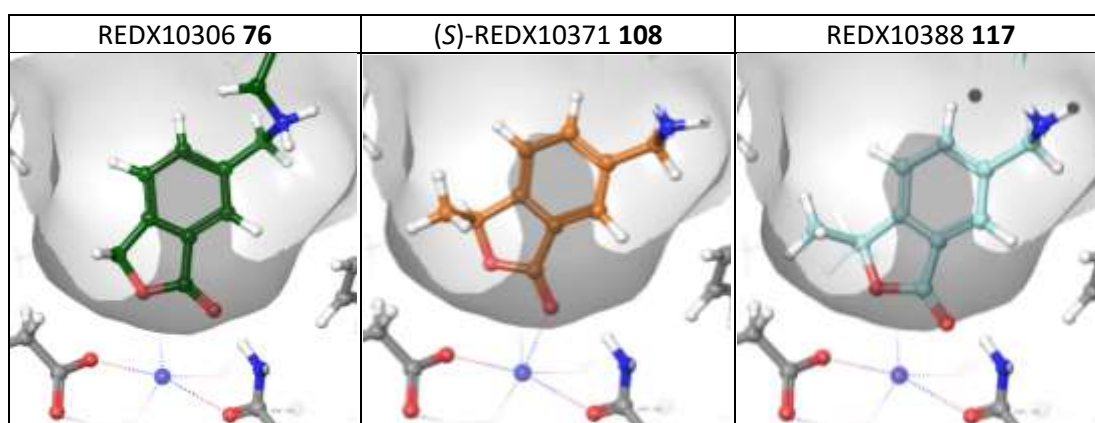
REDX10306 **76**	(*S*)-REDX10371 **108**	REDX10388 **117**

Computationally derived binding poses for 6,5-phenyl lactone (REDX10306 **76**, green, left), 3-methylated ((*S*)-REDX10371 **108**, orange, centre) and 3,3-dimethylated derivative (REDX10388 **117**, blue, right) in paraoxonase (PDB: 3SRG[73]), visualised using Maestro (v10.6).

Figure 58

It was observed that subtleties in the steric bulk of the lactone containing region of the scaffold may have a large influence on the ability of the compound to bind to the active site of paraoxonase. The non-decorated compound, REDX10306 **76**, was hypothesised to fit the confines of the active site. Furthermore, the 3-methylated compound, (*S*)-REDX10371 **108**, challenged the steric confines of the active site, but seemed to be tolerated. Importantly, the 3,3-dimethylated compound, REDX10388 **117**, was found to be too bulky for the active site, with the methyl groups and lactone carbonyl observed to protrude against the computationally simulated surface. Although this effect was subtle, the metabolic rate of REDX10388 **117** may be effected by the increase in bulk observed through 3,3-dimethylation, preventing access to the active site of paraoxonase, or through sterically

preventing the attack of water to the carbonyl through blocking the Bürgi-Dunitz angle of attack. Further assessment of each enantiomer of REDX10371 **106** proceeded, to generate a hypothesis as to which isomer could be preferentially degraded by paraoxonase.

(*R*)-REDX10371 **107**	(*S*)-REDX10371 **108**
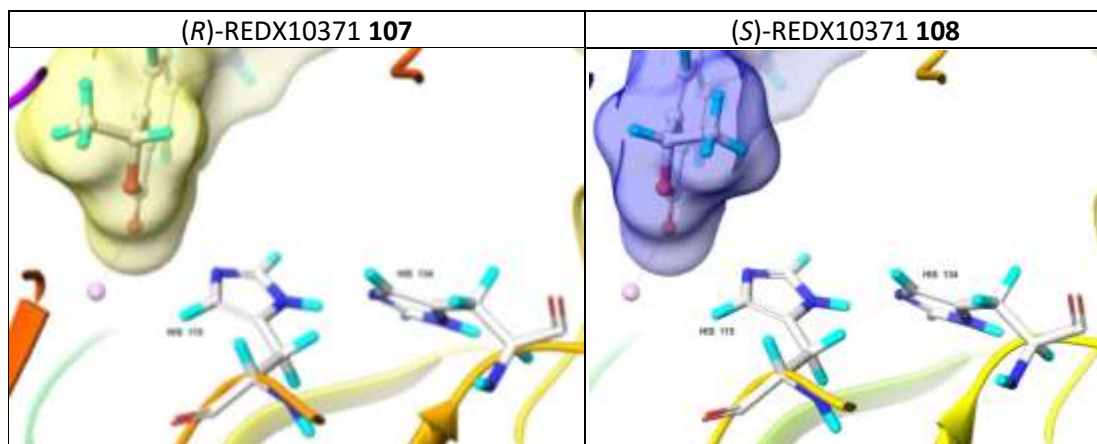
Simulated binding poses for (*R*)-REDX10371 **107** (yellow surface, left) and (*S*)-REDX10371 **108** (blue surface, right) in paraoxonase (PDB: 3SRG[73]), visualised using Maestro (v10.6).

Figure 59

Although the exact mechanism of substrate hydrolysis by paraoxonase is the subject of debate, the generally accepted mechanism involves the shuttling of a water molecule from His115 to the reactive carbonyl centre of the ligand. It was therefore hypothesised that minimising steric bulk near His115 may result in a more rapidly hydrolysed substrate. Thus, (*S*)-enantiomer **108** seemed to project steric bulk into a space that may prevent efficient attack of the water molecule, whereas (*R*)-enantiomer **107** may encourage hydrolysis by removing this hindrance (**Figure 59**). However, due to complexities in synthesis, and in order to provide evidence to support the computational effort, both isomers were prepared according to the method outlined in **Section 3.4.9**, and their separation was undertaken by chiral supercritical fluid chromatography (**Section 3.4.10**).

Following the separation of both enantiomers, absolute configuration was required. Due to limitations in being able to obtain crystals of sufficient quality for X-ray crystal structure analysis, an alternative method of structural determination was necessary. Optical rotation was utilised to tentatively assign each enantiomer, on the assumption that their optical rotation paralleled the optical rotation of similar analogues from the literature. Substituted (*R*) and (*S*) analogues were observed to have the same direction of optical rotation; negative rotation for (*S*)-enantiomers and positive rotation for (*R*)-enantiomers (**Table 53**).

(S)-enantiomers					(R)-enantiomers				
	Ref.	%ee	[α]	Conc. (g/100 mL)		Ref.	%ee	[α]	Conc. (g/100 mL)
H	87	99	-39.5	1	H	88	95	+37.1	0.83
Me		99	-36.0		Me		97	+31.8	0.84
F		99	-19.6		Cl		93	+32.9	1.44
Cl		99	-33.7		Br		93	+34.7	0.68
NO$_2$	89	93	-28.6	0.37	CO$_2$Et		93	+20.4	0.91
CO$_2$Me		95	-27.2	0.50	All literature values measured in CHCl$_3$ as a solvent				
C(CH$_3$)$_3$		98	-28.3	1.63					
OMe	87	99	-17.4	0.50					

Measured optical rotation values for enantiomers of phenyl lactone fragment.

Table 53

It was acknowledged that this method of assignment could not conclusively prove absolute configuration. However, as clear trends were observed from the literature, the compounds were cautiously assigned (R) and (S) on the basis of direction of their optical rotation (**Table 54**). The enantiomer with the negative alpha value was tentatively assigned as (S)-REDX10371 **108**, whereas the positive alpha value was tentatively assigned as (R)-REDX10371 **107**. Antibacterial analysis of the compounds could then proceed.

(S)-REDX10371 **108**	(R)-REDX10371 **107**
$[\alpha]_D^{20}$= -10.2 at 0.171 g/100 mL	$[\alpha]_D^{20}$ = +13.7 at 0.168 g/100 mL

Tentative assignment of enantiomers based on direction of optical rotation.

Table 54

3.7.4.3 Antibacterial activity of 3-methyl phenyl lactone series

Following the successful synthesis of alkylated compounds **106** and **117** (**Section 3.4.9** and **Section 3.4.12**), their antibacterial properties were determined (**Table 55**). Comparison against REDX10306 **76** allowed trends in activity to be highlighted.
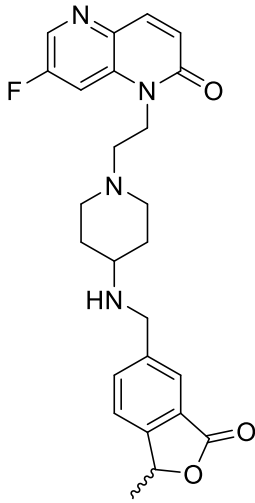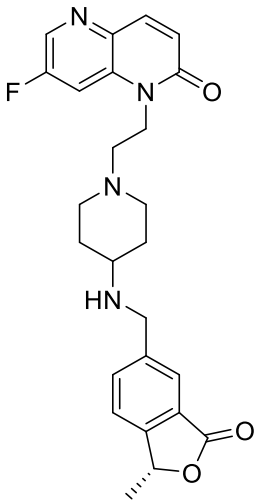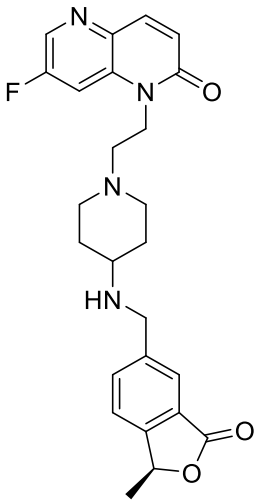
Redx No.		REDX10306 **76**	REDX10371 **106**	REDX10388 **117**
Structure				
MIC (µg/mL)	*A. baumannii* NCTC134203	4	0.25	1
	E. coli ATCC25922	4	0.5	2
	H. influenzae ATCC49247	1	0.5	1
	K. pneumoniae ATCC70060	64	16	64
	P. aeruginosa ATCC27853	64	16	32
	S. aureus ATCC29213	0.25	0.12	0.12
	S. pneumoniae ATCC49619	0.5	0.12	0.12
	E. coli W4573	4	0.5	1
	E. coli N43	< 0.06	0.015	0.06
Measured logD$_{7.4}$		0.1 (estimate)	0.43	0.84

Antibacterial properties for REDX10306 **76**, REDX10371 **106** and REDX10388 **117**.

Table 55

The antibacterial results proved that the additional steric bulk of the ligand was not only tolerated within the active site of DNA gyrase, but preferred. The potency was found to improve approximately 2 to 3-fold against the majority of tested pathogens, agreeing with the proposed effect of incorporating lipophilic moieties within the southern pocket of DNA

gyrase. Furthermore, increasing the logD$_{7.4}$ of the analogues may have resulted in higher bacterial permeability, increasing potency. The antibacterial activities of REDX10371 **106** and REDX10388 **117** were in line with the predefined target profile for a potential soft drug, as determined at the start of the research programme (**Section 2.10**). Profiling of the 3-methylated series continued by assessing each enantiomer of REDX10371 **106** (as obtained in **Section 3.4.10**) against the panel of bacterial isolates, including strains of antibiotic resistant *S. aureus* (**Table 56**).

Redx No.		REDX10371 **106**	(*R*)-REDX10371 **107**	(*S*)-REDX10371 **108**
Structure				
MIC (µg/mL)	*A. baumannii* NCTC134203	0.25	0.5	0.25
	E. coli ATCC25922	0.5	0.5	0.5
	H. influenzae ATCC49247	0.5	0.5	0.25
	P. aeruginosa ATCC27853	16	8	8
	S. pneumoniae ATCC49619	0.12	0.06	0.06
	S. aureus ATCC29213	0.12	0.06	0.12
	S. aureus VRS8	-	0.06	0.06
	S. aureus NRS482	0.12	0.12	0.25

Comparison of antibacterial properties for the racemate and both enantiomers of REDX10371 **106**, against the bacterial panel, including drug-resistant strains of *S. aureus*.

Table 56

Enantiomers **107** and **108** were found to be within one-fold as active against the tested bacterial strains, highlighting the non-discriminatory nature of the symmetrical NBTI binding site (**Section 2.1**). To reinforce the merits of targeting a non-fluoroquinolone

binding site, two strains of *S. aureus* were selected with differing resistance profiles, in order to determine if any cross-resistance was observed. *S. aureus* VRS8 is known to be a multi-drug resistant strain of MRSA, which has grown resistance to both vancomycin and clinically utilised fluoroquinolones. *S. aureus* NRS482 is a similarly resistant strain, which is resistant to erythromycin and fluoroquinolones. Potency was retained against the resistant strains, suggesting an alternative to the fluoroquinolone binding site was being targeted. The ability to maintain activity against relevant drug-resistant bacterial strains was an important milestone for the research project, reinforcing the merits of targeting a novel binding site. Subsequently, the synthesis of the hypothesised metabolites (**Section 3.4.11**) highlighted the reduction in antibacterial activity observed upon lactone hydrolysis.

Redx No.		REDX10725 **109**	(*R*)-REDX10725 **110**	(*S*)-REDX10725 **111**
Structure				
MIC (µg/mL)	*A. baumannii* NCTC134203	32	32	32
	E. coli ATCC25922	64	32	32
	H. influenzae ATCC49247	32	32	16
	P. aeruginosa ATCC27853	> 64	> 64	> 64
	S. pneumoniae ATCC49619	4	2	4
	S. aureus ATCC29213	8	4	32
	S. aureus VRS8	8	4	16
	S. aureus NRS482	16	8	32

Comparison of antibacterial properties for the racemate and both enantiomers of REDX10725 **109**, against the bacterial panel, including drug-resistant strains of *S. aureus*.

Table 57

The potency of hydrolysed compounds **109 – 111** confirmed a large drop in antibacterial activity, consistent with the soft drug targeting strategy. However, it was observed that antibacterial activity was not completely removed upon hydrolysis. This was proposed to be due to the highly potent nature of the parent compound, resulting in residual activity remaining upon metabolism. Furthermore, the possibility of lactone re-formation during the assessment of antibacterial activity may result in potency being falsely attributed to the hydroxy-acids, although it would, in fact, be caused by the ring-closed material.

3.7.4.4   Frequency of resistance of 3-methyl phenyl lactone series

An important parameter to monitor in antibacterial drug discovery is the speed at which drug-resistant bacterial strains can emerge. In order to assess this, the frequency of resistance to a certain antibacterial is commonly determined through single passage of the bacterial culture, followed by testing the resultant mutants to a dose of antibiotic equal to multiples of the MIC. In essence, the assay measures the spontaneous emergence of resistant bacteria to a given antibiotic, allowing conclusions to be drawn regarding the rapidity of resistance emerging in a clinical setting. The result is given as a number, relating to the frequency at which resistance to the antibiotic arises. For example, in-house analysis of gepotidacin **9** yielded a frequency of resistance against *S. aureus* ATCC29213 of 2.03×10^{-7}, which refers to a single resistant strain in approximately every 20 million bacteria. In order to determine how a soft drug approach to antibacterial research may affect the observed frequency of resistance, REDX10370 **105** and REDX10387 **116** were selected for assessment, and compared to known antibacterial compounds ciprofloxacin **122** and gepotidacin **9** (**Table 58**).

It was observed that although the tested compounds were more susceptible to resistance mechanisms than ciprofloxacin **122**, which binds in the fluoroquinolone binding site, they were equally as susceptible as gepotidacin **9**, a GlaxoSmithKline NBTI-type compound, currently in Phase II clinical trials. Encouragingly, this data suggested a soft drug approach to antibacterial research did not detrimentally affect the frequency of emergence of resistant strains. One limitation to the study is the lack of information regarding the fitness and viability of the resistant mutants. This is particularly important as the mutation may be associated with an unacceptably high energy sacrifice, preventing the mutants from being able to be particularly virulent. Further studies would need to be performed in order to sequence the mutant strains and determine the mutation which results in resistance.

Ciprofloxacin **122**		
Gepotidacin **9**	REDX10370 **105**	REDX10387 **116**

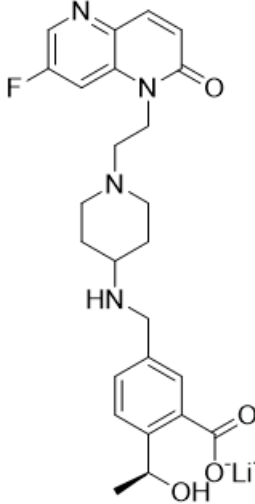| Compound	Frequency of Resistance (4 × MIC)
Ciprofloxacin **122**	4.45×10^{-9}
Gepotidacin (in-house data) **9**	2.03×10^{-7}
REDX10370 **105**	1.14×10^{-7}
REDX10387 **116**	9.30×10^{-8}
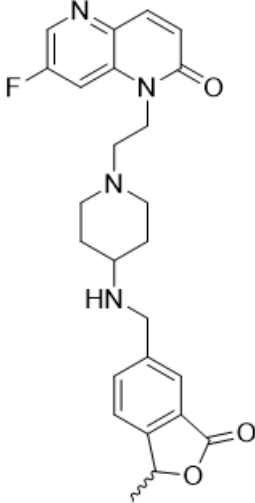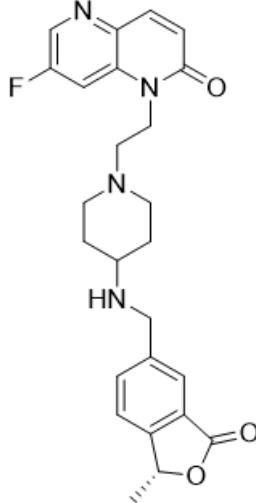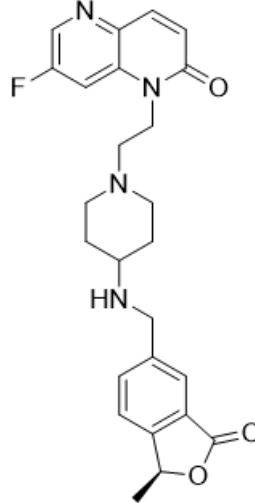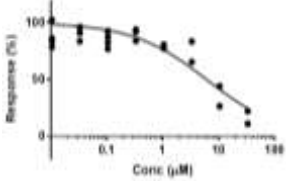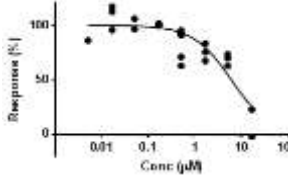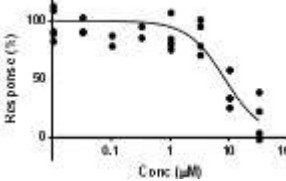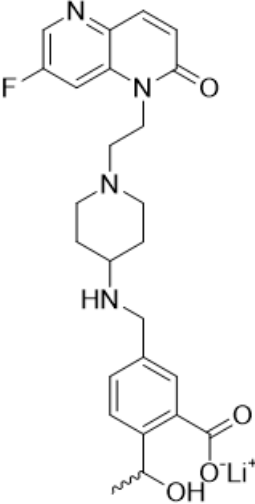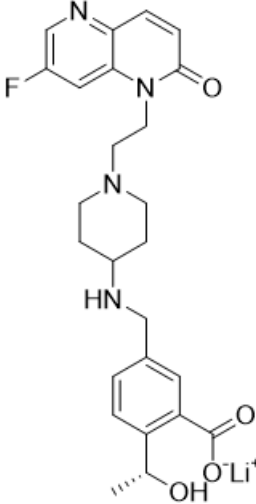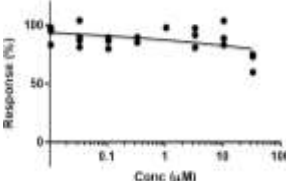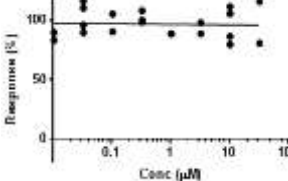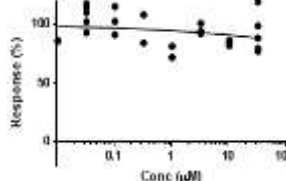
Frequency of resistance (*S. aureus* ATCC29213) for soft drug and literature compounds.

Table 58

Furthermore, frequency of resistance can be reduced by increasing the concentration of the compound. Although measuring the frequency of resistance is commonly performed at 4 times the minimum inhibitory concentration, when gepotidacin was tested at concentrations of 8 times the MIC, the frequency of resistance fell to $< 8.56 \times 10^{-9}$. This suggested higher blood levels of the drug could delay the emergence of resistance pathogens. Further testing of key soft drug analogues at higher concentrations could show similar trends, and would be required before a clinical candidate could be selected.

3.7.4.5 Toxicity of 3-methyl phenyl lactone series

Due to the positive influence of 3-methylation and 3,3-dimethylation on the antibacterial properties of the soft drug series, further assessment progressed. Cardiotoxicity (hERG channel inhibition) and cytotoxicity (hepG2 cell viability) were measured to determine the toxicity of the parent compounds in comparison to their suspected metabolites (**Table 59**).

Redx No.	REDX10371 **106**	(*R*)-REDX10371 **107**	(*S*)-REDX10371 **108**
Structure			
hepG2 (CC$_{50}$)	> 256 µg/mL	> 128 µg/mL	> 128 µg/mL
hERG (IC$_{50}$)	6.1 µM	6.0 µM	8.5 µM
hERG inhibition profile			

Redx No.	REDX10725 **109**	(*R*)-REDX10725 **110**	(*S*)-REDX10725 **111**
Structure			
hepG2 (CC$_{50}$)	> 256 µg/mL	> 128 µg/mL	> 128 µg/mL
hERG (IC$_{50}$)	> 33 µM	> 33 µM	> 33 µM
hERG inhibition profile			

Cytotoxicity and cardiotoxicity results for methylated lactone compounds.

Table 59

Gratifyingly, both the parents and suspected metabolites were found to show no cytotoxicity when incubated with hepG2 cells (**Table 59**). Furthermore, the reduction in hERG channel inhibition observed between a parent and suspected metabolite pair provided additional evidence for the merits of a soft drug approach to minimising the cardiotoxicity of a series. Importantly, each hydrolysed metabolite was found to be hERG inactive, with minimal inhibition being observed at the maximum concentration of 33 µM, highlighting the utility of such an approach.

3.7.4.6 Stability studies of 3-methylated phenyl lactone analogues

Encouraged by the antibacterial activity, toxicity and frequency of resistance profiles for the methylated lactone scaffolds, human plasma and S9 lung stabilities of the series' were measured to allow further development of the structure-stability relationship.

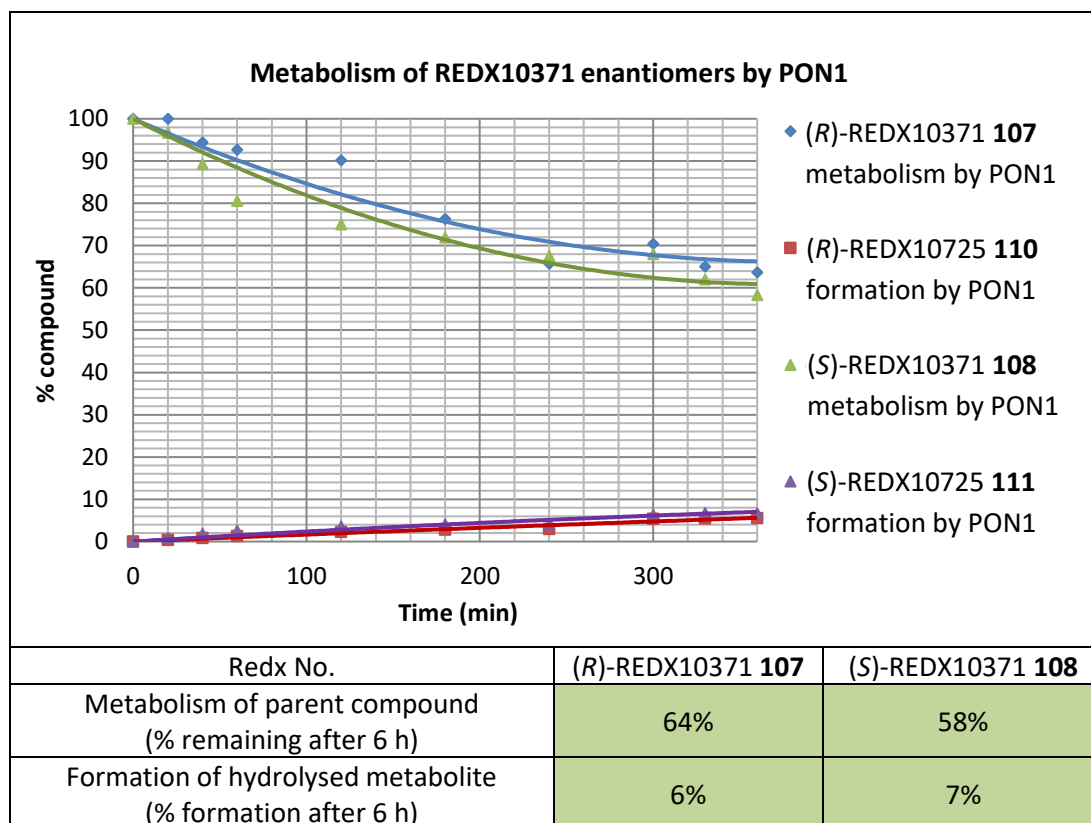| Redx No.	REDX10306 **76**	REDX10371 **106**	REDX10388 **117**
Human plasma stability (100% plasma, % remaining after 2 h)	75%	49%	100%
Human S9 lung fraction stability (5 mg/mL, % remaining after 2 h)	-	100%	-

Comparison of stability profiles for REDX10306 **76**, REDX10371 **106** and REDX10388 **117**.

Table 60

When incubated with human plasma, REDX10388 **117** was observed to be stable, whereas REDX10306 **76** was seen to be partially metabolised. Gratifyingly, REDX10371 **106** was found to be metabolised to a greater extent, with an approximate half-life of 2 hours (**Table 60**). In comparison, upon incubation with human S9 lung fraction, REDX10371 **106** was shown to be stable, with no metabolism being observed after 2 hours, reinforcing the strategy of selective targeting of a metabolising enzyme present in plasma but not in the lungs. This result was in agreement with the literature, which suggested methylation may increase the rate of metabolic decay.[86] Furthermore, evidence was obtained to support the computational model, which suggested 3,3-dimethylation may sterically prevent the attack of the carbonyl from a nearby water molecule.

(R)-REDX10371 **107**	REDX10388 **117**
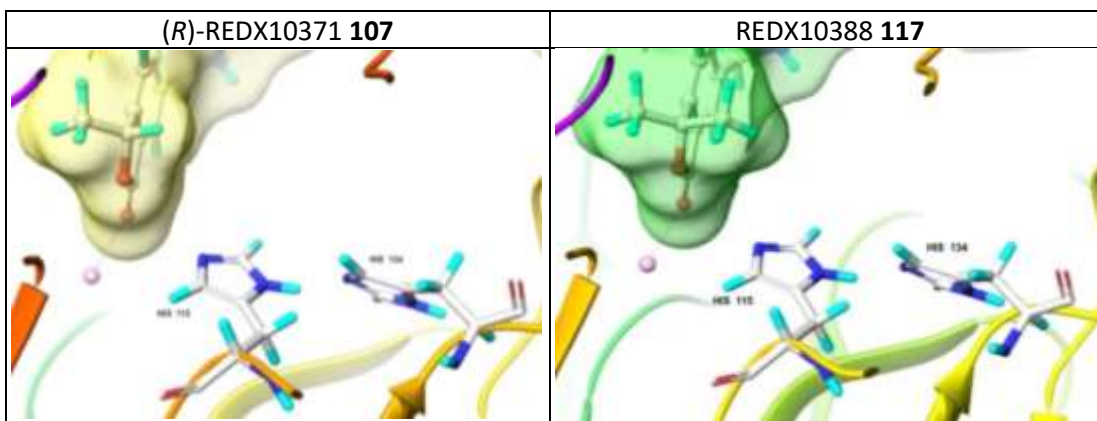
Simluations of (R)-REDX10371 **107** and REDX10388 **117** in paraoxonase (PDB: 3SRG[73]), visualised using Maestro (v10.6).

Figure 60

As observed from the computationally derived binding mode (**Figure 60**), the Bürgi-Dunitz angle of attack may be sterically blocked from by flanking methyl groups in REDX10388 **117**. However, due to the less sterically hindered conformation of (R)-REDX10371 **107**, the angle of attack is no longer obstructed. Furthermore, as previously suggested (**Section 3.7.4.2**), each enantiomer of REDX10371 **106** may be metabolised at different rates by paraoxonase, due to the natural chirality of enzymes, and the proximity to His115.

Redx No.	REDX10371 **106**	(R)-REDX10371 **107**	(S)-REDX10371 **108**
Human plasma stability (100% plasma, % remaining after 2 h)	49%	57%	72%
Human S9 lung fraction stability (5 mg/mL, % remaining after 2 h)	100%	100%	100%

Stability profiles for REDX10371 **106**, (R)-REDX10371 **107** and (S)-REDX10371 **108**.

Table 61

It was observed that both enantiomers degraded upon incubation with human plasma (**Table 61**). This result countered the prediction generated from the computational model, in which it was predicted that (S)-REDX10371 **108** may be stable due to the steric hindrance provided by the methyl group. The observed instability of (S)-REDX10371 **108** could indicate metabolism by other enzymes within the plasma, or could suggest the binding site within paraoxonase is more flexible, and therefore able to accommodate more steric bulk, than previously hypothesised. The steric confines of the active site could be assessed through increasing the steric bulk of the alkyl group by using alternatives such as ethyl, propyl or *iso*-

propyl groups. Additionally, obtaining an X-ray crystal structure of an NBTI-type inhibitor bound within paraoxonase would aid elucidation of the binding mode, and could explain the similarity in plasma instability between the enantiomers of REDX10371 **106**.

Encouraged by the differential stability profiles upon incubation with human plasma and human S9 lung fraction, the ability to develop the soft drug series relied on the ability to prove instability was due to paraoxonase-based metabolism. Although all experimental evidence thus far, combined with computational support, suggested metabolism by paraoxonase, this was to be confirmed by assessing stability against the isolated enzyme. As this type of stability assay was not routinely performed within the pharmaceutical industry, in-house development of conditions was undertaken, yielding a robust, useable and reliable assay. Due to the cost implications of obtaining isolated active paraoxonase enzyme, only the most promising compounds were assessed for their stability. (*R*)-REDX10371 **107** and (*S*)-REDX10371 **108** were therefore incubated with a buffered solution of paraoxonase enzyme and samples at each time point were taken and analysed for both the parent compound remaining, and the existence of the suspected metabolite.

Redx No.	(*R*)-REDX10371 **107**	(*S*)-REDX10371 **108**
Metabolism of parent compound (% remaining after 6 h)	64%	58%
Formation of hydrolysed metabolite (% formation after 6 h)	6%	7%

Paraoxonase stability for (*R*)-REDX10371 **107** and (*S*)-REDX10371 **108**.

Figure 61

It was determined that both enantiomers of REDX10371 **106** were unstable to paraoxonase, with a decrease in the parent compound concentration, and an increase in the concentration of the suspected metabolite, being observed (**Figure 61**). It could be hypothesised that other metabolites may be being formed due to the difference between the trends for metabolism of the parent compounds, and the formation of the metabolites. However, this was determined to be caused by the difference in chromophore strength between the parent and the metabolite, with the metabolite having a chromophore approximately 10 times weaker than the parent. Additionally, it would initially seem as though the compounds were more stable in paraoxonase than in human plasma. Due to limitations in obtaining functional paraoxonase enzyme from commercial suppliers, the exact concentration of the enzyme supplied was unknown. Furthermore, the concentration of paraoxonase within the plasma was also unknown, and would require full enzymatic profiling to determine the concentrations of each enzyme contained within the pooled plasma. As a result, the stability data for human plasma and paraoxonase cannot be compared, and should instead be utilised in parallel. The reported data, combined with the lack of hydrolysis within human S9 lung fraction, provided proof of concept that both enantiomers were substrates for paraoxonase, with additional proof being observed through the generation of the predicted ring-opened metabolite. The similar instability of both enantiomers reinforced the limitations in the paraoxonase computational model, and suggested a much higher level of flexibility within the active site of the enzyme than was previously hypothesised.

As a result of the high stability of (*S*)-REDX10371 **108** within human S9 lung fraction, and the observed paraoxonase-based metabolism, the compound was selected for an *in vivo* pharmacokinetics (PK) study, providing evidence to support the antibacterial soft drug hypothesis.

3.8 *In vivo* pharmacokinetics study of (*S*)-REDX10371 (108)

The positive *in vitro* results that were obtained for (*S*)-REDX10371 **108** allowed the investigation of *in vivo* pharmacokinetic (PK) properties of the series to follow. To ensure the most efficient use of the animal subjects in the study, the following aims were set, prior to designing the investigation:

1. Determine whether lung tissue concentrations following local delivery of (*S*)-REDX10371 **108** could be appropriately high to infer an antibacterial effect *in vivo*, whilst limiting systemic exposure to below anticipated toxic levels.
2. Provide evidence to support the hypothesis that low systemic exposure was a result of paraoxonase-based metabolism of (*S*)-REDX10371 **108**, leading to formation of the suspected metabolite, (*S*)-REDX10725 **111**.

As a result, a PK study was designed to challenge the aims, which was split into two smaller investigations. In the first, mice were dosed intravenously (IV) with (*S*)-REDX10371 **108** (2 mg/kg) whereas for the second portion of the study, intratracheal (IT) dosing (3 mg/kg) ensured maximal concentrations of the parent compound entering the lungs. Although intratracheal dosing would not be performed in a clinical setting, it was selected as the cleanest method of ensuring the majority of the dose went directly into the lungs of the mice. In order to comply with standard ethical practices, the number of mice used in the study was minimal (n = 3 for each time point), and the animals were observed throughout for any signs of ill health. During both portions of the study, the mice were euthanised at a range of time points (0.25, 0.5, 1, 2, 3, 6, 8 and 24 h), at which, plasma and lung tissue samples were collected. The samples were then analysed by LCMS for (*S*)-REDX10371 **108** and its suspected metabolite, (*S*)-REDX10725 **111**, allowing concentration-time profiles to be generated for analysis.

3.8.1 Intravenous dosing of (*S*)-REDX10371 (108)

Following intravenous dosing of (*S*)-REDX10371 **108** (2 mg/kg), plasma and lung tissue samples provided a method to study the concentration of the parent compound over the course of the study. Results were compared to an in-house investigation performed using GSK2140944 **9** (gepotidacin), an NBTI-type inhibitor currently in Phase II clinical trials (**Figure 62**).

Mean plasma and lung concentration-time profiles following IV dosing (2 mg/kg) of (*S*)-REDX10371 (108) and GSK2140944 (9)
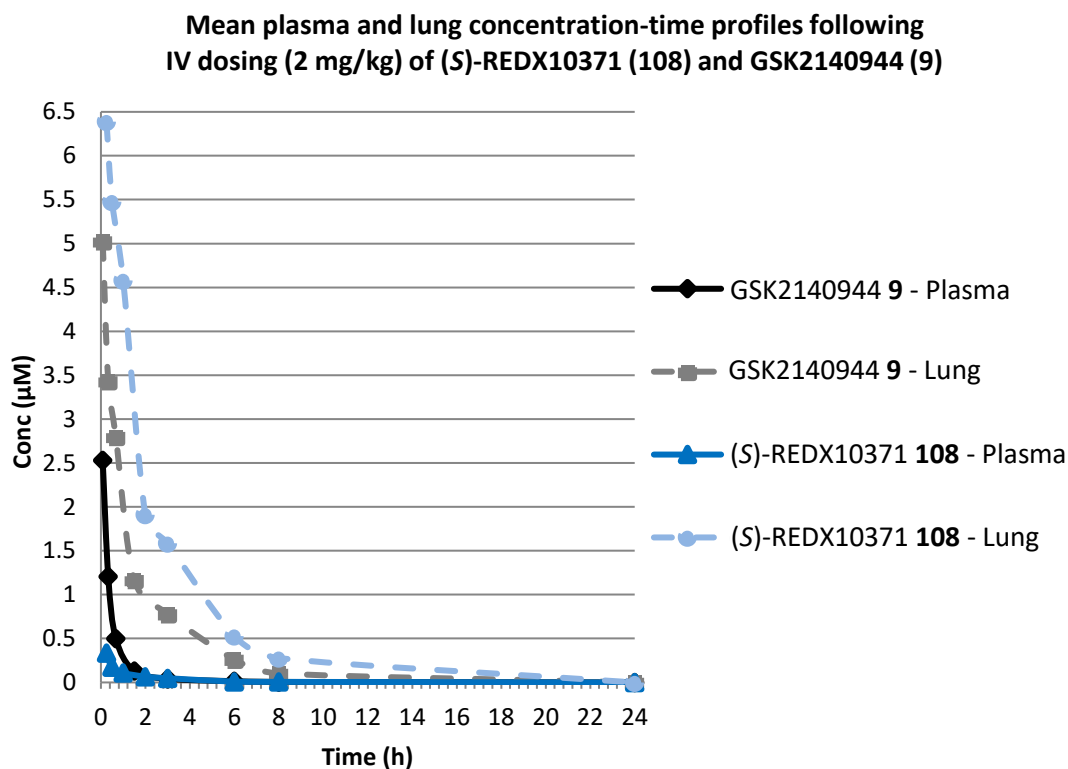
	GSK2140944 **9**		(*S*)-REDX10371 **108**	
	Plasma	Lung	Plasma	Lung
$t_{1/2}$ (h)	1.50	1.85	1.62	1.98
AUC (ng.h/mL)	664.8	3301.4	221.2	6621.7

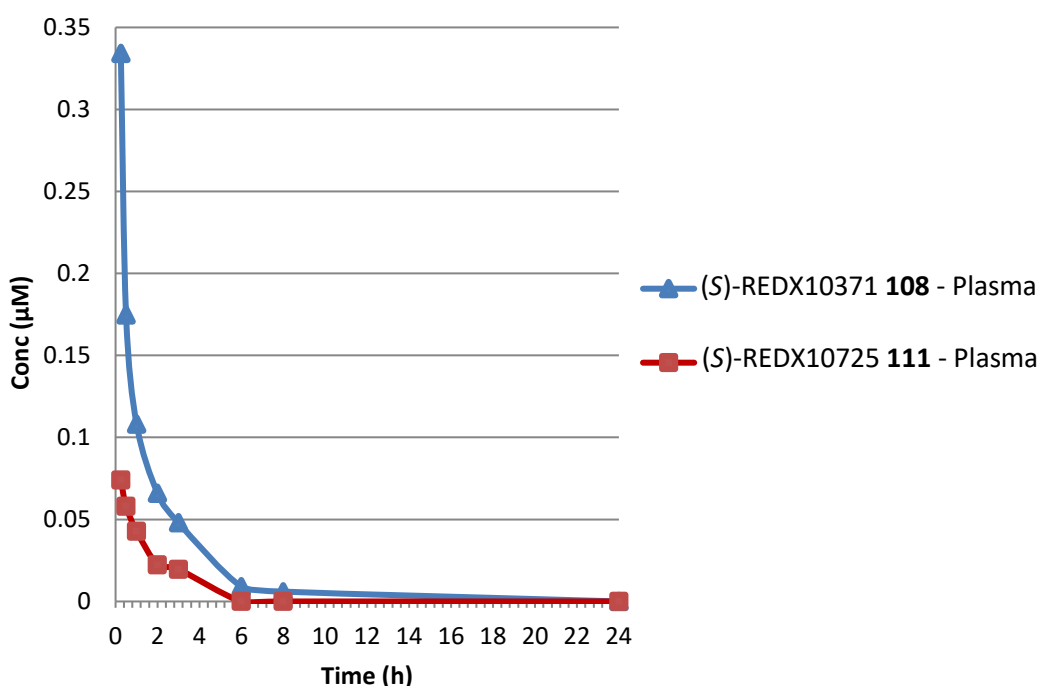Plasma and lung concentration-time profiles following IV doses of (*S*)-REDX10371 **108** and GSK2140944 **9**.

Figure 62

Although the given dose was predicted to be lower than that necessary to be therapeutically effective, no ill health was observed in the mice throughout the course of the study, providing an early positive indication of low toxicity. Both compounds were observed to accumulate within the lungs of the mice following an IV dose, resulting in a higher concentration of compound being observed in the lung tissue than in the plasma (**Figure 62**). This was hypothesised to be a serendipitous result of the structure and polarity of the NBTI scaffold. It was considered that the compound may pass easily from the blood into the lungs (aided by the large blood flow available to the lungs), however the physiochemical properties prevented its immediate re-entry to the systemic circulation, resulting in higher concentrations observed within the lung tissue than the plasma. Additionally, hepatic and plasma-based metabolism may decrease the concentration of (*S*)-REDX10371 **108** in the systemic circulation, increasing the difference between the

observed concentrations. As it was envisioned that a successful antibacterial soft drug would be dosed *via* an inhaler to minimise plasma-based metabolism, this trend, although positive, was deemed of minimal importance.

More significantly, the exposure, as indicated from the area under the curve (AUC), was observed to be approximately 66% lower for (*S*)-REDX10371 **108** (221.2 ng.h/mL), compared to GSK2140944 **9** (664.8 ng.h/mL) (**Figure 62**). This data reinforced the potential ability of a soft drug approach to minimise systemic exposure, and was deemed an important milestone for the project.

Mean plasma concentration-time profiles following IV dosing (2 mg/kg) of (*S*)-REDX10371 (108)

	(*S*)-REDX10371 **108**	(*S*)-REDX10725 **111**
$t_{1/2}$ (h)	1.62	1.21
Clearance (mL/min/kg)	146.4	-
AUC (ng.h/mL)	221.2	60.9

Plasma concentration-time profiles for (*S*)-REDX10371 **108** and (*S*)-REDX10725 **111** following an IV dose of (*S*)-REDX10371 **108**.

Figure 63

Throughout the IV study, the concentration of (*S*)-REDX10371 **108** was observed to rapidly decrease in the plasma (**Figure 63**). In order to elucidate whether clearance could be rationalised by metabolism by the liver, or if an extrahepatic component was contributing,

the clearance of (*S*)-REDX10371 **108** was compared to literature values. Mouse liver blood flow has been reported to be 90 mL/min/kg,[90] however, clearance of (*S*)-REDX10371 **108** was measured to be 146.4 mL/min/kg. As the clearance was recorded to be higher than the maximum capable by the liver in a single pass, plasma-based metabolism was hypothesised to contribute to the additional metabolic component.

The concentrations of the parent soft drug were determined to near the minimum levels for quantification after 8 h, and have a $t_{1/2}$ of approximately 97 min. Importantly, (*S*)-REDX10725 **111** was also observed to be present in the plasma samples, providing evidence to support that metabolism of the southern ring was a prominent metabolic route. In order to clarify if other routes of metabolism were occurring, mass spectrometry guided metabolite identification was performed, confirming the only metabolite observed at a significant concentration was (*S*)-REDX10725 **111**. It was therefore assumed that due to the high polarity of (*S*)-REDX10725 **111**, biliary and urinary excretion was likely to result in its rapid elimination from the body. In future studies, parent excretion and metabolic routes could be understood further by collection of the bile and urine, and performing mass spectrometry analysis on these samples.

3.8.2 Intratracheal dosing of (*S*)-REDX10371 (108)

Performing a parallel study of (*S*)-REDX10371 **108** dosed intratracheally (3 mg/kg), allowed a more appropriate representation of drug levels to be presented, through mimicking a similar dosing regimen to that anticipated to be used within the clinic. Systemic exposure (as indicated from the AUC values) of the parent compound was observed to be approximately 40% lower when dosed intratracheally, highlighting that an IV dosing regimen was likely to result in higher systemic exposure, and therefore have a greater potential to be more hazardous in a clinical setting. Furthermore, even though a higher dose (3 mg/kg) was given during the IT study compared to the IV study (2 mg/kg), the systemic exposure was reduced. Comparison of IV and IT dosing regimens indicated that high levels of drug were achieved within the lung tissue, regardless of the route of administration (**Figure 64**).

**Mean plasma and lung concentration-time profiles following
IV (2 mg/kg) and IT (3 mg/kg) dosing of (*S*)-REDX10371 (108)**

Legend:
- (*S*)-REDX10371 **108** - IV - Lung
- (*S*)-REDX10371 **108** - IT - Lung
- (*S*)-REDX10371 **108** - IV - Plasma
- (*S*)-REDX10371 **108** - IT - Plasma
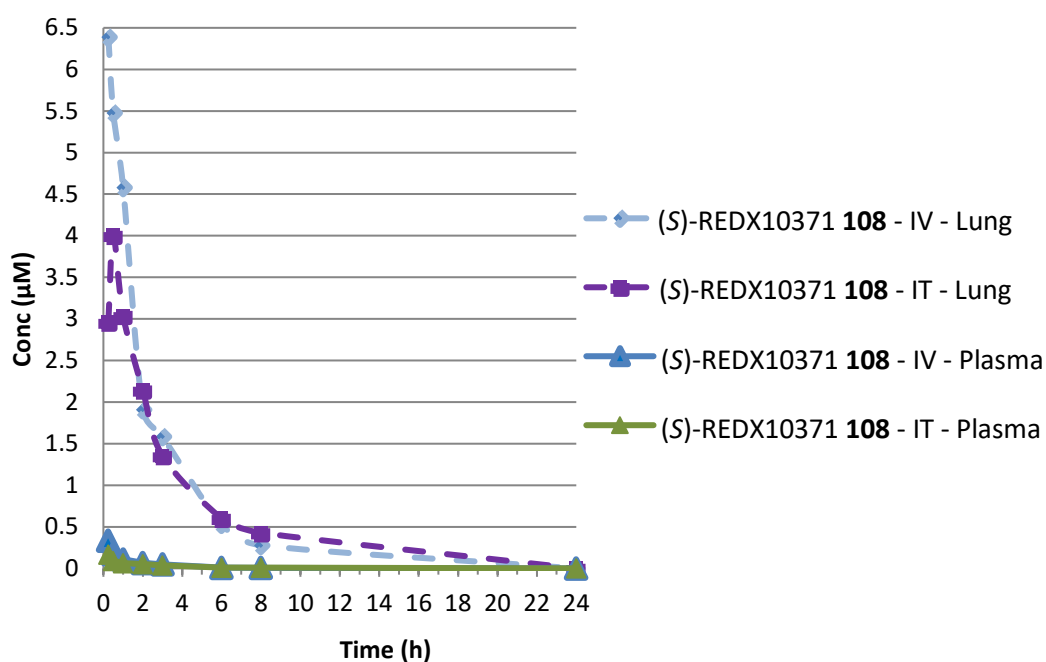
	Intravenous (*S*)-REDX10371 **108**		Intratracheal (*S*)-REDX10371 **108**	
	Plasma	Lung	Plasma	Lung
$t_{1/2}$ (h)	1.62	1.98	2.10	2.97
AUC (ng.h/mL)	221.2	6621.7	130.1	5092.7

Lung tissue concentration-time profiles following an IV or IT dose of (*S*)-REDX10371 **108**.

Figure 64

Following an IV dose, the drug compound will likely rapidly equilibrate throughout the bodily tissue. Due to the large blood supply available to the lungs, high levels of (*S*)-REDX10371 **108** were observed within the lung tissue following IV administration (**Figure 64**). As previously discussed, high lung tissue concentrations are commonly observed for NBTI-type compounds, regardless of their initial design as inhaled agents. For the IT dose, a well-defined initial absorption phase of the PK profile was observed, consistent with delayed tissue penetration following local delivery, and partial mucociliary airway clearance.

Furthermore, premature metabolism was not observed, with very low levels of (*S*)-REDX10725 **111** being observed within the lung tissue during the course of the investigation. The varying stability properties observed for (*S*)-REDX10371 **108** in the lung tissue compared to the plasma was indicative of metabolism by enzyme(s) present in the blood, but absent in the lungs. Combined with the known instability of the compound to

paraoxonase, as determined through incubation with the isolated enzyme, it was assumed that specific targeting of paraoxonase-based metabolism had been successfully achieved.

In order to highlight the potential merits of a soft drug approach to antibacterial research, systemic exposure to the toxic parent compound should be minimal. To illustrate the potential therapeutic window (green area) for (*S*)-REDX10371 **108**, the concentrations of parent compound in the lung tissue and the plasma were compared (**Figure 65**), along with boundaries indicating the antibacterial MIC for *S. aureus* (0.27 µM, yellow boundary) and the hERG IC_{50} (8.5 µM, red boundary).

Mean plasma and lung concentration-time profiles following IT dosing (2 mg/kg) of (*S*)-REDX10371 (108)
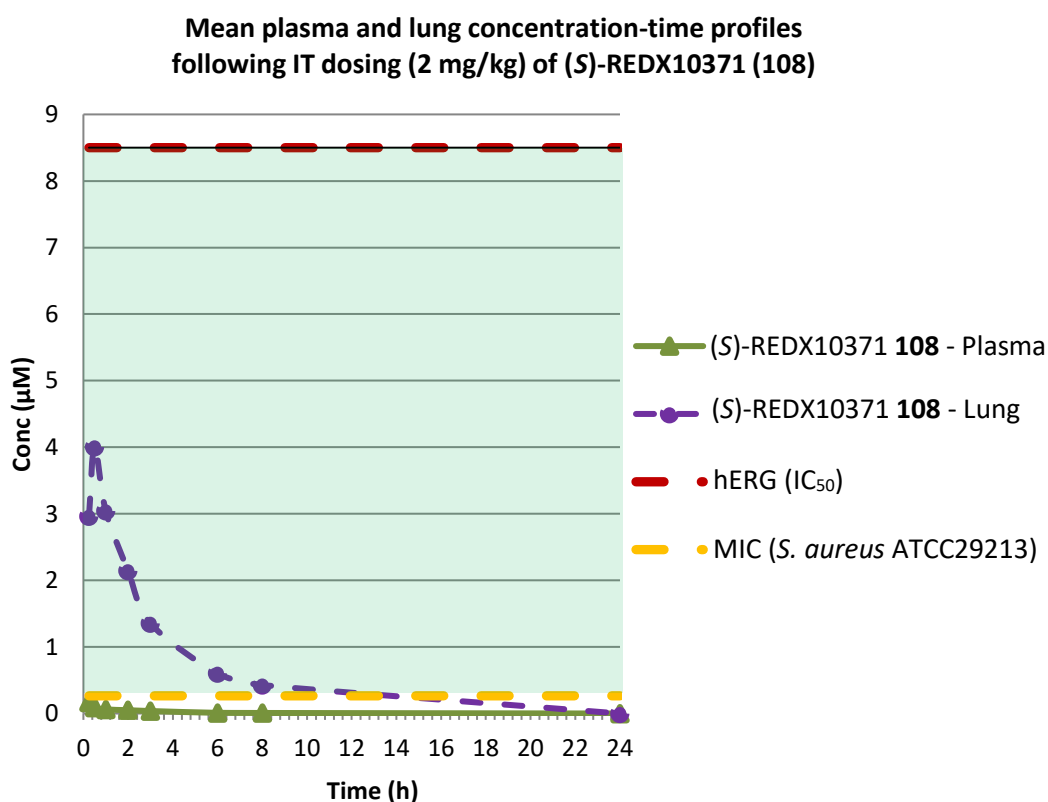
Plasma and lung tissue concentration-time profiles following IT dose of (*S*)-REDX10371 **108**.

Figure 65

The therapeutic window is thought of as a range of doses capable of producing a therapeutic response, without causing adverse effects. Therefore, the larger the difference between the MIC and the hERG IC_{50}, the larger the therapeutic window, and, in theory, the less toxic the drug. The levels of (*S*)-REDX10371 **108** in the lung tissue (purple line) were much greater than the MIC for *S. aureus* (yellow boundary), indicating a potential antibacterial effect *in vivo*. However, without performing an efficacy study, this cannot be confirmed. It was found that the maximum systemic concentrations of (*S*)-REDX10371 **108**

(green line) were approximately 50 times less than the hERG IC$_{50}$ (red boundary) (C$_{max}$ = 0.17 µM vs. hERG (IC$_{50}$) = 8.5 µM), providing compelling evidence of minimal risk of cardiotoxicity. However, further work would require increased doses in order to determine a therapeutically relevant dose *in vivo*. As a result of dose escalation, it should be expected that both the lung tissue and plasma levels of the parent compound will increase. Although the resulting lung tissue levels will likely be much greater than the hERG IC$_{50}$, as long as the plasma levels remain consistently lower than the hERG IC$_{50}$, the risks associated with cardiotoxicity should be reduced.

3.8.3 Summary of *in vivo* pharmacokinetics study

The antibacterial soft drug concept was challenged through intravenous and intratracheal dosing of the lead compound, (*S*)-REDX10371 **108**, and subsequent identification of parent and metabolite concentrations within the plasma and lung tissue at a series of time points.

Crucially, the concentration of (*S*)-REDX10371 **108** was observed to rapidly decrease in the plasma, which was accompanied by the appearance of the lactone-hydrolysed compound, (*S*)-REDX10725 **111**. After investigation into the metabolites formed during the study, no evidence was observed to support alternative metabolic routes, confirming lactone hydrolysis as the primary route of metabolism. This was consistent with paraoxonase-based metabolism, as indicated from the previously measured instability against the isolated paraoxonase enzyme. Levels of (*S*)-REDX10725 **111** were found to decrease throughout the experiment, concordant with swift excretion. Due to the highly polar nature of the metabolite, biliary and urinary excretion was presumed to be rapid.

In comparison to the unstable nature of (*S*)-REDX10371 **108** in the blood, lung tissue stability was observed to be high. This was determined through the low levels of (*S*)-REDX10725 **108** being observed within the lung tissue, and was consistent with the previously measured stability in human S9 lung fraction.

Finally, the low levels of (*S*)-REDX10371 **108** observed in the plasma following intratracheal dosing highlighted a therapeutic window for the lead compound. Although dose escalation studies would be required to determine an efficacious dose *in vivo*, the available data strongly indicated a soft drug approach could be a successful method of increasing the therapeutic window, by lowering systemic exposure to the toxic parent compound.

3.9   Conclusions

At the outset of the research programme, the possibility of generating a successful | soft drug antibacterial compound was theoretical.
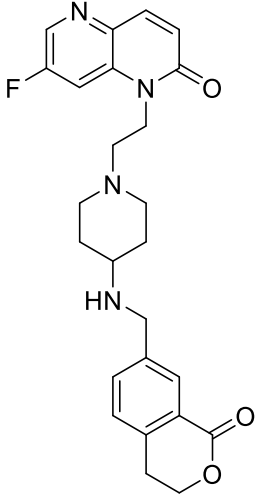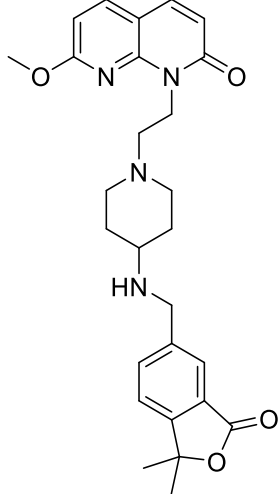
NBTI-type DNA gyrase inhibitors have gained considerable research interest throughout recent years, however, widespread hERG inhibition has broadly resulted in the termination of a variety of antibacterial chemical series. As a result, the hypothesis of generating a soft drug antibacterial compound originated *via* a thorough investigation of the literature surrounding both NBTI research and soft drug therapies.

Novel probe compounds were synthesised from intermediates that have not been reported in the literature, and were observed to have moderate antibacterial activity. Differing stability profiles in human plasma and in human S9 lung fraction provided early encouraging results of paraoxonase targeting. However, instability to phosphate buffer prompted a reinvestigation of the scaffold and allowed a second generation of compounds to be conceived. Building on the initial success of the research project, additional revised goals were set, in order to further develop the series towards drug-like chemical space.

With the aid of computational simulation, compounds were triaged in order to efficiently challenge and build meaningful structure-activity and structure-stability relationships. The synthetic route to second generation novel compounds was successfully streamlined, substituting troublesome, low-yielding reactions for a more robust synthetic route, allowing the facile synthesis of a range of soft drug probe compounds. The antibacterial properties of the series were successfully improved, yielding compounds that not only had activity against the predefined target pathogens, but retained activity against multidrug resistant strains of *S. aureus* and a selection of gram-negative bacteria.

The chemical stability of the series was also improved, yielding compounds that were no longer unstable to phosphate buffered conditions. However, along with this increase in stability came additional stability to human plasma.

Of the alternative scaffolds that were investigated, REDX10386 **91** and REDX10387 **116** were observed to be templates with the potential to be developed further. In particular, the antibacterial activity and hERG properties were consistent with the target profiles required for an NBTI-type soft drug, however the compounds were found to be consistently stable in human plasma (**Table 62**).

Redx No.		REDX10386 **91**	REDX10387 **116**
Structure	Target criteria		
MIC (µg/mL)	*S. aureus* ATCC29213	≤ 1	0.12	0.015
	S. aureus NRS482		0.12	0.06
	S. pneumoniae ATCC49619		0.12	0.06
	H. influenzae ATCC49247		1	1
	P. aeruginosa ATCC27853	(or ≤ 1)	16	16
Stability to buffered conditions		Stable	Stable	Stable
Plasma stability (% parent remaining after 2 h)		$t_{1/2} < 2$ h	94%	96%
S9 lung fraction stability		Stable	Stable	-
hepG2 (CC_{50}, µg/mL)	Parent	> 128	> 128	-
	Metabolite	> 128	> 128	-
hERG (IC_{50}, µM)	Parent	-	20.6	3.6
	Metabolite	> 33	> 33	-
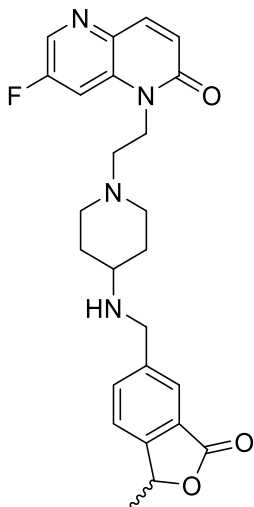
Summary of properties of REDX10386 **91** and REDX10387 **116**.

Table 62

Despite having potent antibacterial properties, the high plasma stability of REDX10386 **91** and REDX10387 **116** prevented further development of the series'. However, it could be hypothesised that future optimisation of these templates could afford the required stability profile of a soft drug compound. Unfortunately, due to time constraints and resources, these scaffolds were reserved for development at a later date, and an alternative chemical series was revisited to allow optimisation to proceed.

Optimisation of plasma instability was guided through sparse literature precedence, culminating in the synthesis of REDX10371 **106**, a compound which was partially unstable in human plasma and stable in human S9 lung fraction (**Table 63**). As a result of analogue synthesis, a potential trend between logD$_{7.4}$ and plasma instability was highlighted,

suggesting an affinity for paraoxonase to a particular $logD_{7.4}$ range, which has yet to be reported within the literature.

Redx No.			REDX10371 **106**
Structure		Target criteria	
MIC (µg/mL)	*S. aureus* ATCC29213	≤ 1	0.12
	S. aureus NRS482		0.12
	S. pneumoniae ATCC49619		0.12
	H. influenzae ATCC49247		0.5
	P. aeruginosa ATCC27853	(or ≤ 1)	16
Stability to buffered conditions		Stable	Stable
Plasma stability (% parent remaining after 2 h)		$t_{1/2} < 2$ h	49%
S9 lung fraction stability		Stable	Stable
hepG2 (CC_{50}, µg/mL)	Parent	> 128	> 128
	Metabolite	> 128	> 128
hERG (IC_{50}, µM)	Parent	-	6.1
	Metabolite	> 33	> 33

Summary of properties of REDX10371 **106**.

Table 63

Further profiling of REDX10371 **106** progressed through enantiomeric separation, allowing the enantiomers to be individually assessed. Development and optimisation of a paraoxonase stability assay allowed the metabolism of each enantiomer to be attributed to the paraoxonase enzyme, with additional evidence being observed from the generation of the suspected ring-opened metabolite. This is the first evidence to be reported of an NBTI-type DNA gyrase inhibitor showing instability to the paraoxonase enzyme.

Progress in the area can be exemplified through consideration of the growth from an initial soft drug concept, to culmination in challenging the hypothesis through an *in vivo* mouse PK model.

Mouse PK data confirmed the instability of (*S*)-REDX10371 **108** to mouse plasma. Furthermore, metabolite identification provided evidence to support only (*S*)-REDX10725 **111**, the hydrolysed-lactone metabolite, was being formed. Following an intratracheal dose, lung tissue concentrations were observed to be greater than the MIC for *S. aureus*, while systemic plasma exposure was very low. Furthermore, plasma exposure to (*S*)-REDX10371 **108** was found to be lower than that observed for gepotidacin **9**, an NBTI currently in Phase II clinical trials.

Much progress has been made from the initial conception of the idea of an antibacterial soft drug. Proof of concept has not only been achieved *in vitro*, but also *in vivo*. Assay data has been utilised to simultaneously optimise the antibacterial properties, stability profiles, and toxicity of the series, culminating in the synthesis and purification of a lead compound, (*S*)-REDX10371 **108**. This compound was progressed to a mouse PK study, providing *in vivo* evidence to support the merits of a soft drug approach to antibacterial research.

3.10 Future work

3.10.1 Future synthetic chemistry

Although success was achieved with regards to initial proof of concept for an antibacterial soft drug therapy, further work in the area could allow development of the series, yielding a more drug-like compound. Due to the success of the project in achieving high antibacterial potency, further work should be focussed on methods of optimising the stability profile of the series.

Initially, a scan of alternative northern groups could shed light on the contribution of the bicyclic scaffold to stability. As previously discussed, a potential trend between increasing polarity and a decrease in plasma stability has been hypothesised (**Table 64**).

	REDX10141 **59**	REDX10307 **74**	REDX10159 **75**	REDX10306 **76**
Measured logD$_{7.4}$	0.95	0.7*	0.52	0.1*
Human plasma stability (100% plasma, % remaining after 2 h)	96% (n =2)	82% (n = 2)	70% (n = 4)	75% (n = 2)

*Value predicted using previously observed trends. Human plasma stability for soft drug probe compounds **59** and **74 – 76**.

Table 64

Further analogue synthesis spanning a larger logD$_{7.4}$ range of northern groups, and subsequent analysis of the plasma stability of the parent compounds, could allow trends between logD$_{7.4}$ and paraoxonase-based metabolism to be explored.

Additionally, obtaining an X-ray crystal structure of a metabolically liable compound bound to the paraoxonase binding site could yield important information regarding the binding mode of NBTI-type compounds within paraoxonase. Understanding how larger molecules bind in the catalytic site of paraoxonase may allow more rapid development of the series with regards to optimising the metabolic instability. Furthermore, if obtaining an X-ray crystal structure was successful, the mechanism of action of the enzyme could be clarified, increasing the understanding of paraoxonase in a wider scientific context.

It was hypothesised that the most lucrative area of optimisation would be surrounding substitution of the phenyl lactone scaffold. Understanding how electron-withdrawing groups (EWGs) and electron-donating groups (EDGs) may affect the metabolic stability of the parent compound was deemed the most likely method of fine-tuning the plasma stability (**Figure 66**).
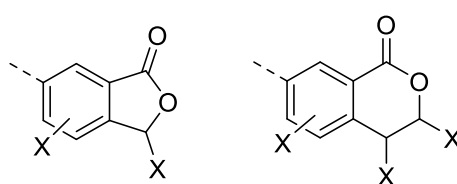
where X = EDG/EWG

Substituted phenyl lactone templates.

Figure 66

Possible decorated scaffolds could be triaged *via* computational analysis, utilising a combination of molecular dynamics simulations and overlays to assess possible binding interactions and clashes with the paraoxonase binding site. Further simulation of electron

density of substituted analogues should help analyse how electron-withdrawing groups and electron-donating groups affect the electropositive nature of the carbonyl carbon. Additionally, increasing the length of the alkyl chain from a methyl group in REDX10371 **106** to an ethyl or *iso*-propyl group, could allow further fine tuning of stability properties. A careful combination of optimisation of the scaffold for the paraoxonase binding site, whilst simultaneously maintaining binding interactions with DNA gyrase, would be necessary to ensure antibacterial activity was preserved.

Although a wide array of compounds could be generated to probe the structure-activity and structure-stability relationships, it would be expected that highly electron-withdrawing groups which maintain lipophilicity in the active site of DNA gyrase could be potentially lucrative. A potential analogue that could be synthesised is a trifluoromethylated derivative, as shown in **Figure 67**.
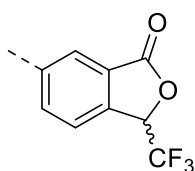
Trifluoromethylated derivative.

Figure 67

Withdrawing electron density from the carbonyl unit should result in a more electropositive centre which is more susceptible to nucleophilic attack by a neighbouring water molecule. A second southern group of potential interest could be synthesised by combining results that have been generated through the research programme. Combining the known stability of the 6-membered scaffold, with the hydrolytic lability of the pyridyl system, could engineer a successfully metabolically labile 6,6-pyridyl lactone hybrid (**Figure 68**).

6,6-pyridyl lactone hybrid.
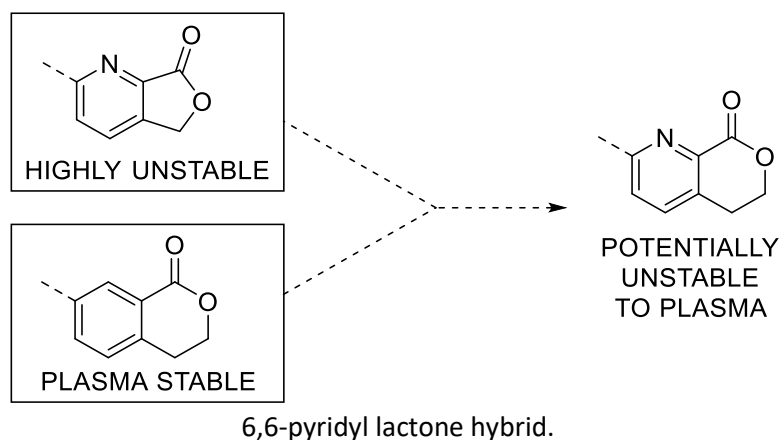
Figure 68

Although the prospective compounds suggested in **Figure 66** to **Figure 68**, could yield lucrative, highly plasma unstable motifs, another promising progression of the project could utilise more suited NBTI-type scaffolds. It has been reported in the literature that 5- and 6-membered lactones are highly unstable to paraoxonase.[59] It could therefore be hypothesised that the observed additional stability of the synthesised NBTI soft drug hybrids thus far can be attributed to the fused lactone system. As a result, an alternative NBTI series that has shown promising antibacterial properties in the literature could be modified to include a metabolically liable substituent (**Figure 69**).
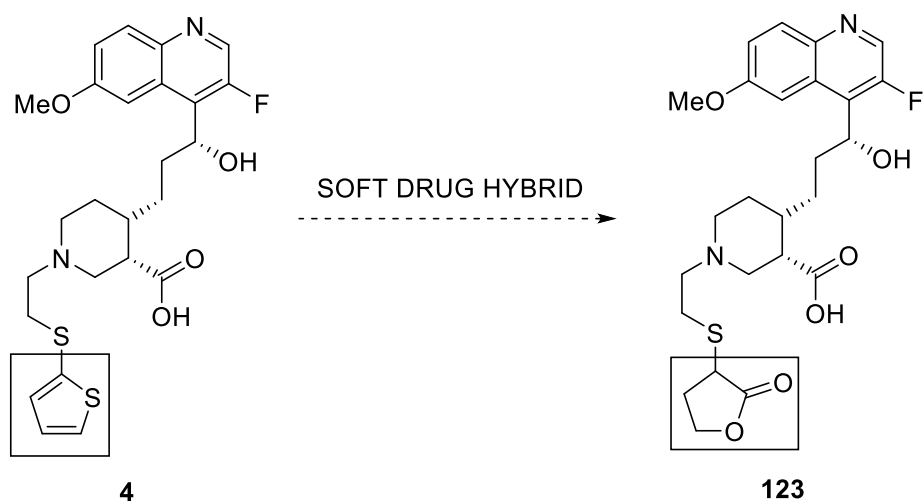
NXL101 **4** and possible soft drug derivative **123**.

Figure 69

NXL101 **4**, an NBTI that progressed to Phase I clinical trials before being withdrawn for hERG related cardiotoxicity, could be a suitable compound, from which, a soft drug series could be generated. Clearly, optimisation of the steric and, in particular, electronic nature of the southern group would have to progress to ensure antibacterial activity was maintained. However, the introduction of a thiol-linked γ-lactone has been previously shown to result in rapid paraoxonase-based metabolism.[59] A similar instability could be hypothesised for soft drug analogue **123**, yielding a compound that is selectively metabolised by paraoxonase in human plasma, and is therefore stable within the lungs.

Although computational models and existing literature suggested the most promising position for the hydrolysable unit to be incorporated was in the southern region of the molecule, the structure-activity relationship of the soft drug scaffold could be further challenged by modifying the location of the metabolic liability. For example, integration of a hydrolysable northern or central group may provide a novel approach to affording a rapidly

metabolised compound. However, an investigation of this magnitude would likely require complete reoptimisation of antibacterial and physiochemical properties, before conclusions could be drawn about the success of the replacement.

3.10.2 Future ADME studies

Due to the multifaceted nature of drug discovery, a plethora of *in vitro* and *in vivo* studies would be required before a clinical candidate could be declared. ADME work would continue to focus on tolerability and determining a more therapeutically relevant dose.

Understanding the percentage of free drug in the systemic circulation and in the lung tissue would allow quantification of the binding of the drug to lung and plasma proteins. Using this data, more accurate predictions surrounding the dose required for *in vivo* efficacy could be made. As only the free drug will be capable of having a therapeutic effect, a highly protein bound drug may prevent drug action. However, for a soft drug, this may have the potential benefit of lowering the rate of metabolism and reducing toxicity.

Dose escalation studies could then progress, assessing the toxicity of an increased dose of compound in a non-diseased rodent model. The data from this study would not only provide safety data with regards to off-target and potentially toxic side effects of treatment, but would allow the plasma and lung concentrations of the drug to be monitored at more therapeutically relevant doses. In addition, urine and bile could be collected from the animals, allowing the concentrations of the parent compound and its metabolite to be tracked throughout the study, reinforcing the expected metabolic hypothesis. If toxicity was observed, the compound could be tested against a range of standard toxicological assays (Ames/Cerep) to allow understanding and potential optimisation of toxicity.

If low toxicity was observed at increased doses, the efficacy of the soft drug could then be assessed in an *in vivo* lung infection model. In this study, a rodent would first be infected with a bacterial strain of choice. Upon treatment with the selected compound, the resulting change in the number of bacterial colonies would allow the antibacterial activity to be assessed *in vivo*.

Due to the underlying cardiotoxic risks associated with NBTI research, it would be envisioned that an *in vivo* cardiotoxicology study using telemetered animals could be prioritised. This would provide a read-out of potential QT prolongation or other

cardiovascular risks. Performing this study early would derisk the series, and, if cardiotoxicity was deemed a potential risk at this stage, further optimisation of the series could proceed prior to initiating more costly studies. Optimisation would likely take the form of increasing the rate of hydrolysis of the parent soft drug compound, using the methods outlined above.

3.11 Experimental

3.11.1 General remarks

NMR spectra were obtained on either a) LC Bruker AV500 using a 5 mm QNP probe (giving 500 MHz ^{1}H NMR spectra and 125 MHz ^{13}C NMR spectra), or b) LC Bruker AV400 using a 5 mm PABBO BB probe (giving 400 MHz ^{1}H NMR spectra and 101 MHz ^{13}C NMR spectra), as stated in the experimental. Coupling constants are reported in Hz and refer to $^3J_{H-H}$ interactions unless otherwise stated.

Preparative high-performance liquid chromatography (HPLC) was performed using an XBridgeTM prep C_{18} μm OBD × 100 mm column, flow rate = 20 mL/min, Waters 2767 as a sample manager and 0.05% NH_3 as a modifier.

High resolution mass spectrometry (HRMS) was conducted on a LTQ Orbitrap XL MS using MeOH + 10% NH_4OAc as a mobile phase in association with the EPSRC UK National Mass Spectrometry Facility (NMSF).

Infra-red (IR) spectrometry was performed on a Nicolet 380 FT-IR, scanning wavelengths of 400-4000 cm^{-1}.

The melting point (M.pt) of a compound was determined using a Büchi B-540 melting point apparatus.

Liquid chromatography mass spectrometry (LCMS), for Method A and Method B, were carried out on a Waters Alliance ZQ MS using H_2O and MeCN mobile phase with pH modification as detailed under Method A or B, where relevant. Wavelengths were 254 and 210 nm. For Method C, LCMS was carried out on a Waters Acquity UPLC system equipped with a SQ Detector 2.

Method A (Basic pH)

Column: YMC-Triart C_{18} 50 × 2 mm, 5 μm. Flow rate: 0.8 mL/min. Injection volume: 5 μL.

Mobile Phase   A H_2O

B   MeCN

C   50% H_2O / 50% MeCN + 1.0% ammonia

Time (min)	A (%)	B (%)	C (%)
0	95	0	5
4	0	95	5
4.4	0	95	5
4.5	95	5	0
4.5	STOP		

Table 65

Method B (Acidic pH)

Column: YMC-Triart C_{18} 50 × 2 mm, 5 μm. Flow rate: 0.8 mL/min. Injection volume: 5 μL.

Mobile Phase   A H_2O

B   MeCN

C   50% H_2O / 50% MeCN + 1% formic acid

Time (min)	A (%)	B (%)	C (%)
0	95	0	5
4	0	95	5
4.4	0	95	5
4.5	95	5	0
4.5	STOP		

Table 66

Method C (Acidic pH, SQD)

Column: YMC Triart C_{18} 50 × 2 mm, 5 μm. Flow rate: 0.6 mL/min. Injection volume: 2 μL.

Mobile Phase   A H_2O + 0.1% formic acid

B   MeCN + 0.1% formic acid

Time (min)	A (%)	B (%)
0	95	5
0.3	95	5
2	5	95
2.6	95	5
3	95	5
3	STOP	

Table 67

3.11.2 Procedures

2-methylfuro[3,4-*b*]pyridine-5,7-dione (30)[91]
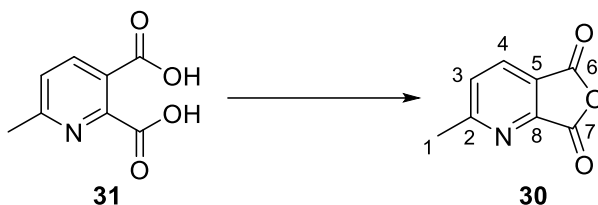
Following the procedure of Di Fabio,[91] a solution of 6-methylpyridine-2,3-dicarboxylic acid **31** (10 g, 55.2 mmol) in acetic anhydride (26 mL, 276 mmol) was heated at 100 °C under nitrogen for 16 h. The reaction mixture was concentrated *in vacuo* to give 2-methylfuro[3,4-*b*]pyridine-5,7-dione **30** (9.0 g, 55.2 mmol, 100% yield) as a brown solid.

δ_H (500 MHz, DMSO-d_6) 8.40 (d, *J* = 8.0 Hz, 1H, 4-ArH), 7.81 (d, *J* = 8.0 Hz, 1H, 3-ArH), 2.72 (s, 3H, 1-CH$_3$). ^{1}H NMR spectrum consistent with that reported by Di Fabio.[91]

2-methoxycarbonyl-6-methyl-pyridine-3-carboxylic acid (32)[76]
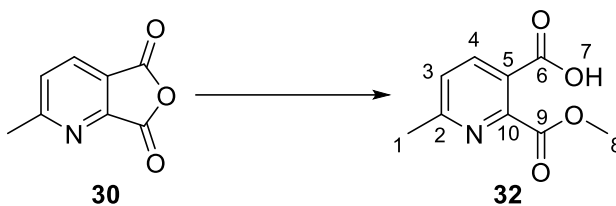
Following the procedure of Metobo *et al.*,[76] to an ice-cold solution of 2-methylfuro[3,4-*b*]pyridine-5,7-dione **30** (160 mg, 0.98 mmol) in THF (6 mL) was added indium(III) triflate (510 mg, 0.91 mmol) followed by MeOH (6 mL). The reaction was stirred at RT for 16 h then partitioned between water (5 mL) and EtOAc (5 mL). The organic layer was extracted with water (3 × 10 mL), NH$_4$Cl (sat. aq., 10 mL), brine (10 mL) and dried over MgSO$_4$, filtered, and concentrated *in vacuo* to give 2-methoxycarbonyl-6-methyl-pyridine-3-carboxylic acid **32** (180 mg, 0.92 mmol, 94% yield) as a yellow solid.

δ_H (500 MHz, DMSO-d_6) 13.59 (s, 1H, 7-OH), 8.17 (d, *J* = 8.1 Hz, 1H, 4-ArH), 7.50 (d, *J* = 8.1 Hz, 1H, 3-ArH), 3.81 (s, 3H, 8-CH$_3$), 2.54 (s, 3H, 1-CH$_3$). ^{1}H NMR spectrum consistent with that reported by Di Fabio.[91]

General Procedure A for reduction of a carboxylic acid with BH₃.THF

29 → **28**
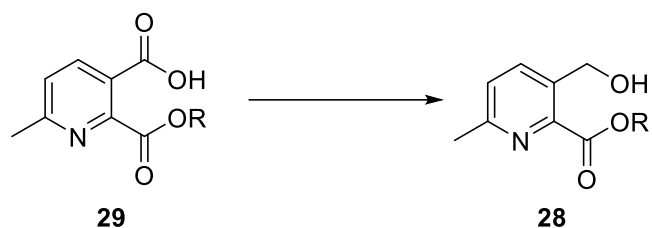
To an ice cold solution of the appropriate substrate **29** (0.22 – 0.92 mmol) in (anhydrous) THF was added borane-THF (1M) portion-wise. The reaction mixture was stirred at a specified temperature for an allotted time, after which LCMS analysis determined the success of the reaction. Where applicable, after completion, the reaction was quenched with the addition of water, and stirred overnight. The mixture was extracted with EtOAc and the organic layer was dried over MgSO₄, filtered, concentrated *in vacuo* and purified by silica gel column chromatography to give the desired product **28**.

Following *General Procedure A*, data are reported as: (a) amount of substrate, (b) amount of solvent, (c) amount of borane-THF, (d) reaction temperature, (e) reaction time and (f) outcome/conversion.

Reduction of methyl 3-(hydroxymethyl)-6-methyl-pyridine-2-carboxylate (33)


32 → **33**
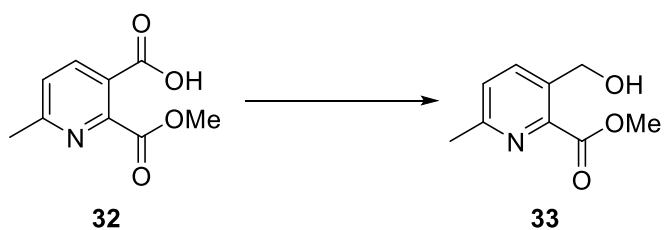
Entry 1. (a) 180 mg, 0.92 mmol, (b) 1 mL, (c) 0.92 mL, 0.92 mmol, (d) 25 °C, (e) 24 h, (f) 0%.

Entry 2. (a) 100 mg, 0.51 mmol, (b) 1 mL, (c) 0.51 mL, 0.51 mmol, (d) 25 °C, (e) 3 h, (f) 0%.

Entry 3. (a) 106 mg, 0.54 mmol, (b) 1 mL, (c) 1.08 mL, 1.08 mmol, (d) 25 °C, (e) 2 h, (f) 0%.

Entry 5. (a) 123 mg, 0.63 mmol, (b) 1.2 mL, (c) 0.63 mL, 0.63 mmol, (d) 25 °C, (e) 48 h, (f) Degradation.

Entry 6. (a) 100 mg, 0.51 mmol, (b) 1 mL, (c) 2.56 mL, 2.56 mmol, (d) 25 °C, (e) 72 h, (f) Over reduction.

Entry 7. (a) 100 mg, 0.51 mmol, (b) 2 mL, (c) 2.05 mL, 2.05 mmol, (d) -78 °C, (e) 3 h, (f) Trace.

Entry 8. (a) 100 mg, 0.51 mmol, (b) 2 mL, (c) 2.05 mL, 2.05 mmol, (d) -40 °C, (e) 1 h, (f) Trace.

Entry 9. (a) 100 mg, 0.51 mmol, (b) 2 mL, (c) 2.05 mL, 2.05 mmol, (d) -10 °C, (e) 0.5 h, (f) Over reduction.

Crude ^{1}H NMR spectroscopy (DMSO-d_6) showed existence of 2 × CH_2 peaks at 4.73 and 4.29 ppm. Possible structure suggested being over-reduced product (diol), consistent with crude ^{1}H NMR spectrum. LCMS consistent with over-reduced product ((Method B) R_T = 1.17 min, [M+H]+ 154.4 (100% purity)).

Reduction of methyl 3-(hydroxymethyl)-6-methyl-pyridine-2-carboxylate (33) using SOCl$_2$

32   **33**
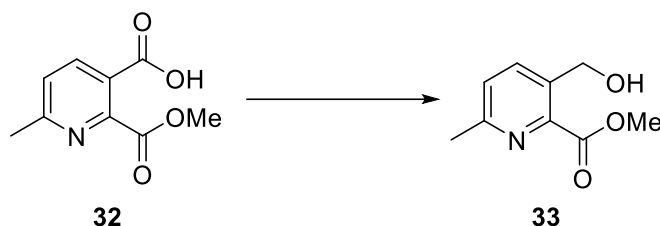
Following an adapted procedure from Han,[92] a solution of 2-methoxycarbonyl-6-methyl-pyridine-3-carboxylic acid **32** (144 mg, 0.74 mmol) in SOCl$_2$ (1 mL, 13.71 mmol) was heated at 80 °C for 2 h, then concentrated *in vacuo*. The resulting residue was dissolved in THF (0.7 mL) and was cooled in an ice bath. NaBH$_4$ (27.9 mg, 0.74 mmol) was added, and the reaction mixture was stirred at RT for 1 h, then was poured onto iced water and extracted with DCM (2 x 5 mL). The combined organics were dried over MgSO$_4$, filtered and concentrated *in vacuo* to give a crude residue. NMR spectroscopy showed the existence of 2 × CH_2 peaks, consistent with over reduction of the starting material.

2-*iso*-propoxycarbonyl-6-methyl-pyridine-3-carboxylic acid (34)[76]
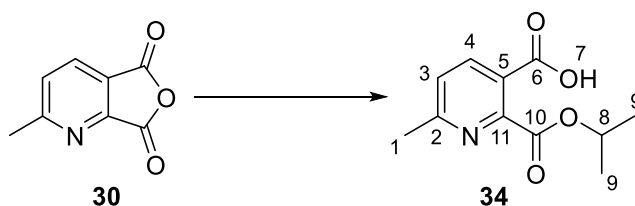
30   **34**

Following the procedure of Metobo *et al.*,[76] to an ice-cold solution of 2-methylfuro[3,4-b]pyridine-5,7-dione **30** (960 mg, 5.88 mmol) in THF (28 mL) was added indium(III) triflate (3.44 g, 6.12 mmol) followed by IPA (28 mL). The reaction was stirred at RT for 16 h then partitioned between water (50 mL) and EtOAc (50 mL). The organic layer was extracted with water (3 × 50 mL), NH$_4$Cl solution (sat. aq., 50 mL), brine (50 mL) and dried over

MgSO$_4$, filtered, and concentrated *in vacuo* to give 2-*iso*-propoxycarbonyl-6-methyl-pyridine-3-carboxylic acid **34** (884 mg, 3.96 mmol, 67% yield) as a yellow solid.

M.pt.: 130 - 137 °C.

ν$_{max}$ (KBr): 3079, 2940 (O-H stretch), 2858 (C-H stretch), 1740 (C=O (ester) stretch), 1720 (C=O (acid) stretch), 1591, 1296, 1263, 1107, 1075, 793 cm^{-1}.

δ$_H$ (500 MHz, DMSO-d$_6$) 13.56 (s, 1H, 7-OH), 8.15 (d, *J* = 8.1 Hz, 1H, 4-ArH), 7.48 (d, *J* = 8.1 Hz, 1H, 3-ArH), 5.15 – 5.11 (m, 1H, 8-CH), 2.54 (s, 3H, 1-CH$_3$), 1.28 (d, *J* = 6.4 Hz, 6H, 2 × 9-CH$_3$).

δ$_C$ (125 MHz, DMSO-d$_6$) 166.0 (10-C), 165.9 (6-C), 161.5 (2-C), 151.8 (11-C), 138.2 (4-C), 124.2 (3-C), 122.0 (5-C), 68.9 (8-C), 23.9 (1-C), 21.2 (2 × 9-C).

LCMS (Method B) R$_T$ = 1.79 min, [M+H]+ 224.0 (100% purity).

HRMS: (C$_{11}$H$_{14}$NO$_4$) [M+H]+ requires 224.0917, found [M+H]+ 224.0918.

HMBC cross-peak observed between 6-C (165.9 ppm) and 4-ArH (8.15 ppm). No cross-peak observed for 10-C (166.0 ppm) with 4-ArH, proving the desired structural isomer configuration.

Reduction of *iso*-propyl 3-(hydroxymethyl)-6-methyl-pyridine-2-carboxylate (35)
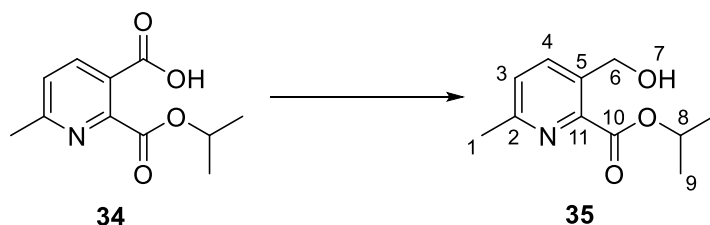
Following *General Procedure A*, data are reported as: (a) amount of substrate, (b) amount of solvent, (c) amount of borane-THF, (d) reaction temperature, (e) reaction time and (f) outcome/conversion. Where appropriate, (g) chromatography conditions, and (h) isolated yield are also reported.

Entry 1. (a) 50 mg, 0.22 mmol, (b) 1 mL, (c) 1.12 mL, 1.12 mmol, (d) 25 °C, (e) 72 h, (f) Trace.

Entry 2. (a) 50 mg, 0.22 mmol, (b) 1 mL, (c) 2.24 mL, 2.24 mmol, (d) 25 °C, (e) 4 h, (f) 80%.

Entry 3. (a) 93 mg, 0.42 mmol, (b) 1 mL, (c) 4.17 mL, 4.17 mmol, (d) 25 °C, (e) 5 h, (f) 80%, (g) 0-100% EtOAc in petroleum ether (bp. 40-60), (h) 40%; white solid.

δ_H (500 MHz, DMSO-d₆) 7.88 (d, J = 8.1 Hz, 1H, 4-ArH), 7.41 (d, J = 8.1 Hz, 1H, 3-ArH), 5.15 – 5.10 (m, 1H, 8-CH), 4.64 (s, 2H, 6-CH₂), 2.47 (s, 3H, 1-CH₃), 1.31 (d, J = 6.3 Hz, 6H, 2 × 9-CH₃).

δ_H (500 MHz, DMSO-d₆) 7.88 (d, J = 8.1 Hz, 1H, 4-ArH), 7.41 (d, J = 8.1 Hz, 1H, 3-ArH), 5.15 – 5.10 (m, 1H, 8-CH), 4.64 (s, 2H, 6-CH₂), 2.47 (s, 3H, 1-CH₃), 1.31 (d, J = 6.3 Hz, 6H, 2 × 9-CH₃).

LCMS (Method B) R_T = 1.64 min, [M+H]+ 210.0 (85% purity), R_T = 2.33 min, [M+H]+ 210.1 (15% purity).

2-methyl-5*H*-furo[3,4-*b*]pyridin-7-one (27)
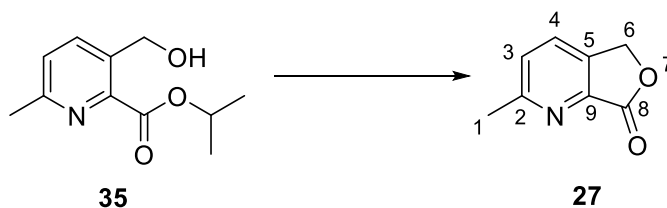
To a solution of *iso*-propyl 3-(hydroxymethyl)-6-methyl-pyridine-2-carboxylate **35** (30 mg, 0.14 mmol) in IPA (2 mL) was added a few drops of HCl (aqueous, 2 M). The reaction mixture was heated to 45 °C for 16 h, then concentrated *in vacuo* to give 2-methyl-5*H*-furo[3,4-*b*]pyridin-7-one **27** (20 mg, 0.13 mmol, 90% yield) as a white solid.

δ_H (500 MHz, DMSO-d₆) 8.05 (d, J = 8.0 Hz, 1H, 4-ArH), 7.60 (d, J = 8.0 Hz, 1H, 3-ArH), 5.41 (s, 2H, 6-CH₂), 2.61 (s, 3H, 1-CH₃).

LCMS (Method B) R_T = 1.30 min, [M+H]+ 149.9 (100% purity).

HRMS: ($C_8H_8NO_2$) [M+H]+ requires 150.0550, found [M+H]+ 150.0564.

7-oxo-5*H*-furo[3,4-*b*]pyridine-2-carbaldehyde (26)
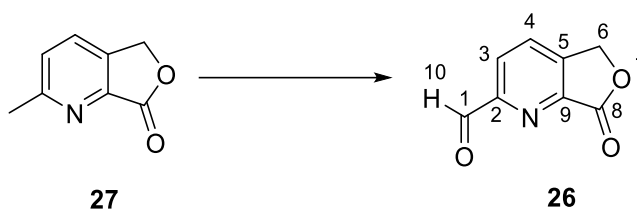
Following the procedure of Chen *et al*.[93] a solution of 2-methyl-5*H*-furo[3,4-*b*]pyridin-7-one **27** (20 mg, 0.13 mmol) and selenium dioxide (19 mg, 0.17 mmol) in 1,4-dioxane (1.6 mL) and water (0.2 mL) was heated under nitrogen to 80 °C for 48 h. After cooling, the mixture was filtered and the filtrate was concentrated *in vacuo*. The crude material was purified by silica gel column chromatography (gradient = 0-100% EtOAc in petroleum ether (bp. 40-60)). The appropriate fractions were combined and concentrated *in vacuo* to give 7-oxo-5*H*-furo[3,4-*b*]pyridine-2-carbaldehyde **26** (6 mg, 0.04 mmol, 27% yield) as a white solid.

M.pt.: 188 - 190 °C.

v_{max} (KBr): 3056, 2964 (C-H stretch) 2925, 2861, 1770 (C=O (lactone) stretch), 1727 (C=O (aldehyde) stretch), 1361, 1303, 1114, 989 cm^{-1}.

δ_H (500 MHz, DMSO-d$_6$) 10.08 (s, 1H, 10-CH), 8.40 (d, J = 7.9 Hz, 1H, 4-ArH), 8.22 (d, J = 7.9 Hz, 1H, 3-ArH), 5.58 (s, 2H, 6-CH$_2$).

δ_C (125 MHz, DMSO-d$_6$) 193.2 (1-C), 168.3 (8-C), 154.8 (2-C), 146.1 (5-C), 144.8 (9-C), 134.2 (4-C), 125.3 (3-C), 68.3 (6-C).

LCMS (Method B) R_T = 1.06 min, [M+H]+ 163.9 (80% purity), 0.82 min, [M+H]+ 163.9 (20% purity).

General Procedure B for reductive amination

A solution of the appropriate aldehyde (0.06 – 4.85 mmol) and amine (0.06 – 4.85 mmol) in a solvent with base (where appropriate) was stirred at RT for 30 min over 3Å molecular sieves. Sodium triacetoxyborohydride (0.17 – 5.33 mmol) was added and the reaction was stirred at RT for 3 h. The reaction mixture was quenched with NaHCO$_3$ (sat. aq.) and the organic phase was separated. The aqueous phase was extracted with DCM and the combined organic phases were dried (MgSO$_4$) and concentrated *in vacuo*. The crude product was purified by silica gel column chromatography. The appropriate fractions were combined and concentrated *in vacuo* to give the desired product.

If additional purification was necessary, the solid was dissolved in DCM and Quadrapure® AK was added. The reaction was stirred at RT for 16 h then filtered to remove the solid supported beads. The filtrate was concentrated *in vacuo* to give the desired product.

Following *General Procedure B*, data are reported as: (a) name and amount of aldehyde, (b) name and amount of amine, (c) name and volume of base (where appropriate), (d) solvent and volume, (e) amount of sodium triacetoxyborohydride, (f) amount of NaHCO$_3$, (g) volume of DCM in extraction, (h) chromatography gradient (where appropriate), (i) additional purification conditions (where appropriate) and (j) isolated product amount and yield.

tert-butyl   N-[1-[2-(7-methoxy-2-oxo-1,8-naphthyridin-1-yl)ethyl]-4-piperidyl]carbamate (36)
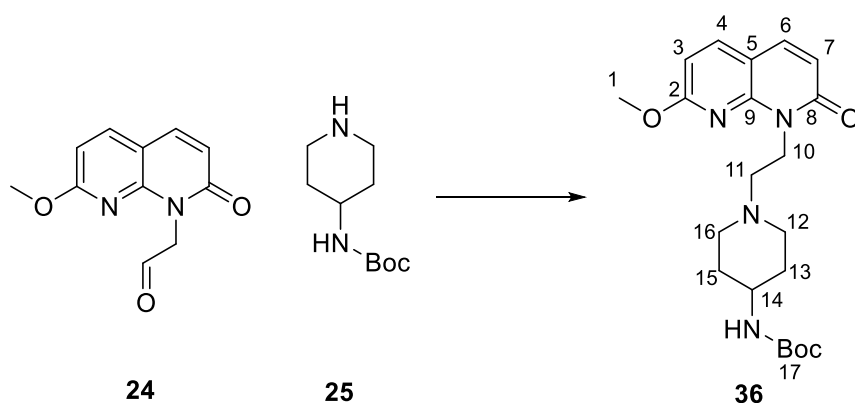
Following *General Procedure B:* (a) 2-(7-methoxy-2-oxo-1,8-naphthyridin-1(2*H*)-yl)acetaldehyde **24**, 150 mg, 0.69 mmol, (b) 4-Boc-aminopiperidine **25**, 138 mg, 0.69 mmol, (d) DCM, 4 mL, (e) 160 mg, 0.75 mmol, (f) 5 mL, (g) 2 × 10 mL, (h) 0-100% EtOAc in petroleum ether (bp. 40-60), (j) 215 mg, 0.53 mmol, 77% yield; colourless oil which crystallised on standing.

δ_H (500 MHz, CDCl$_3$) 7.72 (d, *J* = 8.3 Hz, 1H, 4-ArH), 7.56 (d, *J* = 9.4 Hz, 1H, 6-ArH), 6.61 (d, *J* = 8.3 Hz, 1H, 3-ArH), 6.57 (d, *J* = 9.4 Hz, 1H, 7-ArH), 4.68 – 4.60 (m, 2H, 2 × CH), 4.47 – 4.43 (m, 1H, CH), 4.02 (s, 3H, 1-CH$_3$), 3.50 – 3.46 (m, 1H, CH), 3.08 – 3.04 (m, 2H, 2 × CH), 2.78 – 2.69 (m, 2H, 2 × CH), 2.32 – 2.27 (m, 2H, 2 × CH), 1.99 (s, 1H, CH), 1.97 – 1.89 (m, 2H, 2 × CH), 1.44 (s, 9H, 3 × 17-CH$_3$).

LCMS (Method A) R_T = 2.65 min, [M+H]+ 403.2 (84% purity), R_T = 3.13 min, [M+H]+ 619.2 (5% purity), R_T = 3.52 min, [M+H]+ 803.4 (11% purity).

General Procedure C for Boc deprotection of NBTI scaffold

To a solution of Boc protected NBTI scaffold (0.14 – 3.31 mmol) in MeOH was added HCl (4N in dioxane). The reaction mixture was stirred RT for 16 h then concentrated *in vacuo* and the resulting residue was azeotroped from MeOH twice. The residue was dissolved in minimal MeOH, and diethyl ether was added, causing a solid to precipitate. The solid was triturated twice with diethyl ether and dried under vacuum to give the desired product as an HCl salt.

Following *General Procedure C*, data are reported as: (a) name and amount of substrate, (b) volume of MeOH, (c) volume of HCl (4N in dioxane), (d) isolated product amount and yield.

[1-[2-(7-methoxy-2-oxo-1,8-naphthyridin-1-yl)ethyl]-4-piperidyl]ammonium hydrochloride (37)
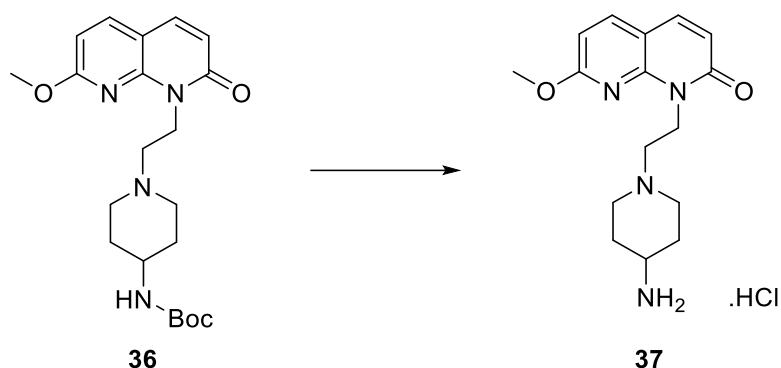
Following *General Procedure C:* (a) *tert*-butyl *N*-[1-[2-(7-methoxy-2-oxo-1,8-naphthyridin-1-yl)ethyl]-4-piperidyl]carbamate **36**, 55 mg, 0.14 mmol, (b) 5 mL, (c) 0.5 mL, (d) 55 mg, 0.16 mmol, 119% yield; white solid.

Diethyl ether was observed in ^{1}H NMR spectrum, and could not be removed from the product under vacuum. It was presumed to be part of the crystal structure, owing to > 100% yield.

2-[[[1-[2-(7-methoxy-2-oxo-1,8-naphthyridin-1-yl)ethyl]-4-piperidyl]amino]methyl]-5*H*-furo[3,4-*b*]pyridin-7-one (23)
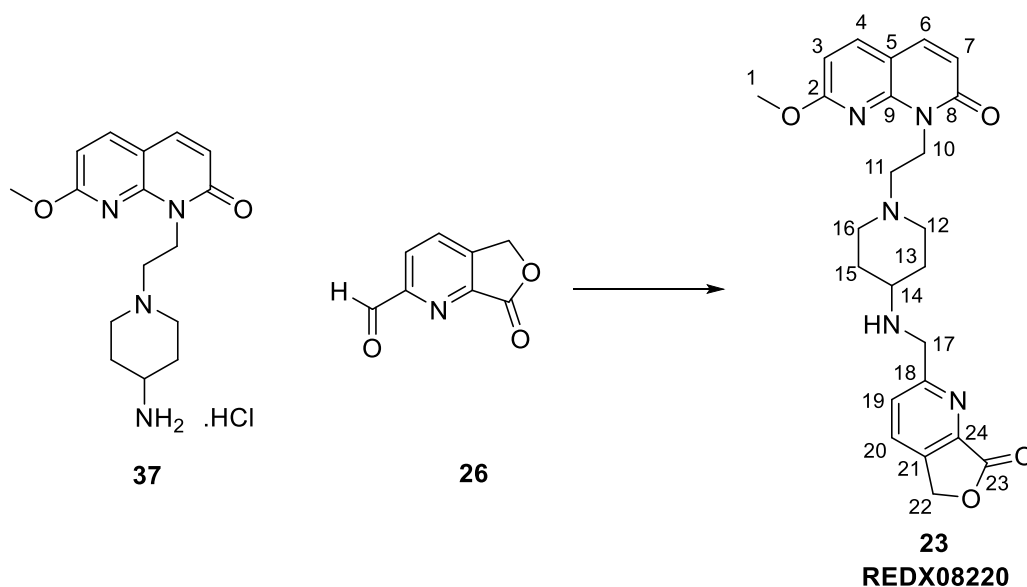
Following *General Procedure B:* (a) 7-oxo-5*H*-furo[3,4-*b*]pyridine-2-carbaldehyde **26**, 25 mg, 0.15 mmol, (b) [1-[2-(7-methoxy-2-oxo-1,8-naphthyridin-1-yl)ethyl]-4-piperidyl]ammonium hydrochloride **37**, 52 mg, 0.15 mmol, (d) DCM, 0.5 mL, (e) 36 mg, 0.17 mmol,

(h) 0-50% MeOH in DCM, (i) DCM, 4 mL, Quadrapure® AK, 210 mg, (j) 5 mg, 0.01 mmol, 7% yield; yellow solid.

M.pt.: glass transition 173 - 174 °C, melting point 193 - 194 °C.

v_{max} (KBr): 3444 (N-H stretch), 2929 (C-H stretch), 1770 (C=O (γ-lactone) stretch), 1651 (C=O (amide) stretch), 1592, 1470, 1395 cm^{-1}.

δ_H (500 MHz, CDCl$_3$) 7.89 (d, J = 7.9 Hz, 1H, 20-ArH), 7.75 − 7.70 (m, 2H, 4-ArH and 19-ArH), 7.58 (d, J = 9.4 Hz, 1H, 6-ArH), 6.62 (d, J = 8.3 Hz, 1H, 3-ArH), 6.57 (d, J = 9.4 Hz, 1H, 7-ArH), 5.39 (s, 2H, 22-CH$_2$), 4.72 (t, J = 7.6 Hz, 2H, 10-CH$_2$), 4.13 (s, 2H, 17-CH$_2$), 4.05 (s, 3H, 1-CH$_3$), 3.22 − 3.15 (m, 2H, 12-CH* and 16-CH*), 2.84 (t, J = 7.6 Hz, 2H, 11-CH$_2$), 2.71 − 2.67 (m, 1H, 14-CH), 2.45 − 2.31 (m, 2H, 12-CH* and 16-CH*), 2.05 − 2.00 (m, 2H, 13-CH* and 15-CH*), 1.66 – 1.57 (m, 2H, 13-CH* and 15-CH*) *axial/equatorial protons could not be assigned.

δ_C (125 MHz, CDCl$_3$) 168.8 (23-C), 164.3 (2-C), 163.6 (18-C), 163.1 (8-C), 148.8 (9-C), 143.8 (24-C), 139.2 (4-C), 139.1 (21-C), 137.4 (6-C), 131.4 (20-C), 126.7 (19-C), 118.9 (7-C), 109.5 (5-C), 106.4 (3-C), 67.8 (22-C), 54.9 (11-C), 54.2 (1-C), 52.1 (12-C or 16-C), 52.0 (12-C or 16-C), 51.6 (17-C), 50.8 (14-C), 38.1 (10-C), 31.4 (13-C or 15-C), 29.7 (13-C or 15-C).

LCMS (Method A) R$_T$ = 2.01 min, [M+H]+ 450.2 (100**%** purity).

HRMS: (C$_{24}$H$_{28}$N$_5$O$_4$) [M+H]+ requires 450.2136, found [M+H]+ 450.2132. Nuclear Overhauser effects observed between the protons indicated below. Due to the complexity of the NOE signals seen for the piperidine ring, a simplified diagram illustrates the connectivity seen without reporting piperidine-piperidine interactions.
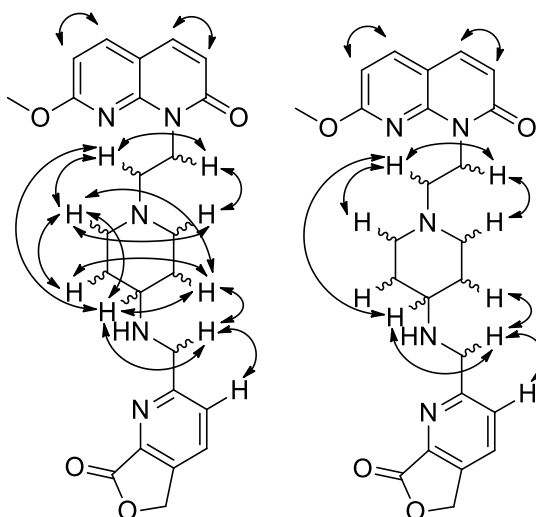
tert-butyl N-[1-[2-(6,7-difluoro-2-oxo-quinoxalin-1-yl)ethyl]-4-piperidyl]carbamate (39)
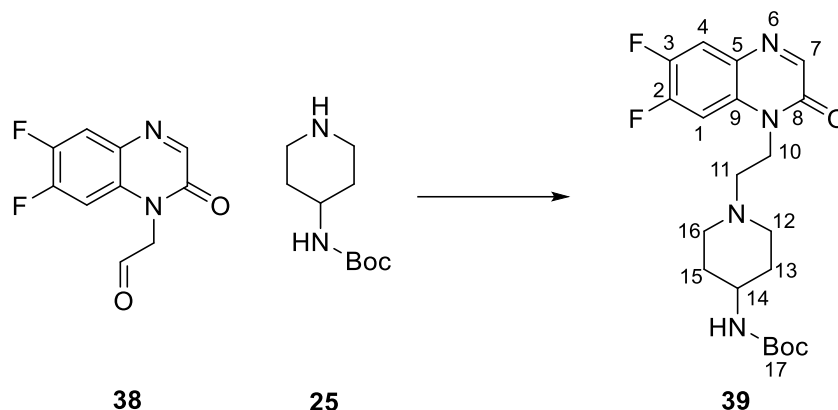
Following *General Procedure B:* (a) 2-(6,7-difluoro-2-oxoquinoxalin-1(2*H*)-yl)acetaldehyde **38**, 273 mg, 1.22 mmol, (b) 4-Boc-aminopiperidine **25**, 250 mg, 1.25 mmol, (d) DCM, 8 mL, (e) 288 mg, 1.36 mmol, (f) 3 mL, (g) 2 × 10 mL, (j) 470 mg, 1.15 mmol, 94% yield; yellow solid.

δ_H (500 MHz, CDCl$_3$) 8.25 (s, 1H, 7-ArH), 7.69 (dd, $^3J_{H-F}$ = 10.0 Hz, $^4J_{H-F}$ = 8.2 Hz, 1H, 4-ArH), 7.26 (dd, $^3J_{H-F}$ = 11.7 Hz, $^4J_{H-F}$= 7.0 Hz, 1H, 1-ArH), 4.45 – 4.40 (m, 1H, NH), 4.28 (t, *J* = 7.0 Hz, 2H, 10-CH$_2$), 3.50 – 3.44 (m, 1H, 14-CH), 2.94 – 2.86 (m, 2H, 12-CH* and 16-CH*), 2.66 (t, *J* = 7.0 Hz, 2H, 11-CH$_2$), 2.26 – 2.22 (m, 2H, 12-CH* and 16-CH*), 1.97 – 1.90 (m, 2H, 13-CH* and 15-CH*), 1.44 (s, 9H, 3 × 17-CH$_3$), 1.39 – 1.36 (m, 2H, 13-CH* and 15-CH*) *axial/equatorial protons could not be assigned.

LCMS (Method A) R_T = 2.84 min, [M+H]+ 409.3 (100% purity).

[1-[2-(6,7-difluoro-2-oxo-quinoxalin-1-yl)ethyl]-4-piperidyl]ammonium hydrochloride (40)
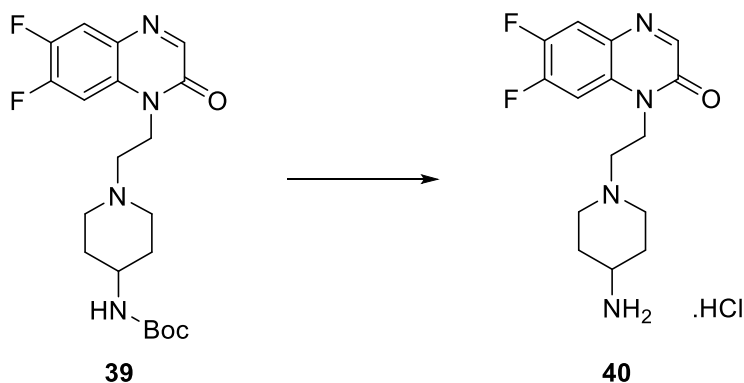
Following *General Procedure C:* (a) *tert*-butyl *N*-[1-[2-(6,7-difluoro-2-oxo-quinoxalin-1-yl)ethyl]-4-piperidyl]carbamate **39**, 470 mg, 1.15 mmol, (b) 40 mL, (c) 4 mL, (d) 436 mg, 1.26 mmol, 110% yield; light brown solid.

Diethyl ether was observed in ^{1}H NMR spectrum, and could not be removed from the product under vacuum. It was presumed to be part of the crystal structure, owing to > 100% yield.

LCMS (Method A) R_T = 2.22 min, [M+H]+ 309.2 (100% purity).

2-[[[1-[2-(6,7-difluoro-2-oxo-quinoxalin-1-yl)ethyl]-4-piperidyl]amino]methyl]-5*H*-furo[3,4-*b*]pyridin-7-one (41)

41
REDX08881
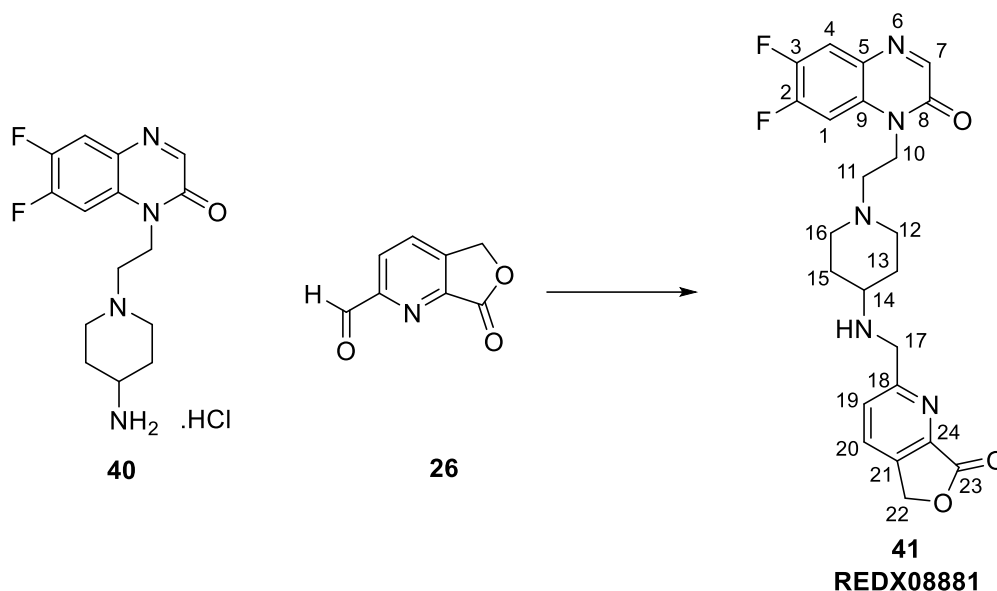
Following *General Procedure B:* (a) 7-oxo-5*H*-furo[3,4-*b*]pyridine-2-carbaldehyde **26**, 24 mg, 0.15 mmol, (b) [1-[2-(6,7-difluoro-2-oxo-quinoxalin-1-yl)ethyl]-4-piperidyl]ammonium chloride **40**, 51 mg, 0.15 mmol, (d) THF, 1 mL, (e) 102 mg, 0.48 mmol, (f) 1 mL, (g) 2 × 10 mL (h) 0-50% MeOH in DCM, (j) 18 mg, 0.04 mmol, 27% yield; orange solid.

M.pt.: 178 - 179 °C.

v_{max} (KBr): 3340 (N-H stretch), 2935, 2779 (C-H stretch) 1777 (C=O (γ-lactone) stretch), 1645 (C=O (amide) stretch), 1622, 1455, 1391, 1358, 1305, 1084, 995 cm^{-1}.

δ_H (500 MHz, CDCl$_3$) 8.25 (s, 1H, 7-ArH), 7.90 − 7.83 (m, 1H, 20-ArH), 7.74 − 7.65 (m, 2H, 4-ArH and 19-ArH), 7.34 − 7.27 (m, 1H, 1-ArH), 5.38 (s, 2H, 22-CH$_2$), 4.29 (t, *J* = 7.0 Hz, 2H, 10-CH$_2$), 4.10 (s, 2H, 17-CH$_2$), 2.99 − 2.91 (m, 2H, 12-CH* and 16-CH*), 2.66 (t, *J* = 7.0 Hz, 2H, 11-CH$_2$), 2.60 − 2.50 (m, 1H, 14-CH), 2.20 − 2.16 (m, 2H, 12-CH* and 16-CH*), 1.96 − 1.88 (m, 2H, 13-CH* and 15-CH*), 1.49 − 1.34 (m, 2H, 13-CH* and 15-CH*) *axial/equatorial protons could not be assigned.

δ_C (125 MHz, CDCl$_3$) 164.5 (23-C), 154.4 (8-C), 152.0 (dd, $^1J_{C-F}$ = 252.2 Hz, $^2J_{C-F}$ = 14.2 Hz, 3-C), 150.5 (7-C), 146.6 (dd, $^1J_{C-F}$ = 252.2 Hz, $^2J_{C-F}$ = 14.2 Hz, 2-C) 143.8 (21-C and 24-C), 139.0 (18-C), 131.2 (20-C), 130.1 (dd, $^3J_{C-F}$ = 9.1 Hz, $^4J_{C-F}$ = 1.4 Hz, 9-C), 129.9 (dd, $^3J_{C-F}$ = 9.1 Hz, $^4J_{C-F}$ = 2.5 Hz, 5-C) 126.6 (19-C), 118.1 (d, $^2J_{C-F}$ = 19.5 Hz, 4-C), 102.9 (d, $^2J_{C-F}$ = 23.7 Hz, 1-C), 67.7 (22-C), 54.9 (11-C), 54.6 (14-C), 52.8 (12-C and 16-C), 52.1 (17-C), 41.0 (10-C), 32.7 (13-C and 15-C).

LCMS (Method A) R$_T$ = 2.17 min, [M+H]+ 456.2 (100% purity).

HRMS: (C$_{23}$H$_{24}$N$_5$O$_3$F$_2$) [M+H]+ requires 456.1842, found [M+H]+ 456.1839.

General Procedure D for lactone hydrolysis

To a solution of lactone containing compound (0.01 – 0.03 mmol) in solvent was added lithium hydroxide monohydrate. The reaction mixture was stirred at RT for 16 h then concentrated *in vacuo* to give the desired product.

Where necessary, further purification by reverse phase preparative-HPLC was undertaken, and the appropriate fractions were concentrated using a Genevac to give the purified product.

Following *General Procedure D*, data are reported as: (a) name and amount of starting material, (b) volume of solvent, (c) amount of lithium hydroxide monohydrate, (d) isolated as lithium salt/purified further, (e) isolated product amount and yield.

3-(hydroxymethyl)-6-[[[1-[2-(7-methoxy-2-oxo-1,8-naphthyridin-1-yl)ethyl]-4-piperidyl]amino]methyl]pyridine-2-carboxylic acid (42)

23

42
REDX08495
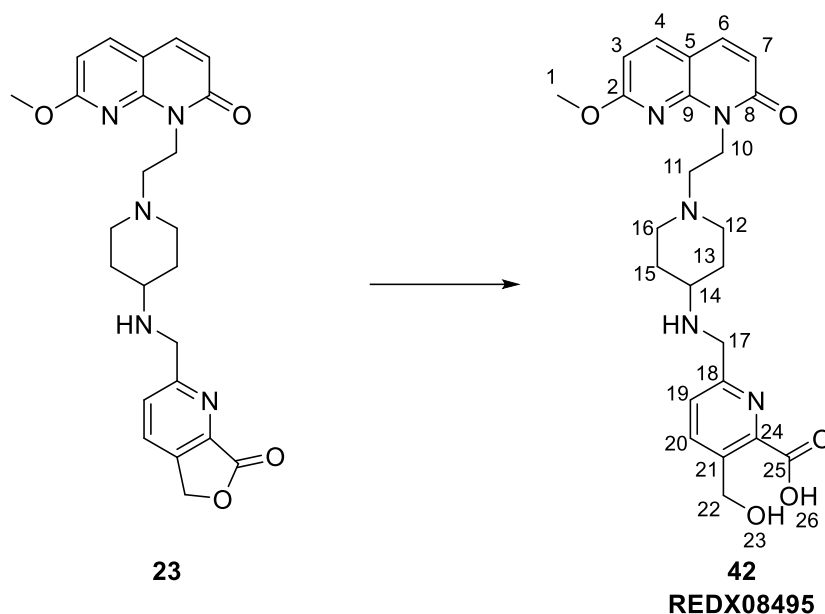
Following *General Procedure D*: (a) 2-[[[1-[2-(7-methoxy-2-oxo-1,8-naphthyridin-1-yl)ethyl]-4-piperidyl]amino]methyl]-5*H*-furo[3,4-*b*]pyridin-7-one **23**, 10 mg, 0.02 mmol, (b) water, 2 mL, (c) 6 mg, 0.14 mmol, (d) purified *via* reverse phase preparative-HPLC, (e) 7 mg, 0.015 mmol, 67% yield; white solid.

δ_H (500 MHz, CD$_3$OD) 7.87 (d, *J* = 8.5 Hz, 1H, 4-ArH), 7.85 (d, *J* = 7.9 Hz, 1H, 20-ArH), 7.75 (d, *J* = 9.4 Hz, 1H, 6-ArH), 7.32 (d, *J* = 7.9 Hz, 1H, 19-ArH), 6.64 (d, *J* = 8.5 Hz, 1H, 3-ArH), 6.46 (d, *J* = 9.4 Hz, 1H, 7-ArH), 4.73 (s, 2H, 22-CH$_2$), 4.63 − 4.58 (m, 2H, 10-CH$_2$), 4.22 (s, 2H, 17-CH$_2$), 3.96 (s, 3H, 1-CH$_3$), 3.16 − 3.12 (m, 2H, 2 × piperidine-CH), 3.08 − 2.99 (m, 1H, 14-CH), 2.74 − 2.69 (m, 2H, 11-CH$_2$), 2.20 − 2.10 (m, 2H, 2 × piperidine-CH), 2.10 − 2.01 (m, 2H, 2 × piperidine-CH), 1.62 − 1.52 (m, 2H, 2 × piperidine-CH). A DMSO impurity was observed by ^{1}H NMR spectroscopy, which could not be removed by drying overnight, and was presumably trapped in the crystal structure. This was presumed to have originated from the preparative-HPLC, which uses a mixture of MeCN, H$_2$O and DMSO to inject each sample. Molar ratio of product:DMSO - 1:0.83.

LCMS (Method A) R$_T$ = 1.27 min, [M+H]+ 468.1 (100**%** purity).

6-[[[1-[2-(6,7-difluoro-2-oxo-quinoxalin-1-yl)ethyl]-4-piperidyl]amino]methyl]-3-(hydroxymethyl)pyridine-2-carboxylic acid (43)

41

43
REDX08911
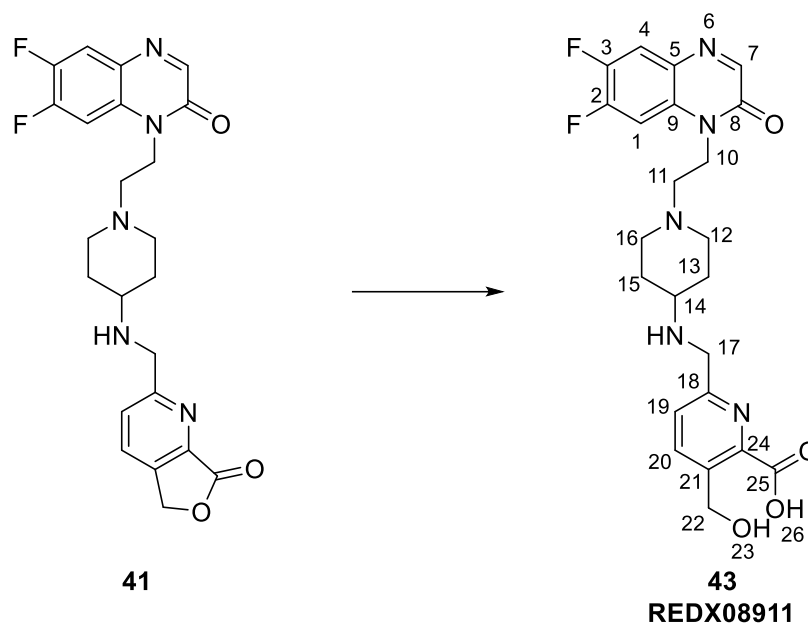
Following *General Procedure D*: (a) 2-[[[1-[2-(6,7-difluoro-2-oxo-quinoxalin-1-yl)ethyl]-4-piperidyl]amino]methyl-5*H*-furo[3,4-*b*]pyridin-7-one **41**, 10 mg, 0.02 mmol, (b) water, 2 mL, (c) 5 mg, 0.12 mmol, (d) purified *via* reverse phase preparative-HPLC, (e) 8 mg, 0.017 mmol, 77% yield; white solid.

δ_H (500 MHz, CD$_3$OD) 8.10 (s, 1H, 7-ArH), 7.79 (d, *J* = 7.9 Hz, 1H, 20-ArH), 7.68 (dd, $^3J_{H\text{-}F}$ = 10.4 Hz, $^4J_{H\text{-}F}$ = 8.3 Hz, 1H, 4-ArH), 7.57 (dd, $^3J_{H\text{-}F}$ = 12.2 Hz, $^4J_{H\text{-}F}$ = 7.2 Hz, 1H, 1-ArH), 7.29 (d, *J* = 7.9 Hz, 1H, 19-ArH), 4.68 (s, 2H, 22-CH$_2$), 4.30 (t, *J* = 6.8 Hz, 2H, 10-CH$_2$), 4.03 (s, 2H, 17-CH$_2$), 3.04 − 2.98 (m, 2H, 2 × piperidine-CH), 2.79 − 2.75 (m, 1H, 14-CH), 2.61 (t, *J* = 6.8 Hz, 2H, 11-CH$_2$), 2.12 − 2.03 (m, 2H, 2 × piperidine-CH), 2.00 − 1.93 (m, 2H, 2 × piperidine-CH), 1.51 − 1.40 (m, 2H, 2 × piperidine-CH). A DMSO impurity was observed by ^{1}H NMR spectroscopy, which could not be removed by drying overnight, and was presumably trapped in the crystal structure. This was presumed to have originated from the preparative-HPLC, which uses a mixture of MeCN, H$_2$O and DMSO to inject each sample. Molar ratio of product:DMSO - 1:0.71.

LCMS (Method A) R$_T$ = 1.32 min, [M+H]+ 474.3 (100% purity).

2-methyl-7*H*-furo[3,4-*b*]pyridin-5-one (44)[78]
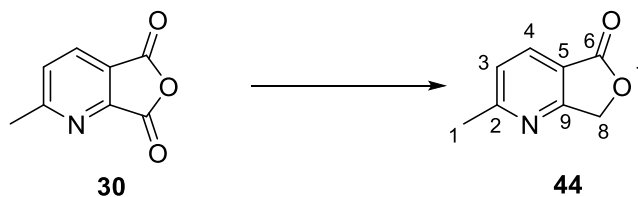
Following the procedure of Boral *et al.*[78] to a solution of 2-methylfuro[3,4-*b*]pyridine-5,7-dione **30** (541 mg, 3.32 mmol) in THF (5 mL) at 15 °C was added sodium borohydride (131 mg, 3.46 mmol) followed by acetic acid (glacial, 0.4 mL, 6.99 mmol) dropwise. The reaction was stirred at 15 °C for 4 h and was concentrated *in vacuo*. The resulting residue was treated with acetic acid (glacial, 1.2 mL, 20.98 mmol) and acetic anhydride (1.2 mL, 12.7 mmol) and the solution was stirred at 100 °C for 3 h, then cooled to RT and concentrated *in vacuo*. The residue was partitioned between brine (10 mL) and DCM (10 mL). The organic phase was extracted with brine (10 mL), dried (MgSO$_4$), concentrated *in vacuo* and purified by silica gel column chromatography (gradient = 5-50% EtOAc in petroleum ether (bp. 40-60)). The appropriate fractions were concentrated *in vacuo* to give 2-methyl-7*H*-furo[3,4-*b*]pyridin-5-one **44** (280 mg, 1.87 mmol, 57% yield) as an off-white crystalline solid.

δ_H (500 MHz, DMSO-d$_6$) 8.31 – 8.22 (m, 1H, 4-ArH), 7.62 – 7.56 (m, 1H, 3-ArH), 5.46 (s, 2H, 8-CH$_2$), 2.79 – 2.66 (m, 3H, 1-CH$_3$).

δ_C (125 MHz, DMSO-d$_6$) 169.1 (C-6), 167.0 (2-C), 165.5 (9-C), 133.8 (4-C), 123.8 (3-C), 116.3 (5-C), 70.2 (8-C), 24.5 (1-C).

LCMS (Method B) R$_T$ = 1.38 min, [M+H]+ 150.0 (100% purity).

HRMS: (C$_8$H$_8$NO$_2$) [M+H]+ requires 150.0550, found [M+H]+ 150.0546.

5-oxo-7*H*-furo[3,4-*b*]pyridine-2-carbaldehyde (45)
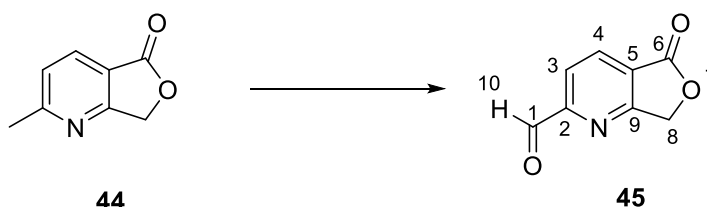
Following the procedure of Chen *et al.*,[93] a solution of 2-methyl-7*H*-furo[3,4-*b*]pyridin-5-one **44** (59 mg, 0.40 mmol) and selenium dioxide (48 mg, 0.43 mmol) in 1,4-dioxane (0.5 mL) was heated under nitrogen at 100 °C for 10 h in a Biotage Initiator microwave reactor. After

cooling, the mixture was filtered and the filtrate was concentrated *in vacuo*. The crude material was purified by silica gel column chromatography (gradient = 0-100% EtOAc in petroleum ether (bp. 40-60)). The appropriate fractions were combined and concentrated *in vacuo* to give 5-oxo-7*H*-furo[3,4-*b*]pyridine-2-carbaldehyde **45** (9 mg, 0.06 mmol, 14% yield) as a yellow solid.

δ_H (500 MHz, DMSO-d_6) 10.11 (s, 1H, 10-H), 8.54 (d, *J* = 7.9 Hz, 1H, 4-ArH), 8.10 (d, *J* = 7.9 Hz, 1H, 3-ArH), 5.57 (s, 2H, 8-CH$_2$).

δ_C (125 MHz, DMSO-d_6) 192.6 (1-C), 168.1 (2-C), 167.2 (6-C), 155.9 (9-C), 135.6 (4-C), 122.4 (5-C), 122.2 (3-C), 70.5 (8-C).

LCMS (Method B) R_T = 1.12 min, [M+H]+ 164.0 (93% purity), R_T = 1.53 min, [M+H]+ 150.0 (7% purity).

2-[[[1-[2-(7-methoxy-2-oxo-1,8-naphthyridin-1-yl)ethyl]-4-piperidyl]amino]methyl]-7*H*-furo[3,4-*b*]pyridin-5-one (46)
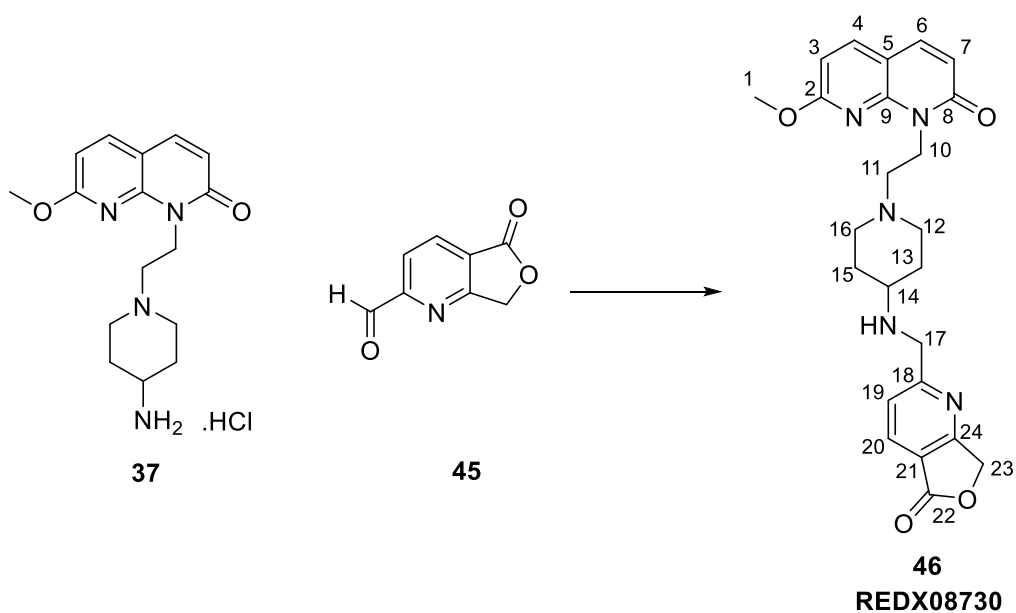
Following *General Procedure B:* (a) 5-oxo-7*H*-furo[3,4-*b*]pyridine-2-carbaldehyde **45**, 9 mg, 0.06 mmol, (b) [1-[2-(7-methoxy-2-oxo-1,8-naphthyridin-1-yl)ethyl]-4-piperidyl]ammonium chloride **37**, 19 mg, 0.06 mmol, (d) THF, 1 mL, (e) 42 mg, 0.20 mmol, (f) 5 mL, (g) 2 × 10 mL, (h) 0-50% MeOH in DCM, (j) 2 mg, 0.004 mmol, 8% yield; orange solid.

δ_H (500 MHz, CDCl$_3$) 8.15 (d, *J* = 8.0 Hz, 1H, 20-ArH), 7.72 (d, *J* = 8.4 Hz, 1H, 4-ArH), 7.57 (d, *J* = 9.4 Hz, 1H, 6-ArH), 7.55 (d, *J* = 8.0 Hz, 1H, 19-ArH), 6.62 (d, *J* = 8.4 Hz, 1H, 3-ArH), 6.57 (d, *J* = 9.4 Hz, 1H, 7-ArH), 5.31 (s, 2H, 23-CH$_2$), 4.67 (t, *J* = 7.7 Hz, 2H, 10-CH$_2$), 4.09 (s, 2H,

17-CH$_2$), 4.03 (s, 3H, 1-CH$_3$), 3.16 − 3.07 (m, 2H, 12-CH* and 16-CH*), 2.80 − 2.71 (m, 2H, 11-CH$_2$), 2.61 − 2.52 (m, 1H, 14-CH), 2.30 − 2.16 (m, 2H, 12-CH* and 16-CH*), 1.99 − 1.90 (m, 2H, 13-CH* and 15-CH*), 1.69-1.62 (m, 2H, 13-CH* and 15-CH*) *axial/equatorial protons could not be assigned.

δ$_C$ (125 MHz, CDCl$_3$) 167.9 (18-C), 167.4 (22-C), 165.3 (24-C), 164.2 (2-C), 163.5 (8-C), 148.8 (9-C), 139.3 (4-C), 137.2 (6-C), 134.3 (20-C), 122.6 (19-C), 119.0 (7-C), 118.5 (21-C), 109.6 (5-C), 106.1 (3-C), 70.5 (23-C), 55.2 (11-C), 54.7 (14-C), 54.0 (1-C), 52.6 (12-C and 16-C), 52.3 (17-C), 38.7 (10-C), 33.5 (13-C or 15-C), 31.3 (13-C or 15-C).

LCMS (Method A) R$_T$ = 2.20 min, [M+H]+ 450.3 (100% purity).

2-[[[1-[2-(6,7-difluoro-2-oxo-quinoxalin-1-yl)ethyl]-4-piperidyl]amino]methyl]-7*H*-furo[3,4-*b*]pyridin-5-one (47)

40   **45**   **47**

REDX08942
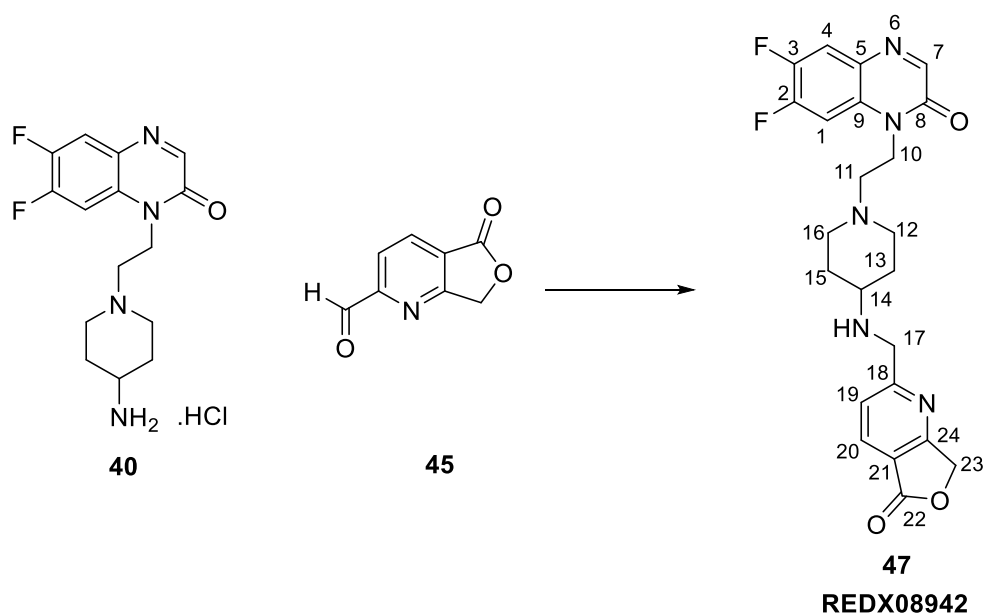
Following *General Procedure B:* (a) 5-oxo-7*H*-furo[3,4-*b*]pyridine-2-carbaldehyde **45**, 17 mg, 0.10 mmol, (b) [1-[2-(6,7-difluoro-2-oxo-quinoxalin-1-yl)ethyl]-4-piperidyl]ammonium chloride **40**, 19 mg, 0.06 mmol, (d) THF, 2 mL, (e) 72 mg, 0.34 mmol, (f) 5 mL, (g) 2 × 10 mL, (h) 0-50% MeOH in DCM, (j) 17 mg, 0.04 mmol, 36% yield; yellow solid.

M.pt.: 146 - 147 °C.

ν$_{max}$ (KBr): 3331 (N-H stretch), 2938, 2821 (C-H aliphatic stretch), 1769 (C=O (γ-lactone) stretch), 1660 (C=O (amide) stretch), 1596, 1455, 1390, 1354, 1305, 1050, 1002 cm^{-1}.

δ_H (500 MHz, CD$_3$OD) 8.14 – 8.09 (m, 2H, 7-ArH and 20-ArH), 7.68 (dd, $^3J_{H-F}$ = 10.4 Hz, $^4J_{H-F}$ = 8.4 Hz, 1H, 4-ArH), 7.59 – 7.52 (m, 2H, 1-ArH and 19-ArH), 5.27 (s, 2H, 23-CH$_2$), 4.30 (t, J = 6.9 Hz, 2H, 10-CH$_2$), 3.98 (s, 2H, 17-CH$_2$), 2.98 – 2.92 (m, 2H, 12-CH* and 16-CH*), 2.59 (t, J = 6.9 Hz, 2H, 11-CH$_2$), 2.51 – 2.44 (m, 1H, 14-CH), 2.10 – 2.05 (m, 2H, 12-CH* and 16-CH*), 1.90 – 1.82 (m, 2H, 13-CH* and 15-CH*), 1.39 – 1.29 (m, 2H, 13-CH* and 15-CH*) *axial/equatorial protons could not be assigned.

δ_C (125 MHz, CD$_3$OD) 166.7 (22-C), 154.8 (8-C), 152.7 (24-C), 150.7 (d, $^1J_{C-F}$ = 232.5 Hz, 3-C), 145.6 (d, $^1J_{C-F}$ = 250.0 Hz, 2-C), 134.07 (20-C or 7-C), 134.06 (20-C or 7-C), 130.5 (18-C), 130.1 (9-C), 129.9 (5-C), 122.9 (19-C), 117.5 (4-C and 21-C), 103.8 (1-C), 70.7 (23-C), 54.2 (11-C), 54.1 (14-C), 52.8 (12-C or 16-C), 52.6 (12-C or 16-C), 50.7 (17-C), 40.1 (10-C), 31.22 (13-C or 15-C), 31.19 (13-C or 15-C).

LCMS (Method A) R$_T$ = 2.23 min, [M+H]+ 456.2 (100% purity).

HRMS: (C$_{23}$H$_{24}$N$_5$O$_3$F$_2$) [M+H]+ requires 456.1842, found [M+H]+ 456.1837.

General procedure E for Heck reaction

Following an adapted procedure from Blades *et al.*,[94] to a solution of halogenated starting material (1.41 – 2.97 mmol) and Pd(^{t}Bu$_3$P)$_2$ in triethylamine in a sparged microwave vial was added butyl prop-2-enoate. The vial was purged with sequential applications of vacuum and nitrogen, and then heated at 155 °C for 20 min. The reaction mixture was cooled to RT, filtered then concentrated *in vacuo*. The resulting crude product was purified by silica gel column chromatography and the appropriate fractions were concentrated *in vacuo* to give the desired product.

Following *General Procedure E*, data are reported as: (a) name and amount of halogenated starting material, (b) amount of Pd(^{t}Bu$_3$P)$_2$, (c) amount of triethylamine, (d) amount of butyl prop-2-enoate, (e) chromatography gradient, (f) isolated product amount and yield.

**Butyl (*E*)-3-(3-oxo-1*H*-isobenzofuran-5-yl)prop-2-enoate (61)**
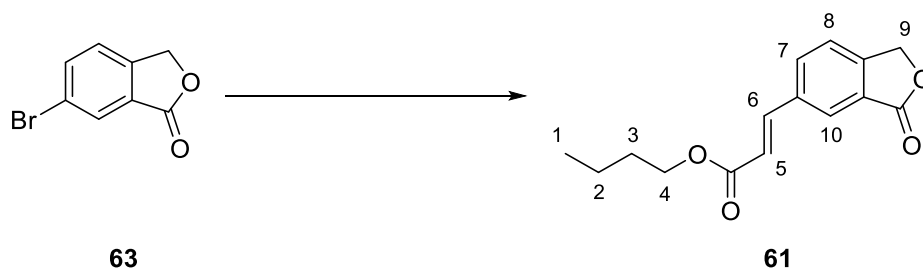
Following *General Procedure E*: (a) 6-bromoisobenzofuran-1(3*H*)-one **63**, 380 mg, 1.78 mmol, (b) 57 mg, 0.11 mmol, (c) 1.24 mL, 8.92 mmol, (d) 0.38 mL, 2.71 mmol, (e) 0-100% EtOAc in petroleum ether (bp. 40-60), (f) 230 mg, 0.88 mmol, 50% yield; brown solid.

δ_H (500 MHz, CDCl$_3$) 8.08 (s, 1H, 10-ArH), 7.86 – 7.81 (m, 1H, 7-ArH or 8-ArH), 7.74 (d, *J* = 16.1 Hz, 1H, 6-CH), 7.56 – 7.50 (m, 1H, 7-ArH or 8-ArH), 6.55 (d, *J* = 16.1 Hz, 1H, 5-CH), 5.36 (s, 2H, 9-CH$_2$), 4.23 (t, *J* = 6.7 Hz, 2H, 4-CH$_2$), 1.75 – 1.66 (m, 2H, 3-CH$_2$), 1.49 – 1.38 (m, 2H, 2-CH$_2$), 0.98 (t, *J* = 7.4 Hz, 3H, 1-CH$_3$).

LCMS (Method A) R$_T$ = 2.69 min. No ionisation observed.

General procedure F for oxidative cleavage

Following an adapted procedure from Yamada *et al.*,[95] to a solution of osmium tetroxide (4 wt% in H$_2$O) and acrylate (0.54 – 1.62 mmol) in water and THF was added sodium periodate under nitrogen. The reaction mixture was stirred at RT for 16 h then partitioned between brine and DCM. The aqueous phase was washed with DCM and the combined organic layers were dried (MgSO$_4$), filtered and concentrated *in vacuo*. The crude product was purified by silica gel column chromatography and the appropriate fractions were combined and concentrated *in vacuo* then triturated with diethyl ether to give the desired product.

Following *General Procedure F*, data are reported as: (a) amount of osmium tetroxide, (b) name and amount of acrylate, (c) volume of water, (d) volume of THF, (e) amount of sodium periodate, (f) volume of brine in extraction, (g) volume of DCM in extraction, (h) chromatography gradient, (i) isolated product amount and yield.

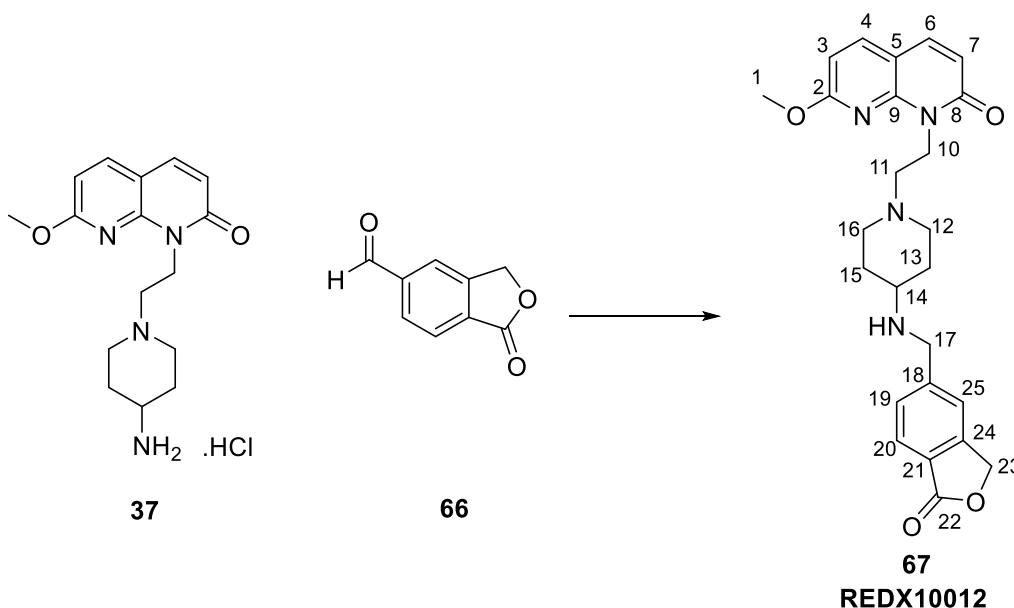**3-oxo-1*H*-isobenzofuran-5-carbaldehyde (60)**
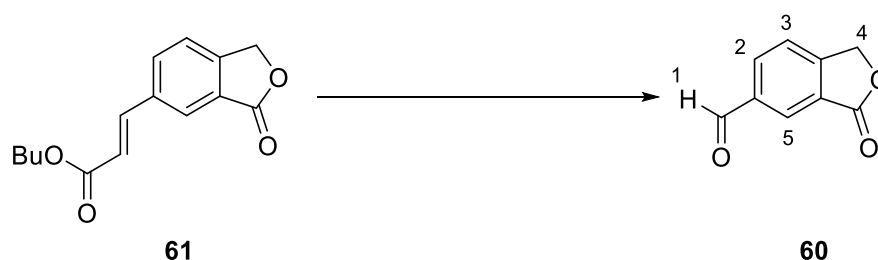
Following *General Procedure F*: (a) 0.22 mL, 0.04 mmol, (b) butyl (*E*)-3-(3-oxo-1,3-dihydroisobenzofuran-5-yl)acrylate **61**, 230 mg, 0.88 mmol, (c) 2.5 mL, (d) 2.5 mL,

(e) 567 mg, 2.65 mmol, (f) 2 mL, (g) 2 × 5 mL, (h) 0-100% DCM in petroleum ether (bp. 40-60), (i) 140 mg, 0.86 mmol, 98% yield; brown solid.

δ_H (500 MHz, CDCl$_3$) 10.14 (s, 1H, 1-CH), 8.42 (d, $^4J_{H-H}$ = 1.5 Hz, 1H, 5-ArH), 8.25 (dd, J = 7.9 Hz, $^4J_{H-H}$ = 1.5 Hz, 1H, 2-ArH), 7.69 (d, J = 7.9 Hz, 1H, 3-ArH), 5.42 (s, 2H, 4-CH$_2$).

LCMS (Method A) R$_T$ = 1.10 min [M+H]- 161.0 (100% purity).

7-methoxy-1-[2-[4-[(3-oxo-1H-isobenzofuran-5-yl)methylamino]-1-piperidyl]ethyl]-1,8-naphthyridin-2-one (59)
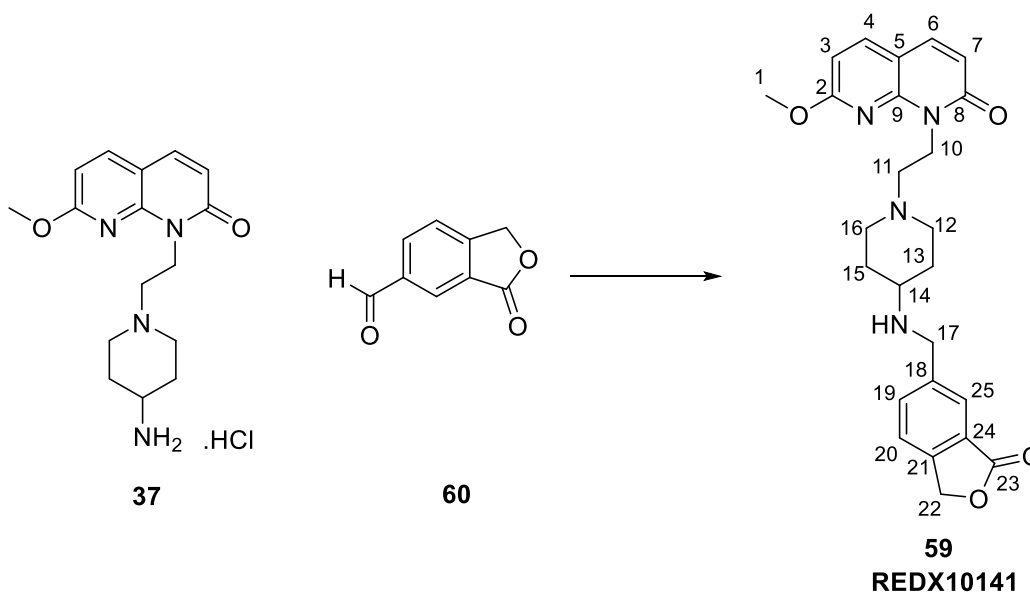
Following *General Procedure B:* (a) 3-oxo-1H-isobenzofuran-5-carbaldehyde **60**, 20 mg, 0.12 mmol, (b) [1-[2-(7-methoxy-2-oxo-1,8-naphthyridin-1-yl)ethyl]-4-piperidyl]ammonium chloride **37**, 40 mg, 0.12 mmol, (c) triethylamine, 19 μL, 0.14 mmol, (d) DCM, 0.5 mL, (e) 75 mg, 0.35 mmol, (f) 2 mL, (g) 2 × 5 mL, (h) 0-50% MeOH in DCM, (j) 16 mg, 0.04 mmol, 30% yield; white solid.

M.pt.: 147 - 149 °C.

ν_{max} (neat): 3438 (N-H stretch), 2935 (C-H stretch), 2810, 1761 (C=O (γ-lactone) stretch), 1654 (C=O (amide) stretch), 1590, 1448, 1311, 1275, 1055, 999 cm^{-1}.

δ_H (400 MHz, CDCl$_3$) 7.95 − 7.90 (m, 1H, 25-ArH), 7.78 (dd, J = 7.9 Hz, $^4J_{H-H}$ = 1.5 Hz, 1H, 19-ArH), 7.74 (d, J = 8.4 Hz, 1H, 4-ArH), 7.59 (d, J = 9.5 Hz, 1H, 6-ArH), 7.49 (dd, J = 7.9 Hz, $^5J_{H-H}$ = 0.9 Hz, 1H, 20-ArH), 6.64 (d, J = 8.4 Hz, 1H, 3-ArH), 6.58 (d, J = 9.5 Hz, 1H, 7-ArH), 5.32 (s, 2H, 22-CH$_2$), 4.76 − 4.69 (m, 2H, 10-CH$_2$), 4.06 (s, 3H, 1-CH$_3$), 3.98 (s, 2H, 17-CH$_2$), 3.23 − 3.16 (m, 2H, 12-CH* and 16-CH*), 2.89 − 2.83 (m, 2H, 11-CH$_2$), 2.72 − 2.63 (m, 1H, 14-CH),

2.44 – 2.33 (m, 2H, 12-CH* and 16-CH*), 2.08 – 2.01 (m, 2H, 13-CH* and 15-CH*) 1.69 – 1.58 (m, 2H, 13-CH* and 15-CH*) *axial/equatorial protons could not be assigned.

δ_C (125 MHz, CDCl$_3$) 171.1 (23-C), 164.2 (2-C), 163.1 (8-C), 148.8 (9-C), 145.4 (24-C), 142.4 (18-C), 139.0 (19-C), 137.3 (6-C), 134.3 (4-C), 126.0 (21-C), 124.9 (25-C), 122.1 (20-C), 119.0 (7-C), 109.5 (5-C), 106.2 (3-C), 69.6 (22-C), 55.2 (11-C), 54.0 (1-C), 53.8 (14-C), 52.4 (12-C and 16-C), 50.1 (17-C), 38.5 (10-C), 32.3 (13-C and 15-C).

LCMS (Method C) R_T = 0.95 mins, [M+H]+ 449.4 (100%).

HRMS: (C$_{25}$H$_{28}$N$_4$O$_4$) [M+H]+ requires 449.2183, found [M+H]+ 449.2180.

Butyl (*E*)-3-(1-oxo-3*H*-isobenzofuran-5-yl)prop-2-enoate (65)

64   **65**
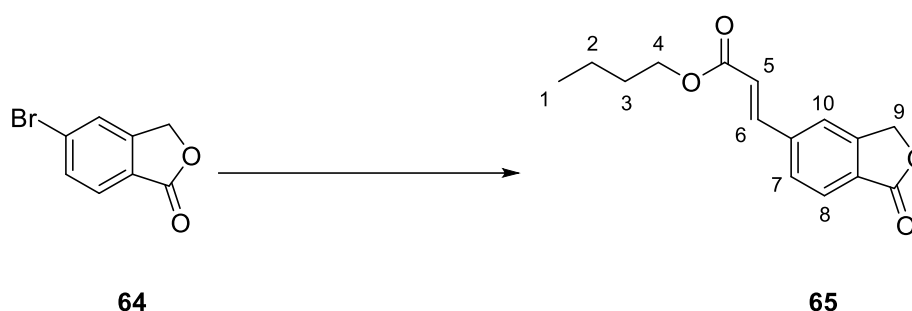
Following *General Procedure E*: (a) 5-bromoisobenzofuran-1(3*H*)-one **64**, 300 mg, 1.41 mmol, (b) 45 mg, 0.09 mmol, (c) 0.98 mL, 7.04 mmol, (d) 0.30 mL, 2.08 mmol, (e) 0-100% EtOAc in petroleum ether (bp. 40-60), (f) 140 mg, 0.54 mmol, 38% yield; brown oil.

δ_H (500 MHz, CDCl$_3$) 7.94 (d, *J* = 8.0 Hz, 1H, 8-ArH), 7.75 (d, *J* = 16.1 Hz, 1H, 6-CH), 7.69 (dd, *J* = 8.0 Hz, $^4J_{H-H}$ = 1.2 Hz, 1H, 7-ArH), 7.62 (d, $^4J_{H-H}$ = 1.2 Hz, 1H, 10-ArH), 6.57 (d, *J* = 16.1 Hz, 1H, 5-CH), 5.35 (s, 2H, 9-CH$_2$), 4.24 (t, *J* = 6.7 Hz, 2H, 4-CH$_2$), 1.74 – 1.66 (m, 2H, 2-CH$_2$), 1.49 – 1.40 (m, 2H, 2-CH$_2$), 0.98 (t, *J* = 7.4 Hz, 3H, 1-CH$_3$).

LCMS (Method A) R_T = 2.71 min. No ionisation observed.

1-oxo-3*H*-isobenzofuran-5-carbaldehyde (66)

65 → **66**
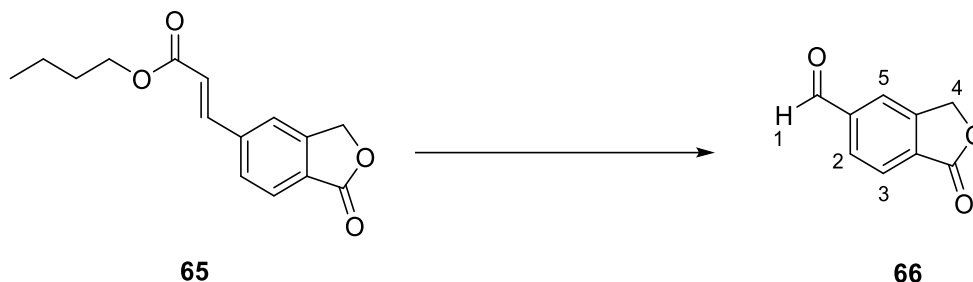
Following *General Procedure F*: (a) 0.13 mL, 0.02 mmol, (b) butyl (*E*)-3-(1-oxo-1,3-dihydroisobenzofuran-5-yl)acrylate **65**, 140 mg, 0.54 mmol, (c) 1.5 mL, (d) 1.5 mL, (e) 345 mg, 1.61 mmol, (f) 2 mL, (g) 2 × 5 mL, (h) 0-100% DCM in petroleum ether (bp. 40-60), (i) 83 mg, 0.51 mmol, 95% yield; brown solid.

δ_H (500 MHz, CDCl$_3$) 10.18 (s, 1H, 1-CH), 8.14 – 8.01 (m, 3H, 3 × ArH), 5.43 (s, 2H, 4-CH$_2$).

LCMS (Method A) R_T = 1.70 mins, [M+H]+ 161.2 (100%).

7-methoxy-1-[2-[4-[(1-oxo-3*H*-isobenzofuran-5-yl)methylamino]-1-piperidyl]ethyl]-1,8-naphthyridin-2-one (67)

37   **66**   **67**
                                REDX10012

Following *General Procedure B:* (a) 1-oxo-3*H*-isobenzofuran-5-carbaldehyde **66**, 20 mg, 0.12 mmol, (b) [1-[2-(7-methoxy-2-oxo-1,8-naphthyridin-1-yl)ethyl]-4-piperidyl]ammonium chloride **37**, 38 mg, 0.11 mmol, (c) triethylamine, 18 μL, 0.13 mmol, (d) DCM, 2 mL, (e) 79 mg, 0.37 mmol, (f) 2 mL, (g) 2 × 5 mL, (h) 0-50% MeOH in DCM, (j) 14 mg, 0.03 mmol, 25% yield; white solid.

M.pt.: 173 - 174 °C.

v_{max} (neat): 3305 (N-H stretch), 2939 (C-H stretch), 2808, 1762 (C=O (γ-lactone) stretch), 1656 (C=O (amide) stretch), 1592, 1493, 1356, 1275, 1045, 840 cm^{-1}.

δ_H (500 MHz, CDCl$_3$) 7.86 (d, J = 7.9 Hz, 1H, 20-ArH), 7.73 (d, J = 8.3 Hz, 1H, 4-ArH), 7.57 (d, J = 9.3 Hz, 1H, 6-ArH), 7.52 (s, 1H, 25-ArH), 7.49 (d, J = 7.9 Hz, 1H, 19-ArH), 6.63 − 6.56 (m, 2H, 3-ArH and 7-ArH), 5.30 (s, 2H, 23-CH$_2$), 4.69 − 4.64 (m, 2H, 10-CH$_2$), 4.02 (s, 3H, 1-CH$_3$), 3.96 (s, 2H, 17-CH$_2$), 3.14 − 3.09 (m, 2H, 12-CH* and 16-CH*), 2.79 − 2.74 (m, 2H, 11-CH$_2$), 2.61 − 2.53 (m, 1H, 14-CH), 2.29 − 2.22 (m, 2H, 12-CH* and 16-CH*), 1.97 − 1.91 (m, 2H, 13-CH* and 15-CH*), 1.53 − 1.42 (m, 2H, 13-CH* and 15-CH*) *axial/equatorial protons could not be assigned.

δ_C (125 MHz, CDCl$_3$) 171.0 (22-C), 164.2 (2-C), 163.1 (8-C), 148.8 (9-C), 148.0 (18-C), 147.1 (21-C), 139.1 (4-C), 137.3 (6-C), 129.0 (19-C), 125.7 (20-C), 124.5 (24-C), 121.4 (25-C), 119.0 (7-C), 109.5 (5-C) 106.2 (3-C), 69.6 (23-C), 55.2 (11-C), 54.2 (14-C), 53.9 (1-C), 52.4 (12-C and 16-C), 50.5 (17-C), 38.6 (10-C), 32.4 (13-C and 15-C).

LCMS (Method A) R_T = 2.46 mins, [M+H]+ 449.29 (100% purity).

HRMS: (C$_{25}$H$_{28}$N$_4$O$_4$) [M+H]+ requires 449.2183, found [M+H]+ 449.2181.

6,7-difluoro-1-[2-[4-[(3-oxo-1H-isobenzofuran-5-yl)methylamino]-1-piperidyl]ethyl]quinoxalin-2-one (74)
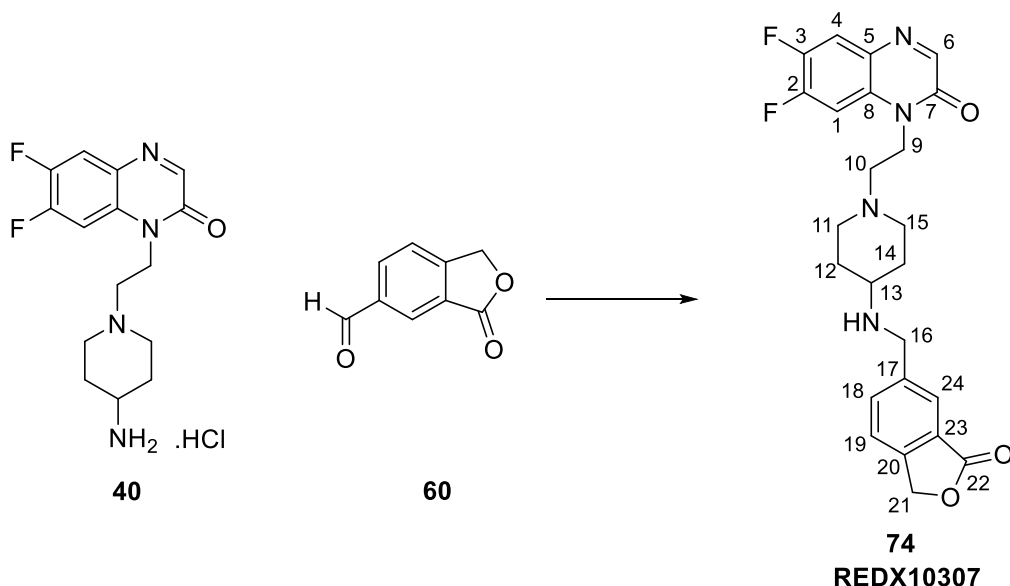
Following *General Procedure B:* (a) 3-oxo-1H-isobenzofuran-5-carbaldehyde **60**, 10 mg, 0.07 mmol, (b) [1-[2-(6,7-difluoro-2-oxo-quinoxalin-1-yl)ethyl]-4-piperidyl]ammonium

chloride **40**, 20 mg, 0.06 mmol, (c) triethylamine, 10 μL, 0.07 mmol, (d) THF, 1 mL, (e) 39 mg, 0.19 mmol, (f) 2 mL, (g) 2 × 5 mL, (h) 0-50% MeOH in DCM, (j) 4 mg, 0.01 mmol, 14% yield; off-white solid.

M.pt.: decomposition observed at 149 - 150 °C.

v_{max} (neat): 3395 (N-H stretch), 2934 (C-H stretch), 2825, 1759 (C=O (γ-lactone) stretch), 1663 (C=O (amide) stretch), 1600, 1561, 1451, 1385, 1361, 1308, 1054, 1002 cm^{-1}.

δ_H (400 MHz, CDCl$_3$) 8.27 (s, 1H, 6-ArH), 7.92 (s, 1H, 24-ArH), 7.76 – 7.69 (m, 2H, 4-ArH and 18-ArH), 7.50 (d, J = 7.9 Hz, 1H, 19-ArH), 7.43 (dd, $^3J_{H-F}$ = 11.6 Hz, $^4J_{H-F}$ = 6.9 Hz, 1H, 1-ArH), 5.34 (s, 2H, 21-CH$_2$), 4.45 – 4.37 (m, 2H, 9-CH$_2$), 3.99 (s, 2H, 16-CH$_2$), 3.21 – 3.08 (m, 2H, 11-CH* and 15-CH*), 2.86 – 2.76 (m, 2H, 10-CH$_2$), 2.76 – 2.66 (m, 1H, 13-CH), 2.09 – 1.96 (m, 2H, 12-CH* and 14-CH*), 1.68 – 1.54 (m, 2H, 12-CH* and 14-CH*)*axial/equatorial protons could not be assigned. 2 × CH (11-CH* and 15-CH*) absent in NMR spectrum. Due to shouldering, peak was presumed to be under water peak (approx. 2.4 ppm). Drying of sample/TFA shake not performed due to lack of material, and the risk of loss during transferring/manipulation.

LCMS (Method C) R_T = 1.01 mins, [M+H]+ 455.4 (100%).

HRMS: (C$_{24}$H$_{24}$F$_2$N$_4$O$_3$) [M+H]+ requires 455.1889, found [M+H]+ 455.1886.

tert-butyl _N_-[1-[2-(7-fluoro-2-oxo-quinoxalin-1-yl)ethyl]-4-piperidyl]carbamate (70)

68   **25**   **70**
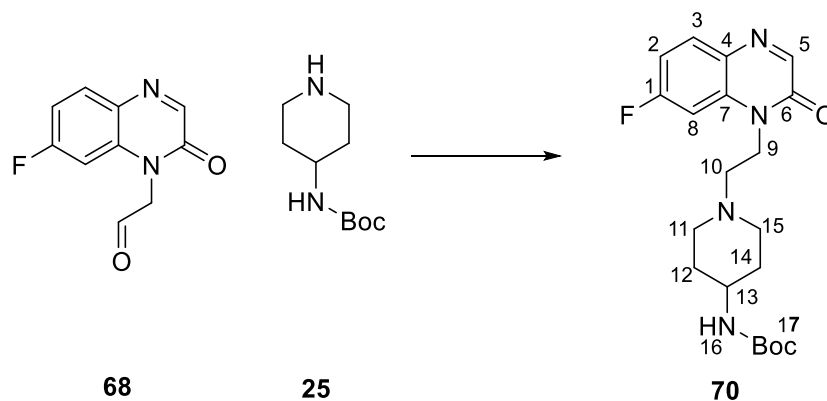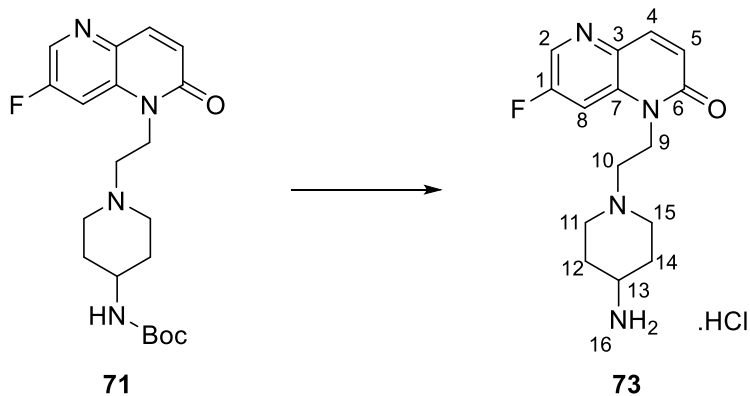
Following _General Procedure B:_ (a) 2-(7-fluoro-2-oxoquinoxalin-1(2_H_)-yl)acetaldehyde **68**, 1 g, 4.85 mmol, (b) 4-Boc-aminopiperidine **25**, 972 mg, 4.85 mmol, (d) THF, 40 mL, (e) 1.13 g, 5.33 mmol, (f) 20 mL, (g) 2 × 30 mL, (h) 0-100% EtOAc in petroleum ether (bp. 40-60), (j) 1.29 g, 3.31 mmol, 68% yield; orange solid.

δ$_H$ (400 MHz, CDCl$_3$) 8.24 (s, 1H, 5-ArH), 7.88 (dd, J = 8.8 Hz, $^3J_{H\text{-}F}$ = 6.0 Hz, 1H, 3-ArH), 7.17 – 7.05 (m, 2H, 8-ArH and 2-ArH), 4.44 (s, 1H, 16-NH), 4.32 (t, J = 7.1 Hz, 2H, 9-CH$_2$), 3.53 – 3.48 (m, 1H, 13-CH), 3.00 – 2.89 (m, 2H, 2 × piperidine-CH), 2.69 (t, J = 7.1 Hz, 2H, 10-CH$_2$), 2.33 – 2.21 (m, 2H, 2 × piperidine-CH), 2.02 – 1.90 (m, 2H, 2 × piperidine-CH), 1.49 – 1.40 (m, 11H, 2 × piperidine-CH and 3 × 17-CH$_3$).

LCMS (Method C) R$_T$ = 1.18 mins, [M+H]+ 391.5 (100%).

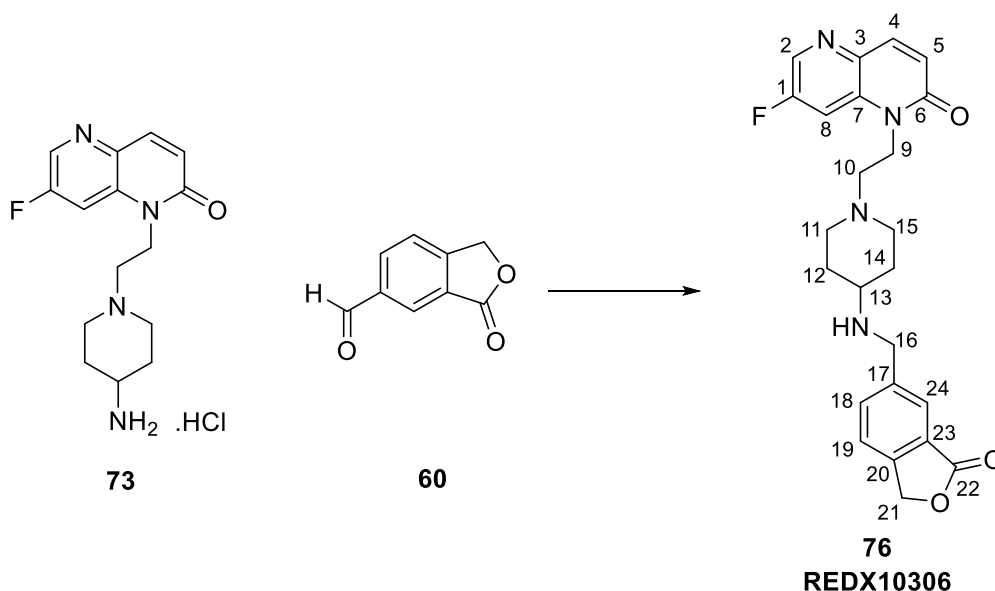**[1-[2-(7-fluoro-2-oxo-quinoxalin-1-yl)ethyl]-4-piperidyl]ammonium chloride (72)**
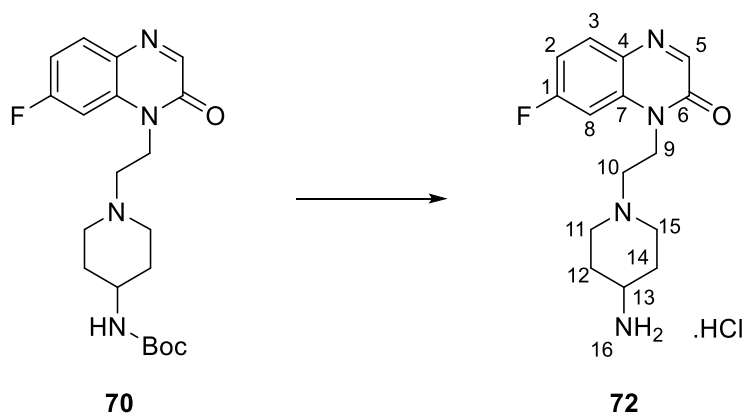
Following *General Procedure C:* (a) *tert*-butyl *N*-[1-[2-(7-fluoro-2-oxo-quinoxalin-1-yl)ethyl]-4-piperidyl]carbamate **70**, 1.29 g, 3.31 mmol, (b) 100 mL, (c) 4 mL, 16 mmol, (d) 1.26 g, 3.84 mmol, 116% crude yield; white solid.

Diethyl ether was observed in ^{1}H NMR spectrum, and could not be removed from the product under vacuum. It was presumed to be part of the crystal structure, owing to > 100% yield.

LCMS (Method C) R$_T$ = 0.49 mins, [M+H]+ 291.3 (100% purity).

7-methoxy-1-[2-[4-[[(3-oxo-1*H*-isobenzofuran-5-yl)methylamino]-1-piperidyl]ethyl]-1,8-naphthyridin-2-one (75)

75
REDX10159
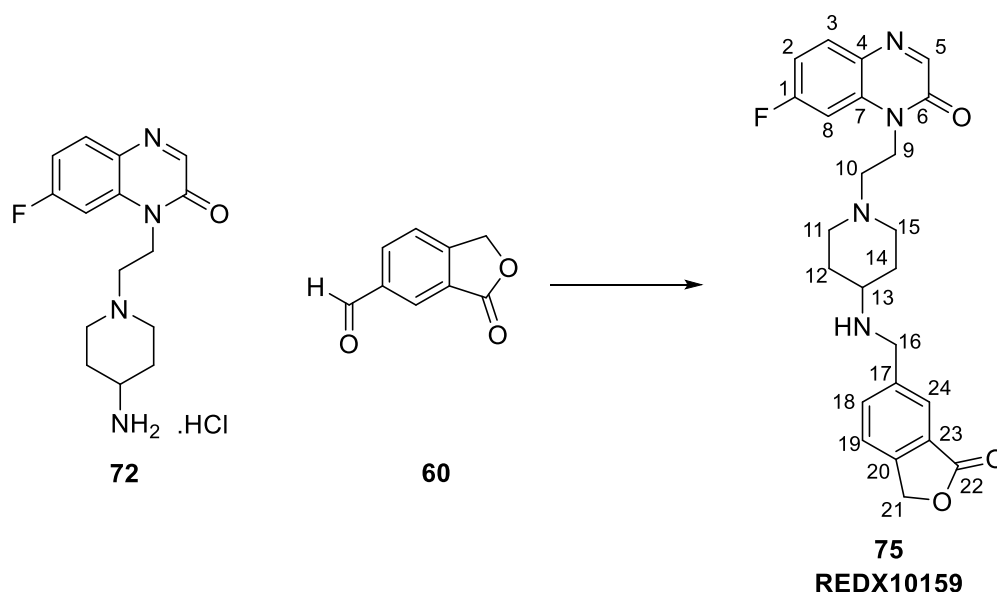
Following *General Procedure B:* (a) 3-oxo-1*H*-isobenzofuran-5-carbaldehyde **60**, 20 mg, 0.12 mmol, (b) [1-[2-(7-fluoro-2-oxo-quinoxalin-1-yl)ethyl]-4-piperidyl]ammonium chloride **72**, 41 mg, 0.13 mmol, (c) triethylamine, 20 μL, 0.14 mmol, (d) THF, 2 mL, (e) 78 mg, 0.37 mmol, (f) 2 mL, (g) 2 × 5 mL, (h) 0-50% MeOH in DCM, (j) 15 mg, 0.03 mmol, 28% yield; off-white solid.

M.pt.: 160 - 162 °C.

v_{max} (neat): 3406 (N-H stretch), 2938 (C-H stretch), 1760 (C=O (γ-lactone) stretch), 1662 (C=O (amide) stretch), 1617, 1589, 1456, 1366, 1312, 1054, 999 cm^{-1}.

δ_H (400 MHz, CDCl$_3$) 8.24 (s, 1H, 5-ArH), 7.91 (s, 1H, 24-ArH), 7.88 (dd, *J* = 8.9 Hz, $^3J_{H-F}$ = 6.0 Hz, 1H, 3-ArH), 7.72 (d, *J* = 7.9 Hz, 1H, 18-ArH), 7.47 (d, *J* = 7.9 Hz, 1H, 19-ArH), 7.17 (dd, $^3J_{H-F}$ = 10.4 Hz, $^4J_{H-H}$ = 2.5 Hz, 1H, 8-ArH), 7.09 (ddd, *J* = 8.9 Hz, $^3J_{H-F}$ = 7.9 Hz, $^4J_{H-H}$ = 2.5 Hz, 1H, 2-ArH), 5.33 (s, 2H, 21-CH$_2$), 4.38 – 4.30 (m, 2H, 9-CH$_2$), 3.95 (s, 2H, 16-CH$_2$), 3.05 – 2.95 (m, 2H, 11-CH* and 15-CH*), 2.73 – 2.66 (m, 2H, 10-CH$_2$), 2.61 – 2.52 (m, 1H, 13-CH), 2.26 – 2.17 (m, 2H, 11-CH* and 15-CH*), 1.97 – 1.91 (m, 2H, 12-CH* and 14-CH*), 1.52 – 1.39 (m, 2H, 12-CH* and 14-CH*) *axial/equatorial protons could not be assigned.

δ_C (101 MHz, CDCl$_3$) 171.1 (22-C), 163.9 (d, $^1J_{C-F}$ = 252.5 Hz, 1-C), 154.7 (6-C), 149.0 (5-C), 145.4 (23-C), 142.4 (17-C), 134.2 (18-C), 132.6 (d, $^3J_{C-F}$ = 11.1 Hz, 3-C), 130.4 (4-C and 7-C), 126.0 (20-C), 124.9 (24-C), 122.1 (19-C), 111.7 (d, $^2J_{C-F}$ = 24.2 Hz, 2-C), 101.1 (d, $^2J_{C-F}$ =

28.3 Hz, 8-C), 69.6 (21-C), 54.6 (10-C), 53.9 (13-C), 52.7 (11-C and 15-C), 50.1 (16-C), 40.4 (9-C), 32.5 (12-C and 14-C).

LCMS (Method C) R_T = 0.95 mins, [M+H]+ 437.4 (100%).

HRMS: ($C_{24}H_{25}FN_4O_3$) [M+H]+ requires 437.1983, found [M+H]+ 437.1983.

tert-butyl *N*-[1-[2-(7-fluoro-2-oxo-1,5-naphthyridin-1-yl)ethyl]-4-piperidyl]carbamate (71)
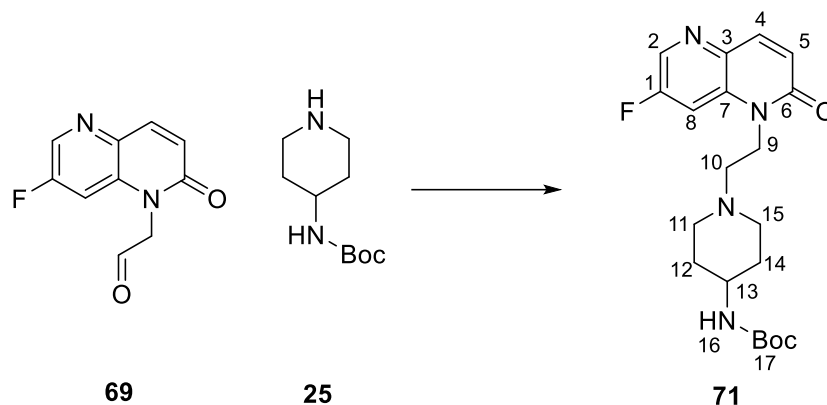
Following *General Procedure B:* (a) 2-(7-fluoro-2-oxo-1,5-naphthyridin-1(2*H*)-yl)acetaldehyde **69**, 800 mg, 3.88 mmol, (b) 4-Boc-aminopiperidine **25**, 778 mg, 3.88 mmol, (d) THF, 40 mL, (e) 904 mg, 4.27 mmol, (f) 20 mL, (g) 2 × 20 mL, (h) 0-100% EtOAc in petroleum ether (bp. 40-60), (j) 1.17 g, 3.00 mmol, 77% yield; white solid.

δ_H (400 MHz, CDCl$_3$) 8.47 − 8.43 (m, 1H, 8-ArH), 7.91 (d, *J* = 9.8 Hz, 1H, 4-ArH), 7.58 − 7.50 (m, 1H, 2-ArH), 6.88 (d, *J* = 9.8 Hz, 1H, 5-ArH), 4.33 (t, *J* = 7.1 Hz, 2H, 9-CH$_2$), 3.53 − 3.48 (m, 1H, 13-CH), 2.97 − 2.89 (m, 2H, 2 × piperidine-CH), 2.67 (t, *J* = 7.1 Hz, 2H, 10-CH$_2$), 2.33 − 2.23 (m, 2H, 2 × piperidine-CH), 2.01 − 1.92 (m, 2H, 2 × piperidine-CH), 1.47 (s, 9H, 3 × 17-CH$_3$), 1.45 − 1.35 (m, 2H, 2 × piperidine-CH).

LCMS (Method C) R_T = 1.13 mins, [M+H]+ 391.4 (100%).

[1-[2-(7-fluoro-2-oxo-1,5-naphthyridin-1-yl)ethyl]-4-piperidyl]ammonium chloride (73)

Following *General Procedure C:* (a) *tert*-butyl *N*-[1-[2-(7-fluoro-2-oxo-1,5-naphthyridin-1-yl)ethyl]-4-piperidyl]carbamate **71**, 1.17 g, 3.00 mmol, (b) 80 mL, (c) 7.49 mL, 29.96 mmol, (d) 1.26 g, 3.86 mmol, 129% crude yield; light pink solid.

Diethyl ether was observed in ^{1}H NMR spectrum, and could not be removed from the product under vacuum. It was presumed to be part of the crystal structure, owing to > 100% yield.

LCMS (Method C) R_T = 0.38 mins, [M+H]+ 291.3 (100% purity).

7-fluoro-1-[2-[4-[(3-oxo-1*H*-isobenzofuran-5-yl)methylamino]-1-piperidyl]ethyl]-1,5-naphthyridin-2-one (76)

Following *General Procedure B:* (a) 3-oxo-1*H*-isobenzofuran-5-carbaldehyde **60**, 20 mg, 0.12 mmol, (b) [1-[2-(7-fluoro-2-oxo-quinoxalin-1-yl)ethyl]-4-piperidyl]ammonium chloride **73**, 41 mg, 0.13 mmol, (c) triethylamine, 21 μL, 0.15 mmol, (d) THF, 2 mL, (e) 78 mg,

0.37 mmol, (f) 2 mL, (g) 2 × 5 mL, (h) 0-50% MeOH in DCM, (j) 5 mg, 0.01 mmol, 9% yield; off-white solid.

M.pt.: 151 − 152 °C.

v_{max} (neat): 3385 (N-H stretch), 2938 (C-H stretch), 2819, 1760 (C=O (γ-lactone) stretch), 1653 (C=O (amide) stretch), 1588, 1456, 1389, 1318, 1052, 1002 cm^{-1}.

δ_H (400 MHz, CDCl$_3$) 8.47 − 8.42 (m, 1H, 8-ArH), 7.95 − 7.87 (m, 2H, 4-ArH and 24-ArH), 7.71 (dd, J = 7.9 Hz, $^4J_{H-H}$ = 1.5 Hz, 1H, 18-ArH), 7.60 (d, $^3J_{H-F}$ = 9.9 Hz, 1H, 2-ArH), 7.47 (d, J = 7.9 Hz, 1H, 19-ArH), 6.88 (d, J = 9.9 Hz, 1H, 5-ArH), 5.33 (s, 2H, 21-CH$_2$), 4.36 (t, J = 7.2 Hz, 2H, 9-CH$_2$), 3.95 (s, 2H, 16-CH$_2$), 3.06 − 3.00 (m, 2H, 11-CH* and 15-CH*), 2.69 (t, J = 7.2 Hz, 2H, 10-CH$_2$), 2.62 − 2.50 (m, 1H, 13-CH), 2.28 − 2.20 (m, 2H, 11-CH* and 15-CH*), 1.97 − 1.93 (m, 2H, 12-CH* and 14-CH*), 1.50 − 1.43 (m, 2H, 12-CH* and 14-CH*) *axial/equatorial protons could not be assigned.

δ_C (101 MHz, CDCl$_3$) 171.2 (22-C), 161.3 (6-C), 159.4 (d, $^1J_{C-F}$ = 260.8 Hz, 1-C), 145.4 (23-C), 142.4 (17-C), 140.2 (4-C), 137.3 (7-C), 135.2 (3-C), 134.2 (18-C), 133.5 (d, $^2J_{C-F}$ = 31.5 Hz, 8-C), 126.0 (20-C), 124.9 (24-C), 124.3 (5-C), 122.1 (19-C), 108.5 (d, $^2J_{C-F}$ = 29.0 Hz, 2-C), 69.6 (21-C), 55.1 (10-C), 53.8 (13-C), 52.7 (11-C and 15-C), 50.2 (16-C), 41.0 (9-C), 32.5 (12-C and 14-C).

LCMS (Method C) R_T = 0.87 mins, [M+H]+ 437.4 (100%).

HRMS: (C$_{24}$H$_{25}$FN$_4$O$_3$) [M+H]+ requires 437.1983, found [M+H]+ 437.1982.

Lithium 2-(hydroxymethyl)-5-[[[1-[2-(7-methoxy-2-oxo-1,8-naphthyridin-1-yl)ethyl]-4-piperidyl]amino]methyl]benzoate (77)
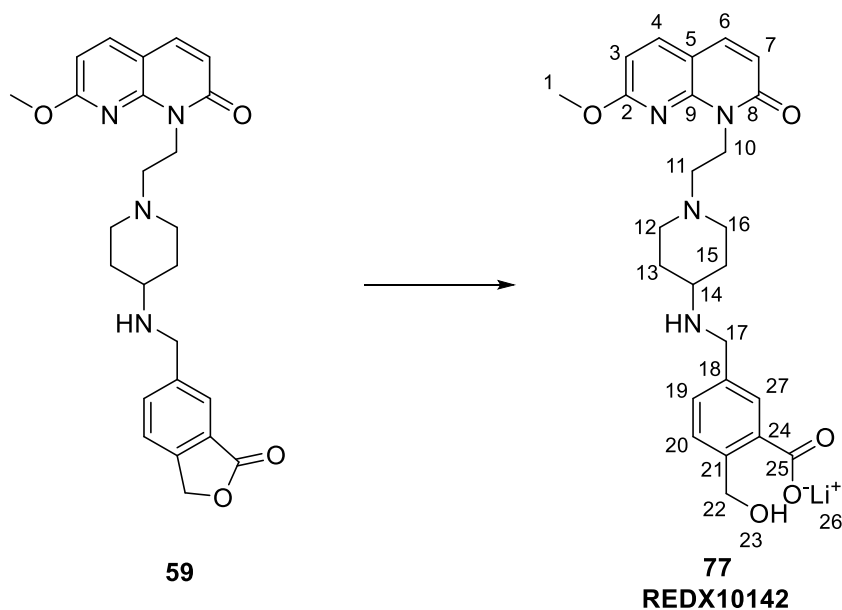
59

77
REDX10142

Following *General Procedure D*: (a) 7-methoxy-1-[2-[4-[(3-oxo-1*H*-isobenzofuran-5-yl)methylamino]-1-piperidyl]ethyl]-1,8-naphthyridin-2-one **59**, 5 mg, 0.01 mmol, (b) THF, 0.2 mL, water, 0.2 mL, (c) 111 µL, 0.1 M, 0.01 mmol, (d) isolated as lithium salt, (e) 4 mg, 0.009 mmol, 77% yield; white solid.

δ_H (400 MHz, DMSO-d$_6$) 8.05 (d, *J* = 8.4 Hz, 1H, 4-ArH), 7.86 (d, *J* = 9.4 Hz, 1H, 6-ArH), 7.69 (s, 1H, 27-ArH), 7.16 (d, *J* = 7.7 Hz, 1H, 19-ArH), 7.07 (d, *J* = 7.7 Hz, 1H, 20-ArH), 6.73 (d, *J* = 8.4 Hz, 1H, 3-ArH), 6.50 (d, *J* = 9.4 Hz, 1H, 7-ArH), 4.50 – 4.45 (m, 2H, 22-CH$_2$), 4.39 (s, 2H, 17-CH$_2$), 3.98 (s, 3H, 1-CH$_3$), 3.73 – 3.68 (m, 2H, 10-CH$_2$), 2.98 – 2.90 (m, 2H, 12-CH* and 16-CH*), 2.56 – 2.56 (m, 1H, 14-CH), 2.47 – 2.45 (m, 2H, 11-CH$_2$), 2.07 – 2.03 (m, 2H, 12-CH* and 16-CH*), 1.85 – 1.77 (m, 2H, 13-CH* and 15-CH*), 1.27 – 1.22 (m, 2H, 13-CH* and 15-CH*) *axial/equatorial protons could not be assigned.

LCMS (Method C) R$_T$ = 0.96 min, [M+H]+ 467.5 (84% purity), R$_T$ = 1.05 min, [M+H]+ 449.4 (16% purity). Minor peak relating to lactone observed in LCMS, but is absent in ^{1}H NMR spectrum.

Lithium 5-[[[1-[2-(7-fluoro-2-oxo-quinoxalin-1-yl)ethyl]-4-piperidyl]amino]methyl]-2-(hydroxymethyl)benzoate (78)
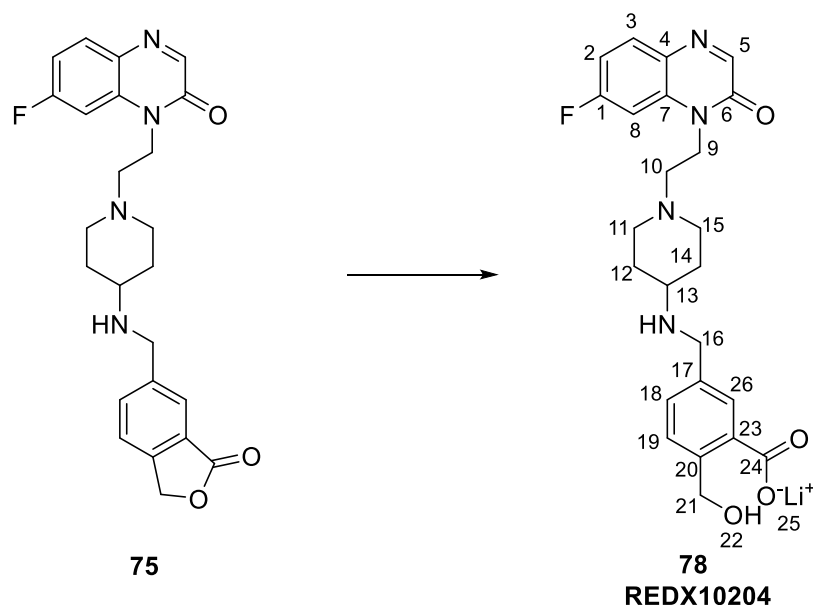
75   **78**
                                    REDX10204

Following *General Procedure D*: (a) 7-methoxy-1-[2-[4-[(3-oxo-1*H*-isobenzofuran-5-yl)methylamino]-1-piperidyl]ethyl]-1,8-naphthyridin-2-one **75**, 4 mg, 0.01 mmol, (b) THF, 0.2 mL, water, 0.2 mL, (c) 0.1 M, 92 μL, 0.01 mmol, (d) isolated as lithium salt, (e) 2 mg, 0.004 mmol, 48% yield; white solid.

δ$_H$ (400 MHz, CD$_3$OD) 8.17 (s, 1H, 5-ArH), 7.91 (dd, J = 8.9 Hz, $^3J_{H-F}$ = 6.0 Hz, 1H, 3-ArH), 7.73 (d, $^4J_{H-H}$ = 1.7 Hz, 1H, 26-ArH), 7.46 (dd, $^3J_{H-F}$ = 10.7 Hz, $^4J_{H-H}$ = 2.5 Hz, 1H, 8-ArH), 7.37 − 7.30 (m, 2H, 18-ArH and 19-ArH), 7.20 (ddd, J = 8.9 Hz, $^3J_{H-F}$ = 8.1 Hz, $^4J_{H-H}$ = 2.5 Hz, 1H, 2-ArH), 4.69 (s, 2H, 21-CH$_2$), 4.45 − 4.39 (m, 2H, 9-CH$_2$), 3.81 (s, 2H, 16-CH$_2$), 3.10 − 3.04 (m, 2H, 11-CH* and 15-CH*), 2.72 − 2.66 (m, 2H, 10-CH$_2$), 2.57 − 2.48 (m, 1H, 13-CH), 2.20 − 2.10 (m, 2H, 11-CH* and 15-CH*), 1.99 − 1.91 (m, 2H, 12-CH* and 14-CH*), 1.51 − 1.39 (m, 2H, 12-CH* and 14-CH*) *axial/equatorial protons could not be assigned.

LCMS (Method C) R$_T$ = 0.86 min, [M+H]+ 455.4 (100% purity).

Butyl (*E*)-3-(3-oxo-1*H*-isobenzofuran-4-yl)prop-2-enoate (81)

83   **81**
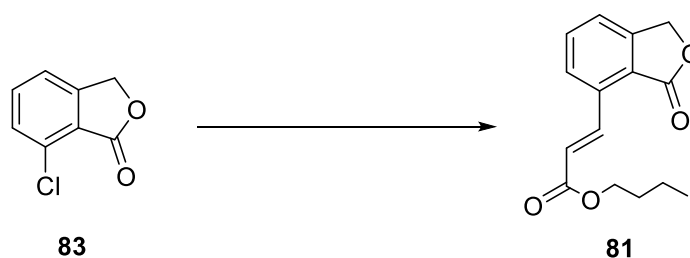
Following *General Procedure E*: (a) 7-chloroisobenzofuran-1(3*H*)-one **83**, 500 mg, 2.97 mmol, (b) 95 mg, 0.19 mmol, (c) 2.07 mL, 14.83 mmol, (d) 0.64 mL, 4.44 mmol, (e) 0-100% EtOAc in petroleum ether (bp. 40-60), (f) 422 mg, 1.62 mmol, 55% yield; brown solid.

LCMS (Method C) R_T = 1.83 min, [M+H]+ 261.2 (100% purity).

3-oxo-1*H*-isobenzofuran-4-carbaldehyde (80)

Following *General Procedure F*: (a) 0.20 mL, 0.03 mmol, (b) butyl (*E*)-3-(3-oxo-1*H*-isobenzofuran-4-yl)prop-2-enoate **81**, 422 mg, 1.62 mmol, (c) 5 mL, (d) 5 mL, (e) 1.04 g, 4.86 mmol, (f) 5 mL, (g) 2 × 5 mL, (h) 0-100% DCM in petroleum ether (bp. 40-60), (i) 202 mg, 1.25 mmol, 77% yield; off-white solid.

M.pt.: 125 - 127 °C.

v_{max} (neat): 2876 (C-H stretch), 1744 (C=O (γ-lactone) stretch), 1693 (C=O (aldehyde) stretch), 1589, 1453, 1242, 1200, 1052 cm^{-1}.

δ_H (400 MHz, CDCl$_3$) 11.13 (s, 1H, 9-CH), 8.13 (dd, *J* = 7.6 Hz, $^4J_{H-H}$ = 0.9 Hz, 1H, 1-ArH), 7.85 (dd, *J* = 7.6 Hz, $^4J_{H-H}$ = 0.9 Hz, 1H, 3-ArH), 7.77 (t, *J* = 7.6 Hz, 1H, 2-ArH), 5.46 (s, 2H, 5-CH$_2$).

δ_C (101 MHz, CDCl$_3$) 188.9 (9-C), 169.8 (6-C), 147.4 (4-C), 134.7 (7-C), 134.3 (3-C), 127.3 (1-C or 2-C), 127.2 (1-C or 2-C), 125.8 (8-C), 69.9 (5-C).

LCMS (Method C) R_T = 1.16 min [M+H]+ 163.1 (100% purity).

HRMS: (C$_9$H$_6$O$_3$) [M+H]+ requires 163.0390, found [M+H]+ 163.0387.

7-methoxy-1-[2-[4-[[(3-oxo-1*H*-isobenzofuran-4-yl)methylamino]-1-piperidyl]ethyl]-1,8-naphthyridin-2-one (84)

84
REDX10248
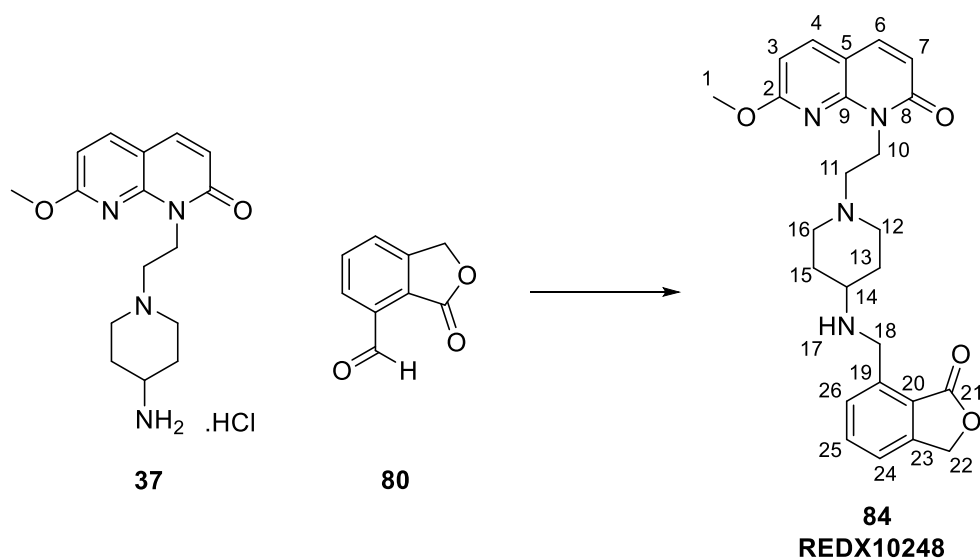
Following *General Procedure B:* (a) 3-oxo-1*H*-isobenzofuran-4-carbaldehyde **80**, 30 mg, 0.19 mmol, (b) [1-[2-(7-methoxy-2-oxo-1,8-naphthyridin-1-yl)ethyl]-4-piperidyl]ammonium chloride **37**, 60 mg, 0.18 mmol, (c) triethylamine, 30 μL, 0.22 mmol, (d) THF, 3 mL, (e) 113 mg, 0.53 mmol, (f) 3 mL, (g) 2 × 10 mL, (h) 0-50% MeOH in DCM, (j) 22 mg, 0.05 mmol, 28% yield; yellow solid.

M.pt.: 96 - 98 °C.

v_{max} (neat): 3414 (N-H stretch), 2949 (C-H stretch), 2824, 1750 (C=O (γ-lactone) stretch), 1650 (C=O (amide) stretch), 1589, 1449, 1397, 1277, 1055, 999 cm^{-1}.

$δ_H$ (400 MHz, CDCl$_3$) 7.73 (d, *J* = 8.4 Hz, 1H, 4-ArH), 7.67 − 7.62 (m, 1H, 25-ArH), 7.58 (d, *J* = 9.4 Hz, 1H, 6-ArH), 7.53 (d, *J* = 7.5 Hz, 1H, 26-ArH), 7.40 (d, *J* = 7.6 Hz, 1H, 24-ArH), 6.63 (d, *J* = 8.4 Hz, 1H, 3-ArH), 6.59 (d, *J* = 9.4 Hz, 1H, 7-ArH), 5.33 (s, 2H, 22-CH$_2$), 4.74 − 4.65 (m, 2H, 10-CH$_2$), 4.26 (s, 2H, 18-CH$_2$), 4.04 (s, 3H, 1-CH$_3$), 3.20 − 3.12 (m, 2H, 12-CH* and 16-CH*), 2.85 − 2.76 (m, 2H, 11-CH$_2$), 2.72 − 2.60 (m, 1H, 14-CH), 2.38 − 2.28 (m, 2H, 12-CH* and 16-CH*), 1.97 (s, 2H, 13-CH* and 15-CH*), 1.61 − 1.55 (m, 2H, 13-CH* and 15-CH*) *axial/equatorial protons could not be assigned.

$δ_C$ (101 MHz, CDCl$_3$) 171.3 (21-C), 164.2 (2-C), 163.1 (8-C), 148.8 (9-C), 147.5 (23-C), 140.8 (19-C), 139.0 (4-C), 137.3 (6-C), 134.3 (25-C), 129.7 (26-C), 123.2 (20-C), 121.0 (24-C), 119.0 (7-C), 109.5 (5-C), 106.3 (3-C), 69.5 (22-C), 54.9 (11-C), 54.0 (1-C), 53.8 (14-C), 52.0 (12-C and 16-C), 46.1 (18-C), 38.3 (10-C), 31.5 (13-C and 15-C).

LCMS (Method C) R_T = 0.99 mins, [M+H]+ 449.4 (100%).

HRMS: ($C_{25}H_{28}N_4O_4$) [M+H]+ requires 449.2183, found [M+H]+ 449.2177.

7-fluoro-1-[2-[4-[(3-oxo-1*H*-isobenzofuran-4-yl)methylamino]-1-piperidyl]ethyl]quinoxalin-2-one (85)
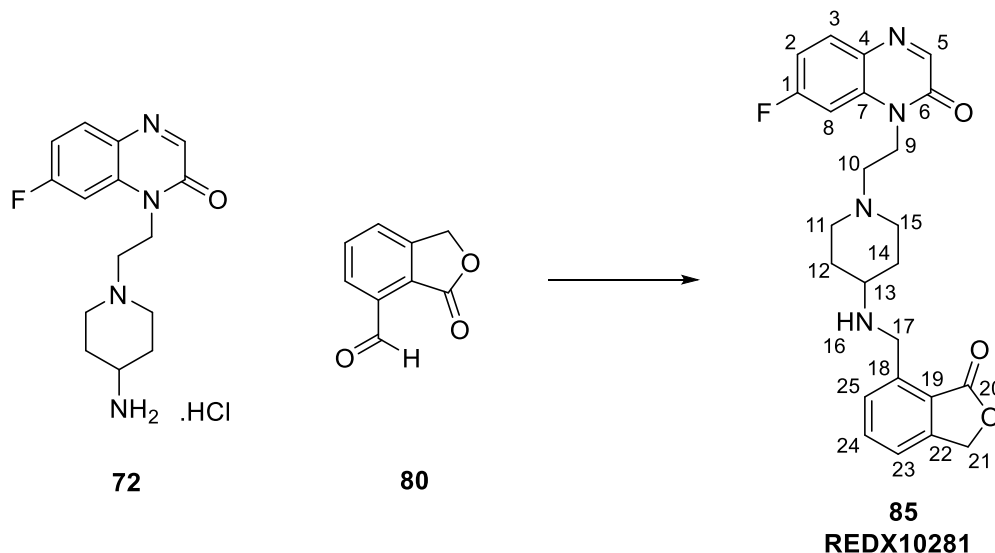
72   **80**

85
REDX10281

Following *General Procedure B:* (a) 3-oxo-1*H*-isobenzofuran-4-carbaldehyde **80**, 30 mg, 0.19 mmol, (b) [1-[2-(7-fluoro-2-oxo-quinoxalin-1-yl)ethyl]-4-piperidyl]ammonium chloride **72**, 63 mg, 0.19 mmol, (c) triethylamine, 32 µL, 0.23 mmol, (d) THF, 3 mL, (e) 118 mg, 0.56 mmol, (f) 3 mL, (g) 2 × 10 mL, (h) 0-50% MeOH in DCM, (j) 24 mg, 0.06 mmol, 30% yield; brown solid.

M.pt.: 152 - 154 °C.

ν_{max} (neat): 3405 (N-H stretch), 2949 (C-H stretch), 2823, 1751 (C=O (γ-lactone) stretch), 1663 (C=O (amide) stretch), 1617, 1589, 1452, 1366, 1316, 1052, 1003 cm^{-1}.

δ_H (400 MHz, CDCl$_3$) 8.23 (s, 1H, 5-ArH), 7.88 (dd, *J* = 8.9 Hz, $^4J_{H-F}$ = 6.0 Hz, 1H, 3-ArH), 7.67 (t, *J* = 7.5 Hz, 1H, 24-ArH), 7.57 (d, *J* = 7.5 Hz, 1H, 25-ArH), 7.43 (d, *J* = 7.5 Hz, 1H, 23-ArH), 7.25 – 7.19 (m, 1H, 8-ArH), 7.09 (ddd, *J* = 8.9 Hz, $^3J_{H-F}$ = 7.9 Hz, $^4J_{H-H}$ = 2.5 Hz, 1H, 2-ArH), 5.35 (s, 2H, 21-CH$_2$), 4.41 – 4.36 (m, 2H, 9-CH$_2$), 4.30 (s, 2H, 17-CH$_2$), 3.14 – 3.05 (m, 2H, 11-CH* and 15-CH*), 2.79 – 2.70 (m, 3H, 10-CH$_2$ and 13-CH), 2.32 (s, 2H, 11-CH* and 15-CH*), 2.06 – 2.01 (m, 2H, 12-CH* and 14-CH*), 1.73 – 1.62 (m, 2H, 12-CH* and 14-CH*) *axial/equatorial protons could not be assigned.

δ_C (101 MHz, CDCl₃) 171.4 (20-C), 164.0 (d, $^1J_{C-F}$ = 202.0 Hz, 1-C), 154.6 (6-C), 148.83 (5-C), 147.6 (22-C), 139.4 (18-C), 134.4 (24-C), 134.2 (25-C), 132.6 (d, $^3J_{C-F}$ = 8.1 Hz, 3-C), 130.4 (4-C or 7-C), 130.1 (4-C or 7-C), 123.4 (19-C), 121.4 (23-C), 111.8 (d, $^2J_{C-F}$ = 19.2 Hz, 2-C), 101.1 (d, $^2J_{C-F}$ = 22.2 Hz, 8-C), 69.7 (21-C), 54.0 (10-C), 52.1 (11-C and 15-C), 50.8 (13-C), 45.9 (17-C), 39.9 (9-C), 30.8 (12-C and 14-C).

LCMS (Method C) R_T = 0.94 mins, [M+H]+ 437.4 (100%).

HRMS: (C₂₄H₂₅FN₄O₃) [M+H]+ requires 437.1983, found [M+H]+ 437.1981.

Lithium 2-(hydroxymethyl)-6-[[[1-[2-(7-methoxy-2-oxo-1,8-naphthyridin-1-yl)ethyl]-4-piperidyl]amino]methyl]benzoate (86)
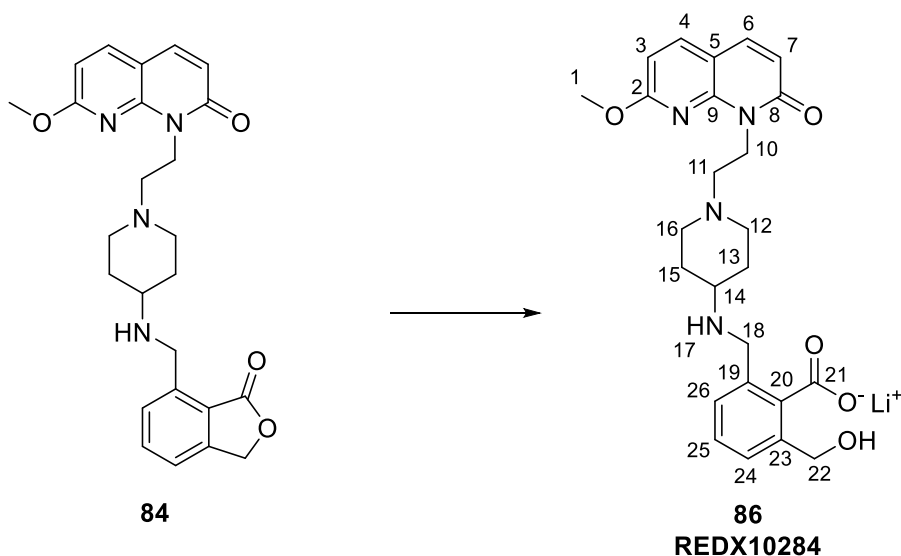
84

86
REDX10284

Following *General Procedure D*: (a) 7-methoxy-1-[2-[4-[(3-oxo-1*H*-isobenzofuran-4-yl)methylamino]-1-piperidyl]ethyl]-1,8-naphthyridin-2-one **84**, 5 mg, 0.01 mmol, (b) THF, 0.2 mL, water, 0.2 mL, (c) 111 µL, 0.1 M, 0.01 mmol, (d) isolated as lithium salt, (e) 5 mg, 0.01 mmol, 97% yield; white solid.

δ_H (400 MHz, CD₃OD) 7.98 (d, *J* = 8.5 Hz, 1H, 4-ArH), 7.86 (d, *J* = 9.4 Hz, 1H, 6-ArH), 7.41 − 7.37 (m, 1H, ArH), 7.29 − 7.22 (m, 2H, 2 × ArH), 6.74 (d, *J* = 8.5 Hz, 1H, 3-ArH), 6.57 (d, *J* = 9.4 Hz, 1H, 7-ArH), 4.75 − 4.65 (m, 4H, 10-CH₂ and 18-CH₂), 4.07 (s, 3H, 1-CH₃), 3.82 (s, 2H, 22-CH₂), 3.18 − 3.10 (m, 2H, 11-CH₂), 2.79 − 2.70 (m, 2H, 12-CH* and 16-CH*), 2.62 − 2.51 (m, 1H, 14-CH), 2.28 − 2.17 (m, 2H, 12-CH* and 16-CH*), 1.99 − 1.94 (m, 2H, 13-CH* and 15-CH*), 1.56 − 1.42 (m, 2H, 13-CH* and 15-CH*) *axial/equatorial protons could not be assigned.

LCMS (Method C) R_T = 0.98 min, [M+H]+ 467.5 (97% purity), R_T = 1.07 min, [M+H]+ 449.5 (3% purity) Minor peak relating to lactone observed in LCMS, but is absent in ^{1}H NMR spectrum.

Butyl (*E*)-3-(1-oxoisochroman-7-yl)prop-2-enoate (88)
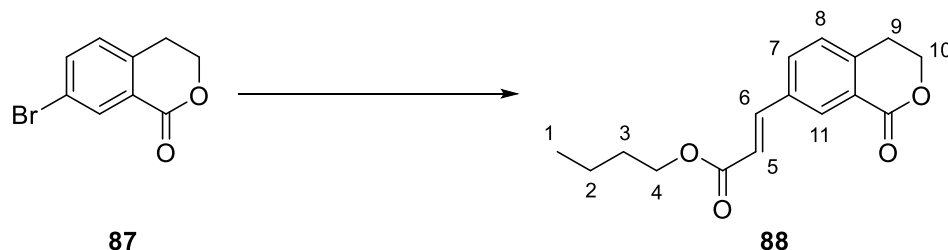
Following *General Procedure E*: (a) 7-bromoisochroman-1-one **87**, 500 mg, 2.20 mmol, (b) 70 mg, 0.14 mmol, (c) 1.53 mL, 11.0 mmol, (d) 0.48 mL, 3.33 mmol, (e) 0-100% EtOAc in petroleum ether (bp. 40-60), (f) 270 mg, 0.98 mmol, 45% yield; brown solid.

δ_H (400 MHz, CDCl$_3$) 8.29 (d, $^4J_{H-H}$ = 1.8 Hz, 1H, 11-ArH), 7.71 (dd, *J* = 7.9 Hz, $^4J_{H-H}$ = 1.8 Hz, 1H, 7-ArH), 7.70 (d, *J* = 16.0 Hz, 1H, 6-CH), 7.33 (d, *J* = 7.9 Hz, 1H, 8-ArH), 6.54 (d, *J* = 16.0 Hz, 1H, 5-CH), 4.58 (t, *J* = 6.0 Hz, 2H, 10-CH$_2$), 4.24 (t, *J* = 6.7 Hz, 2H, 4-CH$_2$), 3.11 (t, *J* = 6.0 Hz, 2H, 9-CH$_2$), 1.78 − 1.65 (m, 2H, 3-CH$_2$), 1.52 − 1.41 (m, 2H, 2-CH$_2$), 0.99 (t, *J* = 7.4 Hz, 3H, 1-CH$_3$).

LCMS (Method C) R_T = 1.83 mins, [M+H]+ 275.2 (100%).

1-oxoisochromane-7-carbaldehyde (89)
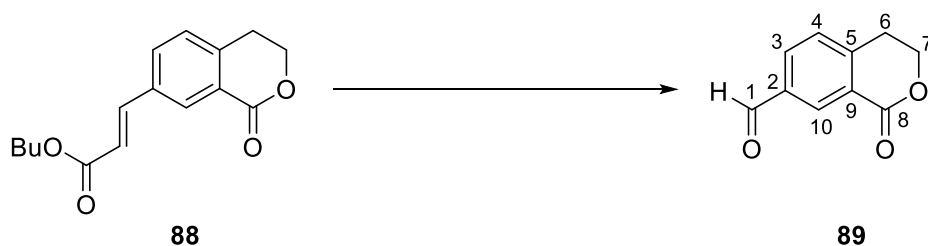
Following *General Procedure F*: (a) 0.12 mL, 0.02 mmol, (b) butyl (*E*)-3-(1-oxoisochroman-7-yl)prop-2-enoate **88**, 270 mg, 0.98 mmol, (c) 2.5 mL, (d) 2.5 mL, (e) 633 mg, 2.96 mmol, (f) 5 mL, (g) 2 × 10 mL, (h) 0-100% DCM in petroleum ether (bp. 40-60), (i) 120 mg, 0.68 mmol, 69% yield; white solid.

M.pt.: 135 - 137 °C.

ν_{max} (neat): 2973, 2918 (C-H stretch), 1717 (C=O (lactone) stretch), 1683 (C=O (aldehyde) stretch), 1609, 1393, 1241, 1172, 1086 cm^{-1}.

δ_H (400 MHz, CDCl$_3$) 10.09 (s, 1H, 1-CH), 8.61 (d, $^4J_{H-H}$ = 1.7 Hz, 1H, 10-ArH), 8.11 (dd, J = 7.9 Hz, $^4J_{H-H}$ = 1.7 Hz, 1H, 3-ArH), 7.49 (dd, J = 7.9 Hz, 1H, 4-ArH), 4.66 − 4.58 (m, 2H, 7-CH$_2$), 3.19 (t, J = 6.0 Hz, 2H, 6-CH$_2$).

δ_C (101 MHz, CDCl$_3$) 190.7 (1-C), 163.9 (8-C), 145.7 (5-C), 136.1 (9-C), 133.2 (10-C), 132.7 (3-C), 128.4 (4-C), 126.3 (2-C), 66.9 (7-C), 28.2 (6-C).

LCMS (Method C) R$_T$ = 1.17 mins, [M+H]+ 177.1 (100%).

HRMS: (C$_{10}$H$_8$O$_3$) [M+H]+ requires 177.0546, found [M+H]+ 177.0545.

7-methoxy-1-[2-[4-[[(1-oxoisochroman-7-yl)methylamino]-1-piperidyl]ethyl]-1,8-naphthyridin-2-one (90)

90
REDX10359
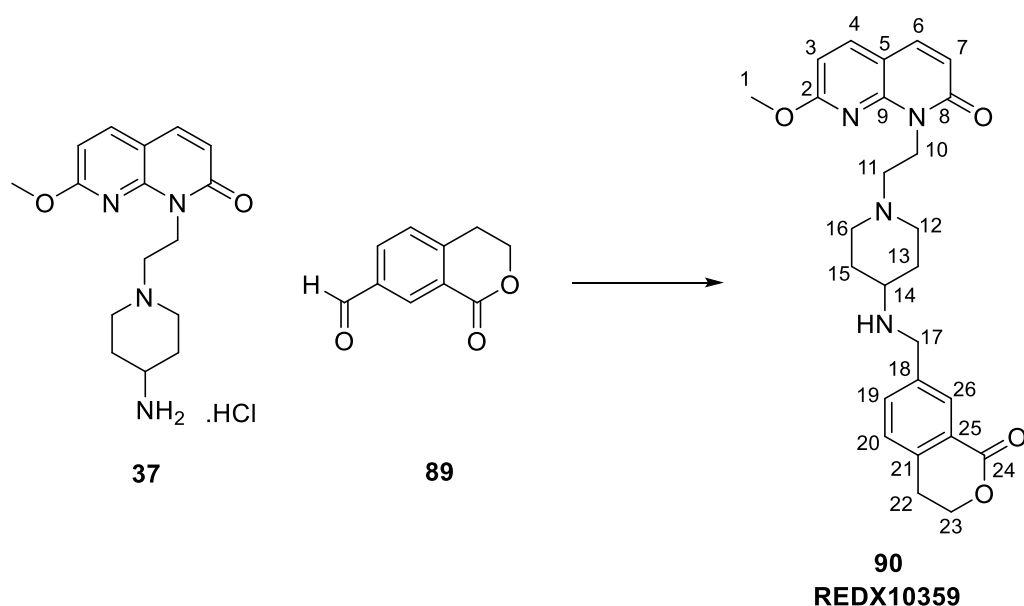
Following *General Procedure B:* (a) 1-oxoisochromane-7-carbaldehyde **89**, 26 mg, 0.15 mmol, (b) [1-[2-(7-methoxy-2-oxo-1,8-naphthyridin-1-yl)ethyl]-4-piperidyl]ammonium chloride **37**, 50 mg, 0.15 mmol, (c) triethylamine, 25 μL, 0.18 mmol, (d) THF, 2 mL, (e) 94 mg, 0.44 mmol, (f) 3 mL, (g) 2 × 10 mL, (h) 0-50% MeOH in DCM, (j) 12 mg, 0.03 mmol, 18% yield; white solid.

M.pt.: 133 - 136 °C.

v$_{max}$ (neat): 3400 (N-H stretch), 2952 (C-H stretch), 2838, 1719 (C=O (γ-lactone) stretch), 1649 (C=O (amide) stretch), 1609, 1397, 1278, 1275, 1055, 1032, 999 cm^{-1}.

δ_H (400 MHz, CDCl$_3$) 8.07 (d, $^4J_{H-H}$ = 1.9 Hz, 1H, 26-ArH), 7.77 − 7.70 (m, 2H, 4-ArH and 19-ArH), 7.60 (d, J = 9.4 Hz, 1H, 6-ArH), 7.31 (d, J = 8.0 Hz, 1H, 20-ArH), 6.64 (d, J = 8.4 Hz,

1H, 3-ArH), 6.59 (d, J = 9.4 Hz, 1H, 7-ArH), 4.79 − 4.69 (m, 2H, 10-CH$_2$), 4.60 − 4.50 (m, 2H, 23-CH$_2$), 4.05 (s, 3H, 1-CH$_3$), 3.97 (s, 2H, 17-CH$_2$), 3.33 − 3.23 (m, 2H, 12-CH* and 16-CH*), 3.07 (t, J = 6.0 Hz, 2H, 22-CH$_2$), 2.96 − 2.86 (m, 2H, 11-CH$_2$), 2.86 − 2.78 (m, 1H, 14-CH), 2.51 − 2.40 (m, 2H, 12-CH* and 16-CH*), 2.14 − 2.05 (m, 2H, 13-CH* and 15-CH*), 1.85 − 1.73 (m, 2H, 13-CH* and 15-CH*) *axial/equatorial protons could not be assigned.

δ_C (101 MHz, CDCl$_3$) 165.0 (24-C), 164.4 (2-C), 163.2 (8-C), 148.6 (9-C), 139.2 (19-C), 139.1 (18-C), 137.6 (6-C), 136.5 (21-C), 134.4 (4-C), 130.5 (26-C), 127.9 (20-C), 125.4 (25-C), 118.8 (7-C), 109.6 (5-C), 106.6 (3-C), 67.3 (23-C), 54.4 (1-C), 54.2 (11-C), 53.0 (14-C), 51.4 (12-C and 16-C), 48.8 (17-C), 37.7 (10-C), 29.6 (13-C and 15-C), 27.6 (22-C).

LCMS (Method C) R$_T$ = 1.02 mins, [M+H]+ 463.4 (100%).

HRMS: (C$_{26}$H$_{30}$N$_4$O$_4$) [M+H]+ requires 463.2340, found [M+H]+ 463.2332.

7-fluoro-1-[2-[4-[(1-oxoisochroman-7-yl)methylamino]-1-piperidyl]ethyl]-1,5-naphthyridin-2-one (91)

73   **89**   **91**
REDX10386
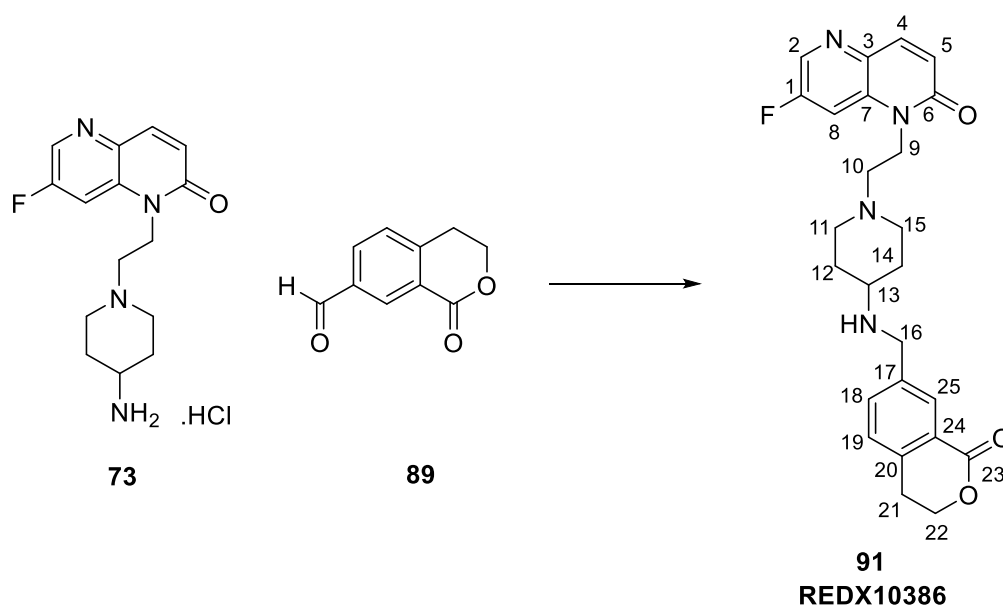
Following *General Procedure B:* (a) 1-oxoisochromane-7-carbaldehyde **89**, 25 mg, 0.14 mmol, (b) [1-[2-(7-fluoro-2-oxo-1,5-naphthyridin-1-yl)ethyl]-4-piperidyl]ammonium chloride **73**, 45 mg, 0.14 mmol, (c) triethylamine, 23 μL, 0.17 mmol, (d) THF, 2 mL, (e) 87 mg, 0.41 mmol, (f) 3 mL, (g) 2 × 10 mL, (h) 0-50% MeOH in DCM, (j) 30 mg, 0.07 mmol, 48% yield; white solid.

M.pt.: glass transition at 159 °C, decomposition at 184 °C.

ν_{max} (neat): 3306 (N-H stretch), 2933 (C-H stretch), 2816, 1721 (C=O (γ-lactone) stretch), 1661 (C=O (amide) stretch), 1590, 1563, 1388, 1314, 1217, 1179, 1126, 1091, 999 cm^{-1}.

δ_H (400 MHz, CDCl$_3$) 8.46 – 8.41 (m, 1H, 2-ArH), 8.06 (d, $^4J_{H-H}$ = 1.9 Hz, 1H, 25-ArH), 7.91 (d, J = 9.8 Hz, 1H, 4-ArH), 7.69 – 7.63 (m, 1H, 8-ArH), 7.58 (dd, J = 7.8 Hz, $^4J_{H-H}$ = 1.9 Hz, 1H, 18-ArH), 7.26 (d, J = 7.8 Hz, 1H, 19-ArH), 6.88 (d, J = 9.8 Hz, 1H, 5-ArH), 4.56 (t, J = 6.4 Hz, 2H, 22-CH$_2$), 4.39 (t, J = 7.3 Hz, 2H, 9-CH$_2$), 3.87 (s, 2H, 16-CH$_2$), 3.09 – 3.00 (m, 4H, 11-CH*, 15-CH* and 21-CH$_2$), 2.71 (t, J = 7.3 Hz, 2H, 10-CH$_2$), 2.64 – 2.54 (m, 1H, 13-CH), 2.33 – 2.23 (m, 2H, 11-CH* and 15-CH*), 1.99 – 1.87 (m, 2H, 12-CH* and 14-CH*), 1.57 – 1.44 (m, 2H, 12-CH* and 14-CH*) *axial/equatorial protons could not be assigned.

δ_C (101 MHz, CDCl$_3$) 165.2 (23-C), 161.3 (6-C), 159.5 (d, $^1J_{C-F}$ = 273.7 Hz, 1-C), 140.2 (4-C and 17-C), 138.3 (20-C), 137.3 (7-C), 135.2 (3-C), 133.6 (18-C), 133.5 (d, $^2J_{C-F}$ = 24.2 Hz, 2-C), 129.8 (25-C), 127.5 (19-C), 125.3 (24-C), 124.3 (5-C), 108.5 (d, $^2J_{C-F}$ = 23.2 Hz, 8-C), 67.4 (22-C), 54.9 (10-C), 53.6 (13-C), 52.6 (11-C and 15-C), 50.1 (16-C), 40.8 (9-C), 32.1 (12-C and 14-C), 27.6 (21-C).

LCMS (Method C) R_T = 0.90 mins, [M+H]+ 451.4 (100% purity).

HRMS: (C$_{25}$H$_{27}$FN$_4$O$_3$) [M+H]+ requires 451.2140, found [M+H]+ 451.2137.

Lithium 5-[[[1-[2-(7-fluoro-2-oxo-1,5-naphthyridin-1-yl)ethyl]-4-piperidyl]amino]methyl]-2-(2-hydroxyethyl)benzoate (92)

91

92
REDX10403
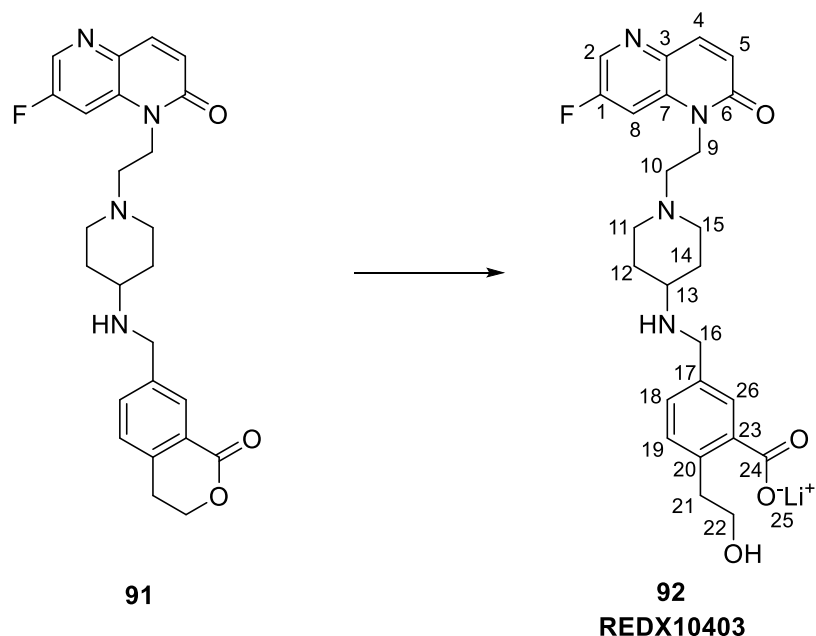
Following *General Procedure D*: (a) 7-fluoro-1-[2-[4-[(1-oxoisochroman-7-yl)methylamino]-1-piperidyl]ethyl]-1,5-naphthyridin-2-one **92**, 7.2 mg, 0.02 mmol, (b) THF, 0.2 mL, water, 0.2 mL, (c) 160 μL, 0.1 M, 0.02 mmol, (d) isolated as lithium salt, (e) 5 mg, 0.01 mmol, 67% yield; white solid.

$δ_H$ (400 MHz, CD₃OD) 8.54 − 8.49 (m, 1H, 2-ArH), 8.04 − 7.95 (m, 2H, 4-ArH and 26-ArH), 7.55 − 7.31 (m, 1H, 8-ArH), 7.33 (dd, *J* = 7.9 Hz, $^4J_{H-H}$ = 2.0 Hz, 1H, 18-ArH), 7.27 (d, *J* = 7.9 Hz, 1H, 19-ArH), 6.89 (d, *J* = 9.8 Hz, 1H, 5-ArH), 4.45 (t, *J* = 7.0 Hz, 2H, 9-CH₂), 3.95 (s, 2H, 16-CH₂), 3.83 − 3.78 (m, 2H, 22-CH₂), 3.16 − 3.05 (m, 4H, 11-CH*, 15-CH* and 21-CH₂), 2.85 − 2.75 (m, 1H, 13-CH), 2.69 (t, *J* = 7.0 Hz, 2H, 10-CH₂), 2.23 − 2.13 (m, 2H, 11-CH* and 15-CH*), 2.09 − 2.01 (m, 2H, 12-CH* and 14-CH*), 1.60 − 1.45 (m, 2H, 12-CH* and 14-CH*) *axial/equatorial protons could not be assigned.

$δ_C$ (101 MHz, CDCl₃) 169.8 (23-C), 161.3 (6-C), 159.5 (d, $^1J_{C-F}$ = 261.6 Hz, 1-C), 141.6 (17-C), 140.3 (4-C), 137.2 (7-C), 137.2 (20-C), 135.2 (3-C), 134.4 (18-C), 133.6 (d, $^2J_{C-F}$ = 25.3 Hz, 2-C), 125.7 (24-C), 125.0 (26-C), 124.2 (5-C), 120.8 (19-C), 108.6 (d, $^2J_{C-F}$ = 23.2 Hz, 8-C), 85.4 (22-C), 54.6 (10-C), 53.5 (13-C), 52.4 (11-C and 15-C), 50.0 (16-C), 40.5 (9-C), 31.8 (12-C and 14-C), 27.4 (21-C).

LCMS (Method C) R_T = 0.79 min, [M+H]+ 469.4 (100% purity).

Methyl 2-acetyl-5-chloro-benzoate (102)
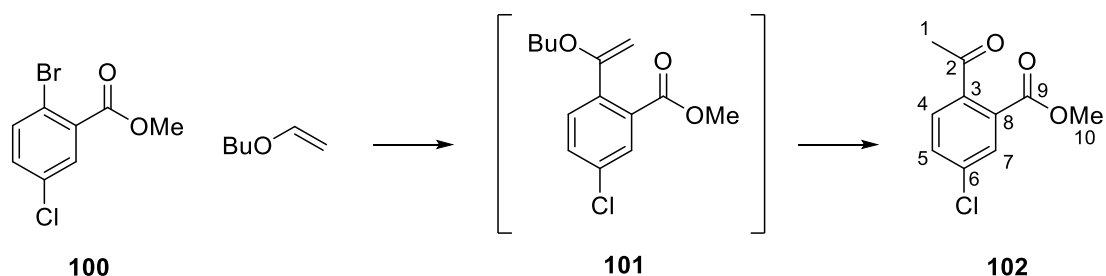
Following an adapted procedure from Springfield *et al.*,[96] to a solution of methyl 2-bromo-5-chlorobenzoate **100** (2 g, 8.02 mmol), tri-*o*-tolylphosphine (354 mg, 1.16 mmol) and Pd(OAc)₂ (54 mg, 0.24 mmol) in MeCN (10 mL) in a microwave vial was added DIPEA (4.33 mL, 24.85 mmol) and butyl vinyl ether (2.07 mL, 16.03 mmol), and the vial was sealed and purged with nitrogen. The reaction vessel was heated to 80 °C in a Biotage Initiator microwave reactor for 2 h. The reaction mixture was cooled to RT and concentrated *in vacuo*, and the resulting residue was azeotroped with toluene (3 mL) and suspended in toluene (5 mL) for 16 h. The reaction mixture was filtered and the precipitate

was washed with toluene (2 × 5 mL). The combined organic layers were cooled in an ice bath under nitrogen, and phosphoric acid (85% wt%, 4.34 mL, 64.99 mmol) was added dropwise over 20 min. The reaction was warmed to RT and stirred for 30 min, after which, the acidic layer was separated and washed with toluene (3 × 5 mL). The combined organic phases were washed with sodium bicarbonate solution (50% aq., 5 mL), then brine (5 mL), then dried (MgSO$_4$), filtered and concentrated *in vacuo* to give methyl 2-acetyl-5-chloro-benzoate **102** (1.32 g, 6.21 mmol, 77% yield) as an orange oil.

δ$_H$ (400 MHz, CDCl$_3$) 7.83 (d, $^4J_{H-H}$ = 2.1 Hz, 1H, 7-ArH), 7.56 (dd, J = 8.2 Hz, $^4J_{H-H}$ = 2.1 Hz, 1H, 5-ArH), 7.42 (d, J = 8.2 Hz, 1H, 4-ArH), 3.93 (s, 3H, 10-CH$_3$), 2.55 (s, 3H, 1-CH$_3$).

LCMS (Method C) R$_T$ = 1.60 mins, [M+H]+ 181.0 (91% purity), R$_T$ = 1.24 mins, [M+H]+ 430.5 (2% purity), R$_T$ = 2.24 mins, [M+H]+ 181.0, 153.0 (7% purity).

Lithium 2-acetyl-5-chloro-benzoate (103)
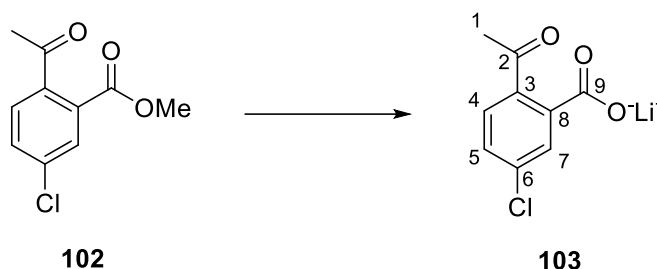
A solution of methyl 2-acetyl-5-chloro-benzoate **102** (500 mg, 2.35 mmol) and LiOH (56 mg, 2.35 mmol) dissolved in THF (2 mL) and H$_2$O (2 mL) was stirred at RT for 1 h, after which, the reaction mixture was concentrated *in vacuo* to give lithium 2-acetyl-5-chloro-benzoate **103** (467 mg, 2.28 mmol, 97% yield) as an orange oil.

δ$_H$ (400 MHz, CD$_3$OD) 7.67 (dd, $^4J_{H-H}$ = 2.0 Hz, $^5J_{H-H}$ = 0.6 Hz, 1H, 7-ArH), 7.41 – 7.39 (m, 2H, 4-ArH and 5-ArH), 2.53 (s, 3H, 1-CH$_3$).

LCMS (Method C) R$_T$ = 1.36 mins, [M+H]- 197.1 (95% purity), R$_T$ = 2.21 mins, [M+H]+ 181.1, 153.1 (5% purity).

6-chloro-3-methyl-3*H*-isobenzofuran-1-one (104)
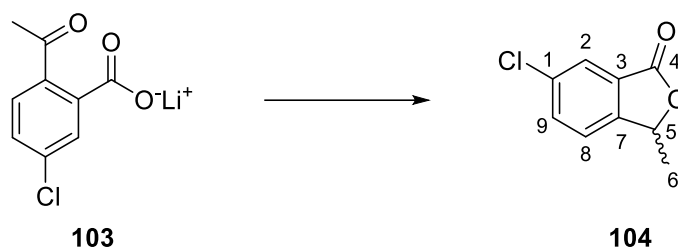
Following an adapted procedure from Lüthy *et al.*,[97] to a solution of 2-acetyl-5-chloro-benzoic acid **103** (467 mg, 2.35 mmol) in sodium hydroxide (2 M, 1.18 mL, 2.35 mmol) was added sodium borohydride (89 mg, 2.35 mmol) portion-wise. The reaction mixture was heated to 100 °C for 30 min, and was then cooled to room temperature and acidified to pH 1 with HCl (conc.). The biphasic system was loaded directly onto a pre-equilibrated cartridge and purified by silica gel column chromatography (gradient = 0-100 EtOAc in petroleum ether (bp. 40-60)). The appropriate fractions were combined then concentrated *in vacuo* to give 6-chloro-3-methyl-3*H*-isobenzofuran-1-one **104** (310 mg, 1.70 mmol, 72% yield) as an orange oil.

δ_H (400 MHz, CDCl$_3$) 7.88 (d, $^4J_{H-H}$ = 1.9 Hz, 1H, 2-ArH), 7.67 (dd, *J* = 8.2 Hz, $^4J_{H-H}$ = 1.9 Hz, 1H, 9-ArH), 7.41 (d, *J* = 8.1 Hz, 1H, 8-ArH), 5.58 (q, *J* = 6.7 Hz, 1H, 5-CH), 1.66 (d, *J* = 6.7 Hz, 3H, 6-CH$_3$).

LCMS (Method C) R$_T$ = 1.55 mins, [M+H]- 183.0 (100% purity).

Butyl (*E*)-3-(1-methyl-3-oxo-1*H*-isobenzofuran-5-yl)prop-2-enoate (94)
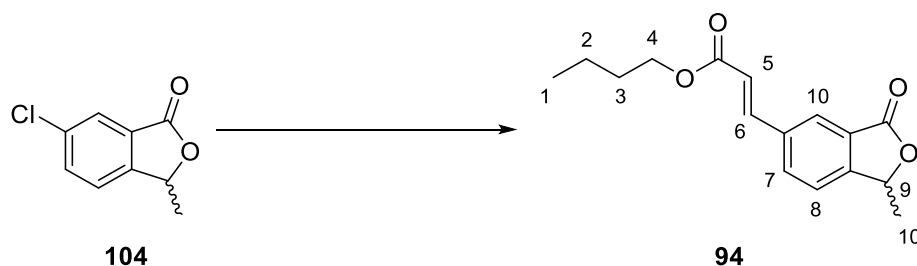
Following *General Procedure E*: (a) 6-chloro-3-methyl-3*H*-isobenzofuran-1-one **104**, 310 mg, 1.70 mmol, (b) 52 mg, 0.10 mmol, (c) 1.18 mL, 8.47 mmol, (d) 0.37 mL, 2.57 mmol, (e) 0-100% EtOAc in petroleum ether (bp. 40-60), (f) 385 mg, 1.40 mmol, 83% yield; brown oil.

δ_H (400 MHz, CDCl$_3$) 7.97 (s, 1H, 10-ArH), 7.74 (d, *J* = 8.0 Hz, 1H, 7-ArH), 7.67 (d, *J* = 16.0 Hz, 1H, 6-CH), 7.40 (d, *J* = 8.0 Hz, 1H, 8-ArH), 6.47 (d, *J* = 16.0 Hz, 1H, 5-CH), 5.52 (q, *J* = 6.8 Hz,

1H, 9-ArH), 4.16 (t, J = 6.9 Hz, 2H, 4-CH$_2$), 1.69 – 1.51 (m, 5H, 3-CH$_2$ and 10-CH$_3$), 1.45 – 1.30 (m, 2H, 2-CH$_2$), 0.90 (t, J = 7.4 Hz, 3H, 1-CH$_3$).

LCMS (Method A) R_T = 2.69 min. No ionisation observed.

1-methyl-3-oxo-1*H*-isobenzofuran-5-carbaldehyde (93)
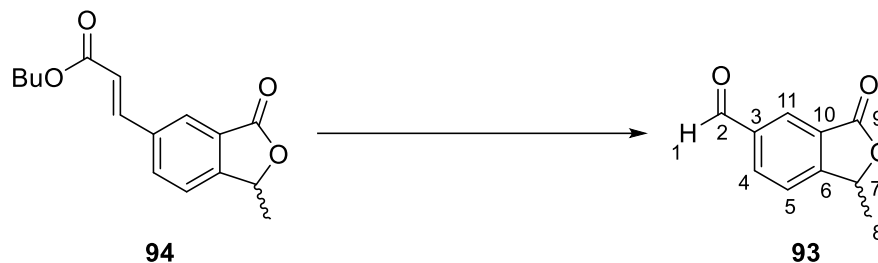
Following *General Procedure F*: (a) 0.38 mL, 0.06 mmol, (b) butyl (*E*)-3-(1-methyl-3-oxo-1*H*-isobenzofuran-5-yl)prop-2-enoate **94,** 385 mg, 1.49 mmol, (c) 3 mL, (d) 3 mL, (e) 956 mg, 4.47 mmol, (f) 5 mL, (g) 2 × 5 mL, (h) 0-100% DCM in petroleum ether (bp. 40-60), (i) 136 mg, 0.77 mmol, 52% yield; white solid.

M.pt.: 89 - 90 °C.

ν_{max} (neat): 3043 (C-H (aliphatic) stretch), 1766 (C=O (γ-lactone) stretch), 1694 (C=O (aldehyde) stretch), 1621, 1441, 1228, 1160, 1116, 1044 cm^{-1}.

δ_H (400 MHz, CDCl$_3$) 10.15 (s, 1H, 1-CH), 8.41 (s, 1H, 11-ArH), 8.26 (d, J = 7.9 Hz, 1H, 4-ArH), 7.64 (d, J = 7.9 Hz, 1H, 5-ArH), 5.68 (q, J = 6.8 Hz, 1H, 7-CH), 1.72 (d, J = 6.8 Hz, 3H, 8-CH$_3$).

δ_C (101 MHz, CDCl$_3$) 190.4 (2-C), 169.0 (9-C), 156.4 (6-C), 137.6 (3-C), 134.1 (4-C), 128.1 (11-C), 127.1 (10-C), 122.6 (5-C), 77.9 (7-C), 20.2 (8-C).

LCMS (Method C) R_T = 1.25 mins, [M+H]+ 177.1.

HRMS: (C$_{10}$H$_8$O$_3$) [M+H]+ requires 177.0546, found [M+H]+ 177.0545.

7-methoxy-1-[2-[4-[[(1-methyl-3-oxo-1*H*-isobenzofuran-5-yl)methylamino]-1-piperidyl]ethyl]-1,8-naphthyridin-2-one (105)

105
REDX10370
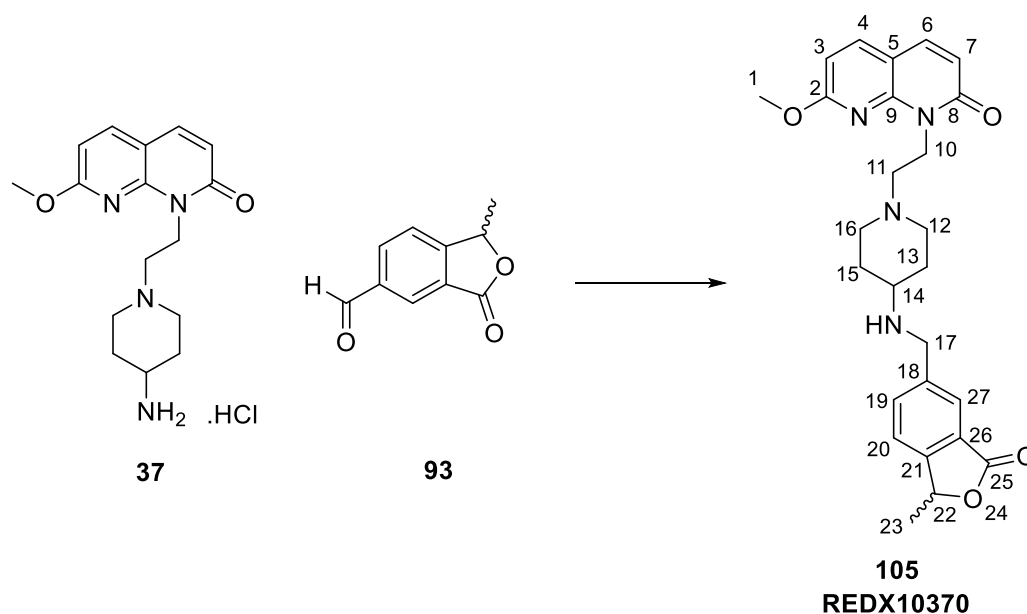
Following *General Procedure B:* (a) 1-methyl-3-oxo-1*H*-isobenzofuran-5-carbaldehyde **93**, 26 mg, 0.15 mmol, (b) [1-[2-(7-methoxy-2-oxo-1,8-naphthyridin-1-yl)ethyl]-4-piperidyl]ammonium chloride **37**, 50 mg, 0.15 mmol, (c) triethylamine, 25 µL, 0.18 mmol, (d) THF, 3 mL, (e) 94 mg, 0.44 mmol, (f) 3 mL, (g) 2 × 10 mL, (h) 0-50% MeOH in DCM, (j) 7 mg, 0.015 mmol, 10% yield; white solid.

δ_H (400 MHz, CDCl$_3$) 7.88 (s, 1H, 27-ArH), 7.79 − 7.70 (m, 2H, 4-ArH and 19-ArH), 7.61 (d, *J* = 9.4 Hz, 1H, 6-ArH), 7.43 (d, *J* = 7.8 Hz, 1H, 20-ArH), 6.66 (d, *J* = 8.4 Hz, 1H, 3-ArH), 6.60 (d, *J* = 9.4 Hz, 1H, 7-ArH), 5.58 (q, *J* = 6.7 Hz, 1H, 22-CH), 4.93 − 4.73 (m, 2H, 10-CH$_2$), 4.09 (s, 3H, 1-CH$_3$), 3.95 (s, 2H, 17-CH$_2$), 3.37 − 3.21 (m, 2H, 12-CH* and 16-CH*), 3.05 − 2.90 (m, 2H, 11-CH$_2$), 2.80 − 2.65 (m, 1H, 14-CH), 2.66 − 2.39 (m, 2H, 12-CH* and 16-CH*), 2.17 − 2.05 (m, 2H, 13-CH* and 15-CH*), 1.74 − 1.68 (m, 2H, 13-CH* and 15-CH*), 1.65 (d, *J* = 6.7 Hz, 3H, 23-CH$_3$) *axial/equatorial protons could not be assigned.

LCMS (Method C) R$_T$ = 1.07 mins, [M+H]+ 463.5 (100%).

7-fluoro-1-[2-[4-[(1-methyl-3-oxo-1*H*-isobenzofuran-5-yl)methylamino]-1-piperidyl]ethyl]-1,5-naphthyridin-2-one (106)

106
REDX10371
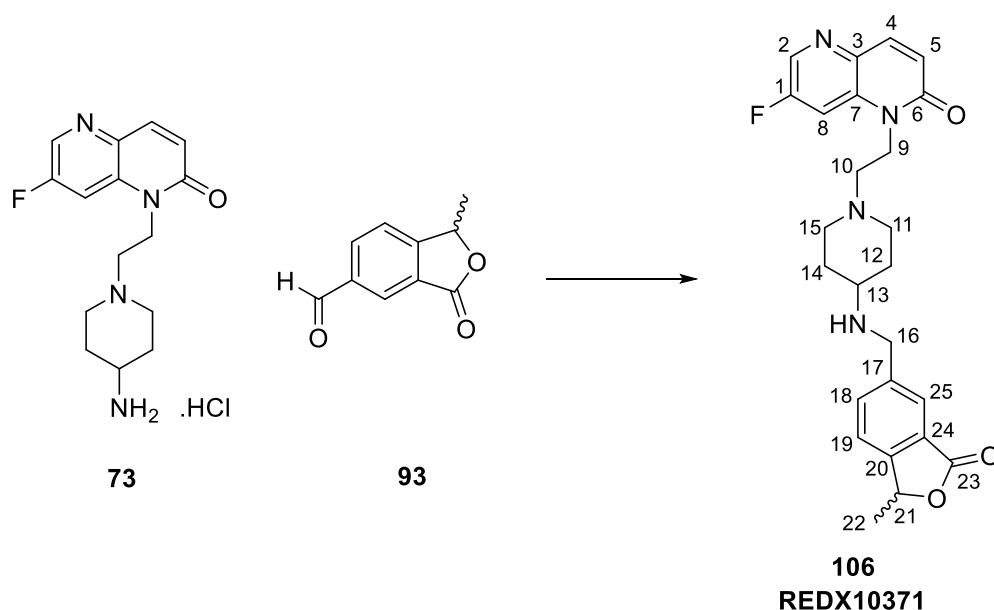
Following *General Procedure B:* (a) 1-methyl-3-oxo-1*H*-isobenzofuran-5-carbaldehyde **93**, 27 mg, 0.15 mmol, (b) [1-[2-(7-fluoro-2-oxo-1,5-naphthyridin-1-yl)ethyl]-4-piperidyl]ammonium chloride **73**, 50 mg, 0.15 mmol, (c) triethylamine, 25 μL, 0.18 mmol, (d) THF, 3 mL, (e) 94 mg, 0.44 mmol, (f) 3 mL, (g) 2 × 10 mL, (h) 0-50% MeOH in DCM, (j) 12 mg, 0.027 mmol, 17% yield; white solid.

M.pt.: decomposition at 136 - 138 °C.

v_{max} (neat): 2962 (C-H stretch), 1746 (C=O (γ-lactone) stretch), 1659 (C=O (amide) stretch), 1588, 1561, 1444, 1310, 1216, 1150, 1044 cm^{-1}.

$δ_H$ (400 MHz, CDCl$_3$) 8.48 − 8.43 (m, 1H, 2-ArH), 7.92 (d, *J* = 9.8 Hz, 1H, 4-ArH), 7.87 (s, 1H, 25-ArH), 7.70 (d, *J* = 7.7 Hz, 1H, 18-ArH), 7.69 − 7.64 (m, 1H, 8-ArH), 7.42 (d, *J* = 7.7 Hz, 1H, 19-ArH), 6.88 (d, *J* = 9.8 Hz, 1H, 5-ArH), 5.58 (q, *J* = 6.7 Hz, 1H, 21-CH), 4.40 (t, *J* = 7.4 Hz, 2H, 9-CH$_2$), 3.94 (s, 2H, 16-CH$_2$), 3.12 − 3.02 (m, 2H, 11-CH* and 15-CH*), 2.74 − 2.68 (m, 2H, 10-CH$_2$), 2.66 − 2.56 (m, 1H, 13-CH), 2.37 − 2.30 (m, 2H, 11-CH* and 15-CH*), 2.02 − 1.94 (m, 2H, 12-CH* and 14-CH*), 1.65 (d, *J* = 6.7 Hz, 3H, 22-CH$_3$), 1.57 − 1.44 (m, 2H, 12-CH* and 14-CH*) *axial/equatorial protons could not be assigned.

$δ_C$ (125 MHz, CDCl$_3$) 171.1 (23-C), 161.3 (6-C), 159.5 (d, $^1J_{C-F}$ = 260.6 Hz, 1-C), 150.1 (20-C), 142.1 (17-C), 140.3 (4-C), 137.2 (7-C), 135.1 (3-C), 134.3 (18-C), 133.5 (d, $^2J_{C-F}$ = 25.3 Hz, 2-C), 126.1 (24-C), 124.9 (25-C), 124.3 (5-C), 121.6 (19-C), 108.6 (d, $^2J_{C-F}$ = 23.2 Hz, 8-C), 77.7

(21-C), 54.8 (10-C), 53.8 (13-C), 52.5 (11-C and 15-C), 50.1 (16-C), 40.7 (9-C), 32.0 (12-C and 14-C), 20.5 (22-C).

LCMS (Method C) R_T = 0.93 mins, [M+H]+ 451.4 (100%).

HRMS: ($C_{25}H_{27}FN_4O_3$) [M+H]+ requires 451.2140, found [M+H]+ 451.2139.

Method for separation of enantiomers of REDX10371 (106)

| **106** | **107** | **108** |
| **REDX10371** | (*R*)-REDX10371 | (*S*)-REDX10371 |
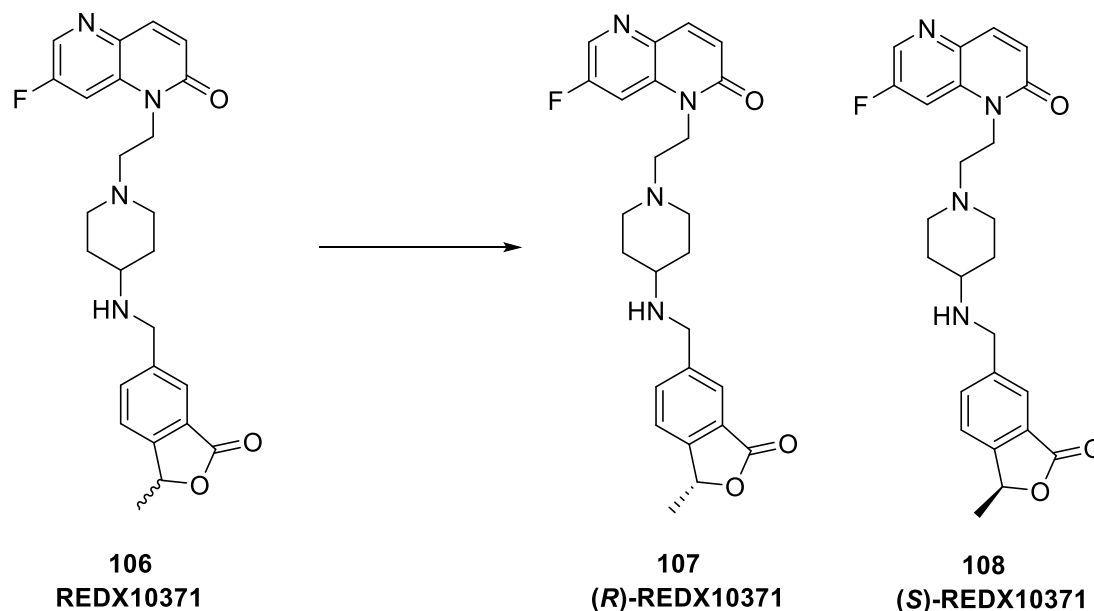
Enantiomers of REDX10371 **106** were separated *via* chiral preparative SFC, carried out on a MG II preparative SFC (SFC-1) using a ChiralPak AD (250 × 30 mm, 5 μm) column. Samples were dissolved in MeOH (25 mL) and injected onto the column portion-wise (4.2 mL aliquots). Mobile phase: 45% EtOH (+0.1% ammonium hydroxide as a modifier) in supercritical CO_2 for 12 min, flow rate = 50 mL/min. After separation, the fractions were concentrated *in vacuo*, before being assessed for their enantiomeric excess by SFC.

(*R*)-7-fluoro-1-(2-(4-(((1-methyl-3-oxo-1,3-dihydroisobenzofuran-5-yl)methyl)amino)piperidin-1-yl)ethyl)-1,5-naphthyridin-2(1*H*)-one (107)

107
(*R*)-REDX10371
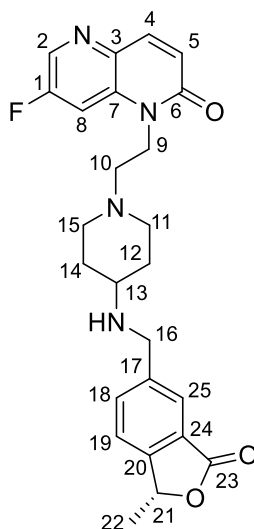
$δ_H$ (400 MHz, CDCl$_3$) 8.47 − 8.42 (m, 1H, 2-ArH), 7.91 (d, *J* = 9.8 Hz, 1H, 4-ArH), 7.87 (s, 1H, 25-ArH), 7.70 (d, *J* = 7.8 Hz, 1H, 18-ArH), 7.66 − 7.60 (m, 1H, 8-ArH), 7.41 (d, *J* = 7.8 Hz, 1H, 19-ArH), 6.88 (d, *J* = 9.8 Hz, 1H, 5-ArH), 5.57 (q, *J* = 6.7 Hz, 1H, 21-CH), 4.38 (t, *J* = 7.3 Hz, 2H, 9-CH$_2$), 3.94 (s, 2H, 16-CH$_2$), 3.08 − 3.00 (m, 2H, 11-CH* and 15-CH*), 2.72 − 2.66 (m, 2H, 10-CH$_2$), 2.60 − 2.53 (m, 1H, 13-CH), 2.30 − 2.19 (m, 2H, 11-CH* and 15-CH*), 1.98 − 1.92 (m, 2H, 12-CH* and 14-CH*), 1.65 (d, *J* = 6.7 Hz, 3H, 22-CH$_3$), 1.51 − 1.40 (m, 2H, 12-CH* and 14-CH*).

LCMS (Method C) R_T = 0.91 mins, [M+H]+ 451.3 (100%).

$[α]_D^{20}$ +13.7 (conc. = 0.168 g/100 mL)

Chiral SFC (for method, see below) R_T = 4.18 min, [M+H]+ 451.2, %ee > 99%.

Enantiomeric excess was determined by analytical SFC, carried out on a Waters UPC2 analytical SFC (SFC-H) using a ChiralPak AD-3 (150 × 4.6 mm, 3 μm) column. Mobile phase: 40% EtOH (+0.05% diethanolamine as a modifier) in supercritical CO$_2$ for 7 min, flow rate = 2.5 mL/min.

(*S*)-7-fluoro-1-(2-(4-(((1-methyl-3-oxo-1,3-dihydroisobenzofuran-5-yl)methyl)amino)piperidin-1-yl)ethyl)-1,5-naphthyridin-2(1*H*)-one (108)

108
(*S*)-REDX10371
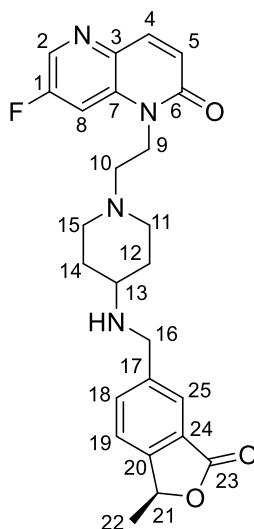
δ_H (400 MHz, CDCl$_3$) 8.47 – 8.41 (m, 1H, 2-ArH), 7.91 (d, *J* = 9.8 Hz, 1H, 4-ArH), 7.87 (s, 1H, 25-ArH), 7.70 (d, *J* = 7.7 Hz, 1H, 18-ArH), 7.64 – 7.58 (m, 1H, 8-ArH), 7.41 (d, *J* = 7.7 Hz, 1H, 19-ArH), 6.88 (d, *J* = 9.8 Hz, 1H, 5-ArH), 5.57 (q, *J* = 6.7 Hz, 1H, 21-CH), 4.37 (t, *J* = 7.3 Hz, 2H, 9-CH$_2$), 3.94 (s, 2H, 16-CH$_2$), 3.04 – 2.97 (m, 2H, 11-CH* and 15-CH*), 2.73 – 2.64 (m, 2H, 10-CH$_2$), 2.60 – 2.55 (m, 1H, 13-CH), 2.29 – 2.19 (m, 2H, 11-CH* and 15-CH*), 1.99 – 1.91 (m, 2H, 12-CH* and 14-CH*), 1.65 (d, *J* = 6.7 Hz, 3H, 22-CH$_3$), 1.50 – 1.41 (m, 2H, 12-CH* and 14-CH*).

LCMS (Method C) R$_T$ = 0.92 mins, [M+H]+ 451.2 (100%).

$[\alpha]_D^{20}$ -10.2 (conc. = 0.171 g/100 mL)

Chiral SFC (for method, see below) R$_T$ = 8.21 min, [M+H]+ 451.2, %ee > 99%.

Enantiomeric excess was determined by analytical SFC, carried out on a Waters UPC2 analytical SFC (SFC-H) using a ChiralPak AD-3 (150 × 4.6 mm, 3 μm) column. Mobile phase: 40% EtOH (+0.05% diethanolamine as a modifier) in supercritical CO$_2$ for 7 min, flow rate = 2.5 mL/min.

**Lithium 5-[[[1-[2-(7-fluoro-2-oxo-1,5-naphthyridin-1-yl)ethyl]-4-piperidyl]amino]methyl]-2-(1-hydroxyethyl)benzoate (109)**
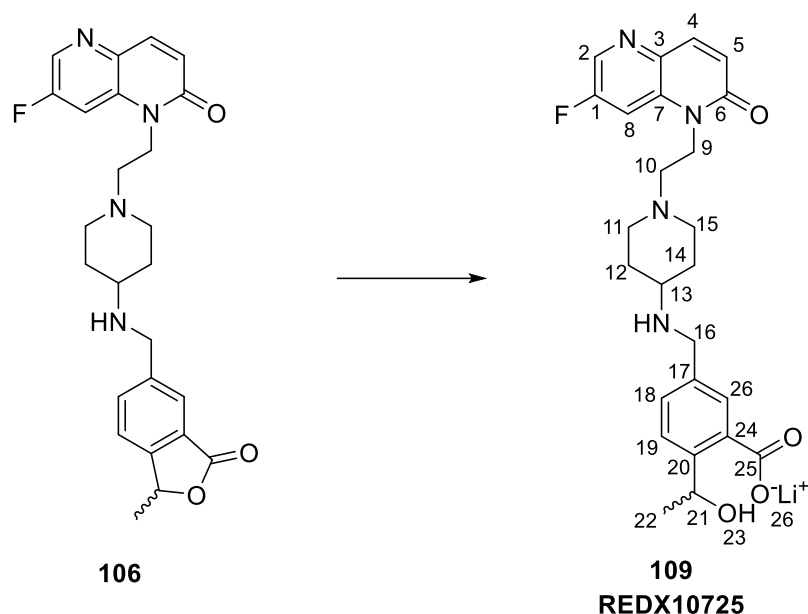
Following *General Procedure D*: (a) 7-fluoro-1-[2-[4-[(1-methyl-3-oxo-1*H*-isobenzofuran-5-yl)methylamino]-1-piperidyl]ethyl]-1,5-naphthyridin-2-one **106,** 11 mg, 0.02 mmol, (b) THF, 0.6 mL, water, 0.6 mL, (c) 240 μL, 0.1 M, 0.02 mmol, (d) isolated as lithium salt, (e) 10 mg, 0.02 mmol, 87% yield; white solid.

δ$_H$ (400 MHz, CD$_3$OD) 8.54 − 8.50 (m, 1H, 2-ArH), 8.04 − 7.95 (m, 2H, 4-ArH and 26-ArH), 7.56 − 7.50 (m, 1H, 8-ArH), 7.40 (d, *J* = 7.8 Hz, 1H, 19-ArH), 7.33 (dd, *J* = 7.8 Hz, $^4J_{H-H}$ = 2.0 Hz, 1H, 18-ArH), 6.89 (d, *J* = 9.8 Hz, 1H, 5-ArH), 5.10 (q, *J* = 6.5 Hz, 1H, 21-CH), 4.45 (t, *J* = 7.0 Hz, 2H, 9-CH$_2$), 3.79 (s, 2H, 16-CH$_2$), 3.10 − 3.02 (m, 2H, 11-CH*, 15-CH*), 2.70 − 2.61 (m, 2H, 10-CH$_2$), 2.58 − 2.47 (m, 1H, 13-CH), 2.21 − 2.10 (m, 2H, 11-CH* and 15-CH*), 1.98 − 1.92 (m, 2H, 12-CH* and 14-CH*), 1.51 (d, *J* = 6.5 Hz, 3H, 22-CH$_3$), 1.47 − 1.40 (m, 2H, 12-CH* and 14-CH*) *axial/equatorial protons could not be assigned.

LCMS (Method C) R$_T$ = 0.63 min, [M+H]+ 469.3 (100% purity).

Lithium 5-[[[1-[2-(7-fluoro-2-oxo-1,5-naphthyridin-1-yl)ethyl]-4-piperidyl]amino]methyl]-2-[(1R)-1-hydroxyethyl]benzoate (110)


107

110
(R)-REDX10725
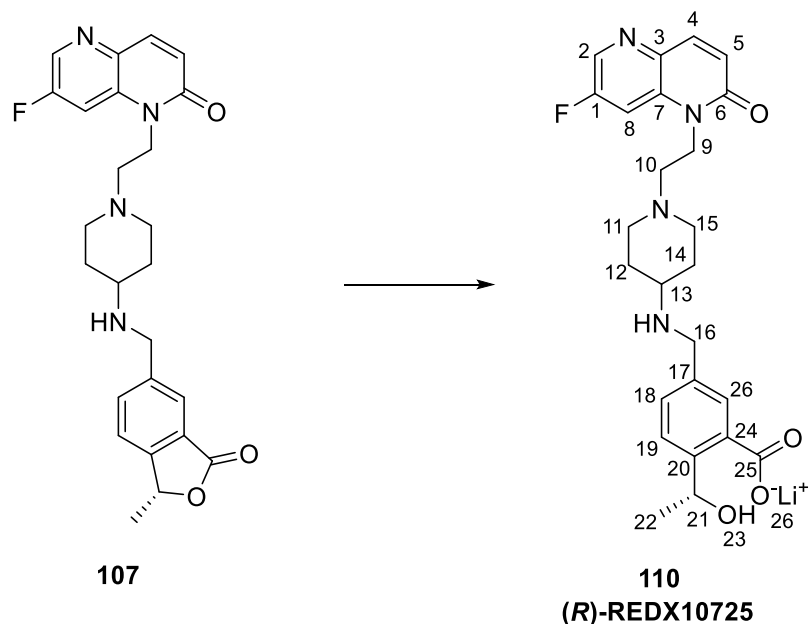
Following *General Procedure D*: (a) 7-fluoro-1-[2-[4-[[(1R)-1-methyl-3-oxo-1H-isobenzofuran -5-yl]methylamino]-1-piperidyl]ethyl]-1,5-naphthyridin-2-one **107**, 12 mg, 0.03 mmol, (b) THF, 0.6 mL, water, 0.6 mL, (c) 260 µL, 0.1 M, 0.03 mmol, (d) isolated as lithium salt, (e) 10 mg, 0.02 mmol, 80% yield; white solid.

δ_H (400 MHz, CD$_3$OD) 8.55 − 8.51 (m, 1H, 2-ArH), 8.04 − 7.95 (m, 2H, 4-ArH and 26-ArH), 7.54 − 7.50 (m, 1H, 8-ArH), 7.40 (d, *J* = 7.8 Hz, 1H, 19-ArH), 7.33 (dd, *J* = 7.8 Hz, $^4J_{H-H}$ = 2.0 Hz, 1H, 18-ArH), 6.89 (d, *J* = 9.8 Hz, 1H, 5-ArH), 5.10 (q, *J* = 6.5 Hz, 1H, 21-CH), 4.45 (t, *J* = 7.0 Hz, 2H, 9-CH$_2$), 3.79 (s, 2H, 16-CH$_2$), 3.10 − 3.02 (m, 2H, 11-CH*, 15-CH*), 2.70 − 2.61 (m, 2H, 10-CH$_2$), 2.58 − 2.47 (m, 1H, 13-CH), 2.21 − 2.10 (m, 2H, 11-CH* and 15-CH*), 1.98 − 1.92 (m, 2H, 12-CH* and 14-CH*), 1.51 (d, *J* = 6.5 Hz, 3H, 22-CH$_3$), 1.47 − 1.40 (m, 2H, 12-CH* and 14-CH*) *axial/equatorial protons could not be assigned.

LCMS (Method C) R$_T$ = 0.63 min, [M+H]+ 469.3 (100% purity).

Lithium 5-[[[1-[2-(7-fluoro-2-oxo-1,5-naphthyridin-1-yl)ethyl]-4-piperidyl]amino]methyl]-2-[(1S)-1-hydroxyethyl]benzoate (111)

108

111
(S)-REDX10725
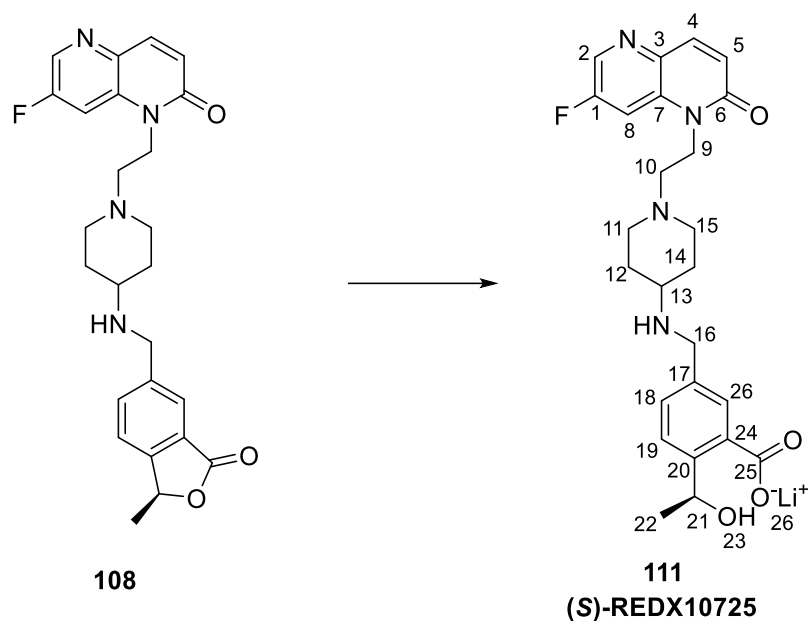
Following *General Procedure D*: (a) 7-fluoro-1-[2-[4-[[(1S)-1-methyl-3-oxo-1H-isobenzofuran-5-yl]methylamino]-1-piperidyl]ethyl]-1,5-naphthyridin-2-one **108**, 11 mg, 0.02 mmol, (b) THF, 0.6 mL, water, 0.6 mL, (c) 240 μL, 0.1 M, 0.02 mmol, (d) isolated as lithium salt, (e) 11 mg, 0.02 mmol, 78% yield; white solid.

δ_H (400 MHz, CD$_3$OD) 8.53 − 8.50 (m, 1H, 2-ArH), 8.04 − 7.95 (m, 2H, 4-ArH and 26-ArH), 7.55 − 7.51 (m, 1H, 8-ArH), 7.40 (d, *J* = 7.8 Hz, 1H, 19-ArH), 7.33 (dd, *J* = 7.8 Hz, $^4J_{H-H}$ = 2.0 Hz, 1H, 18-ArH), 6.89 (d, *J* = 9.8 Hz, 1H, 5-ArH), 5.10 (q, *J* = 6.5 Hz, 1H, 21-CH), 4.45 (t, *J* = 7.0 Hz, 2H, 9-CH$_2$), 3.79 (s, 2H, 16-CH$_2$), 3.10 − 3.02 (m, 2H, 11-CH*, 15-CH*), 2.70 − 2.61 (m, 2H, 10-CH$_2$), 2.58 − 2.47 (m, 1H, 13-CH), 2.21 − 2.10 (m, 2H, 11-CH* and 15-CH*), 1.98 − 1.92 (m, 2H, 12-CH* and 14-CH*), 1.51 (d, *J* = 6.5 Hz, 3H, 22-CH$_3$), 1.47 − 1.40 (m, 2H, 12-CH* and 14-CH*) *axial/equatorial protons could not be assigned.

LCMS (Method C) R$_T$ = 0.63 min, [M+H]+ 469.3 (100% purity).

6-chloro-3,3-dimethyl-isobenzofuran-1-one (113)

103 → **112** → **113**
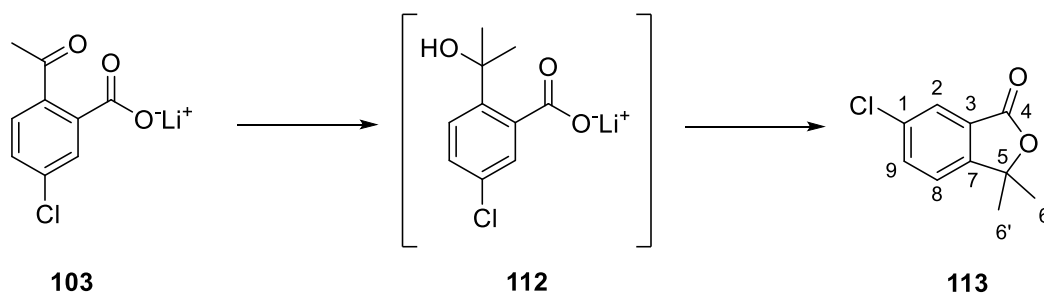
To an ice-cold solution of lithium 2-acetyl-5-chloro-benzoate **103** (550 mg, 2.77 mmol) in dry THF (20 mL) in an ice bath was added MeMgBr (1 M in THF, 5.54 mL, 5.54 mmol) dropwise over 15 min. The reaction mixture was stirred at RT for 1 h, followed by the addition of MeMgBr (1 M in THF, 5.54 mL, 5.54 mmol) dropwise over 15 min. The reaction mixture was stirred for 1 h then HCl (0.5 M, 4 mL) was added followed by EtOAc (10 mL). The aqueous phase was separated and washed with EtOAc (3 × 5 mL), and the combined organic phases were washed with brine (4 mL), dried (MgSO$_4$), filtered and concentrated *in vacuo*. The resulting residue was purified by silica gel column chromatography (gradient = 0-50% EtOAc in petroleum ether (bp. 40-60)). The appropriate fractions were combined and concentrated *in vacuo* to give 6-chloro-3,3-dimethyl-isobenzofuran-1-one **113** (134 mg, 0.68 mmol, 25% yield) as a white crystalline solid.

δ_H (400 MHz, CDCl$_3$) 7.85 (d, $^4J_{H-H}$ = 2.0, $^5J_{H-H}$ = 0.6 Hz, 1H, 2-ArH), 7.65 (dd, J = 8.2 Hz, $^4J_{H-H}$ = 2.0 Hz, 1H, 9-ArH), 7.37 (dd, J = 8.2 Hz, $^5J_{H-H}$ = 0.6 Hz, 1H, 8-ArH), 1.68 (s, 6H, 6-CH$_3$ and 6'-CH$_3$).

LCMS (Method C) R$_T$ = 1.65 mins, [M+H]+ 197.0.

HRMS: (C$_{10}$H$_9$ClO$_2$) [M+H]+ requires 197.0364, found [M+H]+ 197.0363.

Butyl (*E*)-3-(1,1-dimethyl-3-oxo-isobenzofuran-5-yl)prop-2-enoate (114)

113 → **114**
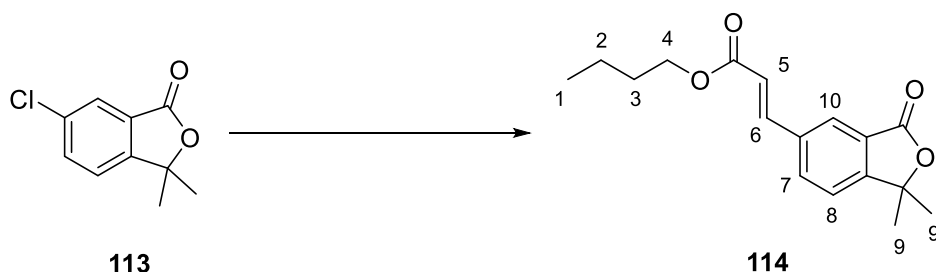
Following *General Procedure E*: (a) 6-chloro-3,3-dimethyl-isobenzofuran-1-one **113**, 370 mg, 1.88 mmol, (b) 58 mg, 0.11 mmol, (c) 1.31 mL, 9.38 mmol, (d) 0.41 mL, 2.82 mmol,

(e) 0-50% EtOAc in petroleum ether (bp. 40-60), (f) 280 mg, 0.97 mmol, 52% yield; orange oil.

δ_H (400 MHz, CDCl$_3$) 8.03 (m, $^4J_{H-H}$ = 1.5 Hz, $^5J_{H-H}$ = 0.7 Hz, 1H, 10-ArH), 7.82 (dd, J = 8.0 Hz, $^4J_{H-H}$ = 1.5 Hz, 1H, 7-ArH), 7.75 (d, J = 16.0 Hz, 1H, 6-CH), 7.45 (dd, J = 8.0 Hz, $^5J_{H-H}$ = 0.7 Hz, 1H, 8-ArH), 6.54 (d, J = 16.0 Hz, 1H, 5-CH), 4.25 (t, J = 6.7 Hz, 2H, 4-CH$_2$), 1.76 − 1.70 (m, 2H, 3-CH$_2$), 1.70 (s, 6H, 9-CH$_3$ and 9'-CH$_3$), 1.53 − 1.40 (m, 2H, 2-CH$_2$), 0.99 (t, J = 7.4 Hz, 3H, 1-CH$_3$).

LCMS (Method C) R$_T$ = 1.94 mins, [M+H]+ 289.3 (84% purity), R$_T$ = 1.90 mins, [M+H]+ 289.3 (16% purity).

1,1-dimethyl-3-oxo-isobenzofuran-5-carbaldehyde (115)
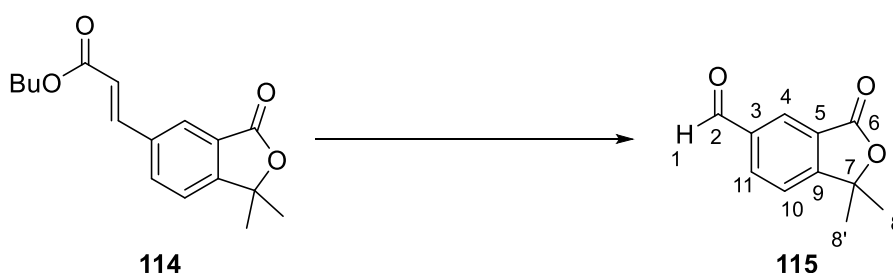
Following *General Procedure F*: (a) 0.25 mL, 0.04 mmol, (b) butyl (*E*)-3-(1,1-dimethyl-3-oxo-isobenzofuran-5-yl)prop-2-enoate **114,** 280 mg, 1.03 mmol, (c) 2 mL, (d) 2 mL, (e) 660 mg, 3.08 mmol, (f) 2 mL, (g) 2 × 5 mL, (i) 148 mg, 0.78 mmol, 76% yield; white solid.

M.pt.: 161 − 162 °C.

v_{max} (neat) = 2990 (C-H stretch), 1762 (C=O (γ-lactone) stretch), 1695 (C=O (aldehyde) stretch), 1620, 1392, 1370, 1186, 1095 cm^{-1}.

δ_H (400 MHz, CDCl$_3$) 10.14 (s, 1H, 1-CH), 8.38 (dd, $^4J_{H-H}$ = 1.4 Hz, $^5J_{H-H}$ = 0.7 Hz, 1H, 4-ArH), 8.25 (dd, J = 7.9 Hz, $^4J_{H-H}$ = 1.4 Hz, 1H, 11-ArH), 7.60 (dd, J = 7.9 Hz, $^5J_{H-H}$ = 0.7 Hz, 1H, 10-ArH), 1.73 (s, 6H, 8-CH$_3$ and 8'-CH$_3$).

δ_C (101 MHz, CDCl$_3$) 190.4 (2-C), 168.3 (6-C), 160.2 (9-C), 137.5 (3-C), 134.2 (11-C), 128.3 (4-C), 126.6 (5-C), 121.8 (10-C), 85.7 (7-C), 27.2 (8-C and 8'-C).

LCMS (Method C) R$_T$ = 1.36 mins, [M+H]+ 191.0 (91% purity), R$_T$ = 1.25 mins, [M+H]+ 207.1 (9% purity).

HRMS: (C$_{11}$H$_{10}$O$_3$) [M+H]+ requires 191.0703, found [M+H]+ 191.0702.

1-[2-[4-[(1,1-dimethyl-3-oxo-isobenzofuran-5-yl)methylamino]-1-piperidyl]ethyl]-7-methoxy-1,8-naphthyridin-2-one (116)
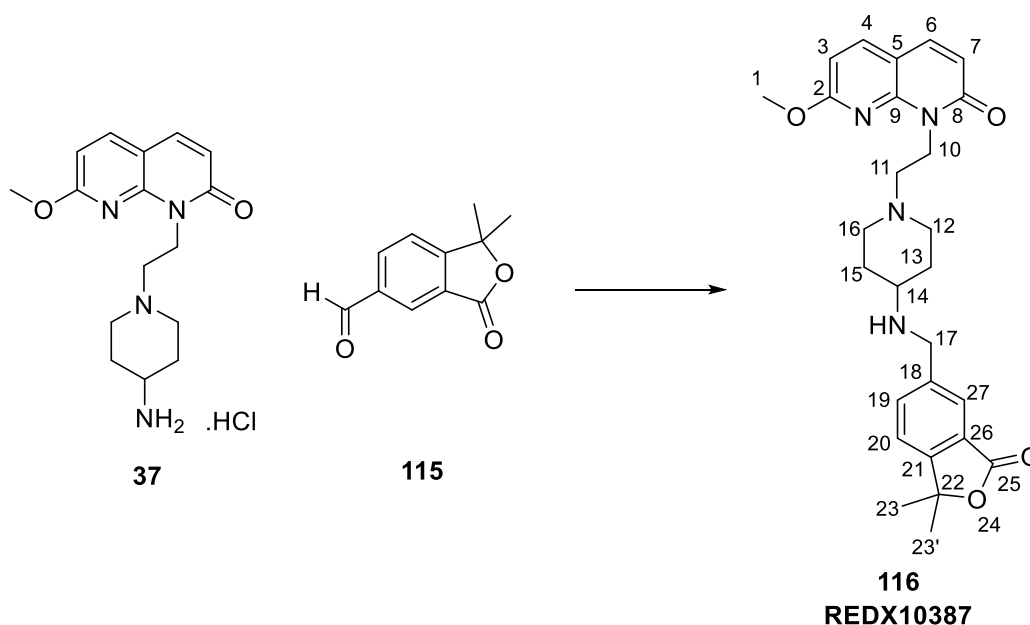
116
REDX10387

Following *General Procedure B:* (a) 1,1-dimethyl-3-oxo-isobenzofuran-5-carbaldehyde **115**, 28 mg, 0.15 mmol, (b) [1-[2-(7-methoxy-2-oxo-1,8-naphthyridin-1-yl)ethyl]-4-piperidyl]ammonium chloride **37**, 50 mg, 0.15 mmol, (c) triethylamine, 25 µL, 0.18 mmol, (d) THF, 3 mL, (e) 94 mg, 0.44 mmol, (f) 3 mL, (g) 2 × 10 mL, (h) 0-50% MeOH in DCM, (j) 4 mg, 0.008 mmol, 6% yield; white solid.

M.pt.: decomposition at 199 - 200 °C.

v_{max} (neat): 3395 (N-H stretch), 2976, 2934 (C-H stretch), 1753 (C=O (γ-lactone) stretch), 1656 (C=O (amide) stretch), 1592, 1494, 1448, 1395, 1355, 1276, 1127, 1040 cm^{-1}.

δ_H (400 MHz, CDCl$_3$) 7.86 (dd, $^4J_{H-H}$ = 1.5 Hz, $^5J_{H-H}$ = 0.7 Hz, 1H, 27-ArH), 7.79 (dd, J = 7.8 Hz, $^4J_{H-H}$ = 1.5 Hz, 1H, 19-ArH), 7.74 (d, J = 8.4 Hz, 1H, 4-ArH), 7.59 (d, J = 9.4 Hz, 1H, 6-ArH), 7.40 (dd, J = 7.8 Hz, $^5J_{H-H}$ = 0.7 Hz, 1H, 20-ArH), 6.63 (d, J = 8.4 Hz, 1H, 3-ArH), 6.57 (d, J = 9.4 Hz, 1H, 7-ArH), 4.77 – 4.68 (m, 2H, 10-CH$_2$), 4.05 (s, 3H, 1-CH$_3$), 3.98 (s, 2H, 17-CH$_2$), 3.25 – 3.20 (m, 2H, 12-CH* and 16-CH*), 2.91 – 2.82 (m, 2H, 11-CH$_2$), 2.77 – 2.67 (m, 1H, 14-CH), 2.45 – 2.39 (m, 2H, 12-CH* and 16-CH*), 2.12 – 2.03 (m, 2H, 13-CH* and 15-CH*), 1.74 – 1.66 (m, 2H, 13-CH* and 15-CH*), 1.65 (s, 6H, 23-CH$_3$ and 23'-CH$_3$) *axial/equatorial protons could not be assigned.

δ_C (101 MHz, CDCl$_3$) 169.7 (25-C), 164.3 (2-C), 163.1 (8-C), 154.3 (21-C), 148.7 (9-C), 140.0 (18-C), 139.1 (4-C), 137.5 (6-C), 134.8 (19-C), 125.7 (26-C), 125.4 (27-C), 121.0 (20-C), 118.9

(7-C), 109.5 (5-C), 106.4 (3-C), 85.5 (22-C), 54.9 (11-C), 54.2 (1-C), 53.3 (14-C), 51.9 (12-C and 16-C), 49.4 (17-C), 38.1 (10-C), 30.9 (13-C and 15-C), 27.3 (23-C and 23'-C).

LCMS (Method C) R_T = 1.11 mins, [M+H]+ 477.5 (100% purity).

HRMS: ($C_{27}H_{32}N_4O_4$) [M+H]+ requires 477.2496, found [M+H]+ 477.2485.

1-[2-[4-[(1,1-dimethyl-3-oxo-isobenzofuran-5-yl)methylamino]-1-piperidyl]ethyl]-7-fluoro-1,5-naphthyridin-2-one (117)
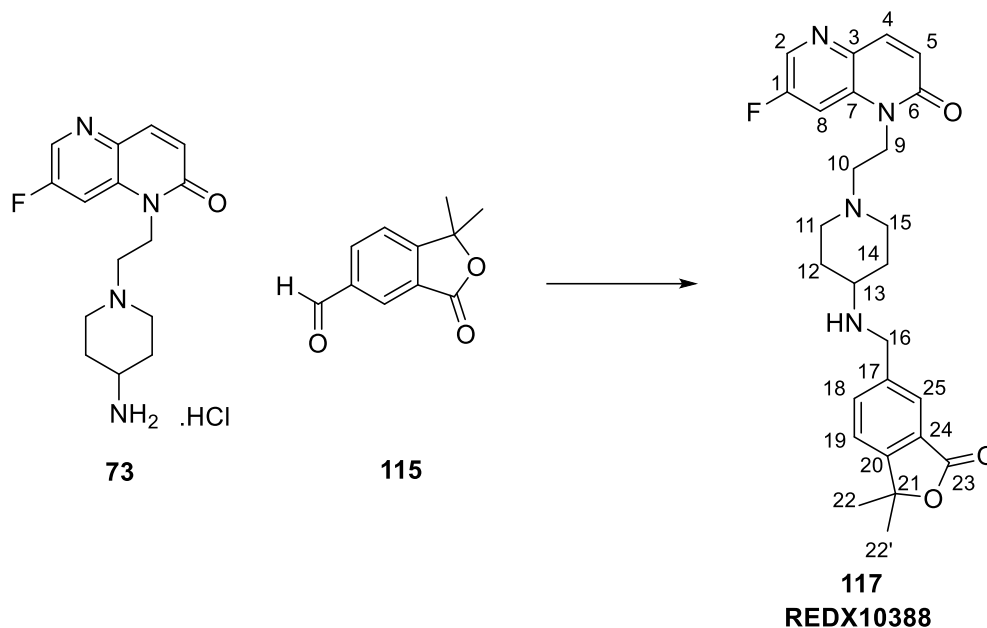
73   **115**

117
REDX10388

Following *General Procedure B:* (a) 1,1-dimethyl-3-oxo-isobenzofuran-5-carbaldehyde **115**, 28 mg, 0.15 mmol, (b) [1-[2-(7-methoxy-2-oxo-1,8-naphthyridin-1-yl)ethyl]-4-piperidyl]ammonium chloride **73**, 48 mg, 0.15 mmol, (c) triethylamine, 25 µL, 0.18 mmol, (d) THF, 3 mL, (e) 94 mg, 0.44 mmol, (f) 3 mL, (g) 2 × 10 mL, (h) 0-50% MeOH in DCM, (j) 6 mg, 0.013 mmol, 9% yield; white solid.

M.pt.: decomposition at 189 - 191 °C.

v_{max} (neat): 2980 (C-H stretch), 2930, 1747 (C=O (γ-lactone) stretch), 1656 (C=O (amide) stretch), 1589, 1562, 1455, 1388, 1324, 1217, 1130, 1046 cm^{-1}.

$δ_H$ (400 MHz, CDCl$_3$) 8.46 − 8.42 (m, 1H, 2-ArH), 7.91 (d, *J* = 9.8 Hz, 1H, 4-ArH), 7.83 (s, 1H, 25-ArH), 7.73 − 7.62 (m, 2H, 8-ArH and 18-ArH), 7.38 (d, *J* = 7.8 Hz, 1H, 19-ArH), 6.88 (d, *J* = 9.8 Hz, 1H, 5-ArH), 4.40 (t, *J* = 7.4 Hz, 2H, 9-CH$_2$), 3.94 (s, 2H, 16-CH$_2$), 3.12 − 3.04 (m, 2H, 11-CH* and 15-CH*), 2.77 − 2.68 (m, 2H, 10-CH$_2$), 2.68 − 2.57 (m, 1H, 13-CH), 2.36 − 2.26 (m, 2H, 11-CH* and 15-CH*), 2.03 − 1.94 (m, 2H, 12-CH* and 14-CH*), 1.67 (s, 6H, 22-CH$_3$

and 22'-CH$_3$), 1.55 – 1.49 (m, 2H, 12-CH* and 14-CH*) *axial/equatorial protons could not be assigned.

δ_C (101 MHz, CDCl$_3$) 169.8 (23-C), 161.3 (6-C), 159.5 (d, $^1J_{C-F}$ = 261.6 Hz, 1-C), 154.0 (20-C), 141.6 (17-C), 140.3 (4-C), 137.2 (d, $^3J_{C-F}$ = 6.1 Hz, 7-C), 135.2 (3-C), 134.4 (18-C), 133.6 (d, $^2J_{C-F}$ = 25.3 Hz, 2-C), 125.7 (24-C), 125.0 (25-C), 124.2 (5-C), 120.8 (19-C), 108.6 (d, $^2J_{C-F}$ = 23.2 Hz, 8-C), 85.4 (21-C), 54.6 (10-C), 53.5 (13-C), 52.4 (11-C and 15-C), 50.0 (16-C), 40.5 (9-C), 31.8 (12-C and 14-C), 27.4 (22-C and 22'-C).

LCMS (Method C) R$_T$ = 1.01 mins, [M+H]+ 465.5 (100%).

HRMS: (C$_{26}$H$_{29}$FN$_4$O$_3$) [M+H]+ requires 465.2296, found [M+H]+ 465.2289.

3.11.3 Additional methods and protocols

3.11.3.1 Molecular dynamics

Each compound to be assessed was individually docked within the crystal structure of the relevant enzyme (paraoxonase – PDB: 3SRG,[73] DNA gyrase subunit A – PDB: 2XCS[36]), using the binding mode observed in the X-ray crystal structure as the basis for a knowledge-based alignment. The enzymatic cell unit was then computationally saturated with water molecules (non-bonded cut-off of 10 Å), preparing the system for molecular dynamics through a default relaxation process (including a minimisation step, followed by 4 short molecular dynamics simulations (3 × 12 ps, 1 × 24 ps)). The entire dynamic system (approximately 45,000 atoms for paraoxonase, approximately 232,000 atoms for gyrase A) was then modelled (10 ns for paraoxonase, 8 ns for gyrase A) at a temperature of 300K using OPLS_2005 as a force field[98] in Desmond v2.3.[99] Constant temperature (300K) and pressure (1 atm) were maintained using the Berendsen coupling algorithm, in accordance with procedures for constant-temperature, constant-pressure (NPT) ensembles.

The movement of each atom within the system was simulated, including all solvent molecules, and a "snapshot" of the system was taken at regular intervals, resulting in over 2000 frames of the dynamic enzymatic system. The resulting trajectories for each system was then analysed using Maestro (v10.6), monitoring how key interactions developed over the course of the experiment.

3.11.3.2 Human plasma stability

Human plasma samples (either diluted 1:1 with phosphate buffer, or used without dilution) were incubated (Thermomixer, 37 °C, 700 rpm) and spiked with test compound (1 µM, 1%

final DMSO concentration). Aliquots (25 µL) were removed at a series of time points (24 h assay with phosphate buffer: 0 min, 5 min, 30 min, 1 h, 2 h, 3 h, 5 h, 23 h and 24 h; 2 h assay without buffer: 0 min, 5 min, 10 min, 15 min, 30 min, 45 min, 1 h, 2 h) and quenched into ice cold acetonitrile containing propranolol as an internal standard. After completion of the assay, the samples were centrifuged (4000 rpm, 10 min, 4 °C) and the supernatant was analysed by HPLC.

3.11.3.3 Human S9 lung fraction stability

Human S9 lung fraction samples (either diluted to 0.5 mg/mL with phosphate buffer, or used without dilution at 5 mg/mL) were incubated (Thermomixer, 37 °C, 700 rpm) with NADPH solution (2.5 µL, 100 mM, phosphate buffer). Test compound was spiked into the sample (1 µM, 1% final DMSO concentration). Aliquots (25 µL) were removed at a series of time points (24 h assay with phosphate buffer: 0 min, 5 min, 30 min, 1 h, 2 h, 3 h, 5 h, 23 h and 24 h; 2 h assay without buffer: 0 min, 5 min, 10 min, 15 min, 30 min, 45 min, 1 h, 2 h) and quenched into ice cold acetonitrile containing propranolol as an internal standard. After completion of the assay, the samples were centrifuged (4000 rpm, 10 min, 4 °C) and the supernatant was analysed by HPLC.

3.11.3.4 Paraoxonase 1 stability

Human PON1 (QQ isoform) was diluted in phosphate buffered saline (1:5) and aliquots (293 µL) were incubated (Thermomixer, 37 °C, 700 rpm) and spiked with test compound in MeOH (7 µL, 400 µM). The assay incubations were performed in duplicate (n = 2), with a control incubation included which contained no PON1 (i.e. 300 µL PBS). Aliquots (25 µL) were removed at a series of time points (0 min, 20 min, 40 min, 1 h, 2 h, 3 h, 4 h, 5 h, 6 h) and quenched into ice cold acetonitrile containing propranolol as an internal standard. After completion of the assay, the samples were centrifuged (4000 rpm, 30 min, 4 °C) and the supernatant was analysed by HPLC.

3.11.3.5 MIC determination

MICs were determined by the broth microdilution or agar dilution procedure according to the CLSI guidelines.[100] For broth microdilution, the test compound was subjected to 2-fold serial dilution in a 96-well microtitre plate, giving a typical final concentration range of 0.25 − 128 µg/mL and a maximum final concentration of 1% DMSO. For agar dilution, the test compound was subjected to 2-fold serial dilution in a 24-well plate, giving a typical final compound concentration range of 0.03 − 128 µg/mL and a maximum final solvent

concentration of 1% DMSO. Strains were grown in cation-adjusted Mueller–Hinton broth (CA-MHB) or agar (CA-MHA) with or without 5% lysed horse blood at 37 °C in an ambient atmosphere, in haemophilus testing medium broth at 37 °C in an ambient atmosphere, or in gonococcal broth or agar supplemented with Vitox at 37 °C in an atmosphere containing 5% CO_2. The MIC was determined as the lowest concentration of compound that inhibits visible growth following a 16 – 24 h incubation period. Results presented are representative of at least two experiments.

3.11.3.6 HepG2 cytotoxicity determination

HepG2 cells (ATCC HB-8065) were seeded at a density of 20,000 cells per well and incubated for 24 h at 37 °C in an atmosphere of 5% CO_2. Cells were then exposed to a doubling dilution series of the test compound. After 24 h of incubation, the viability of the cells was determined using CellTiter-Glow® (Promega, WI, USA), according to the manufacturer's instructions. Each experiment was carried out in duplicate and the results reported as the average concentration of test compound inhibiting 50% of cell viability (CC_{50}).

3.12 References

1. Fleming, A. *Br. J. Exp. Pathol.* **1929**, *10*, 226-236.
2. Brown, E. D.; Wright, G. D. *Nature* **2016**, *529*, 336-343.
3. Acred, P.; Brown, D. M.; Turner, D. H.; Wilson, M. J. *Br. J. Pharmacol. Chemother.* **1962**, *18*, 356-369.
4. Marra, A. *Future Microbiol.* **2011**, *6*, 707-709.
5. Rice, L. B. *J. Infect. Dis.* **2008**, *197*, 1079-1081.
6. Wang, H.; Chen, M.; Ni, Y.; Liu, Y.; Sun, H.; Yu, Y.; Yu, X.; Mei, Y.; Liu, M.; Sun, Z.; Chu, Y.; Hu, Z.; Huang, X. *Int. J. Antimicrob. Agents* **2010**, *35*, 227-234.
7. van Hal, S. J.; Jensen, S. O.; Vaska, V. L.; Espedido, B. A.; Paterson, D. L.; Gosbell, I. B. *Clin. Microbiol. Rev.* **2012**, *25*, 362-86.
8. Gaspar, M. C.; Couet, W.; Olivier, J. C.; Pais, A. A.; Sousa, J. J. *Eur. J. Clin. Microbiol. Infect. Dis.* **2013**, *32*, 1231-52.
9. Theuretzbacher, U. *J. Glob. Antimicrob. Resist. 1*, 63-69.
10. Jap, B. K.; Walian, P. J. *Physiol. Rev.* **1996**, *76*, 1073-88.
11. Brown, L.; Wolf, J. M.; Prados-Rosales, R.; Casadevall, A. *Nat. Rev. Micro.* **2015**, *13*, 620-630.
12. Fernández, L.; Hancock, R. E. W. *Clin. Microbiol. Rev.* **2012**, *25*, 661-681.
13. Allen, H. K.; Donato, J.; Wang, H. H.; Cloud-Hansen, K. A.; Davies, J.; Handelsman, J. *Nat. Rev. Micro.* **2010**, *8*, 251-259.
14. Watson, J. D.; Crick, F. H. C. *Nature* **1953**, *171*, 737-738.
15. Pauling, L.; Corey, R. B. *Proc. Natl. Acad. Sci. U.S.A.* **1953**, *39*, 84-97.
16. Rosenberg, J. M.; Seeman, N. C.; Kim, J. J. P.; Suddath, F. L.; Nicholas, H. B.; Rich, A. *Nature* **1973**, *243*, 150-154.
17. Emmerson, A. M.; Jones, A. M. *J. Antimicrob. Chemother.* **2003**, *51*, 13-20.
18. Lewis, K. *Nat. Rev. Drug Discov.* **2013**, *12*, 371-387.
19. LeBon, J. M.; Kado, C. I.; Rosenthal, L. J.; Chirikjian, J. G. *Proc. Natl. Acad. Sci.* **1978**, *75*, 4097-4101.
20. Wang, J. C. *J. Mol. Biol.* **1971**, *55*, 523-533.
21. Wang, J. C. *Nat. Rev. Mol. Cell Biol.* **2002**, *3*, 430-440.
22. Vos, S. M.; Tretter, E. M.; Schmidt, B. H.; Berger, J. M. *Nat. Rev. Mol. Cell Biol.* **2011**, *12*, 827-841.
23. Luijsterburg, M. S.; White, M. F.; van Driel, R.; Dame, R. T. *Crit. Rev. Biochem. Mol. Biol.* **2008**, *43*, 393-418.
24. Forterre, P.; Gribaldo, S.; Gadelle, D.; Serre, M.-C. *Biochimie* **2007**, *89*, 427-446.
25. Mani, N.; Gross, C. H.; Parsons, J. D.; Hanzelka, B.; Muh, U.; Mullin, S.; Liao, Y.; Grillot, A. L.; Stamos, D.; Charifson, P. S.; Grossman, T. H. *Antimicrob. Agents Chemother.* **2006**, *50*, 1228-1237.
26. Pray, L. *Nature Education* **2008**, *1*.
27. Huddleston, J. R. *Infect. Drug Resist.* **2014**, *7*, 167.
28. Oblak, M.; Kotnik, M.; Solmajer, T. *Curr. Med. Chem.* **2007**, *14*, 2033-2047.
29. Takiff, H. E.; Salazar, L.; Guerrero, C.; Philipp, W.; Huang, W. M.; Kreiswirth, B.; Cole, S. T.; Jacobs, W. R.; Telenti, A. *Antimicrob. Agents Chemother.* **1994**, *38*, 773-780.
30. Leow, P.; Stubbings, W.; Labischinski, H. Selection and Characterisation of Finafloxacin, Ciprofloxacin and Levofloxacin Resistant Mutants of Escherichia coli. In *48th ICAAC*, Washington DC, 2008.
31. Saxena, S.; Samala, G.; Renuka, J.; Sridevi, J. P.; Yogeeswari, P.; Sriram, D. *Bioorg. Med. Chem.* **2015**, *23*, 1402-1412.
32. Jacoby, G. A. *Clin. Infect. Dis.* **2005**, *41*, S120-S126.
33. Mayer, C.; Janin, Y. L. *Chem. Rev.* **2014**, *114*, 2313-2342.

34. Laponogov, I.; Sohi, M. K.; Veselkov, D. A.; Pan, X.-S.; Sawhney, R.; Thompson, A. W.; McAuley, K. E.; Fisher, L. M.; Sanderson, M. R. *Nat. Struct. Mol. Biol.* **2009**, *16*, 667-669.
35. Tari, L. W.; Li, X.; Trzoss, M.; Bensen, D. C.; Chen, Z.; Lam, T.; Zhang, J.; Lee, S. J.; Hough, G.; Phillipson, D.; Akers-Rodriguez, S.; Cunningham, M. L.; Kwan, B. P.; Nelson, K. J.; Castellano, A.; Locke, J. B.; Brown-Driver, V.; Murphy, T. M.; Ong, V. S.; Pillar, C. M.; Shinabarger, D. L.; Nix, J.; Lightstone, F. C.; Wong, S. E.; Nguyen, T. B.; Shaw, K. J.; Finn, J. *PLOS ONE* **2013**, *8*, e84409.
36. Bax, B. D.; Chan, P. F.; Eggleston, D. S.; Fosberry, A.; Gentry, D. R.; Gorrec, F.; Giordano, I.; Hann, M. M.; Hennessy, A.; Hibbs, M.; Huang, J.; Jones, E.; Jones, J.; Brown, K. K.; Lewis, C. J.; May, E. W.; Saunders, M. R.; Singh, O.; Spitzfaden, C. E.; Shen, C.; Shillings, A.; Theobald, A. J.; Wohlkonig, A.; Pearson, N. D.; Gwynn, M. N. *Nature* **2010**, *466*, 935-940.
37. Lewis, R. J.; Singh, O. M.; Smith, C. V.; Skarzynski, T.; Maxwell, A.; Wonacott, A. J.; Wigley, D. B. *EMBO J.* **1996**, *15*, 1412-1420.
38. Charifson, P. S.; Grillot, A.-L.; Grossman, T. H.; Parsons, J. D.; Badia, M.; Bellon, S.; Deininger, D. D.; Drumm, J. E.; Gross, C. H.; LeTiran, A.; Liao, Y.; Mani, N.; Nicolau, D. P.; Perola, E.; Ronkin, S.; Shannon, D.; Swenson, L. L.; Tang, Q.; Tessier, P. R.; Tian, S.-K.; Trudeau, M.; Wang, T.; Wei, Y.; Zhang, H.; Stamos, D. *J. Med. Chem.* **2008**, *51*, 5243-5263.
39. Coates, W. J.; Gwynn, M. N.; Hatton, I. K.; Masters, P. J.; Pearson, N. D.; Rahman, S. S.; Slocombe, B.; Warrack, J. D. WO 1999037635A1. **1999**
40. Miles, T. J.; Barfoot, C.; Brooks, G.; Brown, P.; Chen, D.; Dabbs, S.; Davies, D. T.; Downie, D. L.; Eyrisch, S.; Giordano, I.; Gwynn, M. N.; Hennessy, A.; Hoover, J.; Huang, J.; Jones, G.; Markwell, R.; Rittenhouse, S.; Xiang, H.; Pearson, N. *Bioorg. Med. Chem. Lett.* **2011**, *21*, 7483-7488.
41. Reck, F.; Alm, R.; Brassil, P.; Newman, J.; DeJonge, B.; Eyermann, C. J.; Breault, G.; Breen, J.; Comita-Prevoir, J.; Cronin, M.; Davis, H.; Ehmann, D.; Galullo, V.; Geng, B.; Grebe, T.; Morningstar, M.; Walker, P.; Hayter, B.; Fisher, S. *J. Med. Chem.* **2011**, *54*, 7834-7847.
42. Mitton-Fry, M. J.; Brickner, S. J.; Hamel, J. C.; Brennan, L.; Casavant, J. M.; Chen, M.; Chen, T.; Ding, X.; Driscoll, J.; Hardink, J.; Hoang, T.; Hua, E.; Huband, M. D.; Maloney, M.; Marfat, A.; McCurdy, S. P.; McLeod, D.; Plotkin, M.; Reilly, U.; Robinson, S.; Schafer, J.; Shepard, R. M.; Smith, J. F.; Stone, G. G.; Subramanyam, C.; Yoon, K.; Yuan, W.; Zaniewski, R. P.; Zook, C. *Bioorg. Med. Chem. Lett.* **2013**, *23*, 2955-2961.
43. Hameed P, S.; Manjrekar, P.; Raichurkar, A.; Shinde, V.; Puttur, J.; Shanbhag, G.; Chinnapattu, M.; Patil, V.; Rudrapatana, S.; Sharma, S.; Kumar, C. N. N.; Nandishaiah, R.; Madhavapeddi, P.; Sriram, D.; Solapure, S.; Sambandamurthy, V. K. *ACS Med. Chem. Lett.* **2015**, *6*, 741-746.
44. Black, M. T.; Stachyra, T.; Platel, D.; Girard, A.-M.; Claudon, M.; Bruneau, J.-M.; Miossec, C. *Antimicrob. Agents Chemother.* **2008**, *52*, 3339-3349.
45. Tomašić, T.; Mašič, L. *Curr. Top. Med. Chem.* **2013**, *14*, 130-151.
46. Sanguinetti, M. C.; Tristani-Firouzi, M. *Nature* **2006**, *440*, 463-469.
47. Reck, F.; Ehmann, D. E.; Dougherty, T. J.; Newman, J. V.; Hopkins, S.; Stone, G.; Agrawal, N.; Ciaccio, P.; McNulty, J.; Barthlow, H.; O'Donnell, J.; Goteti, K.; Breen, J.; Comita-Prevoir, J.; Cornebise, M.; Cronin, M.; Eyermann, C. J.; Geng, B.; Carr, G. R.; Pandarinathan, L.; Tang, X.; Cottone, A.; Zhao, L.; Bezdenejnih-Snyder, N. *Bioorg. Med. Chem.* **2014**, *22*, 5392-5409.
48. Jamieson, C.; Moir, E. M.; Rankovic, Z.; Wishart, G. *J. Med. Chem.* **2006**, *49*, 5029-5046.

49. Brown, D. G.; May-Dracka, T. L.; Gagnon, M. M.; Tommasi, R. *J. Med. Chem.* **2014**, *57*, 10144-10161.

50. Rankovic, Z.; Cai, J.; Kerr, J.; Fradera, X.; Robinson, J.; Mistry, A.; Finlay, W.; McGarry, G.; Andrews, F.; Caulfield, W.; Cumming, I.; Dempster, M.; Waller, J.; Arbuckle, W.; Anderson, M.; Martin, I.; Mitchell, A.; Long, C.; Baugh, M.; Westwood, P.; Kinghorn, E.; Jones, P.; Uitdehaag, J. C. M.; van Zeeland, M.; Potin, D.; Saniere, L.; Fouquet, A.; Chevallier, F.; Deronzier, H.; Dorleans, C.; Nicolai, E. *Bioorg. Med. Chem. Lett.* **2010**, *20*, 6237-6241.

51. Zhang, H.-C.; Derian, C. K.; McComsey, D. F.; White, K. B.; Ye, H.; Hecker, L. R.; Li, J.; Addo, M. F.; Croll, D.; Eckardt, A. J.; Smith, C. E.; Li, Q.; Cheung, W.-M.; Conway, B. R.; Emanuel, S.; Demarest, K. T.; Andrade-Gordon, P.; Damiano, B. P.; Maryanoff, B. E. *J. Med. Chem.* **2005**, *48*, 1725-1728.

52. Biedenbach, D. J.; Bouchillon, S. K.; Hackel, M.; Miller, L. A.; Scangarella-Oman, N. E.; Jakielaszek, C.; Sahm, D. F. *Antimicrob. Agents Chemother.* **2016**.

53. Singh, S. B. *Bioorg. Med. Chem. Lett.* **2014**, *24*, 3683-3689.

54. Bodor, N.; Buchwald, P. *Pharmacol. Ther.* **1997**, *76*, 1-27.

55. Bodor, N. *Adv. Drug Deliv. Rev.* **1995**, *16*, 21-38.

56. Buchwald, P.; Bodor, N. *Pharmazie* **2014**, *69*, 403-413.

57. Fukami, T.; Yokoi, T. *Drug Metab. Pharmacokinet.* **2012**, *27*, 466-477.

58. Bodor, N.; Buchwald, P. *Curr. Pharm. Des.* **2006**, *12*, 3241-3260.

59. Biggadike, K.; Angell, R. M.; Burgess, C. M.; Farrell, R. M.; Hancock, A. P.; Harker, A. J.; Irving, W. R.; Ioannou, C.; Procopiou, P. A.; Shaw, R. E.; Solanke, Y. E.; Singh, O. M. P.; Snowden, M. A.; Stubbs, R. J.; Walton, S.; Weston, H. E. *J. Med. Chem.* **2000**, *43*, 19-21.

60. Perlmutter, J. I.; Forbes, L. T.; Krysan, D. J.; Ebsworth-Mojica, K.; Colquhoun, J. M.; Wang, J. L.; Dunman, P. M.; Flaherty, D. P. *J. Med. Chem.* **2014**, *57*, 8540-8562.

61. Thompson, D.; Oster, G. *JAMA* **1996**, *275*, 1339-1341; Lu, H. R.; Hermans, A. N.; Gallacher, D. J. *Br. J. Pharmacol.* **2012**, *166*, 1490-1502.

62. Adamantia, L.; Torres, A. *Expert Opin. Pharmacother.* **2014**, *15*, 2307-2318.

63. Osiyemi, O.; Dickinson, G. *Curr. Infect. Dis. Rep.* **2000**, *2*, 207-214.

64. Gupta, M. R.; Valentine, V. G.; Walker, J. E., Jr.; Lombard, G. A.; LaPlace, S. G.; Seoane, L.; Taylor, D. E.; Dhillon, G. S. *Transpl. Infect. Dis.* **2009**, *11*, 424-31.

65. Ratjen, F. A. *Respir. Care* **2009**, *54*, 595-605.

66. Høiby, N. *BMC Med.* **2011**, *9*, 1-7.

67. Rose, L. M.; Neale, R. *Sci. Transl. Med.* **2010**, *2*, 63mr4.

68. Sawicki, G. S.; Signorovitch, J. E.; Zhang, J.; Latremouille-Viau, D.; von Wartburg, M.; Wu, E. Q.; Shi, L. *Pediatr. Pulmonol.* **2012**, *47*, 44-52.

69. Olaitan, A. O.; Morand, S.; Rolain, J.-M. *Int. J. Antimicrob. Agents* **2016**, *47*, 1-3.

70. Davies, J. C. *Paediatr. Respir. Rev.* **2002**, *3*, 128-134.

71. Draganov, D. I.; La Du, B. N. *Naunyn Schmiedebergs Arch. Pharmacol.* **2004**, *369*, 78-88.

72. Miles, T. J.; Fau, A. J.; Barfoot, C.; Brooks, G.; Brown, P.; Chen, D.; Dabbs, S.; Davies, D. T.; Downie, D. L.; Eyrisch, S.; Gallagher, T.; Giordano, I.; Gwynn, M. N.; Hennessy, A.; Hoover, J.; Huang, J.; Jones, G.; Markwell, R.; Miller, W. H.; Minthorn, E. A.; Rittenhouse, S.; Seefeld, M.; Pearson, N. *Bioorg. Med. Chem. Lett.* **2011**, *21*, 7489-95.

73. Ben-David, M.; Elias, M.; Filippi, J.-J.; Duñach, E.; Silman, I.; Sussman, J. L.; Tawfik, D. S. *J. Mol. Biol.* **2012**, *418*, 181-196.

74. Billecke, S.; Draganov, D.; Counsell, R.; Stetson, P.; Watson, C.; Hsu, C.; Du, B. N. L. *Drug Metab. Dispos.* **2000**, *28*, 1335-1342.

75. Hioki, T.; Fukami, T.; Nakajima, M.; Yokoi, T. *Drug Metab. Dispos.* **2011**, *39*, 1345-52.

76. Metobo, S. E.; Jabri, S. Y.; Aktoudianakis, E.; Evans, J.; Jin, H.; Kim, C. U. *Tetrahedron Lett.* **2013**, *54*, 6782-6784.

77. Yu, Z.; Alesso, S.; Pears, D.; Worthington, P. A.; Luke, R. W. A.; Bradley, M. *Tetrahedron Lett.* **2000**, *41*, 8963-8967.

78. Boral, S.; Guo, X.; Wang, S.; Wurster, J. A.; Malone, T. C. US 20080045526A1. **2008**.

79. Barlaam, B.; Ducray, R.; Brempt, C. L.-v. d.; Plé, P.; Bardelle, C.; Brooks, N.; Coleman, T.; Cross, D.; Kettle, J. G.; Read, J. *Bioorg. Med. Chem. Lett.* **2011**, *21*, 2207-2211.

80. Singh, S. B.; Kaelin, D. E.; Wu, J.; Miesel, L.; Tan, C. M.; Gill, C.; Black, T.; Nargund, R.; Meinke, P. T.; Olsen, D. B.; Lagrutta, A.; Wei, C.; Peng, X.; Wang, X.; Fukuda, H.; Kishii, R.; Takei, M.; Takeuchi, T.; Shibue, T.; Ohata, K.; Takano, H.; Ban, S.; Nishimura, A.; Fukuda, Y. *Bioorg. Med. Chem. Lett.* **2015**, *25*, 2473-8.

81. Boland, S.; Bourin, A.; Alen, J.; Geraets, J.; Schroeders, P.; Castermans, K.; Kindt, N.; Boumans, N.; Panitti, L.; Fransen, S.; Vanormelingen, J.; Stassen, J. M.; Leysen, D.; Defert, O. *J. Med. Chem.* **2015**, *58*, 4309-4324.

82. El Seoud, O. A.; Ruasse, M.-F.; Rodrigues, W. A. *J. Chem. Soc., Perkin Trans. 2* **2002**, 1053-1058.

83. Hartzell, J. D.; Kim, A. S.; Kortepeter, M. G.; Moran, K. A. *MedGenMed* **2007**, *9*, 4-4.

84. Tommasi, R.; Brown, D. G.; Walkup, G. K.; Manchester, J. I.; Miller, A. A. *Nat. Rev. Drug Discov.* **2015**, *14*, 529.

85. Kuhn, B.; Mohr, P.; Stahl, M. *J. Med. Chem.* **2010**, *53*, 2601-2611.

86. Draganov, D. I.; Teiber, J. F.; Speelman, A.; Osawa, Y.; Sunahara, R.; La Du, B. N. *J. Lipid Res.* **2005**, *46*, 1239-1247.

87. Mangas-Sánchez, J.; Busto, E.; Gotor-Fernández, V.; Gotor, V. *Org. Lett.* **2012**, *14*, 1444-1447.

88. Yang, J.; Yoshikai, N. *J. Am. Chem. Soc.* **2014**, *136*, 16748-16751.

89. Phan, D. H. T.; Kim, B.; Dong, V. M. *J. Am. Chem. Soc.* **2009**, *131*, 15608-15609.

90. Davies, B.; Morris, T. *Pharm. Res.* **1993**, *10*, 1093-1095.

91. Di Fabio, R. WO 2011023578A1. **2011**.

92. Han, J. WO 2015081891A1. **2015**.

93. Chen, L.; Yan, C.; Du, B.-B.; Wu, K.; Zhang, L.-Y.; Yin, S.-Y.; Pan, M. *Inorg. Chem. Commun.* **2014**, *47*, 13-16.

94. Blades, K.; Glossop, S. C. *Synthesis* **2017**, *49*, 554-556.

95. Yamada, H.; Nagao, K.; Dokei, K.; Kasai, Y.; Michihata, N. *J. Am. Chem. Soc.* **2008**, *130*, 7566-7567.

96. Springfield, S. A.; Doubleday, W. W.; Buono, F.; Couturier, M. A.; Lear, Y.; Favreau, D.; Levesque, K.; Manchand, P. S.; Frieser, M.; Cocuzza, A. J. US 20100056792. **2010**.

97. Lüthy, C.; Zondler, H.; Rapold, T.; Seifert, G.; Urwyler, B.; Heinis, T.; Steinrücken, H. C.; Allen, J. *Pest Manag. Sci.* **2001**, *57*, 205-224.

98. Shivakumar, D.; Williams, J.; Wu, Y.; Damm, W.; Shelley, J.; Sherman, W. *J. Chem. Theory Comput.* **2010**, *6*, 1509-1519.

99. Bowers, K. J.; Chow, E.; Xu, H.; Dror, R. O.; Eastwood, M. P.; Gregersen, B. A.; Klepeis, J. L.; Kolossvary, I.; Moraes, M. A.; Sacerdoti, F. D.; Salmon, J. K.; Shan, Y.; Shaw, D. E. Scalable algorithms for molecular dynamics simulations on commodity clusters. In *Proceedings of the 2006 ACM/IEEE conference on Supercomputing*, ACM: Tampa, Florida, 2006; p 84.

100. *Clinical and Laboratory Standards Institute. Methods for Dilution Antimicrobial Susceptibility Tests for Bacteria That Grow Aerobically; Approved Standard—Ninth Edition*. CLSI, Wayne, PA, USA, 2012.

Chapter 4:
Investigation into toxicity and antibacterial trends for a series of GyrB/ParE inhibitors

4　Inhibitors of GyrB/ParE

4.1　Revisiting alternative binding sites of DNA gyrase

Fluoroquinolones have been shown to bind to subunit A and subunit C of DNA gyrase and topoisomerase IV, respectively. As has been previously discussed, the selective targeting of alternative binding sites on DNA gyrase that elicit the same phenotypic response is a potentially lucrative area of antibacterial research (**Section 1.6**).

Throughout **Chapter 2** and **Chapter 3**, inhibition of the NBTI binding site on subunit A (**Figure 1**) exemplified a currently underutilised method of overcoming commonly encountered antibacterial drug resistance. This approach allowed a series of soft drug inhibitors to be developed, which maintained potency against drug resistant strains of *S. aureus*. To date, however, therapies that target alternative binding sites of DNA gyrase remain clinically unused.

Inhibition of the ATPase binding site on gyrase B (**Figure 1**) has been highlighted as a potential method of disrupting DNA gyrase function, causing bacterial cell death. However, although they have been well studied within the literature and have had historical clinical use, no inhibitors of the ATPase binding site are currently therapeutically utilised.

As a result, a second branch of in-house research evolved, aiming to target drug resistant bacteria by focusing on inhibition of the ATPase binding site of DNA gyrase subunit B.
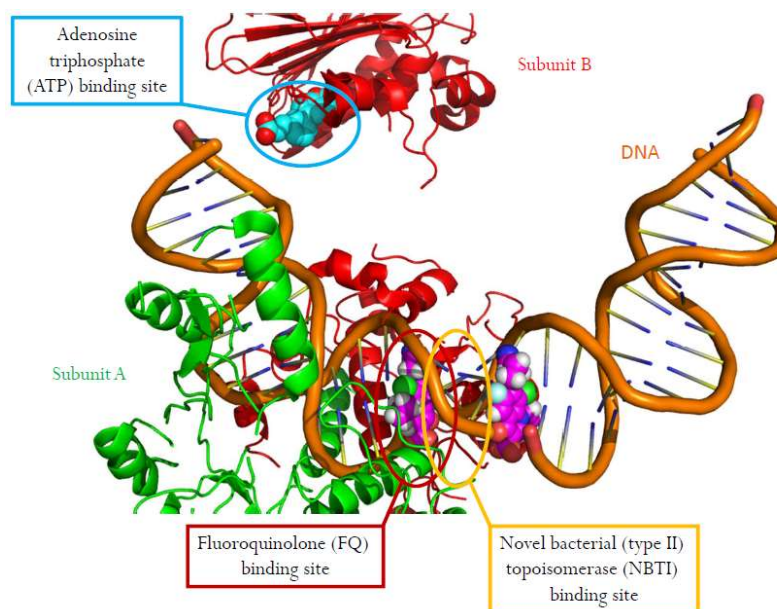
Revisiting the binding sites of DNA gyrase.

Figure 1

4.1.1 The ATPase binding site

For illustrative purposes, key interactions between the ATPase site on DNA gyrase and a known inhibitor are shown in **Figure 2**.
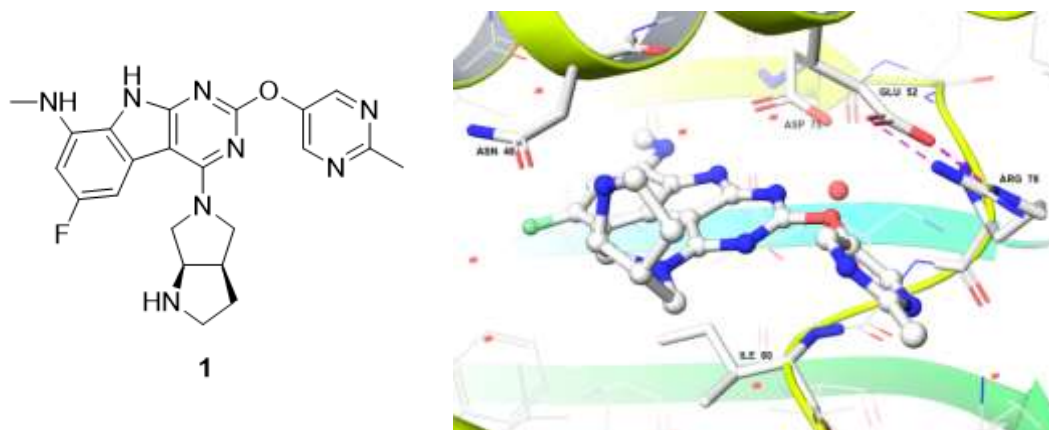
X-ray crystal structure (PDB: 4K4O) of Trius Therapeutics tricyclic core compound **1** crystallised with *E. coli* gyrase B active site.[1] Figure generated using Maestro (v10.6).

Figure 2

As reported by Tari *et al.*,[1] the Trius Therapeutics series, exemplified by compound **1**, exhibited several key interactions with the active site (**Figure 2**). The tricyclic core made three strong binding interactions with Asp75, two directly (aniline and pyrrole N-H) and one *via* a highly conserved water molecule (pyrimidine nitrogen, water highlighted in red). These polar interactions were maintained throughout many different series of compounds, and provided a method of comparing a variety of inhibitor scaffolds. The fluorine atom was observed to fill a small lipophilic pocket and resulted in broad-spectrum activity for the series in question. The cyclic amine appendage contributed to the potency of the series by either making a direct hydrogen-bond with Asn48, or through a conserved water network to Asp75. Furthermore, the pyrimidine ring was observed to sit directly under the plane of the cationic amine in Arg78, suggesting a π-cation interaction further increased the molecules affinity for the active site. Additionally, a water-mediated interaction was observed between a nitrogen in the pyrimidine ring and a distant arginine (not shown in **Figure 2**). A lipophilic shelf was created at the bottom of the active site with Ile80. The importance of the lipophilicity of the floor of the active site was reinforced by the loss of activity when bulky polar groups were used as replacements for the cyclic amine.[2]

Inhibitors of this binding site have been shown to be potent antibacterial agents, and, in some cases, have shown superior activity against mycobacteria such as *M. tuberculosis*.

4.2 Introduction to tuberculosis

Tuberculosis (TB) is the disease caused when *M. tuberculosis* colonises within the body, primarily in the pulmonary alveoli.[3] The resulting disease has been reported by the World Health Organisation to be among the top killer infectious diseases worldwide, with 9.6 million people contracting the disease in 2014 and 1.5 million dying as a result of infection.[4] Furthermore, approximately one third of the world's population has latent (asymptomatic) TB, with 10% of this subset at risk of becoming symptomatic within their lifetime.[4] Symptoms of the disease include coughing, fever, chest pains, weight loss and haemoptysis (coughing up of blood from the respiratory tract).

4.2.1 Current anti-tuberculosis therapy

Current tuberculosis treatment is intensive and complex, consisting of a cocktail of four antimicrobial drugs (isoniazid **2**, pyrazinamide **3**, ethambutol **4** and rifampicin **5**, **Figure 3**) which must be carefully administered daily for six months.[5]

2

Isoniazid

3

Pyrazinamide

4

Ethambutol

5

Rifampicin
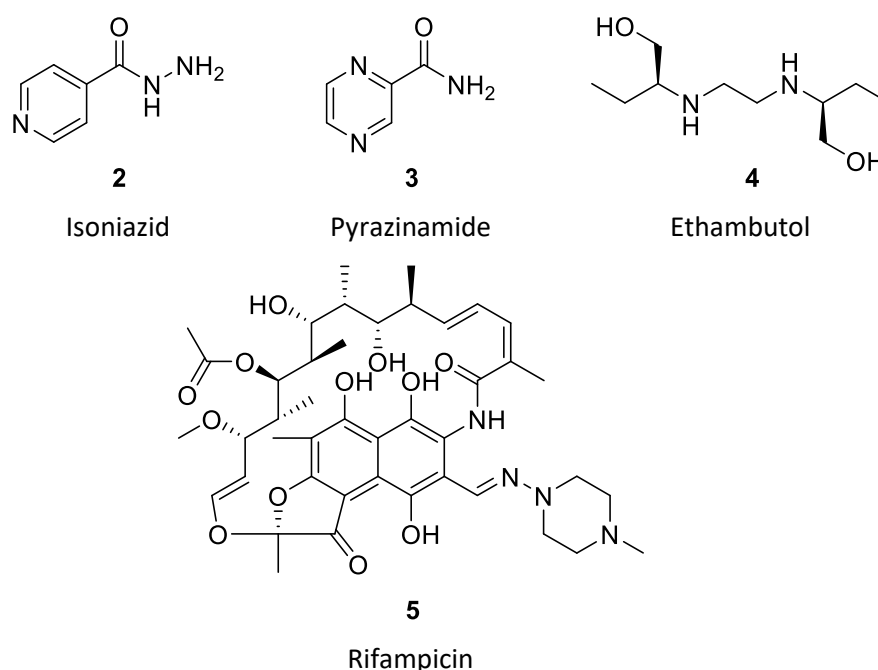
Figure 3

The treatment for tuberculosis infections has been carefully considered, with multiple biological pathways being simultaneously targeted. Isoniazid **2** is a known inhibitor of mycolic acid biosynthesis.[6] As mycolic acids are key components of the mycobacterial cell wall, inhibition results in a defective cell wall, and, ultimately, cell death. Unfortunately, little is known about the mechanism of action of pyrazinamide **3**, and it has been suggested

that it is in fact a prodrug, forming pyrazinoic acid which can then accumulate within the mycobacterial cell.[7] Ethambutol **4** is able to inhibit cell wall synthesis through inhibition of arabinosyl transferase, paralleling the therapeutic effect seen from isoniazid treatment.[6] The final component of the multidrug therapy is rifampicin **5**, an inhibitor of RNA polymerase. Without the ability to synthesise RNA, the mycobacterium is unable to form proteins, resulting in cell death.[6]

The prolonged and complicated multidrug nature of the current tuberculosis treatment results in very poor patient compliance, undoubtedly resulting in high levels of resistant mycobacteria being generated from dosing regimens being poorly adhered to. Resistance to current tuberculosis therapies is increasing, with multidrug-resistant TB (MDR-TB), i.e. TB that fails to respond to treatment from first-line antibiotics, being observed in every country where TB is found. Furthermore, cases of extensively drug-resistant tuberculosis (XDR-TB; i.e. TB that is resistant to treatment from isoniazid, rifampicin and any fluoroquinolone, and at least one of three injectable second-line antibiotics; amikacin, kanamycin or capreomycin) are growing, indicating particular strains of the mycobacteria are becoming increasingly resistant to second-line anti-TB drugs.[4]

As a result of the complex treatment regimens and the emergence of increasingly resistant strains of tuberculosis, there is an urgent necessity for novel anti-mycobacterial pharmaceuticals. In order to improve patient compliance, an ideal therapy should be shorter than is currently available (< 6 months), and the daily pill burden should be reduced. A new therapy should be active against MDR-TB and XDR-TB, and should have very low toxicity, in accordance with the likely prolonged dosing regimens.[5] Research into the area of novel DNA gyrase subunit B inhibitors has been extensive, with a variety of original series being disclosed in the literature. In order to assess the competitor landscape prior to the commencement of the research project, a review of the existing work in the area was performed.

4.3   Case histories

4.3.1   Naturally occurring inhibitors

The research area of inhibitors which target the ATPase site on GyrB/ParE topoisomerase type II enzymes is highly competitive. In the 60 years since the first inhibitor, novobiocin **6**, was discovered, many pharmaceutical companies have developed their own series of compounds, with the primary goal of producing a novel therapy for bacterial infections.

Initial insight into the potentially lucrative area of GyrB/ParE inhibitors was exemplified through the discovery of naturally occurring aminocoumarin antibacterial agents, novobiocin 6[8, 9] and clorobiocin 7 (**Figure 4**).[10] These first generation antibiotics were found through a screening programme and were used extensively before the investigation of their mechanism of action was undertaken.[11]
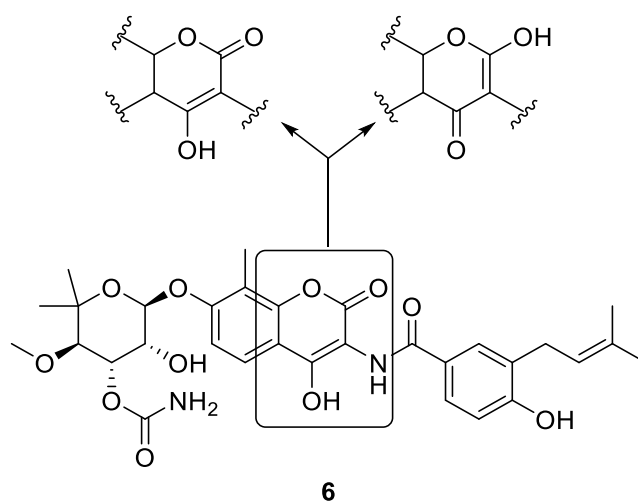
Novobiocin **6** with site of possible tautomerism highlighted.
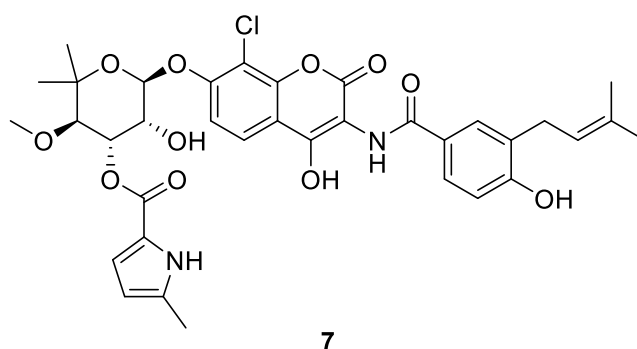
Naturally occurring antibiotic clorobiocin **7**.

Figure 4

Novobiocin **6** and clorobiocin **7** are naturally produced by the *Streptomyces* species of bacteria and have been shown to have similar binding modes. Both inhibitors partially overlapped with the ATPase domain, with the L-noviose sugar portion interacting with Asp73, while the coumarin ring bound to the Arg136 residue.[12] Binding to the GyrB/ParE ATPase sites on DNA gyrase/topoisomerase IV prevented ATP hydrolysis, causing enzymatic failure and bacterial cell death. Although tautomerism between the 4-hydroxycoumarin and 2-hydroxychromone was possible (**Figure 4**), structural determination of the major active tautomer has been unsuccessful.[13] It can be hypothesised that, regardless of the most

stable tautomeric form in solution, the presence of the target protein will have a substantial influence on the tautomeric ratio, forcing the lowest energy tautomeric form required for binding. In 1964, novobiocin **6** was successfully marketed by Pharmacia and Upjohn as Albamycin® and was found to be particularly potent against *S. aureus* pathogens (minimum inhibitory concentration (MIC) ≤ 0.12 μg/mL), allowing effective treatment of methicillin-resistant *S. aureus* (MRSA) infections.[14] However, fears around the cytotoxicity of novobiocin **6**, particularly through cross inhibition of eukaryotic Hsp90, an important protein involved in aiding the folding of other proteins, led to its withdrawal from the market.[15] Although this resulted in a fall in the use of aminocoumarin based inhibitors for treating bacterial infections, the repurposing of novobiocin **6** for the treatment of cancer is ongoing.[16] Moreover, current research in aminocoumarin antibiotics is still proceeding, with the current focus on avoiding antibiotic resistance and lowering cytotoxicity.[11]

More recently, a new structural class of naturally occurring GyrB/ParE inhibitors has been discovered. Kibdelomycin **8** (**Figure 5**), a naturally occurring antibiotic isolated from *Actinobacterium kibdelosporangium*, was reported in 2011 by Merck and has been shown to exhibit similar potencies to novobiocin **6** and clorobiocin **7**, particularly against gram-positive pathogens such as *S. aureus* and *E. faecalis*.[17]
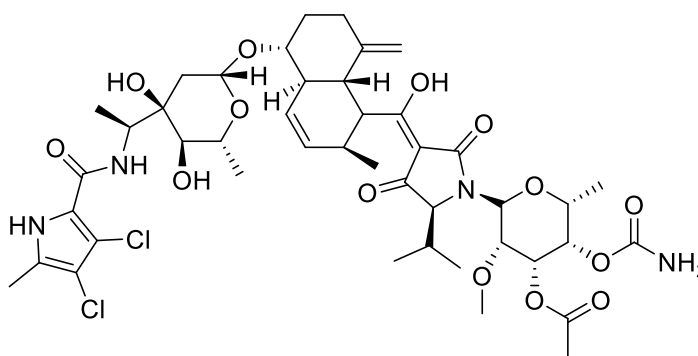
8

Kibdelomycin **8**.

Figure 5

Furthermore, kibdelomycin **8** has been shown to have a very low frequency of resistance ($< 5 \times 10^{-10}$), and no cross-resistance to existing inhibitors, highlighting the utility of targeting a novel binding site.[17] However, in common with other naturally occurring antibiotics, toxicity may still be an issue for this series, although no data has yet been published in this regard. The publication of this novel, naturally occurring antibacterial class

of compounds highlighted the discovery of new drug scaffolds, and demonstrated that these scaffolds can be derived from naturally occurring antibiotics. Nevertheless, due to increasing pressure from antibiotic resistance, novel synthetic small molecule antibiotics are in demand more than ever before.

4.3.2 The Vertex Pharmaceuticals series

In comparison to the naturally occurring inhibitors, a wave of interest in fully synthetic GyrB/ParE inhibitors was initially generated by work published by Vertex Pharmaceuticals. After performing a high throughput screen of almost 30,000 molecules, a benzimidazole class of compounds, of which compound **9** (**Figure 6**) is an example, was discovered.[18] This compound acted as an inhibitor of the ATPase region of GyrB, with a modest potency of 2 µM against the *S. aureus* DNA gyrase enzyme. However, the potency of the hit was limited against whole-cell *S. aureus*, with an MIC of > 16 µg/mL, even in the absence of human serum.[18]
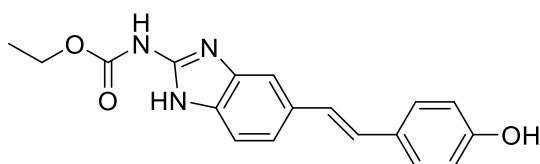
9

Benzimidazole **9**.

Figure 6

Although the initial hit had low antibacterial activity, the compound provided a starting point for the optimisation of the series, which soon yielded very potent inhibitors, such as optimised benzimidazole **10** (**Figure 7**).
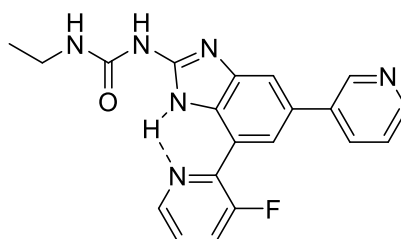
10

Optimised benzimidazole **10**.

Figure 7

Benzimidazole **10** was shown to have potencies against *S. aureus* DNA gyrase of 0.014 µM. This translated into low MICs of 0.031 µg/mL and 0.5 µg/mL for *S. aureus* in the absence of human serum and in the presence of human serum, respectively. It was observed that the co-planarity of the pyridyl group in benzimidazole **10** resulted in a beneficial increase in potency, and, more importantly, a compound less affected by the addition of human serum. This observation was supported by quantum mechanical rotational barrier calculations, suggesting the internal hydrogen bonding of the fluoro-pyridyl substituent to the imidazole induced a pre-organisation for the binding site (**Figure 7**). The compound in question was able to successfully dual target both DNA gyrase and topoisomerase IV (topo IV), resulting in a low frequency of resistance, and was shown to be potent in *in vivo* rodent models of infection. Furthermore, improved physiochemical properties compared to benzimidazole **9** reduced the ADME liabilities of the series. However, a recent paper released by Vertex Pharmaceuticals has revealed that benzimidazole **10** suffered from unfortunate CYP inhibition, a short half-life and generally poor physicochemical properties.[19] Further assessment of the inhibitor showed a reactive metabolite was covalently binding to liver proteins, causing a potential safety liability.[19] A successful round of optimisation, employing a "metabolic shift strategy", was performed, resulting in tetrahydrofuran-substituted benzimidazole **11** (**Figure 8**).[19]

11
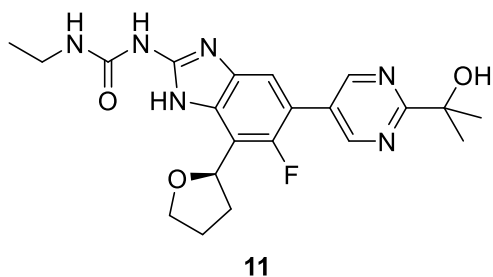
Tetrahydrofuran-substituted benzimidazole **11**.

Figure 8

By replacing the pyrimidine substituent with a tetrahydrofuran ring, the researchers were able to circumvent the formation of dangerous metabolites by forcing metabolism to occur away from the urea, where the initial reactive metabolites were being formed. This strategy was shown to be successful through *in vivo* testing, which resulted in a very low probability of covalently labelled liver proteins. Additionally, compound **11** retained antibacterial activity, with MICs against *S. aureus* and *E. faecalis* of 0.016 µg/mL, resulting in its selection as a preclinical candidate.[19]

4.3.3 The Evotec Ltd. series

Research in the area of fused bicyclic ATPase inhibitors continued with work published by Evotec Ltd. in 2009, which sought to replace the benzimidazole scaffold (previously used by Vertex Pharmaceuticals) with a novel pharmacophore.[20] The triazolopyridine template was chosen to develop the structure-activity relationship of the series, which, in turn, produced optimised compound **12** (**Figure 9**) below.
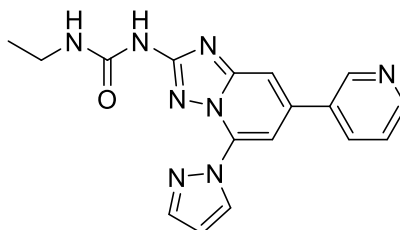
Triazolopyridine **12**.

Figure 9

The researchers managed to increase the potency of their series from a modest MIC against *S. aureus* of 32 µg/mL for their initial hit, to a reasonable potency of 2 µg/mL. The MICs achieved by Evotec Ltd. provided proof that alternative scaffolds to those published by Vertex Pharmaceuticals were also tolerated in the ATPase site on GyrB/ParE. Furthermore, their lead triazolopyridine **12** was shown to be non-cytotoxic in a cellular health assay, with a hepG2 CC_{50} of > 64 µg/mL, prompting further work on the series, specifically aimed towards optimising the pharmacokinetic properties and potency towards gram-positive pathogens.[20] The results published by Evotec Ltd. showed a non-toxic bioisostere of the Vertex Pharmaceutical benzimidazole series could inhibit the ATPase site in GyrB/ParE. This provided evidence to support the hypothesis of Vertex Pharmaceuticals, that a novel antibacterial therapy could be developed which did not rely on the fluoroquinolone binding site.

4.3.4 The Pfizer series

From the modest results achieved by smaller companies, larger pharmaceutical organisations, such as Pfizer, began working in the area. They, again, used the benzimidazole scaffold as a starting point, with structural novelty derived from manipulation of the central core to create an imidazolopyridine **13** (**Figure 10**).[2]
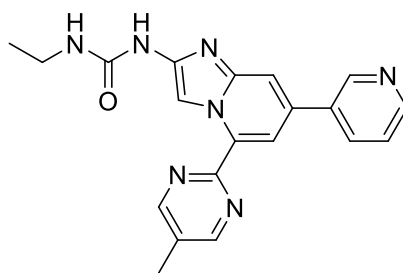
Imidazolopyridine **13**.

Figure 10

The ability of the Pfizer scientists to manipulate the central region of their small molecule inhibitor reinforced the bioisosterism of this core. Furthermore, their series proved more potent than many of the competitors in the area, with MICs of 0.5 µg/mL against *S. aureus* and MRSA, and an even greater potency against *S. pneumoniae* of 0.125 µg/mL. Interestingly, optimisation around the methyl vector of the pyrimidine revealed that substituents that were polar in nature, or that forced a three-dimensional geometry, were not tolerated and resulted in a reduced activity. This observation was consistent with the reported binding mode, where a lipophilic shelf, formed by Ile80, was present along the lower half of the molecule, disfavouring bulky polar substrates. Imidazolopyridine **13** was selected for additional studies; however, the results of these findings have not yet been published. Further work continued around the same series, by replacement of the pyridine substituent in imidazolopyridine **13** to give pyridone **14** (**Figure 11**).[2]
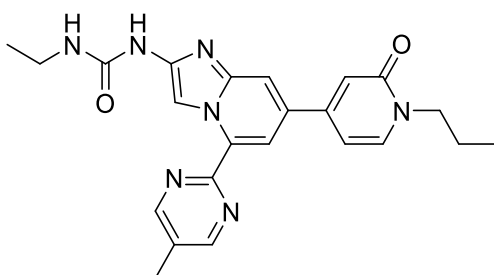
Pyridone **14**.

Figure 11

Fortunately, substitution with the pyridone resulted in an increase in antibacterial activity, with pyridone **14** having an approximate 2-fold boost in potency, giving MICs against *S. aureus* and *S. pneumoniae* of 0.125 and 0.06 µg/mL respectively. Unfortunately, work on

the pyridone series was terminated as the researchers could not achieve the desired equal balance between GyrB and ParE activity. Instead, a preference for GyrB activity resulted, with an enzymatic potency of 0.097 μM, compared to ParE inhibition of 1.02 μM.[2]

Although failure to balance GyrB and ParE activity would present a liability to a dual targeting approach, it could be hypothesised that the high potencies of this series may lend themselves to application for a different disease target. For example, *M. tuberculosis* has only a single topoisomerase IIA enzyme; DNA gyrase, and no topoisomerase IV (**Section 1.5**).[12] Thus, this series of inhibitors may provide a good starting point for the design of a novel tuberculosis treatment, specifically targeting DNA gyrase. However, as the cell walls of mycobacterium vary drastically from the traditional gram-positive and gram-negative cell wall structure, major optimisation of physiochemical properties, including $logD_{7.4}$, would have to take place before *M. tuberculosis* antibacterial activity could be expected.

4.3.5 The AstraZeneca series

AstraZeneca took a different approach to discovering a unique class of ATPase inhibitors.[21] They observed similarities between the H-bond donor/H-bond acceptor motif of previous GyrB/ParE inhibitors and their own in-house kinase inhibitor programme, and sought a method to transfer knowledge between these projects. Therefore, a virtual library of kinase inhibitor fragments were screened against the DNA gyrase binding site, which resulted in the discovery of azaindole **15** (**Figure 12**).
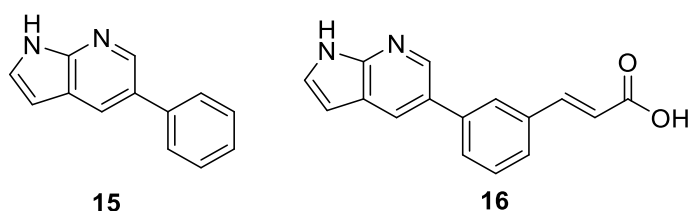
Fragment hit azaindole **15** and cinnamic acid **16**.

Figure 12

Azaindole **15** was found to have a 5-phenyl substituent in the required vector to access a second, activity-boosting, interaction. The *trans*-cinnamic acid **16** (**Figure 12**) was therefore synthesised in order to exploit an additional salt bridge interaction with nearby Arg140. This remarkably simple structure was found to have an IC_{50} against *S. pneumoniae* ParE of 7.7 μM, highlighting the key interactions required for binding to the protein. However, as

expected, the MICs of this probe compound were > 200 µM due to the non-optimised physiochemical properties, no doubt resulting in high efflux and poor membrane permeability. Seeking to increase the potency of their series, the authors looked to introduce a third "hinge-binding" interaction, as had been used for previous urea motifs. An amide substituent was added to establish this interaction, and nitrogen rich heterocycles were substituted on the 4-position in order to interact with the lipophilic shelf.[21]
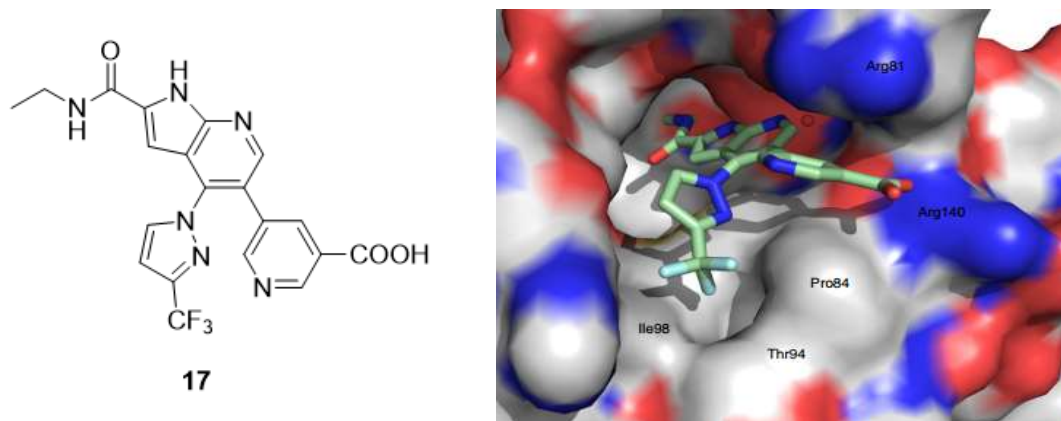
Azaindole **17** and X-ray crystal structure of azaindole **17** in *S. pneumoniae* ParE. Used with permission from Manchester *et al*.[21]

Figure 13

Thus, optimised azaindole **17** (**Figure 13**) showed spectacular potency, with an IC_{50} against *S. pneumoniae* ParE of 5 nM. Rationale for this high activity was postulated from the X-ray crystal structure (**Figure 13**), showing high charge and shape complementarity for the bound complex. However, the antibacterial activity of the compound was much poorer, with an MIC against *S. aureus* of > 11 µg/mL. This was attributed to poor physicochemical properties and highlighted the exceptional importance of these properties in antibacterial drug design. It was hypothesised that the low $logD_{7.4}$ (-0.99) of azaindole **17** resulted in minimal permeability of the drug in crossing cellular membranes. This theory was supported by increasing the $logD_{7.4}$, by replacing the pyridine acid substituent on the 5-position with a cyano moiety, increasing the $logD_{7.4}$ to 2.6. A drop in activity against the isolated enzyme was observed, in accordance with the removal of a key binding interaction, however, antibacterial MICs improved dramatically to 1.3 µg/mL against *S. aureus*. Fine tuning of the physicochemical properties, while optimising key interactions, resulted in potent inhibitor **18** (**Figure 14**) with MICs of 0.05 and 0.1 µg/mL against *S. aureus* and MRSA respectively.
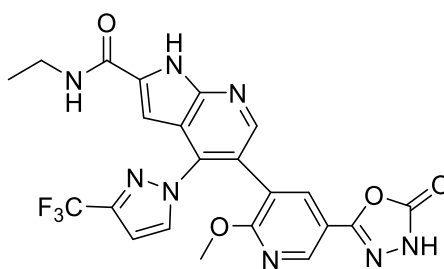
Optimised azaindole **18**.

Figure 14

The work carried out by AstraZeneca proved that a novel inhibitor of the ATPase site of GyrB/ParE could be successfully discovered through a fragment-based screen. Investigation of this series is reportedly ongoing, with future work being directed at optimisation of physiochemical properties, possibly focussing on lowering the toxicity and increasing the therapeutic window of the lead compound.[21]

4.3.6 The Trius Therapeutics series

Of particular relevance to the proposed research is the work performed by Trius Therapeutics. In a similar manner to AstraZeneca, a fragment-based crystallographic screen was used to identify a bioisostere to the previously reported cores, ensuring conservation of the adjacent hydrogen-bond donor-acceptor hinge region.[22] The screen yielded a pyrrolopyrimidine template **19** (**Figure 15**), which possessed the desired vectors to allow optimisation to proceed.
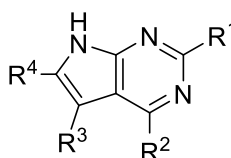
Pyrrolopyrimidine core **19**.

Figure 15

Each vector was optimised in turn, allowing the fine-tuning of interactions within the active site, resulting in an extremely potent pyrrolopyrimidine **20** (**Figure 16**).[22]
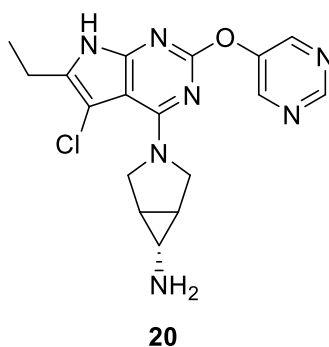
Optimised pyrrolopyrimidine **20**.

Figure 16

Pyrrolopyrimidine **20** was found to have potencies against *E. faecalis* GyrB and ParE of < 1 nM, which translated into MICs of ≤ 2 µg/mL against a wide range of gram-positive and gram-negative pathogens such as *S. aureus*, *S pneumoniae* and *E. coli*. However, potencies fell against the harder to target gram-negative strains, with MICs of 32 µg/mL against *P. aeruginosa* and 64 µg/mL against *K. pneumoniae*.[22, 23] Although the potencies of this series were encouraging, no toxicity data in the form of hERG or hepG2 measurements were reported, highlighting the early stage of this published work. Research by Trius Therapeutics within the area of pyrrolopyrimidines is reportedly ongoing, however no further publications have been released to date. However, it was reported that failure to successfully improve potency while maintaining low lipophilicity and molecular weight meant that an alternative scaffold became increasingly attractive.[1] As a result, a second series of compounds has since been disclosed by Trius Therapeutics.[1, 24] Building on the success of the pyrrolopyrimidine series, an alternative vector was used to expand into a lipophilic pocket, resulting in compound **21** (**Figure 17**), with a tricyclic core, aimed at treating multi-drug resistant gram-negative infections.

21
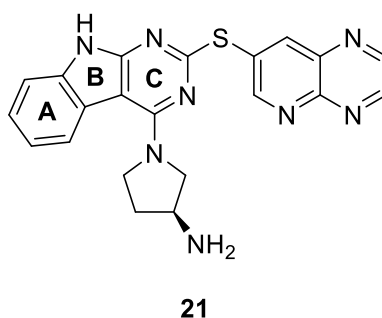
Tricyclic core hit **21**.

Figure 17

Compound **21** was well tolerated in the active site, giving sub-micromolar potencies against *E. coli* and *E. faecalis* GyrB and ParE enzymes.[1] Furthermore, the ability to build off ring **A** allowed the authors to further optimise the key binding interactions. Subsequent elaboration of the tricyclic core revealed that an aminomethyl substituent at the 8-position could strengthen the existing interactions with the protein by adding an extra H-bond donor. Additionally, it was observed that substitution of a fluorine atom at the 6-position resulted in broad-spectrum activity against GyrB and ParE. Optimisation of the pyrrolidine substituent revealed diamines at the 4-position were found to be the most permeable and least effluxed due to having an optimal distribution of charged and neutral states at physiological pH.[1] A combination of all optimised vectors gave inhibitor **1** (**Figure 18**).
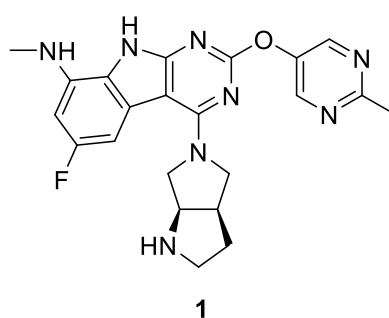
Optimised Trius Therapeutics inhibitor[1] **1**.

Figure 18

The authors reported exceptional activities for this compound, where it was found to be more potent against many of the tested bacteria than ciprofloxacin and vancomycin, both common clinically used antibiotics. The benefits of the tricyclic core were exemplified with MICs of less than 0.01 µg/mL for common gram-positive pathogens (*S. aureus* and *E. faecalis*), dropping off to an acceptable < 1 µg/mL for most gram-negative bacteria. Furthermore, a low frequency of resistance (< 1.9 x 10^{-11}) reflected positively on the ability of the optimised inhibitor **1** to dual target against DNA gyrase and topoisomerase IV.[1]

Unfortunately, no further publications have emerged from Trius Therapeutics in the area of GyrB inhibitors with a tricyclic core. This may be due to the fact that work is ongoing, or because the firm was acquired by Cubist Pharmaceuticals in July 2013, who were then purchased by Merck & Co. in 2015, resulting in a possible restructuring of priorities. Regardless, although low toxicity was hypothesised for the novel core,[1] no toxicity data has been published for the Trius Therapeutics series. However, recent unpublished in-house data suggested that, in general, compounds containing the tricyclic core were highly toxic

against the hepG2 cell line ($CC_{50} < 10$ µg/mL). This presented a major liability, which must be overcome for the series to progress.

As the authors were attempting to achieve broad-spectrum gram-negative activity, several alterations could be made to deliver an effective treatment against other pathogens, such as *M. tuberculosis*. For example, it could be hypothesised that the fluorine in the 6-position that was required for broad-spectrum gram-negative activity could be removed when targeting a single *M. tuberculosis* GyrB enzyme.

Furthermore, the optimisation of $logD_{7.4}$ and other physiochemical properties that was undertaken by the authors at Trius Therapeutics could, arguably, not confer high *M. tuberculosis* activity. As the cell wall structure of mycobacteria (such as *M. tuberculosis*) differs greatly from gram-positive and gram-negative cells, optimisation would have to be revisited with respect to the new disease target.

Table 1 summarises the key compounds of each series discussed in **Section 4.3**, along with their activity and current status.

4.3.7 Case histories - summary
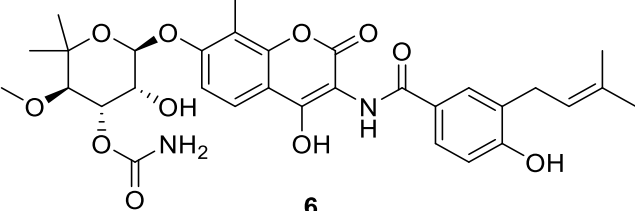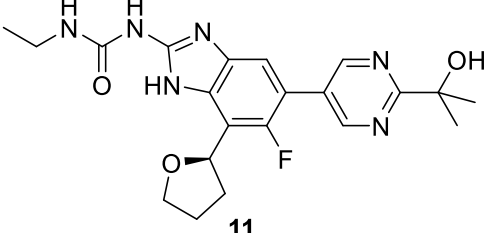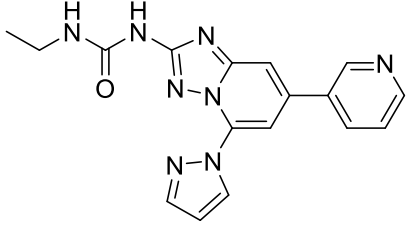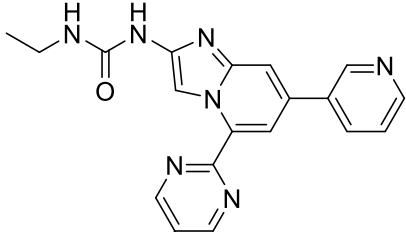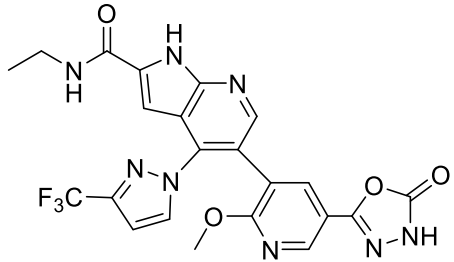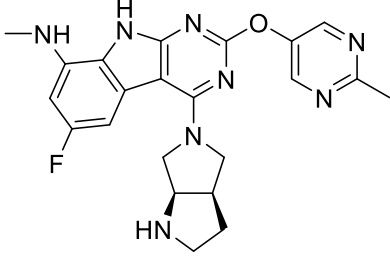
6	**Naturally occurring inhibitors** (e.g. novobiocin)[8] *S. aureus* MIC ≤ 0.12 µg/mL[14] Withdrawn by FDA for cytotoxicity[15]
11	**Vertex Pharmaceuticals** *S. aureus* MIC = 0.016 µg/mL[19] Preclinical candidate selected[19]
12	**Evotec Ltd.** *S. aureus* MIC = 2 µg/mL[20] hepG2 CC_{50} > 64 µg/mL[20] Pharmacokinetic optimisation ongoing (unpublished)[20]
13	**Pfizer** *S. aureus* MIC = 0.5 µg/mL[2] Further work ongoing (unpublished)[2]
18	**AstraZeneca** *S. aureus* MIC = 0.05 µg/mL[21] Optimisation of physiochemical properties ongoing[21]
1	**Trius Therapeutics** *S. aureus* MIC < 10 ng/mL[1] Low frequency of resistance (< 1.9 x 10^{-11})[1] hepG2 CC_{50} of similar analogues < 10 µg/mL[25]

Table 1

4.4 Proposed work

The proposed work was guided by the following results, obtained in-house before the beginning of the research programme. Building on the success of the work published by Trius Therapeutics,[1] Redx Pharma saw an opportunity to optimise the tricyclic core series by exploring uncharted chemical space around this scaffold. This was initially achieved by attempting to optimise the heterocyclic substituent, resulting in ether linked analogues similar in structure to those previously disclosed by Trius Therapeutics. Remarkably, it was discovered that amide derivatives of the tricyclic core had not been reported by Trius Therapeutics, and the synthesis of these analogues was therefore performed in-house. It was hypothesised that replacing the ether linkage with an amide may provide a new vector through which optimisation could occur. Several heterocyclic amides were synthesised, with varying antibacterial properties.
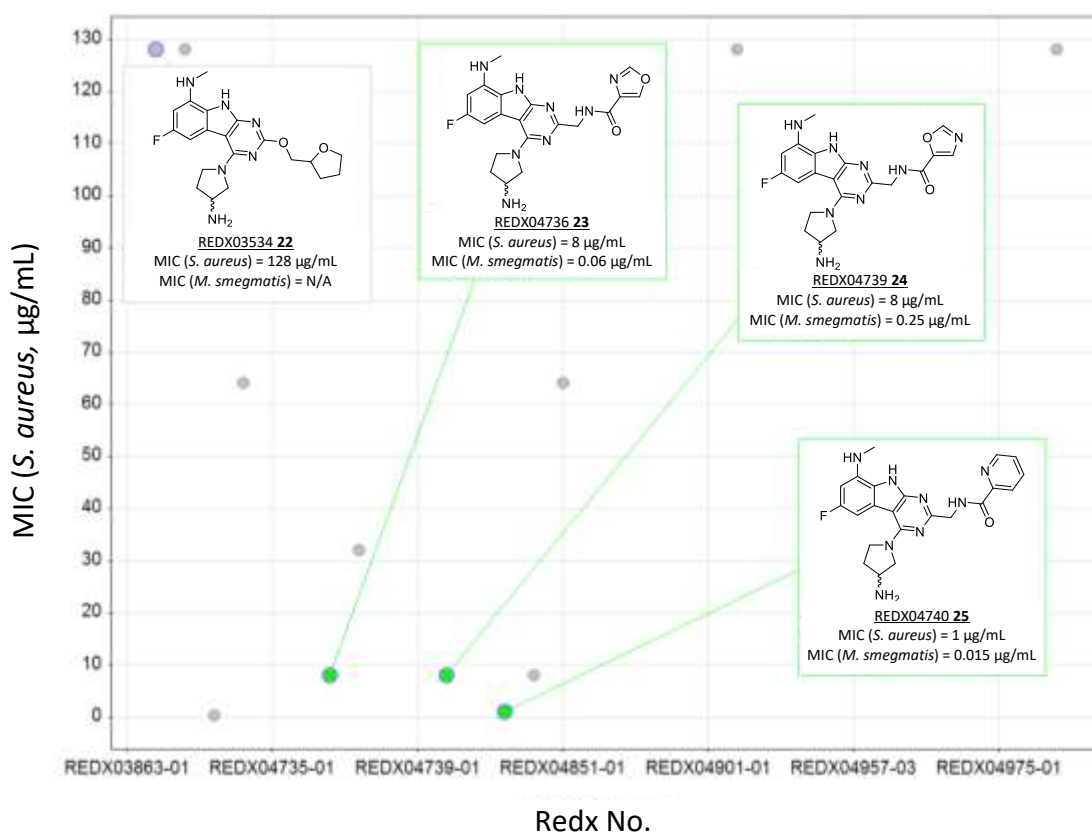
S. aureus activity for compounds synthesised before the beginning of the research programme. Highlighted (green) are compounds with MIC (*M. smegmatis*) ≤ 0.25 μg/mL.

Figure 19

Prior to the commencement of the research programme, only twelve target compounds had been synthesised in the series (**Figure 19**). Of these compounds, three were assessed

against *M. smegmatis*, showing exceptional potency. Unfortunately, due to changing priorities and limited resources, Redx Pharma chose to abandon the series. However, of particular interest were two isomeric compounds, REDX04736 **23** and REDX04739 **24** (**Figure 20**), which differed only in the attachment point to the oxazole substituent.
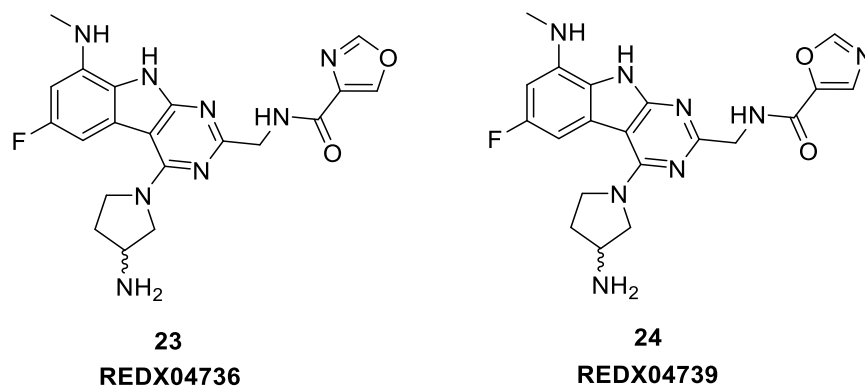
REDX04736 **23** and REDX04739 **24**.

Figure 20

REDX04736 **23** and REDX04739 **24** were synthesised from the route reported by McGarry *et al.* (**Section 4.7**). The antibacterial properties of these compounds against broad spectrum gram-positive and gram-negative pathogens were modest, with variable activities in accordance with the differing cellular structures (**Table 2**). However, the antibacterial activities against *M. smegmatis* (MIC = 0.12 µg/mL for REDX04736 **23**, MIC = 0.25 µg/mL for REDX04739 **24**) were encouraging. *M. smegmatis* is widely used as a surrogate strain for *M. tuberculosis,* and therefore high activity against *M. tuberculosis* was predicted.[26]

It was observed that the potency against *M. tuberculosis* (H37Rv) paralleled the high activity against *M. smegmatis* (ATCC19420), opening up a potentially lucrative area of research in treating tuberculosis infections.

		REDX04736 **23**	REDX04739 **24**
MICs (µg/mL)	*P. aeruginosa* ATCC27853	128	32
	E. coli ATCC25922	0.5	4
	H. influenzae ATCC49247	1	1
	S. aureus ATCC29213	8	8
	E. faecalis ATCC29212	0.06	1
	S. pneumoniae ATCC49619	0.12	1
	M. smegmatis ATCC19420	0.12	0.25
	M. tuberculosis H37Rv	< 0.06	< 0.03
hERG inhibition		-	30% (at 33 µM)
hepG2 (CC$_{50}$, µg/mL)		10.1	> 16

Key for relevant biological and physiochemical results			
MICs (µg/mL)	≤ 1	2 – 16	≥ 32
hERG inhibition (% at 33 µM)	< 20%		≥ 20%
hepG2 (CC$_{50}$, µg/mL)	≥ 16		< 16

Antibacterial and physiochemical profiles for REDX04736 **23** and REDX04739 **24**.

Table 2

As cytotoxicity data was never disclosed by Trius Therapeutics, a key compound from the tricyclic core series (REDX03863 **26**, **Figure 21**) was synthesised in-house and was found to be cytotoxic in a hepG2 cell viability assay. Furthermore, the majority of compounds synthesised in-house before the commencement of the project were also cytotoxic. Although REDX04736 **23** and REDX04739 **24** were seen to have similar antibacterial and physiochemical properties, the contrast between the two isomers became apparent when assessing each compound's cellular toxicity (**Figure 21**).
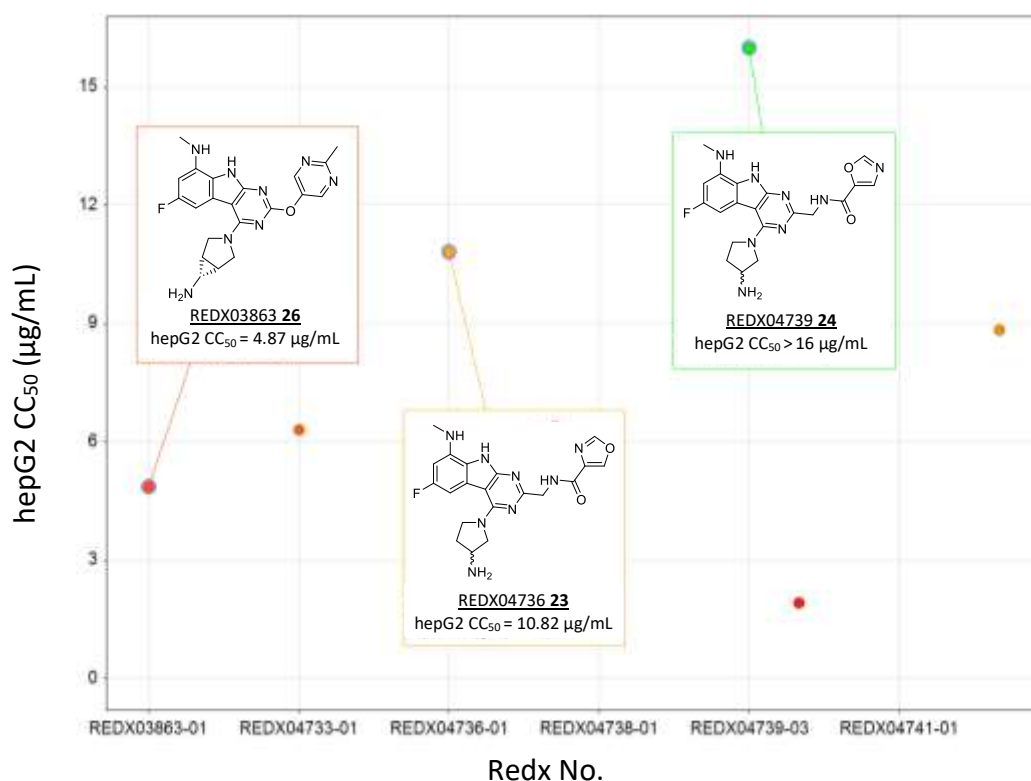
hepG2 toxicity for REDX04736 **23**, REDX04739 **24** and REDX03863 **26**.

Figure 21

REDX04736 **23** was found to be highly cytotoxic (hepG2 CC_{50} = 10.1 µg/mL). In contrast, REDX04739 **24** showed no sign of cytotoxicity (hepG2 CC_{50} > 16 µg/mL). However, the low solubility of REDX04739 **24** prevented higher concentrations than 16 µg/mL to be achieved, precluding further toxicity data from being collected. Nevertheless, the results indicated an unusual difference in cellular toxicity between the isomers, with a clear toxic response being observed for REDX04736 **23** compared to REDX04739 **24** (**Figure 22**).
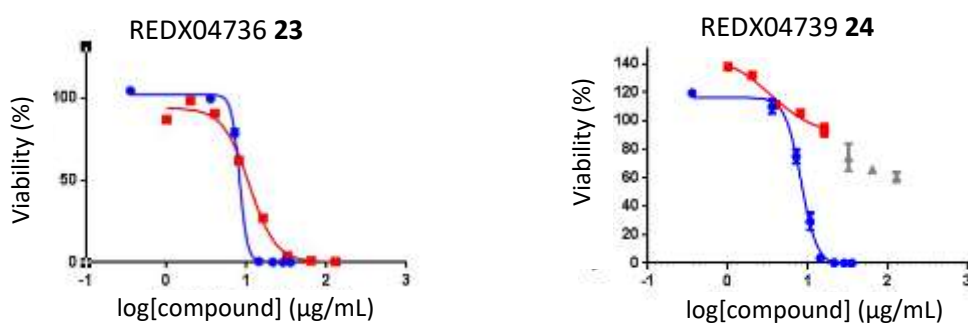
hepG2 curves (red) for REDX04736 **23**, REDX04739 **24** against chlorpromazine (blue).

Figure 22

4.5   Objectives

At the beginning of the research project, the following objectives were set:

1. Synthesise analogues of REDX04739 **24** with alternate amine substituents (**Figure 23**). Monitoring the effects on antibacterial activity may aid development of a structure-activity relationship surrounding the optimal $logD_{7.4}$ and pK_a required for *M. tuberculosis* activity.

2. Synthesise analogues of REDX04739 **24** with alternate oxazole amide moieties (**Figure 23**). Matched pair analysis may aid elucidation of toxicity trends, determining if the toxicity difference observed between REDX04736 **23** and REDX04739 **24** was a singularity or a property of the series.
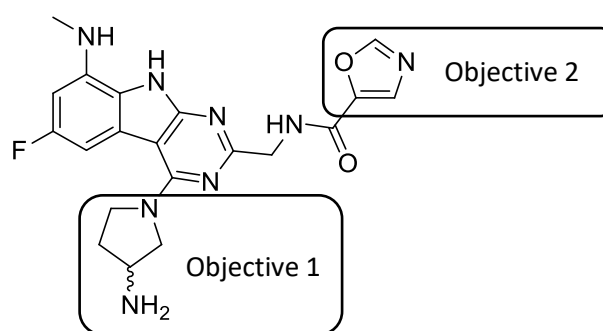
REDX04739 **24**, with areas for analogue synthesis highlighted.

Figure 23

3. Obtain relevant data to support optimisation, including antibacterial activity, hepG2 cell viability and hERG inhibition, where appropriate.

4. Where appropriate, aid rationalisation of experimentally observed trends through computational modelling.

4.6   Introduction to publication

In the following section (**Section 4.7**), the progress achieved throughout this part of the research programme is summarised by inclusion of the following peer-reviewed publication (McGarry *et al.*, *Bioorg. Med. Chem. Lett.* **2018**, *28*, 2998-3003). All compounds reported in **Section 4.7** (except compounds **8** and **2aa** – **2ad**) were synthesised as part of the current research programme, in order to investigate the impact that the structural modification of the amide and pyrrolidine appendages had on the activity and cytotoxicity of the series. For convenience, compounds reported in **Section 4.7** have been given alternative numbering (**Table 3**), to allow further discussion of results within this report.

Compound numbering in publication	Alternative compound numbering
2aa	REDX04740 **25**
2ab	REDX03863 **26**
2ac	REDX04736 **23**
2ad	REDX04739 **24**
2bc	REDX07942 **27**
2bd	REDX07774 **28**
2be	REDX07966 **29**
2cd	REDX08027 **30**
2ce	REDX08049 **31**
2cf	REDX08066 **32**
2cg	REDX09133 **33**
2ch	REDX09147 **34**
2dd	REDX08191 **35**
2de	REDX08230 **36**
2df	REDX08271 **37**
2di	REDX08365 **38**

Compound numbering for publication and research programme.

Table 3
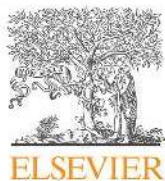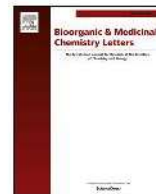
Design, synthesis and antibacterial properties of pyrimido[4,5-*b*]indol-8-amine inhibitors of DNA gyrase

David H. McGarry[a,*], Ian R. Cooper[a], Rolf Walker[a], Catherine E. Warrilow[a], Mark Pichowicz[a], Andrew J. Ratcliffe[a], Anne-Marie Salisbury[a], Victoria J. Savage[a], Emmanuel Moyo[a], John Maclean[a], Andrew Smith[a], Cédric Charrier[a], Neil R. Stokes[a], David M. Lindsay[b], William J. Kerr[b]

[a] *Redx Pharma, Alderley Park, Cheshire SK10 4TG, United Kingdom*
[b] *Department of Pure and Applied Chemistry, University of Strathclyde, WestCHEM, Thomas Graham Building, 295 Cathedral Street, Glasgow G1 1XL, United Kingdom*

ARTICLE INFO

ABSTRACT

According to the World Health Organization (WHO), approximately 1.7 million deaths per year are caused by tuberculosis infections. Furthermore, it has been predicted that, by 2050, antibacterial resistance will be the cause of approximately 10 million deaths annually if the issue is not tackled. As a result, novel approaches to treating broad-spectrum bacterial infections are of vital importance. During the course of our wider efforts to discover unique methods of targeting multidrug-resistant (MDR) pathogens, we identified a novel series of amide-linked pyrimido[4,5-*b*]indol-8-amine inhibitors of bacterial type II topoisomerases. Compounds from the series were highly potent against gram-positive bacteria and mycobacteria, with excellent potency being retained against a panel of relevant *Mycobacterium tuberculosis* drug-resistant clinical isolates.

Antibiotic resistance is rapidly becoming prevalent in both a clinical and a community setting. Alarmingly, it is predicted that failure to address this issue could lead to approximately 10 million deaths per year by 2050.[1] A recent report by the WHO identified tuberculosis (TB) as a global priority for research and development due to its status as the number one global infectious disease killer, causing 1.7 million deaths per year.[2] A further 12 priority pathogens were identified, consisting of *Acinetobacter baumannii, Pseudomonas aeruginosa, Enterobacteriaceae, Enterococcus faecium, Staphylococcus aureus, Helicobacter pylori, Campylobacter* spp, *Salmonellae, Neisseria gonorrhoeae, Streptococcus pneumoniae, Haemophilus influenzae* and *Shigella* spp.

Antibiotics such as fluoroquinolones have had great clinical success, however, bacteria have evolved resistance to entire classes of antibiotics. Overexpression of efflux pumps, target-specific mutations, modifications to the bacterial cell wall and the generation of drug-inactivating enzymes can all contribute to bacterial resistance.[3] Consequently, research into chemical series' with the ability to target drug-resistant bacteria are of utmost importance. One method of overcoming site-specific mutation resistance is to target alternative binding sites which are capable of inducing the same phenotypic response.

DNA gyrase and topoisomerase IV are two examples of highly homologous bacterial type IIA topoisomerases which have the ability to break, reorganise and religate DNA strands.[4] Without recourse to these enzymes, bacteria are not able to appropriately manipulate the topology of their DNA, resulting in eventual cellular death. Fluoroquinolones target the DNA binding site of topoisomerases in order to elicit their therapeutic effect, however, recent publications have focused on inhibition at an alternative site (the ATPase sites on GyrB/ParE on DNA gyrase/topoisomerase IV respectively) in order to circumvent resistance mechanisms. In the 60 years since the first GyrB/ParE inhibitor, novobiocin 1 (Fig. 1), was discovered, many chemical series have been developed through fragment-based screening, high-throughput screening and scaffold hopping.[5–10]

Herein we describe the discovery and structure-activity relationship (SAR) of a novel series of amide-linked pyrimido[4,5-*b*]indol-8-amine inhibitors of bacterial type II topoisomerase, which were identified using computational analysis of published GyrB inhibitors and an antibacterial library screen. It was observed in many of the previously published crystal structures of GyrB that a flexible loop adjacent to the ATPase site was poorly ordered, and usually omitted from the deposited coordinates (green arrow, Fig. 2a). Due to the absence of the resolved loop in many structures, proposed interactions in this area have been poorly modelled computationally. However, when an X-ray crystal structure in which this loop was resolved (PDB: 3G7E, green) was

---

* Corresponding author.
E-mail address: d.mcgarry@redxpharma.com (D.H. McGarry).
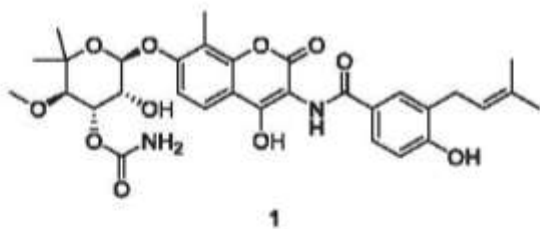
Fig. 1. Novobiocin 1.

overlayed with a range of inhibitors, an unexplored vector near Asp106 was revealed (blue arrow). It was postulated that establishing initial SAR along this vector could serve to both probe the computational model and allow elaboration of a novel inhibitor series. Investigation of the SAR in this way could afford improvements to a variety of PK properties, by highlighting a region of the scaffold from which further optimisation could progress. In combination with these structural studies, an in-house compound library screen identified hit compound 2aa (Fig. 2b, Table 1), where the substituent probing the Asp106 vector is attached via a novel amide linker. This discovery prompted further investigation of the novel amide-linked pyrimido[4,5-b]indol-8-amine scaffold as a means of challenging the SAR in this region.

Utilising the previously reported intermediate 3[11] (Scheme 1) allowed the synthesis of final compounds 2aa-2di to proceed efficiently via a reproducible, reliable route, from which a range of analogues could be generated. Disulfone 3 was identified as an important intermediate, since several points of diversity could be explored from this compound. Substitution with a variety of 3-substituted pyrrolidines yielded compounds 4, with the relative structural configuration established through an observed Nuclear Overhauser effect between the pyrrolidine substituent and the pyrimidine core (Scheme 1).

Aromatic nucleophilic substitution of 4 with sodium cyanide then afforded key intermediate 5 (Scheme 1), which could be elaborated through nitrile reduction, unmasking primary amines of the form 6. Amide coupling with an appropriate carboxylic acid followed by deprotection yielded amides of the form 2aa-2di (Table 1). The carboxylic acids were selected on the basis of their commercial availability and similarity to those previously reported in the literature.

Final compounds 2aa-2di were tested against a panel of antibacterial strains (Table 1), including gram-positive pathogens (E. faecalis and S. aureus), gram-negative pathogens (E. coli) and mycobacteria

(M. smegmatis and M. tuberculosis).

Incorporation of an oxazole moiety at the amide (2ac and 2ad), provided potency against M. smegmatis and M. tuberculosis (Table 1). Interestingly, a potency increase against gram-positive bacteria and mycobacteria was observed upon N,N-dimethylation of the 3-amino-pyrrolidine, consistent with the hypothesised increase in permeability upon removal of the H-bond donating ability of the primary/secondary amine. Encouraged by the improved potency of the oxazole subseries, the SAR was further challenged through subsequent methylation of the oxazole ring. Oxazole methylation tended to increase the potency for a series, however, the position of optimal methylation was variable. Computational methods (See Computational Analysis section, below) were utilised to aid rationalisation of these results. In order to further profile the series, a selection of compounds were tested against a broader panel of gram-positive and gram-negative bacteria, and assessment of their in vitro cytotoxicity was undertaken (Table 2).

Representative compounds were found to partially retain activity against a broader spectrum of bacteria, with no toxic effects observed in a HepG2 mammalian cytotoxicity assay for the majority of the tested compounds. Importantly, examples from the series were found to be more potent against M. tuberculosis than novobiocin 1. Target engagement was confirmed by testing for the ability of the inhibitor to prevent DNA supercoiling, and through its capacity to inhibit ATP hydrolysis (Table 3). Inhibition of human topoisomerase II decatenation highlighted the high bacterial selectivity of the series (Table 3).

As a result of the high potency against M. tuberculosis, representative compounds from our novel series were tested against a panel of bacterial strains bearing mechanisms that rendered them resistant to clinically utilised antibiotics. All the resistant strains used were derived from M. tuberculosis H37Rv, and carried resistance mechanisms as outlined in Table 4.

Gratifyingly, the Redx Pharma series was observed to maintain potency against the tested resistant isolates, highlighting a benefit in the current series compared to the clinically-relevant compounds moxifloxacin, isoniazid, rifampicin and novobiocin.

Computational analysis

Compound 2cf, the result of 2-methylation of the oxazole in 2cd, was found to be 5-fold higher in potency against M. smegmatis compared to the undecorated analogue. Although it was hypothesised that
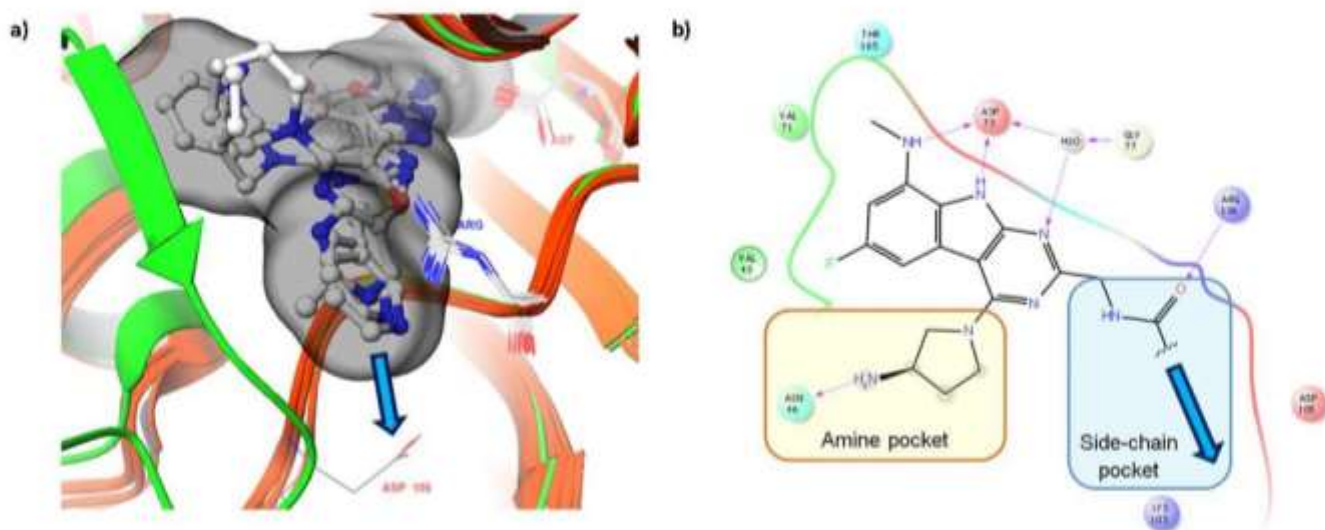

Fig. 2. (a) Proposed vector (blue arrow), from which the inhibitor could be expanded in the side-chain pocket, towards Asp106. Figure generated from overlaying structures of 3G7E,[12] 4K4O[10] and 5D7C.[13] The flexible loop of residues, which are omitted in all structures but present in 3G7E, is highlighted in green. The approximate space-fill surface for the majority of published inhibitors is shown in black. (b) Hypothesised amide-linked pyrimido[4,5-b]indol-8-amine compounds that could utilise a previously underexplored vector (blue arrow). Both figures generated using Maestro Version 10.6.014.[14]

Table 1

In vitro antibacterial activity of novobiocin **1** and amide-linked pyrimido[4,5-*b*]indol-8-amine inhibitors.

Compound	R1	R2	MIC (µg/mL)[a]				
			Ef	Sa	Ec	Ms	Mt
Novobiocin 1	-	-	4 (ref.[15])	0.06	>64	1	4 (ref.[16])
8	a	H	8	8	8	N.D.	N.D.
2aa	a	a	0.25	32	8	N.D.	N.D.
2ab	a	b	0.12	8	4	N.D.	N.D.
2ac	a	c	0.06	8	128	0.12	N.D.
2ad	a	d	1	8	4	0.25	0.25
2bc	b	c	0.25	16	16	0.5	0.12
2bd	b	d	0.5	8	4	0.5	0.03
2be	b	e	0.25	4	4	0.06	0.03
2cd	c	d	0.015	0.5	0.25	0.06	0.06
2ce	c	e	0.03	1	2	0.06	0.06
2cf	c	f	0.015	1	1	0.002	N.D.
2cg	c	g	0.12	0.25	0.5	0.06	0.03
2ch	c	h	0.5	1	4	0.25	0.25
2dd	d	d	0.12	4	4	0.06	0.03
2de	d	e	0.5	8	8	0.03	0.015
2df	d	f	0.25	8	4	0.12	0.015
2di	d	i	1	8	32	0.06	N.D.

[a] Ef (*E. faecalis* ATCC 29212), Sa (*S. aureus* ATCC 29213), Ec (*E. coli* ATCC 25922), Ms (*M. smegmatis* ATCC 19420), Mt (*M. tuberculosis* H37Rv). N.D. (not determined).
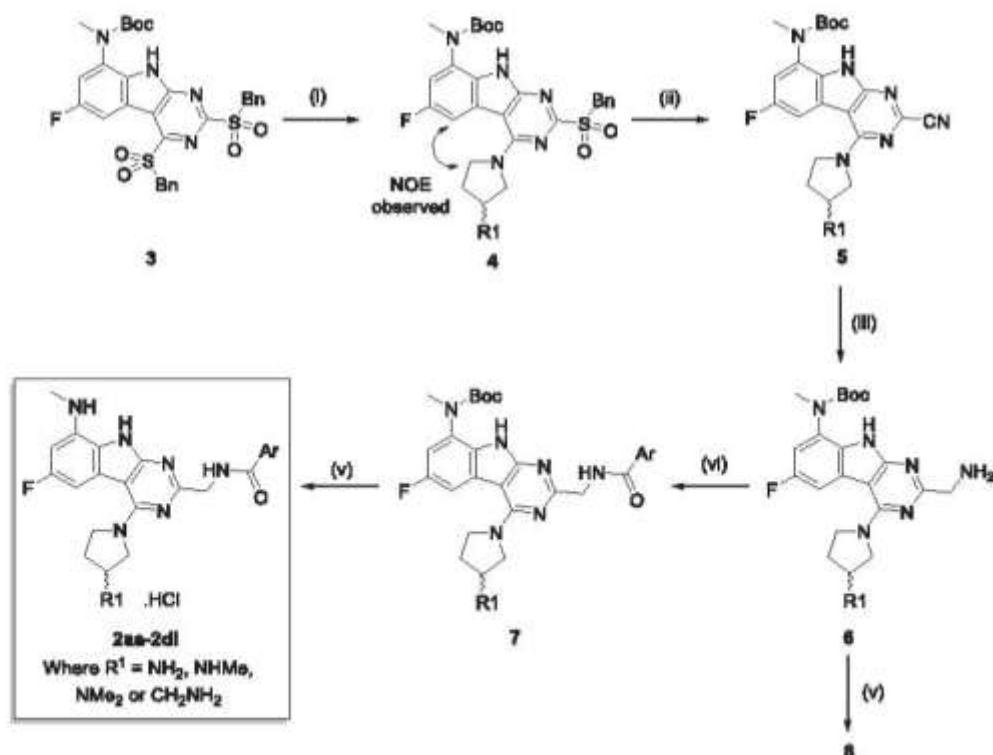
Scheme 1. Use of disulfone **3** to introduce structural diversity. Reagents and conditions: (i) substituted pyrrolidine, K₂CO₃, EtOH, 45 °C, 50 min, MW, 61–89% (ii) NaCN, DMF, 100 °C, 16 h, 60–89% (iii) Raney nickel, H₂, EtOH, rt, 16 h, 68–97% (iv) ArCOOH, EDCI, Et₃N, DCM, rt, 16 h, 13–67% (v) HCl (4N in dioxane), MeOH, rt, 16 h, 14–99%.

Table 2
Extended *in vitro* antibacterial activity and cytotoxicity of novobiocin **1** and a selected amide-linked pyrimido[4,5-*b*]indol-8-amine inhibitors.

Compound	MIC (µg/mL)[a]					HepG2 (IC$_{50}$, µg/mL)[b]
	Ab	Pa	Hi	Se	Sp	
Novobiocin **1**	N.D.	> 64 (Ref.[15])	0.5 (Ref.[15])	0.06 (Ref.[15])	0.5 (Ref.[15])	> 32
2ac	16	128	1	1	0.12	10.82
2ad	8	32	1	1	1	> 16
2bd	> 64	> 64	4	2	2	> 32
2cd	1	> 64	4	0.12	0.12	> 16

[a] Ab (*A. baumannii* NCTC 13420), Pa (*P. aeruginosa* ATCC 27853), Hi (*H. influenzae* ATCC 49247), Se (*S. epidermidis* ATCC 12228), Sp (*S. pneumoniae* ATCC 49619) [b]Hep G2 cells incubated for 24 h at 37 ˚C in 5% CO_2 and viability determined using CellTiter-Glo® (Promega, WI, USA). N.D. (not determined).

Table 3
Target engagement of novobiocin **1** and selected amide-linked pyrimido[4,5-*b*]indol-8-amine inhibitors. N.D. (not determined).

Compound	*M. tuberculosis* gyrase supercoiling inhibition (IC$_{50}$, µM)	*M. tuberculosis* gyrase ATPase inhibition (IC$_{50}$, µM)	Human topoisomerase II decatenation inhibition (% inhibition at 100 µM)
Novobiocin **1**	0.085	0.020	N.D.
2ac	0.005	0.025	5.8%
2ad	0.010	0.059	21.2%

Table 4
In vitro antibacterial activity of clinically used antibiotics and amide-linked pyrimido[4,5-*b*]indol-8-amine inhibitors against resistant isolates.

Compound	Ms	Mt	MIC (µg/mL)[a]		
			FQ-R1 (GyrA D94N substitution)	INH-R1 (truncated at 155 of KatG)	RIF-R1 (RpoB S522L substitution)
Moxifloxacin (FQ)	0.03	N.D.	3.9	0.04	0.04
Isoniazid (INH)	4	N.D.	0.05	> 27	0.014
Rifampicin (RIF)	16	N.D.	0.019	0.013	3.0
Novobiocin **1**	1	4 (Ref.[16])	7.35	6.7	13.5
2ac	0.12	N.D.	0.014	0.013	0.012
2ad	0.25	0.25	0.09	0.09	0.09

[a] Ms (*M. smegmatis* ATCC 19420), Mt (*M. tuberculosis* H37Rv), FQ-R1 (fluoroquinolone-resistant), INH-R1 (isoniazid-resistant), RIF-R1 (rifampicin-resistant). N.D. (not determined). Data collected in May 2015.

the addition of the methyl group may result in improved permeability through increasing lipophilicity, computational simulations were used to determine if the potency increase was due to a specific interaction.
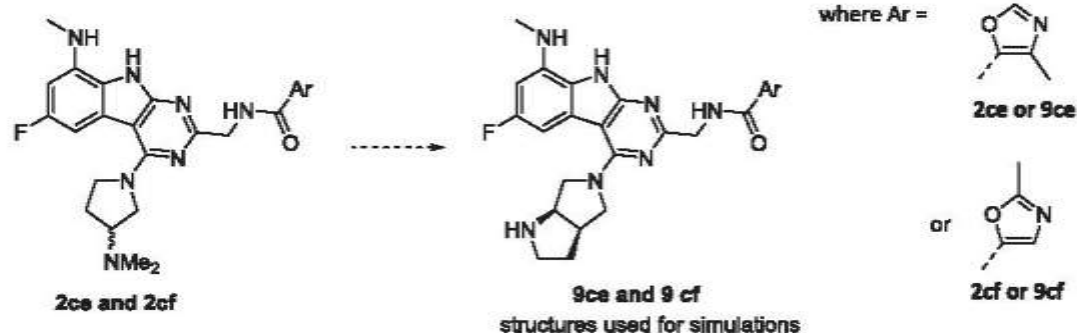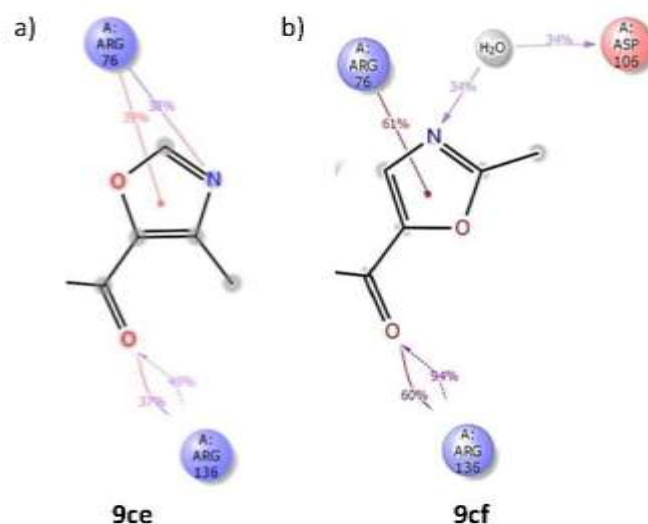
Fig. 4. Interaction maps for structures relating to (a) **9ce** and (b) **9cf**.

Molecular dynamics calculations were performed using Desmond v2.3[17] (see *Experimental* section, below) on two hypothetical analogues relating to **2ce** and **2cf** (**9ce** and **9cf**, Fig. 3). As the most structurally similar analogue with an X-ray crystal structure (PDB: 4K4O[16]) utilised a bicyclic amine in the amine pocket, this was kept consistent throughout the simulations to ensure differences in binding could be rationalised primarily through alterations to the heterocycle inhabiting the side-chain pocket.

The simulation showed that the protein-ligand interactions were stable, and key interactions were consistent with those observed in the X-ray crystal structure of similar GyrB inhibitors, providing confidence in the computational method. The most important binding interactions were found to be hydrogen bonds between the three nitrogen atoms on the tricyclic core and Asp73 and its coordinated water. Furthermore, a strong association of the oxazole ring with Arg76 was concordant with a π-cation interaction, consistent with published observations.[10] As the core of the molecule remained unchanged throughout the simulations, focus was placed on how the heterocyclic amide may effect binding. The resulting interaction maps for the oxazole substituents are shown in Fig. 4, with relative interaction probabilities annotated alongside. For example, an interaction probability of 61% related to the interaction being observed to occur during 61% of the simulation.

Similar residues were observed to be involved in each compound's binding interactions near the amide substituent, however, the extent of the binding was variable. Arg136 formed a hydrogen bond with the amide carbonyl in both simulations. However, in **9cf**, this interaction seemed more stable, with a higher interaction probability (up to 94% compared to up to 49% in **9ce**). This improved interaction in **9cf** was hypothesised to be a result of the oxazole-methyl group in **9ce** causing a steric clash with Arg136 in the active site, discouraging binding
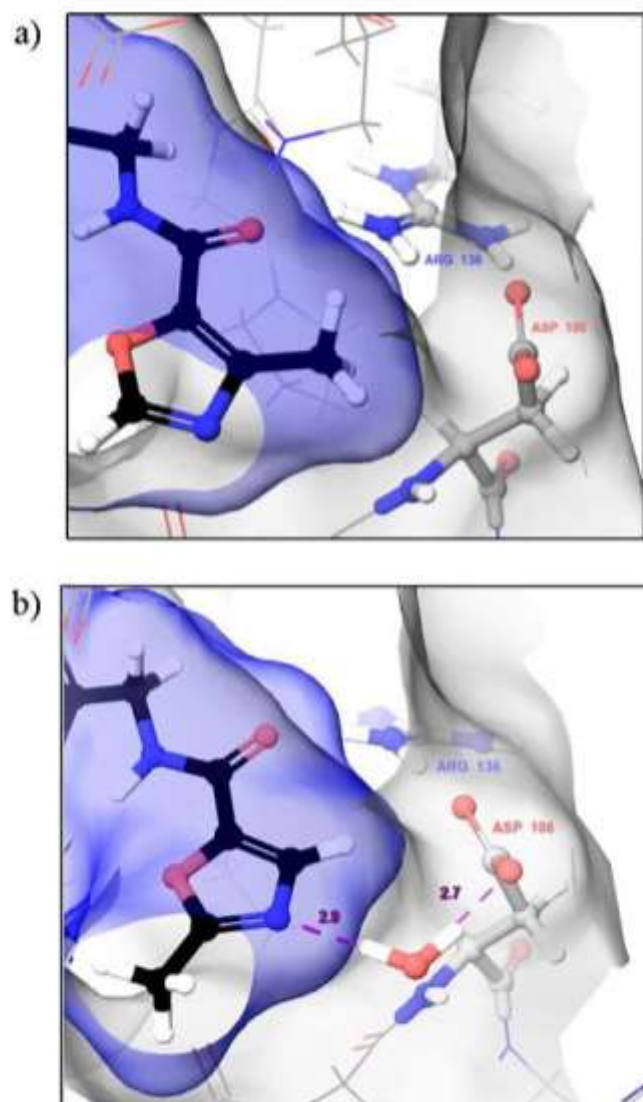

Fig. 3. **9ce**, and **9cf** were used for the computational analysis, as analogues of **2ce** and **2cf** respectively.

Page | 255

Fig. 5. (a) Potential clash of Arg136 with **9ce**, which would be alleviated in **9cf** (b) MD frame of **9cf** highlighting the possible water-mediated interaction made with Asp106.

(Fig. 5a). Movement of the methyl group to the 2-position of the oxazole could alleviate this clash, decreasing the overall energy of the system, and contributing to an increase the potency of the ligand.

Interestingly, an additional potency driving interaction may be picked up by **9cf** to Asp106, which resides on the flexible loop commonly omitted from the majority of deposited X-ray crystal structures. The nitrogen atom in the oxazole ring of **9cf** may be in a more appropriate orientation to bind *via* a water-mediated interaction to Asp106 (Fig. 5b). The existence of this interaction may reflect the increase in *M. smegmatis* potency observed between compounds **2ce** and **2cf**. Furthermore, elaboration along the vector towards Asp106 may provide additional potency-driving interactions to optimise the series.

In summary, utilising computational analysis of previously published crystal structures of GyrB inhibitors in DNA gyrase allowed the development of the current antibacterial series, focussing on improving the activity and spectrum of susceptible bacteria. A combination of expanding into an identified area of the active site, and alteration of permeability through removal of H-bond donors, has successfully yielded antibacterial compounds with potent activity against grampositive bacteria and mycobacteria. Furthermore, the potential of the series has been exemplified through the ability of the compounds to maintain activity against a range of drug-resistant *M. tuberculosis*

clinical isolates. Subsequent alterations of the amide-linked heterocycles have demonstrated steric bulk can not only be tolerated in this area of the protein, but additional potency increasing interactions could be designed into the inhibitors through interaction with Asp106, which resides on the flexible loop.

Experimental

Molecular dynamics

Protein structures were prepared using Maestro's Protein Preparation Wizard (PrepWizard), following the procedure outlined by Sastry et al.[18] Unfortunately, the X-ray crystal structure of 4K4O[10] (*E. faecalis*) was not complete, and the flexible loop of residues that resided near the pyrimidine substituent were omitted, resulting in the use of a complete crystal structure, 3G7E[12] (*E. coli*), instead. The suitability of the proteins to be interchanged was assessed by determining that 68% of residues within the active site were identical. Of the non-identical residues, mutation was commonly observed to be a result of a small change (e.g. VAL to ILE). Each mutated residue was assessed for its contribution to binding, resulting in 95% similarity of the active sites of 4K4O and 3G7E, and could therefore used interchangeably during the computational studies. Furthermore, both sequences were seen to be highly similar to 3ZM7 (*M. tuberculosis*), allowing comparisons in binding to be drawn from simulations of 3G7E. Each compound was docked using a knowledge-based alignment and the protein–ligand complex was solvated and simulated for 8 ns at a temperature of 300 K using the OPLS_2005 force field[19] in Desmond v2.3.[17] The system trajectories were then analysed using Maestro v10.6.014[14], monitoring how key interactions evolved over the course of the experiment.

Declaration of interest

All authors affiliated with Redx Pharma are/were employees of the company and may own shares and/or share options in Redx Pharma Plc.

Supplementary data

Supplementary data associated with this article can be found, in the online version, at http://dx.doi.org/10.1016/j.bmcl.2018.05.049.
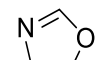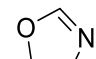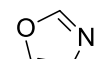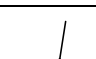
References

1. O'Neill J. Tackling Drug-Resistant Infections Globally: Final Report and Recommendations. 2016.
2. Fact Sheet 104: Tuberculosis. World Health Organisation; October 2017.
3. Allen HK, Donato J, Wang HH, Cloud-Hansen KA, Davies J, Handelsman J. Call of the wild: antibiotic resistance genes in natural environments. *Nat Rev Micro*. 2010;8:251–259.
4. Vos SM, Tretter EM, Schmidt BH, Berger JM. All tangled up: how cells direct, manage and exploit topoisomerase function. *Nat Rev Mol Cell Biol*. 2011;12:827–841.
5. Charifson PS, Grillot A-L, Grossman TH, et al. Novel dual-targeting benzimidazole urea inhibitors of DNA gyrase and topoisomerase IV possessing potent antibacterial activity: intelligent design and evolution through the judicious use of structure-guided design and structure – activity relationships. *J Med Chem*. 2008;51:5243–5263.
6. Starr JT, Sciotti RJ, Hanna DL, et al. 5-(2-Pyrimidinyl)-imidazo[1,2-a]pyridines are antibacterial agents targeting the ATPase domains of DNA gyrase and topoisomerase IV. *Bioorg Med Chem Lett*. 2009;19:5302–5306.

7. Grillot A-L, Tiran AL, Shannon D, et al. Second-generation antibacterial benzimidazole ureas: discovery of a preclinical candidate with reduced metabolic liability. *J Med Chem.* 2014;57:8792–8816.

8. Manchester JI, Dussault DD, Rose JA, et al. Discovery of a novel azaindole class of antibacterial agents targeting the ATPase domains of DNA gyrase and Topoisomerase IV. *Bioorg Med Chem Lett.* 2012;22:5150–5156.

9. East SP, White CB, Barker O, et al. DNA gyrase (GyrB)/topoisomerase IV (ParE) inhibitors: synthesis and antibacterial activity. *Bioorg Med Chem Lett.* 2009;19:894–899.

10. Tari LW, Li X, Trzoss M, et al. Tricyclic GyrB/ParE (TriBE) inhibitors: a new class of broad-spectrum dual-targeting antibacterial agents. *PLOS ONE.* 2013;8:e84409.

11. Cooper I, Pichowicz M, Stokes N. WO 2016067009. 2016.

12. Ronkin SM, Badia M, Bellon S, et al. Discovery of pyrazolthiazoles as novel and potent inhibitors of bacterial gyrase. *Bioorg Med Chem Lett.* 2010;20:2828–2831.

13. Zhang J, Yang Q, Cross JB, et al. Discovery of azaindole ureas as a novel class of bacterial gyrase B inhibitors. *J Med Chem.* 2015;58:8503–8512.

14. Schrödinger Release 2017–3: Maestro, Schrödinger, LLC, New York, NY, 2017.

15. Stokes NR, Thomaides-Brears HB, Barker S, et al. Biological evaluation of benzothiazole ethyl urea inhibitors of bacterial type II topoisomerases. *Antimicrob Agents Chemother.* 2013;57:5977–5986.

16. Chopra S, Matsuyama K, Tran T, et al. *J Antimicrob Chemother.* 2012;67:415–421.

17. Bowers KJ, Chow E, Xu H, et al. Scalable algorithms for molecular dynamics simulations on commodity clusters. In: Proceedings of the 2006 ACM/IEEE conference on Supercomputing. Tampa, Florida: ACM; 2006:84.

18. Sastry MG, Adzhigirey M, Day T, Annabhimoju R, Sherman W. Protein and ligand preparation: parameters, protocols, and influence on virtual screening enrichments. *J Comput Aided Mol Des.* 2013;27:221–234.

19. Shivakumar D, Williams J, Wu Y, Damm W, Shelley J, Sherman W. Prediction of absolute solvation free energies using molecular dynamics free energy perturbation and the OPLS force field. *J Chem Theory Comput.* 2010;6:1509–1519.

Page | 257

4.8 Conclusions

The publication in **Section 4.7** described a combined computational/experimental approach to enhancing the antibacterial activity of a series of GyrB/ParE inhibitors. Although not the focus of this published work, trends in hepG2 cell cytotoxicity were also investigated within this series of compounds (**Table 4**).

		Pyrrolidine			
		NH₂	HN	N	NH₂
Oxazole		REDX04736 **23**	REDX07942 **27**	-	-
		10.82	16 − 32	-	-
		REDX04739 **24**	REDX07774 **28**	REDX08027 **30**	REDX08191 **35**
		> 16	> 32	> 16	-
		-	REDX07966 **29**	REDX08049 **31**	REDX08230 **36**
		-	2 - 4	4 − 8	> 8
		-	-	REDX08066 **32**	REDX08271 **37**
		-	-	> 8	-

hepG2 cytotoxicity results for oxazole analogues (CC$_{50}$, μg/mL).

Table 4

The results generated throughout the research project highlighted the progress made, and provided additional data to support the hypothesised trend in oxazole cytotoxicity, as observed between REDX04736 **23** and REDX04739 **24**. Unfortunately, due to the poor solubility of the substrates, accurate values for hepG2 cytotoxicity could not be determined before the compounds precipitated during the assay conditions. Although absolute values were unable to be recorded, a general trend was observed, consistent with the hypothesised low toxicity of the 5-substituted oxazoles. This unusual apparent non-cytotoxicity may provide a means for optimisation of the compound, progressing towards a potentially successful drug. Furthermore, if the observed trends parallel the toxicity of other literature chemical series, a similar approach could be used to alleviate any toxicity issues seen for competitor compounds.

Gratifyingly, improved antibacterial potency and, in particular, gram-negative activity, was achieved in optimising REDX04739 **24** to yield REDX08027 **30** (**Figure 24**).

24
REDX04739

MIC (*S. aureus*) = 8 µg/mL

MIC (*E. coli*) = 4 µg/mL

➔

➔

30
REDX08027

MIC (*S. aureus*) = 0.015 µg/mL

MIC (*E. coli*) = 0.25 µg/mL

Improvement of potency achieved through analogue synthesis.
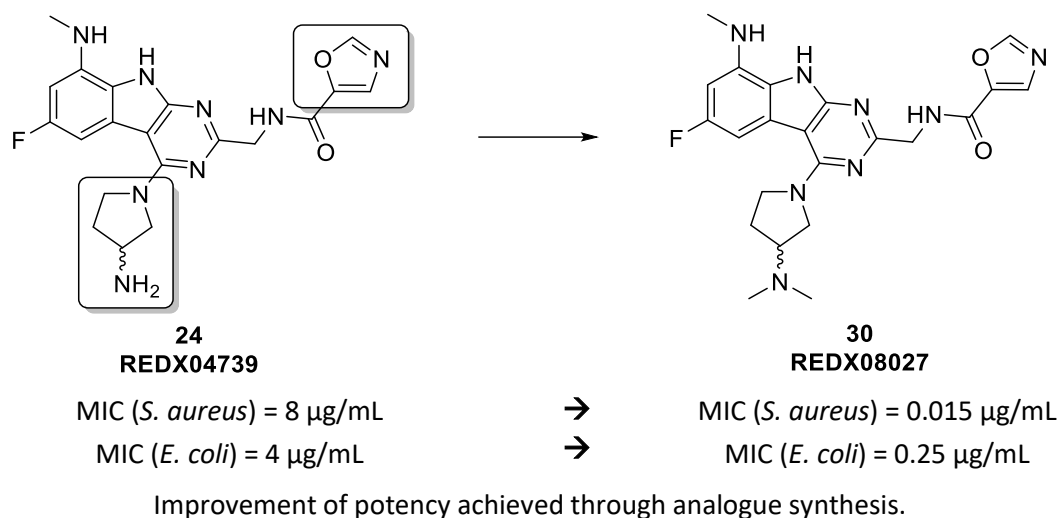
Figure 24

It was hypothesised that an improvement of physiochemical properties may be responsible for the increased potency of the series, allowing more efficient permeability across the bacterial membrane. Although superior potencies were achieved for the optimised compound, further work in this area would be required.

4.9 Future work

As a result of a combined experimental and computational effort, a potential method of increasing the antibacterial potency of the series was identified. Bicyclic analogues of REDX08027 **30** were highlighted as potential targets due to their ability to extend into an under-explored area of the binding site. In particular, azaindole **39** was suggested to be capable of binding to Asp106, resulting in increased affinity for the active site.
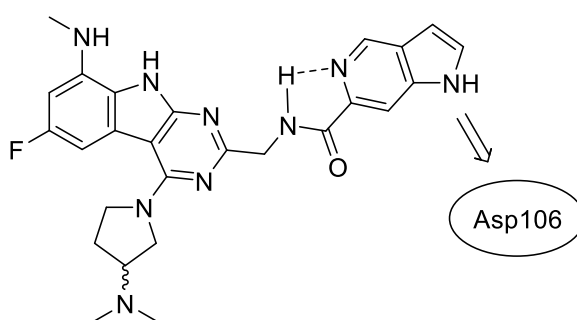
Azaindole **39** which may result in binding to Asp106.

Figure 25

Synthesis of azaindole **39** would allow assessment of the antibacterial activity to be subsequently performed. The nitrogen in the azaindole system was hypothesised to make an internal H-bond with the amide NH, tethering its conformation and forcing the pyrrole substituent into the appropriate vector for binding to Asp106. Furthermore, masking of H-bond donor/acceptor pairs is a known strategy to increase permeability, which may afford a further increase in antibacterial activity.

The success of the bicyclic amide replacement in increasing the activity of the compound would be regarded as indicative of the utility of the computational modelling of DNA gyrase subunit B. If the replacement was successful, the computational modelling would therefore be validated further.

However, as a result of the data collected throughout the research programme, increasing antibacterial activity was not considered a priority. Instead, future optimisation should be focussed on improving the physiochemical properties of the series. Solubility was deemed the most critical property to improve, which would allow for a more accurate assessment of toxicity trends to be performed.

It was envisioned that a key step in improving the solubility of the series would be by removing hydrogen-bond partners in the structure, alleviating the suspected high crystal packing of the compound. Therefore, future synthetic efforts should be focussed upon modifying the potential number of intermolecular hydrogen bonds (**Figure 26**).

37
REDX08271
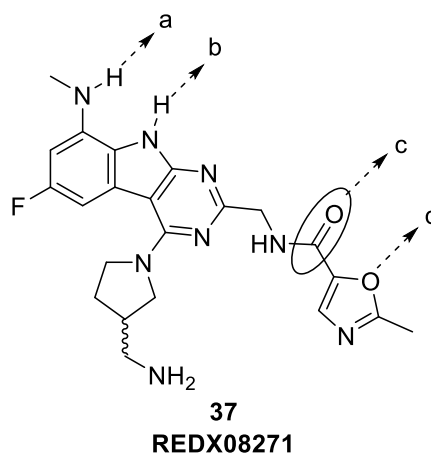
Potential positions of modification to lower crystal packing ability.

Figure 26

Performing the suggested structural modifications to REDX08271 **37** may potentially reduce the ability of the scaffold to form internal H-bonds. Although this may increase solubility by
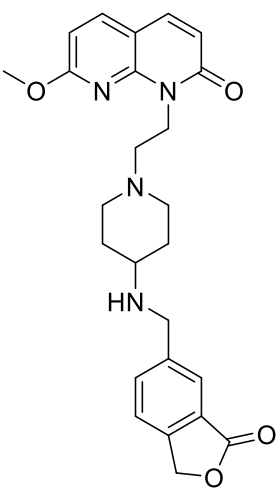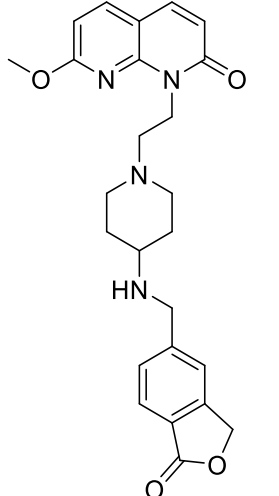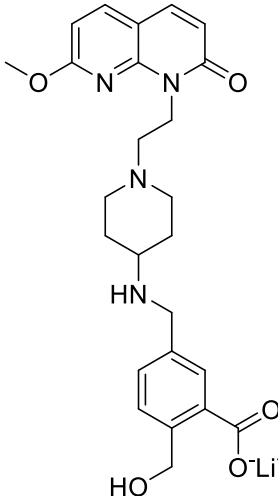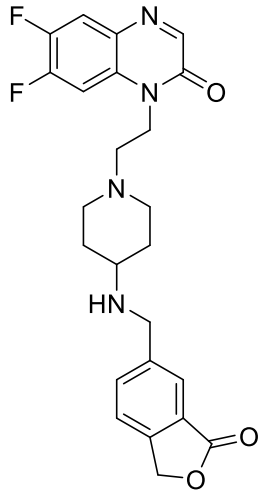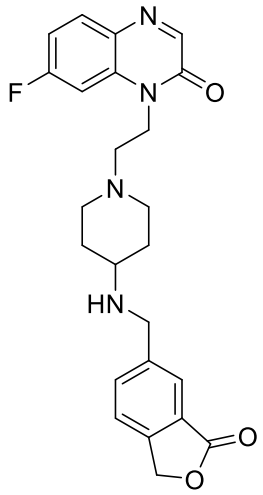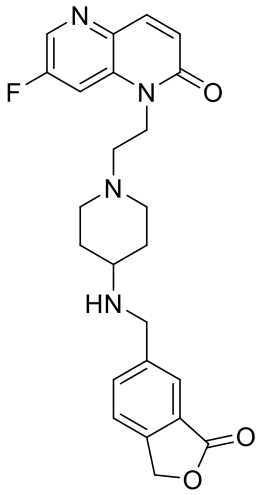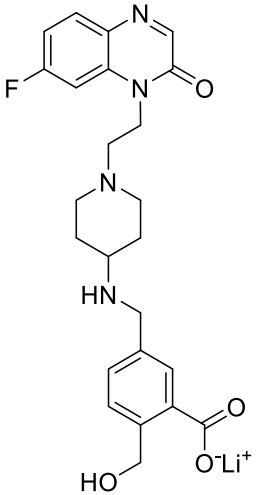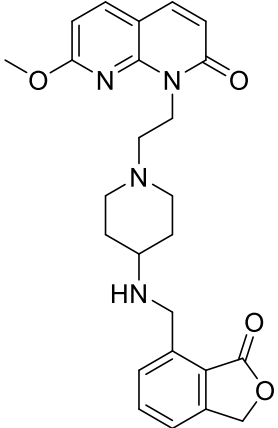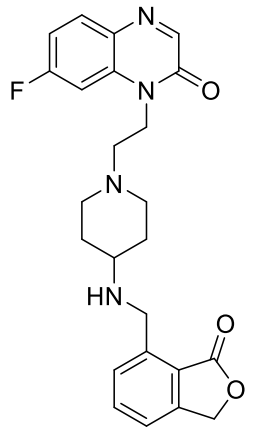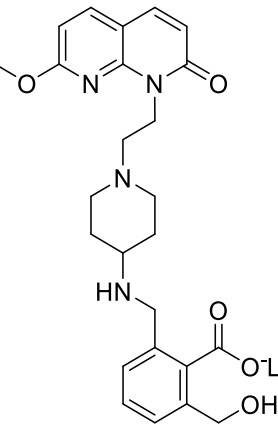
lowering the crystal packing ability of the structure, many of the positions capable of removing H-bond acceptor/donor pairs also play an integral part in the binding of the compound to the active site. A carefully considered approach should utilise computational modelling and efficient synthetic methods to maximise the likelihood of successfully increasing solubility while maintaining activity. Due to the integral nature of the tricyclic core, it could be envisioned that removal of the amide carbonyl (**Figure 26**, position **c**) may result in the disruption of internal H-bonding, while having minimal effect on the antibacterial potency of the series.

4.10 References

1. Tari, L. W.; Li, X.; Trzoss, M.; Bensen, D. C.; Chen, Z.; Lam, T.; Zhang, J.; Lee, S. J.; Hough, G.; Phillipson, D.; Akers-Rodriguez, S.; Cunningham, M. L.; Kwan, B. P.; Nelson, K. J.; Castellano, A.; Locke, J. B.; Brown-Driver, V.; Murphy, T. M.; Ong, V. S.; Pillar, C. M.; Shinabarger, D. L.; Nix, J.; Lightstone, F. C.; Wong, S. E.; Nguyen, T. B.; Shaw, K. J.; Finn, J. *PLOS ONE* **2013**, *8*, e84409.
2. Starr, J. T.; Sciotti, R. J.; Hanna, D. L.; Huband, M. D.; Mullins, L. M.; Cai, H.; Gage, J. W.; Lockard, M.; Rauckhorst, M. R.; Owen, R. M.; Lall, M. S.; Tomilo, M.; Chen, H.; McCurdy, S. P.; Barbachyn, M. R. *Bioorg. Med. Chem. Lett.* **2009**, *19*, 5302-5306.
3. Houben, E. N. G.; Nguyen, L.; Pieters, J. *Curr. Opin. Microbiol.* **2006**, *9*, 76-85.
4. *Fact Sheet 104: Tuberculosis*. World Health Organisation: March 2016. http://www.who.int/mediacentre/factsheets/fs104/en/ (accessed 12/08/2016).
5. Koul, A.; Arnoult, E.; Lounis, N.; Guillemont, J.; Andries, K. *Nature* **2011**, *469*, 483-490.
6. Janin, Y. L. *Bioorg. Med. Chem.* **2007**, *15*, 2479-513.
7. Zhang, Y.; Mitchison, D. *Int. J. Tuberc. Lung Dis.* **2003**, *7*, 6-21.
8. Lewis, R. J.; Singh, O. M.; Smith, C. V.; Skarzynski, T.; Maxwell, A.; Wonacott, A. J.; Wigley, D. B. *EMBO J.* **1996**, *15*, 1412-1420.
9. Hoeksema, H.; Johnson, J. L.; Hinman, J. W. *J. Am. Chem. Soc.* **1955**, *77*, 6710-6711.
10. Tsai, F. T. F.; Singh, O. M. P.; Skarzynski, T.; Wonacott, A. J.; Weston, S.; Tucker, A.; Pauptit, R. A.; Breeze, A. L.; Poyser, J. P.; O'Brien, R.; Ladbury, J. E.; Wigley, D. B. *Proteins* **1997**, *28*, 41-52.
11. Heide, L. *Int. J. Med. Microbiol.* **2014**, *304*, 31-36.
12. Tomašić, T.; Mašič, L. *Curr. Top. Med. Chem.* **2013**, *14*, 130-151.
13. Stammer, C. H.; Walton, E.; Wilson, A. N.; Walker, R. W.; Trenner, N. R.; Holly, F. W.; Folkers, K. *J. Am. Chem. Soc.* **1958**, *80*, 137-140.
14. Ferrero, L.; Cameron, B.; Crouzet, J. *Antimicrob. Agents Chemother.* **1995**, *39*, 1554-1558.
15. Burlison, J. A.; Neckers, L.; Smith, A. B.; Maxwell, A.; Blagg, B. S. J. *J. Am. Chem. Soc.* **2006**, *128*, 15529-15536.
16. Nordenberg, J.; Albukrek, D.; Hadar, T.; Fux, A.; Wasserman, L.; Novogrodsky, A.; Sidi, Y. *Br. J. Cancer* **1992**, *65*, 183-188.
17. Phillips, John W.; Goetz, Michael A.; Smith, Scott K.; Zink, Deborah L.; Polishook, J.; Onishi, R.; Salowe, S.; Wiltsie, J.; Allocco, J.; Sigmund, J.; Dorso, K.; Lee, S.; Skwish, S.; de la Cruz, M.; Martín, J.; Vicente, F.; Genilloud, O.; Lu, J.; Painter, Ronald E.; Young, K.; Overbye, K.; Donald, Robert G. K.; Singh, Sheo B. *Chem. Biol.* **2011**, *18*, 955-965.
18. Charifson, P. S.; Grillot, A.-L.; Grossman, T. H.; Parsons, J. D.; Badia, M.; Bellon, S.; Deininger, D. D.; Drumm, J. E.; Gross, C. H.; LeTiran, A.; Liao, Y.; Mani, N.; Nicolau, D. P.; Perola, E.; Ronkin, S.; Shannon, D.; Swenson, L. L.; Tang, Q.; Tessier, P. R.; Tian, S.-K.; Trudeau, M.; Wang, T.; Wei, Y.; Zhang, H.; Stamos, D. *J. Med. Chem.* **2008**, *51*, 5243-5263.
19. Grillot, A.-L.; Tiran, A. L.; Shannon, D.; Krueger, E.; Liao, Y.; O'Dowd, H.; Tang, Q.; Ronkin, S.; Wang, T.; Waal, N.; Li, P.; Lauffer, D.; Sizensky, E.; Tanoury, J.; Perola, E.; Grossman, T. H.; Doyle, T.; Hanzelka, B.; Jones, S.; Dixit, V.; Ewing, N.; Liao, S.; Boucher, B.; Jacobs, M.; Bennani, Y.; Charifson, P. S. *J. Med. Chem.* **2014**, *57*, 8792-8816.
20. East, S. P.; White, C. B.; Barker, O.; Barker, S.; Bennett, J.; Brown, D.; Boyd, E. A.; Brennan, C.; Chowdhury, C.; Collins, I.; Convers-Reignier, E.; Dymock, B. W.;
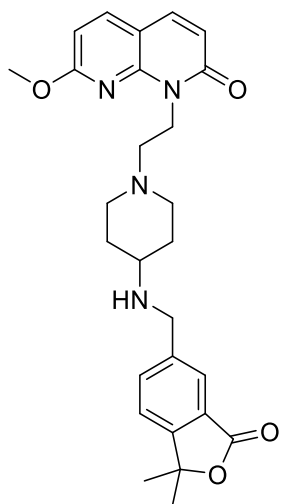
Fletcher, R.; Haydon, D. J.; Gardiner, M.; Hatcher, S.; Ingram, P.; Lancett, P.; Mortenson, P.; Papadopoulos, K.; Smee, C.; Thomaides-Brears, H. B.; Tye, H.; Workman, J.; Czaplewski, L. G. *Bioorg. Med. Chem. Lett.* **2009**, *19*, 894-899.

21.   Manchester, J. I.; Dussault, D. D.; Rose, J. A.; Boriack-Sjodin, P. A.; Uria-Nickelsen, M.; Ioannidis, G.; Bist, S.; Fleming, P.; Hull, K. G. *Bioorg. Med. Chem. Lett.* **2012**, *22*, 5150-5156.

22.   Tari, L. W.; Trzoss, M.; Bensen, D. C.; Li, X.; Chen, Z.; Lam, T.; Zhang, J.; Creighton, C. J.; Cunningham, M. L.; Kwan, B.; Stidham, M.; Shaw, K. J.; Lightstone, F. C.; Wong, S. E.; Nguyen, T. B.; Nix, J.; Finn, J. *Bioorg. Med. Chem. Lett.* **2013**, *23*, 1529-1536.

23.   Trzoss, M.; Bensen, D. C.; Li, X.; Chen, Z.; Lam, T.; Zhang, J.; Creighton, C. J.; Cunningham, M. L.; Kwan, B.; Stidham, M.; Nelson, K.; Brown-Driver, V.; Castellano, A.; Shaw, K. J.; Lightstone, F. C.; Wong, S. E.; Nguyen, T. B.; Finn, J.; Tari, L. W. *Bioorg. Med. Chem. Lett.* **2013**, *23*, 1537-1543.

24.   Finn, J.; Tari, L., William; Chen, Z.; Zhang, J.; Phillipson, D.; Le, S., Joong; Trzoss, M.; Bensen, D.; Li, X.; Teng, M.; Ong, V.; Borchardt, A., John; Lam, T., To. WO 2015038661. **2015**.

25.   *Unpublished data, Redx Pharmaceuticals* **2013**.

26.   Reyrat, J.-M.; Kahn, D. *Trends Microbiol.* **2001**, *9*, 472-473.

5   Appendices

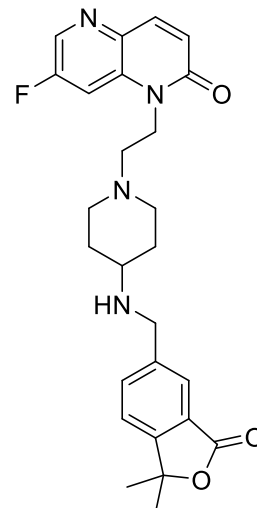## 5.1   Summary of synthesised compounds from Chapter 2

5-membered (undecorated) 6-substituted pyridyl lactone series			
REDX08220 **23**	REDX08881 **41**	REDX08730 **46**	REDX08942 **47**
REDX08495 **42**		REDX08911 **43**	

5.2 Summary of synthesised compounds from Chapter 3

5-membered (undecorated) 6-substituted phenyl lactone series

REDX10141 **59**	REDX10012 **67**	REDX10142 **77**

REDX10307 **74**	REDX10159 **75**	REDX10306 **76**	REDX10204 **78**

5-membered (undecorated) 7-substituted phenyl lactone series

REDX10248 **84**	REDX10281 **85**	REDX10284 **86**

6-membered (undecorated) 6-substituted phenyl lactone series

| REDX10359 **90** | REDX10386 **91** | REDX10403 **92** |

5-membered (methylated) 6-substituted phenyl lactone series

| REDX10370 **105** | REDX10371 **106** | (*R*)-REDX10371 **107** | (*S*)-REDX10371 **108** |

| REDX10725 **109** | (*R*)-REDX10725 **110** | (*S*)-REDX10725 **111** |

5-membered (dimethylated) 6-substituted phenyl lactone series	
REDX10387 **116**	REDX10388 **117**
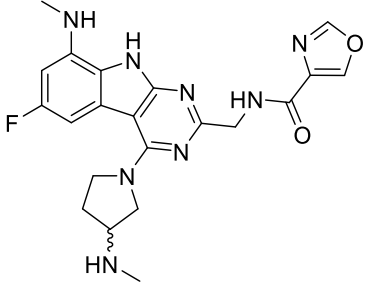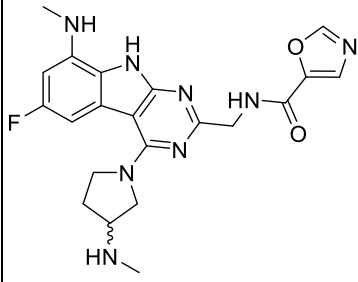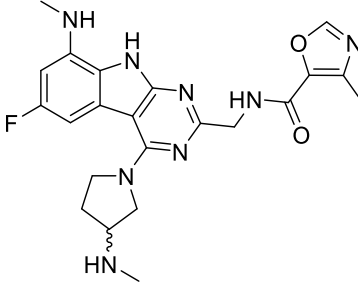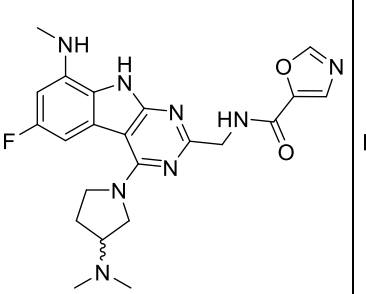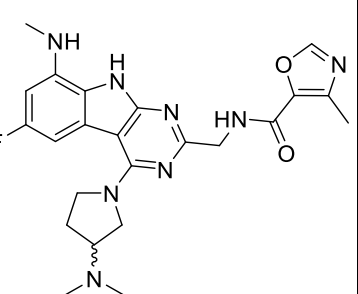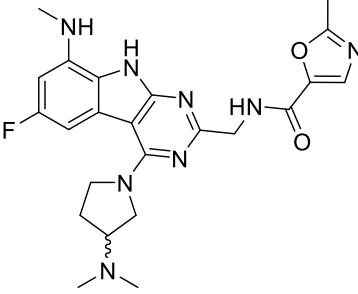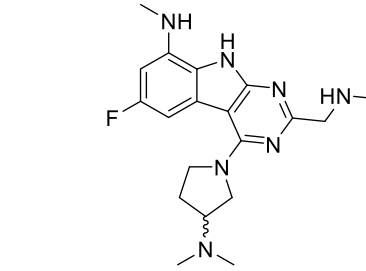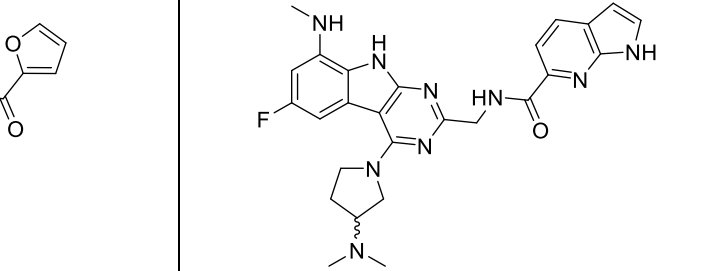
5.3   Summary of synthesised compounds from Chapter 4

N-methylated aminopyrrolidine series		
REDX07942 **27**	REDX07774 **28**	REDX07966 **29**

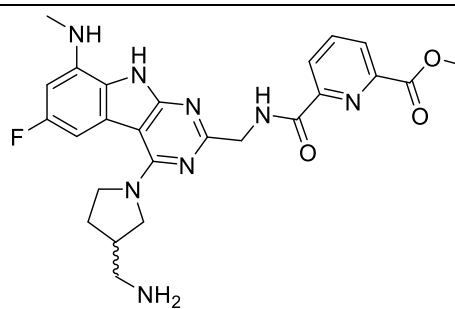| **N,N-dimethylated aminopyrrolidine series**		
REDX08027 **30**	REDX08049 **31**	REDX08066 **32**
REDX09133 **33**		REDX09147 **34**
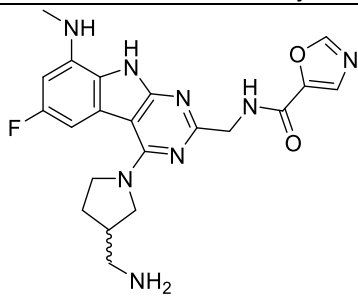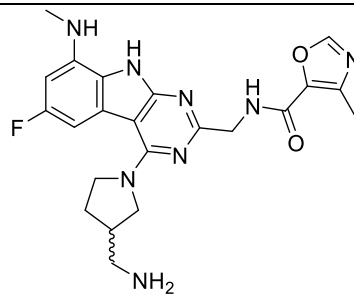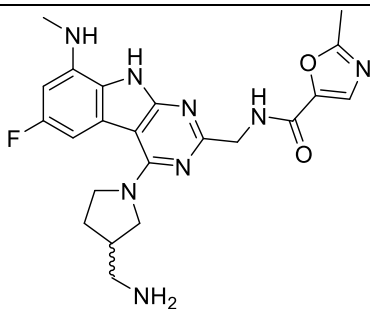
Methylamino aminopyrrolidine series	
REDX08191 **35**	REDX08230 **36**
REDX08271 **37**	REDX08365 **38**